Measurement of the Λ_b polarization and angular parameters in $\Lambda_b \to J/\psi\Lambda$ decays from pp collisions at $\sqrt{s} = 7$ and 8 TeV

Rogelio Reyes Almanza

Department of Physics
Centro de Investigación y Estudios Avanzados

This dissertation is submitted for the degree of
Doctor of Science

CINVESTAV November 2018

I would like to dedicate this work to my parents, brothers and to Perla :) …

Acknowledgements

This gives me an excuse to sit down and think about who along of the PhD gave me knowledge and experience and help. It does not have to be a long letter and it can simply be a note of thanks for the contribution this individual makes and your gratitude for the company, patience, and the hard work.

Immediately after agreeing to work in the PhD with Dr. Heriberto Castilla-Valdez, he told me "You have to go to CERN in 15 days". It was my the first time I was traveling abroad and the news left me in shock. Days before to traveling, Heriberto warned me that Mexicans we do not back out (this is the polite version) and that was how I started the PhD. There were hard days and very good ones but in general I am grateful. So, thank you Heriberto for the guidance, support, patience, advice, chatting and the meetings with jokes.

I would like to thank CMS people, Kirsti Aspola for supporting; the former tracker online team, Derek, Johnny, Mathew, Thomas, Gabrielle, and the Butz, they gave me the first experiences in the collaboration; the RPC manager Gabiella Pugliese for supporting me, and the RPC group for the knowledge and experience in the last years; the conveners of b-Physics group, Sandra Malvezzi, Mario Galanti, Martino Margoni, Alexis Pompilli and Nuno Leonardo for to approve this work and the provided knowledge and experience; Thomas Ferguson and Tommasso Bocalli who pushed and approved this work to the last steps.

My first time at CERN and Fermilab is full of histories. It was nice thanks to many people who are still friends. Thanks to Ana Maria Coacci that has always had the open doors of her home to me. Thank you Christian, Abraham, Luis, Areli, and Jesus Orduña (in FermiLab) mexicans do not leave you alone either. I will always be grateful.

I would like to express my gratitude to Iraq, part of this work was thanks to him, thanks for the company, help in difficult days and your friendship; to Jhovanny Mejia, thanks for sharing your knowledge and time to teach and for your friendship; to my colleagues Mateo, Cecilia, Beto Almada, Heber, I have always learned something new from you; and thank you Yolima for sharing experiences and friendship.

My most sincere respect and gratitude to the high-energy physics group of CMS in CINVESTAV, starting from Dr. Ivan Heredia, part of this work is yours thanks for sharing your knowledge and experience; to Drs. Eduard de la Cruz, Alberto Sanchez, most of the experience I owe to you.

Thanks to the administrative assistants that made my life easier. Thank you Audrey Balzano, Anna Yaneva, Tania Pardo, Nicoletta Barzaghini from CERN and CMS. Thank you Flor Ibañez, Rosemary Ovando, Paty Villar and lizabeth Mote from CINVESTAV.

Thank you CONACYT for solving my education.

Thank you EPLANET for solving a research stay at CERN.

Thank you CINVESTAV for gave me all privileges being student and member of the Physics department. I feel very proud of that.

Last but not least important.

Thanks to my closest friends Cesar, Manolo, Isra, Roma, Chileno lifelong friends.

To my parents mom and dad, my brothers Artur and Abraham, thanks I owe everything to you; and in general thank you family for supporting.

Thank you Perla for all love you have given me since we are together,

But now it's getting late
And the moon is climbing high
I want to celebrate
See it shining in your eye.

Resumen

Los c(charm) and b(bottom) quarks (heavy quarks) tienen masas arriba de la escala de QCD (cromodinamica cuántica), su production y tratamiento teórico debe ser calculable a nivel perturbativo. Hay muchas implementaciones comunes usando este enfoque, las más comunes QCD factorization (QCDF), perturbative QCD (pQCD), heavy-quark-effective theory (HQET) por decir algunas. Bajo este enfoque de quarks pesados se soporta la suposición de que la información proveniente del quark se preserva después de la hadronización.

En este trabajo, un análisis angular del barion Λ_b en los decaimientos $\Lambda_b \rightarrow J/\psi\,\Lambda$, que fue realizado para medir la polarización de y tres parámetros angulares, así com o las amplitudes de helicidad en el decaimiento. El análisis se llevo a cabo tomando datos de colisiones proton-proton a energías del centro de masa de 7 y 8 TeV, colectados por el detector CMS en el LHC. La polarización de medida es de $0.00 \pm 0.06\,(\text{stat}) \pm 0.06\,(\text{syst})$ y el parámetro de asimetría de violation de paridad de $0.14 \pm 0.14\,(\text{stat}) \pm 0.10\,(\text{syst})$. Las medidas son comparadas con varias predicciones teóricas incluyendo aquellas de QCD y con medidas de los experimentos LHCb y ATAS del LHC.

Abstract

The c and b quarks have masses significantly above of the Λ_{QCD} QCD scale, and therefore their production and treatment should be perturbatively calculable. There are many common implementations taking these ideas, the most common QCD factorization (QCDF), perturbative QCD (pQCD), heavy-quark-effective theory (HQET). The assumption heavy quarks remain quark information rather hadronization has support under the heavy quark approach.

In this work, an analysis of the bottom baryon decay is performed to measure the Λ_b polarization and three angular parameters in data from pp collisions at $\sqrt{s} = 7$ and 8 TeV, collected by the CMS experiment at the LHC. The Λ_b polarization is measured to be $0.00 \pm 0.06\,(\text{stat}) \pm 0.06\,(\text{syst})$ and the parity-violating asymmetry parameter is determined to be $0.14 \pm 0.14\,(\text{stat}) \pm 0.10\,(\text{syst})$. The measurements are compared to various theoretical predictions, including those from perturbative quantum chromodynamics.

Table of contents

List of figures

List of tables

Nomenclature

Λ_{QCD} QCD scale

N_{bkg} Number of background events

N_{sig} Number of signal events

Roman Symbols

$\mathcal{L}_{int}$ Integrated luminosity

$\mathcal{L}$ Instantaneous luminosity

P Polarization

Acronyms / Abbreviations

CMSSW CMS software

ATLAS A Toroidal LHC Apparatus (experiment at the CERN physics laboratory)

BS Beam spot

CERN Conseil Europèen pour la Recherche Nuclèaire

CKM Cabibbo Kobayashi Maskawa matrix

CMS Compact Muon Solenoid (experiment at the CERN physics laboratory)

CP Charge-Parity symmetry

CSC Cathode strip chambers

CTF Combinatorial Track Finder

DAQ Data acquisition system

DCA Distance of Closest Approach

dof Degrees of freedom

DT Drift tubes

ECAL Electromagnetic calorimeter

EFT Effective Field Theory

EW Electro-weak

HCAL Hadronic calorimeter

HLT High level trigger

HQET Heavy Quark Effective Theory

IP Interaction point

L1 Level 1 trigger

LEP Large Electron-Positron Collider

LHCb Large Hadron Collider beauty (experiment at the CERN physics laboratory)

LHC Large Hadron Collider

LINAC Linear accelerator

MC Monte Carlo

ML Maximum Likelihood

PAG Physics Analysis Group

PDF Probability density function

PSB Proton Syncroton Booster

PS Proton Syncroton

PV Primary Vertex

QCD Quantum Chromodynamics

QED Quantum Electrodynamics

QFT	Quantum Field Theory
RF	Radio frequency
RPC	Resistive plate chambers
SB	Side Band
SD	Standard Deviation
SM	Standard Model
SPS	Super Proton Syncroton

Chapter 1

Introduction

The b (bottom) quark belongs to the third generation of quarks with its doublet partner the t (top) quark. The existence of the third generation of quark doublet was proposed by Kobayashi and Maskawa [1] in 1973 with their model of the quark mixing matrix (CKM matrix). There is evidence that the quarks exist as bound states (except for the t quark), the existence of quarks has been confirmed by hadrons [1], in particular the three generation was confirmed with the observation of the $b\overline{b}$ meson called $\Upsilon(b\overline{b})$ [2].

Since the b quark is the lighter element of the third generation quark doublet, the decays of b-flavored hadrons occur via generation-changing process through the CKM matrix elements. Because of this, and the fact that the CKM matrix is a 3×3 unitary matrix, many interesting features such as loop and box diagrams, flavor oscillations, as well as charge-parity (CP) asymmetries, can be observed in the weak decays of b-flavored hadrons.

Recent developments in physics of b hadrons (B-physics) include the significant improvement in experimental determination of CKM angle, the increased information on B_S, B_c and Λ_b decays, the precise measurement of Λ_b lifetime and decay angular parameters, the observation of the rare decay $B_S \to \mu^+\mu^-$ with ever increasing precision. Before to continue in the following we shall use nature units ($c = 1$ and $\hbar = 1$) unless otherwise stated.

In high energy collisions, the produced b or $\overline{b}$ quarks can hadronize with different probabilities into the full spectrum of b hadrons, either in ground or excited states. The world average production fraction of b baryons is $f_{\text{baryon}}(b \to \text{baryon}) = 8.5 \pm 1.1\%$ [3] in unbiased sample of weakly decaying b hadrons produced at the

[1] Hadrons are particles composed by quarks. The particles composed by two or three quarks are called mesons and baryons, respectively.

Z resonance, and $f_{\text{baryon}}(\text{b} \to \text{baryon}) = 19.7 \pm 4.6\%$ [3] in $\text{p}\overline{\text{p}}$ collisions, but these values are a mixture of Λ_b, Ξ_b^-, Ξ_b, Ω_b^-, Σ_b [2], etc. For many years, the only well established b baryon was Λ_b (quark composition udb) discovered in 1991 at CERN [4], and the only indirect evidence for Ξ_b (dsb) production from LEP [5, 6]. This situation has changed in the few last years with measurements from Tevatron and LHCb, however measurements of fragmentation fractions $f_{\Lambda_\text{b},\Xi_\text{b}^-,\Omega_\text{b}^-}$ are not well determined and they are presented as a product with the branching fractions, as is the case of $\mathcal{B}(\Lambda_\text{b} \to \text{J}/\psi\,\Lambda) f_{\Lambda_\text{b}} = 5.8 \pm 0.8 \times 10^{-5}$ [3].

A fundamental law of physics CPT invariance is the product of three operations, time reversal T, parity P, i.e. the inversion of the coordinates axes, and particle-antiparticle conjugation C. The CPT invariance implies that the particles and their antiparticles have the same mass , lifetime and spin and all charges of opposite values. The Λ_b particle has a spin 1/2 and positive intrinsic parity $\text{J}^\text{P} = 1/2^+$, however these values have not been measured.

On the other hand, the Λ_b mass m_{Λ_b} has the world-average value of $m_{\Lambda_\text{b}} = 5619.58 \pm 0.17\,\text{MeV}$ and the current world-average lifetime of $\tau_{\Lambda_\text{b}} = 1.470 \pm 0.010\,\text{ps}$ corresponding to the decay length of $c\tau = 440.7\,\mu\text{m}$ [3]. The Λ_b lifetime has a history of discrepancies, however with recent results from LHC experiments, the discrepancy between theory and experiment on the Λ_b lifetime can be considered resolved.

Many aspects of b hadronic decays can be understood through the Heavy Quark Effective Theory (HQET). For hadronic decays one typically uses effective Hamiltonian calculations that rely on a perturbative expansion with Wilson coefficients [7]. In addition some form of factorization hypothesis is commonly used, such that b hadron decays are expressed by the product of two independent currents, one describing the formation of charm meson and the other one the hadronization of the remaining $\overline{\text{c}}\text{s}$ system from the internal emission of W^- boson. Explicitly the Feynman diagram is shown in Figure 1.1.

The decay $\Lambda_\text{b} \to \text{J}/\psi\,\Lambda$ is a rich source of information about the effect of strong interactions in hadronic decays. For this particular decay, perturbative quantum chromodynamics (pQCD) can be applied and therefore a systematic approach can be taken to study its characteristics. Several techniques [8–17] are used to study and calculate the decay amplitudes and the effect of the b quark polarization on this decay. A measurement b quark polarization could provide crucial information about the structure of the new physics.

[2]Baryon states containing a b quark are labeled with a b subscript.

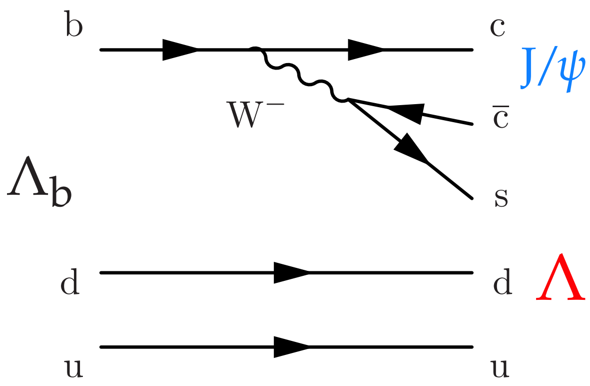

Fig. 1.1 Feynman diagram of $\Lambda_b \to J/\psi\,\Lambda$ decay

The most interesting parameters that can be measured are the polarization, P, and the parity-violating decay asymmetry of the Λ_b, which is called α_b in some papers and is equal to $-\alpha_1$ in the notation used in this analysis. The LHCb and ATLAS experiments have reported measurements on this decay [18, 19]. The LHCb Collaboration measured the Λ_b polarization and the decay amplitudes, while ATLAS assumed a Λ_b polarization of zero and measured the amplitudes. In this paper, a measurement of the Λ_b transverse polarization is presented using the decay $\Lambda_b \to J/\psi\,\Lambda$, with $J/\psi \to \mu^+\mu^-$ and $\Lambda \to p\pi^-$. Charge-conjugate modes are implied throughout this work unless otherwise stated.

The data were collected with the CMS detector in pp collisions at center-of-mass energies of 7 and 8 TeV, corresponding to integrated luminosities of 5.2 and 19.8 fb^{-1}, respectively.

Chapter 2

Theoretical and experimental techniques

In the following sections we review the theoretical framework and tools used in the analysis. The information were extracted from Refs. [20, 21] and different reviews in Ref. [3].

2.1 Preliminary concepts and decays

2.1.1 Spin density matrix and polarization

A particle A with spin J can be represented by a mixture of quantum states $|psi\rangle$, accounting for all possible projections M of the spin which take on values $\{-J, ..., J\}$ then

$$|\psi\rangle = \sum_{M=-J}^{+J} c_M |JM\rangle \tag{2.1}$$

where c_M are complex coefficients. The spin density matrix d of the system is then

$$d = |\psi\rangle \langle\psi| . \tag{2.2}$$

its dimension is $(2J+1) \times (2J+1)$ and has the following properties:

- It is Hermitian $d^\dagger = d$ i.e. the matrix elements $d^*_{M'M} = d_{MM'}$
- Tr(d) = 1.
- The expectation value for an arbitrary physical observable with a corresponding Hermitian operator OP is given by $\langle OP\rangle = \mathrm{Tr}(d\,OP)$.

On the other hand, the polarization characterizes the alignment of the particle spin with a given direction. Consider the set of matrices $\vec{S}$ representing the spin operator. By the definition the polarization vector is given by the expectation value of the spin matrices,

$$\vec{P} = \left\langle \vec{S} \right\rangle = \frac{\mathrm{Tr}(d\vec{S})}{\mathrm{Tr}(d)}, \tag{2.3}$$

where the denominator is a normalization factor. The known case for particles with spin-1/2 where $\vec{S}$ are the Pauli matrices $\vec{\sigma}$ and the spin density matrix is defined by

$$d = \frac{1}{2}(I + \sigma \cdot P). \tag{2.4}$$

A detailed review of the density matrix, polarization are found in Ref. [22] and a generalization of Pauli matrices in Ref. [23].

2.1.2 Decays

Subnuclear physics deals with two types of processes: collisions and decays. In both cases transition amplitude is given by the matrix elements of the interaction Hamiltonian between final $\langle f|$ and initial $|i\rangle$ states

$$M_{fi} = \langle f| H_{\mathrm{int}} |i\rangle .$$

Consider for example a the two-body decay $\mathrm{A} \to \mathrm{B} + \mathrm{C}$. Depending on what we measure, the final state can be defined with more or fewer details, for instance the decay rate $\Gamma_{\mathrm{B+C}}$, or partial width of A into B C channel [1], other quantity is the total width Γ which is the sum of all partial decay rates, or the branching ratio $\mathcal{BR} = \Gamma_{\mathrm{B+C}}/\Gamma$, etc.

We shall recall a few concepts starting with Fermi 'golden rule', which gives the interaction rate W per particle

$$W = 2\pi \left| M_{fi} \right|^2 \rho(E),$$

where E is the total energy and $\rho(E)$ is the phase-space volume (or simply the phase-space) available in the final state. In the non-relativistic formalism the probability of a particle i in the position $\vec{r}_i$ is $|\psi(\vec{r}_i)|^2$. However to have a Lorentz invariant,

[1]Given the initial particle A, we can have different particles in the final state. Each of these processes is called a channel and its decay rate is called the partial decay rate of that channel.

the probability density is defined as $\left|(2E)^{\frac{1}{2}}\psi(\vec{r}_i)\right|^2$ (the factor 2 is due to historical convention).

The number of phase-space per unit volume is $\mathrm{d}^3 p_k/h^3$ for each particle k in the final state. For n particles in the final state the volume of the phase space is therefore

$$\rho_n(E) = (2\pi)^4 \int \prod_{k=1}^{n} \frac{\mathrm{d}^3 p_k}{2E_k(h^3)} \delta(\sum_{k=1}^{n} E_k - E)\delta^3(\sum_{k=1}^{n} p_k - p)$$

or, in nature units ($\hbar = 1$ implies $h = 2\pi$)

$$\rho_n(E) = (2\pi)^4 \int \prod_{k=1}^{n} \frac{\mathrm{d}^3 p_k}{2E_k(2\pi)^3} \delta(\sum_{k=1}^{n} E_k - E)\delta^3(\sum_{k=1}^{n} p_k - p),$$

where p is the total momentum and δ is the Dirac function. In the case of the decay of a particle A with energy E and momentum p, the probability of transition of A into final state f of n particles per unit of time is

$$\Gamma_{fi} = \frac{1}{2E} \int |M_{fi}|^2 (2\pi)^4 \prod_{k=1}^{n} \frac{\mathrm{d}^3 p_k}{2E_k(2\pi)^3} \delta(\sum_{k=1}^{n} E_k - E)\delta^3(\sum_{k=1}^{n} p_k - p). \tag{2.5}$$

With these expressions, we can calculate the measurable quantities once the matrix elements are known. The Standard Model gives the rules to evaluate all the matrix elements in terms of set of constants. Even if we do not have the theoretical instruments for such calculations, we shall be able to understand the physical essence of the predictions of the model and study their experimental verification.

2.2 Standard Model and the CKM matrix

The standard model (SM) provides a simple picture of quarks and leptons and their non-gravitational interactions, which has been verified by many experiments during the last four decades. In brief, the picture is as follows. The matter units are arranged in three families of fermions with spin-1/2. They are two types, leptons and quarks. Both are structureless at the smallest distances probed by the highest-energy accelerators. The leptons are generalizations of the electron, the term denoting particles which, if charged, interact both electromagnetically and weakly; and if neutral, only weakly. By contrast, the quarks interact via all three interactions strong, weak and electromagnetically. The weak and electromagnetic interactions of both quarks and leptons are described in a unified way by the electroweak (EW) theory by Glashow, Salam and Weinberg, which is a generalization of quantum electrodynamics (QED), the theory is described by the symmetry group $SU(2) \times U(1)$. On the other hand, strong interactions of quarks are described by quantum chromodynamics (QCD), which is also an analogous of QED and described by the group symmetry $SU(3)$. The similarity with QED lies in the fact that all three interactions are types of gauge theories. The mediators of those interactions are bosons, particles of spin-1, whose are photons, two $W^{\pm}$, Z^0, and six kind of gluons. The picture is summarized in Fig. 2.1.

Quarks carry color charge, and the gluons mediate the strong interactions between color charged particles. A consequence of the QCD theory is that quarks are strongly bound (confined) in color-neutral composite particles, the hadrons.

In the SM the mass of the quarks, flavor violation and CP violation arise from Yukawa interactions with the Higgs field. The strength of the flavor-changing through a charged W boson are parametrized by entries of the CKM matrix (V_{CKM}) in the charge current J^{μ}_{CC} associated to W boson field the Lagrangian

$$\mathcal{L}_{CC} = -\frac{g}{\sqrt{2}} J^{\mu}_{CC} W^{\dagger}_{\mu} + \text{h.c.}, \tag{2.6}$$

where γ^{μ} are the Dirac matrices notation and h.c. stands for the Hermitian conjugate of the previous terms, the J^{μ}_{CC} is given as

$$J^{\mu}_{CC} = \begin{pmatrix} \overline{\nu_e} & \overline{\nu_\mu} & \overline{\nu_\tau} \end{pmatrix} \gamma^{\mu} \begin{pmatrix} e_L \\ \mu_L \\ \tau_L \end{pmatrix} + \begin{pmatrix} \overline{\text{u}}_L & \overline{\text{c}}_L & \overline{\text{t}}_L \end{pmatrix} \gamma^{\mu} V_{\text{CKM}} \begin{pmatrix} \text{d}_L \\ \text{s}_L \\ \text{b}_L \end{pmatrix}, \tag{2.7}$$

and the CKM matrix is given by

$$V_{\text{CKM}} = \begin{pmatrix} V_{\text{ud}} & V_{\text{us}} & V_{\text{ub}} \\ V_{\text{cd}} & V_{\text{cs}} & V_{\text{cb}} \\ V_{\text{td}} & V_{\text{ts}} & V_{\text{tb}} \end{pmatrix}. \tag{2.8}$$

Mathematically, the CKM matrix is derived from the unitary matrices to transform the weak eigenstates into the mass eigenstates for left-handed quark fields. Physically, the element V_{ij} describes the probability of a transition from one quark flavor i to another quark flavor j. These transitions are proportional to $|V_{ij}|^2$.

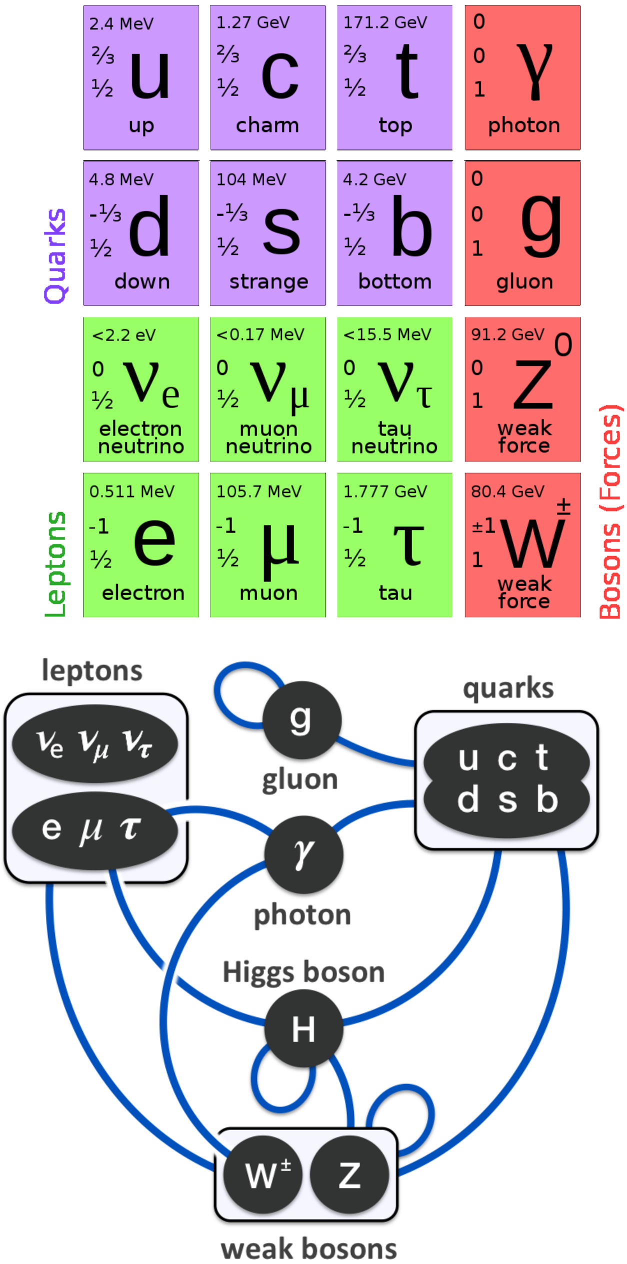

Fig. 2.1 The standard model of elementary particles and their interactions [24].

To deal with strong interactions, depending on the case theoretical approaches and tools have been developed such as perfect symmetries (CP conservation), approximate symmetries (Isospin, flavor $SU(3)$, chiral and heavy quark symmetries). lattice QCD (LQCD), perturbation QCD (pQCD) for exclusive processes, QCD sum rules (QCDSR), etc.

2.3 Effective field theories

Quantum field theories (QFT) provides a precise computational tools for describing physics at highest energies. One of their characteristic features is that they almost inevitably involve multiple length scales. As reviewed in Sec. 2.1 the calculations demands that all possible virtual states and hence all particles be included. Since these particles have widely different masses, the final prediction is sensitive to many scales. This represents a practical point of view because no realistic QFTs can be solved exactly,and one needs to resort to approximation schemes.

Effective field theories (EFTs) provide a general theoretical framework to deal with multi-scale problems of realistic QFTs. This framework aims at reducing such problems to a combination of separate and simpler single-scale problems. EFTs can play a role both within analytic perturbative computations and in the context of non-perturbative numerical simulations.

One of the simplest applications of EFTs to particle physics concerns the description of an underlying theory that is only probed at energy scales $E < \Lambda$. Any particle with mass $m > \Lambda$ cannot be produced as a real state and therefore only leads to short-distances virtual effects. Thus, one can construct an effective theory in which the quantum fluctuations of such heavy particles are "integrated out" form generating functional for Green functions. This results in a simpler theory containing only those degrees of freedom that are relevant to the energy scales under consideration.

2.3.1 Heavy quarks

A heavy quark is by definition a quark with mass much larger than QCD scale [2] ($m_\mathrm{q} \gg \Lambda_\mathrm{QCD}$). In the SM u, d, and s are light quarks, whereas c, b, and t are heavy quarks. These heavy-quarks systems provide prime examples for applications of EFT because provides a natural separation of scales. Physics at m_q scale is a short-distance nature and can be treated pertubatively, while for heavy-quark is always also some hadronic physics governed by the confinement scale Λ_QCD of the strong interaction. Being able to separate the short- to long-distance effects associated with these two scales is crucial for any quantitative description.

[2] $\Lambda_\mathrm{QCD} = 220\,\mathrm{MeV}$

2.4 Expectations on the polarization and asymmetry parameter of Λ_b

In QCD massless quarks conserves helicity and no single-quark polarization can occur. Once the mass parameter is non zero. the helicity conservation can be violated allowing for helicity flip and thus single-flip helicity amplitudes requires imaginary parts of the amplitudes which are only generated in loop corrections.

The polarizations expected from the QCD processes $qq' \to qq'$, $qg \to qg$, $gg \to q\overline{q}$, $qg \to qg$ and $q\overline{q} \to q'\overline{q}'$ are calculated and summarized in Ref. [25]. The largest contributions for the quark polarization come from quark annihilation (~ 0.10) and gluon fusion (~ 0.05). From the calculation in Ref. [25] it follows that the polarization should depend on the quark mass at a given momentum the heaviest quark acquires the largest polarization. The maximum occurs at $m_q/p_q \simeq 0.3$, where m_q and p_q are the quark mass and momentum, respectively, and the b quark polarization is predicted to be greater an order of magnitude than the s quark. It is not possible to measure directly the polarization of a quark (except for top), but it can be deduced from the polarization of the resultant hadrons.

For Λ_b baryons originating from energetic b quark, heavy-quark effective theory (HQET) predicts a large fraction of the transverse b quark polarization to be retained after hadronization [26, 8], while longitudinal polarization should vanish due to parity conservation in strong interactions. Theoretical predictions of the transverse polarization in Λ_b decays are 0.10 [12] and 0.20 [13]. The SM predicts that b quarks from Z^0 have large longitudinal polarization retained by the resultant baryon [26, 9]. The longitudinal Λ_b polarization have been measured at LEP in $e^-e^+ \to Z^0 \to b\overline{b}$, the reported polarizations spread in the range $(-0.79, +0.01)$ [10, 27, 28], while the only measurement of the transverse Λ_b polarization in pp collisions was reported by LHCb [18], excluding a polarization of 0.20 at the level of 2.7 standard deviations.

Λ_b baryons can also be produced as decay products of heavier states by strong decays of $\Sigma_b^{*\pm} \to \Lambda_b \pi^{\pm}$[29–32], where the polarization is partially diluted [12, 33]. These strong decays are experimentally difficult to distinguish from Λ_b that hadronize directly from pp collisions, therefore contribute to the measurement presented in this work.

The parity violating asymmetry parameter of the $\Lambda_b \to J/\psi\,\Lambda$ decay is of particular interest since provide a test for various quark models such pQCD and factorization models. Calculations of this parameter are predicted in many publications. The expectations vary within a wide range, generally between -0.14 and 0.78. Table 2.1

shows the expectations values. A measurement of this parameter is of high interest to point the quark models with realistic predictions.

Table 2.1 Asymmetry parameter predictions in $\Lambda_b \to J/\psi\,\Lambda$ decays.

Method	Value	Reference
Factorization	-0.1	[34]
Factorization	-0.18	[35]
Covariant oscillator quark model	-0.208	[36]
Perturbative QCD	-0.17 to -0.14	[17]
Factorization (HQET)	0.777	[13]
Light front quark model	-0.204	[37]
Covariant confined quark model	-0.07	[16]

2.5 Helicity formalism

The helicity formalism is well suited to relativistic problems because the helicity operator is invariant under both rotations and boost. The formalism provides a method to obtain the angular distributions of a decay particle. It is described in detail in Refs. [38, 39] and more recently in Ref. [40] in its arXiv version. The method derives from conservation of the total angular momentum and CP conservation in strong and electromagnetic decays. A short overview is discussed as follows.

The total angular momentum $\vec{J}$ combines the spin $\vec{S}$ and the orbital angular momentum $\vec{L}$,

$$\vec{J} = \vec{L} + \vec{S}.$$

We now that the total angular momentum of a system is a conserved quantity by Noether's theorem. For a particle with momentum $\vec{p}$ and total angular momentum $\vec{J}$, the helicity operator λ is defined as the projection of the total angular momentum on the momentum direction:

$$\lambda = (\vec{L} + \vec{S}) \cdot \frac{\vec{p}}{|\vec{p}|} = \vec{S} \cdot \frac{\vec{p}}{|\vec{p}|}, \tag{2.9}$$

where the total angular momentum has not component along of the direction of $\hat{p}$. As a consequence from Eq. 2.9 one can construct a relativistic basis where its eigenstates are either of total angular momentum and helicity or linear momentum and helicity. If the m is the spin quantum number thus the eigenvalues of the helicity λ are $2m+1$ with values $\{-m, ..., m\}$.

Let us focus in the two-body decay $A \to B + C$, where A has total angular momentum J_A and spin-projection m_A along a quantization $z-$axis. Thus A can be expressed in the basis of its spin eigenstates $|J_A, m_A\rangle$. Applying the rotation operator $\mathcal{R}(\theta, \varphi, \phi)$[3] it is possible to get the spin eigenstates of the particle A in the center of mass (CM) frame, $|J_A, m'_A\rangle$, with the help of Wigner's D-matrices

$$|J_A, m_A\rangle = \sum_{m'_A} D^{J_A}_{m_A m'_A}(\theta, \varphi, \phi)^* \, |J_A, m'_A\rangle, \tag{2.10}$$

where

$$D^{J_A}_{m_A m'_A}(\theta, \varphi, \phi)^* = \langle J_A, m_A| \, \mathcal{R}(\theta, \varphi, \phi) \, |J_A, m'_A\rangle^* = e^{i m_A \theta} d^{J_A}_{m_A m'_A}(\varphi) e^{i m'_A \phi}, \tag{2.11}$$

and where the small-d Wigner matrix contains known functions of φ that depend on J_A, m_A, and m'_A.

If we choose the rest frame of A with $|J_A, m'_A\rangle$, the final states B and C particles have momenta $\vec{p}_B = p_f$ and $\vec{p}_C = -p_f$ and helicities λ_1 and λ_2, respectively. The key idea in the helicity formalism is that rotational invariance of the helicities allows to define a set of two-particles basis states $|j, m', \lambda_1, \lambda_2\rangle$, where j total angular momentum, angular projection m', and helicities λ_1, λ_2, i.e., the final states can be characterized by the direction of a decay axis given by polar and azimuthal angles (θ, φ, ϕ), and by the helicity states of the decay products.

Since angular momentum conservation requires $m'_A = m'_B + m'_C = \lambda_1 - \lambda_2$ (because Eq. 2.9, and B and C go in opposite directions), it can be demonstrated that the transition amplitude

$$M_{fi} = T^{A\to B+C}_{\lambda_1, \lambda_2} D^{J_A}_{m_A, \lambda_1 - \lambda_2}(\theta, \varphi, \phi)^*, \tag{2.12}$$

where $T^{A\to B+C}_{\lambda_1, \lambda_2}$ are complex constants describing the helicity couplings $J = L + S$ in terms of Clebsch-Gordon coefficients and the helicities $\lambda = \lambda_1 - \lambda_2$. If the decay is strong or electromagnetic, it conserves parity which reduces the number of independent helicity couplings via the relation

$$T^{A\to B+C}_{-\lambda_1, -\lambda_2} = P_A \, P_B \, P_C (-1)^{j_B + j_C - J_A} T^{A\to B+C}_{\lambda_1, \lambda_2}, \tag{2.13}$$

[3] θ, φ and ϕ are the Euler angles

where P stands for the intrinsic parity of a particle. In addition the sum over L and S is constrained by the value of J and takes values $|L - S| \leq J \leq L + S$, next possible helicities are constrained by $|\lambda_1| \leq j_B$, $|\lambda_2| \leq j_C$ and $|\lambda_1 - \lambda_2| \leq J_A$.

2.5.1 Angular distributions

In the collisions $pp \to \Lambda_b + X$, Λ_b is produced by strong interactions originating from energetic b quarks. According to theory a large fraction of transverse polarization is predicted and retained after hadronization, while longitudinal polarization should vanish due to parity conservation in strong mechanism [8, 9, 13].

In pp collisions, we define the transverse polarization of the Λ_b as the mean value of the Λ_b spin along the unit vector:

$$\hat{n} = \frac{\vec{p}_{\text{beam}} \times \vec{p}_{\Lambda_b}}{\left|\vec{p}_{\text{beam}} \times \vec{p}_{\Lambda_b}\right|}, \tag{2.14}$$

normal to its production plane in the rest frame of Λ_b, where $\vec{p}_{\text{beam}}$ is in the direction of the counterclockwise proton beam direction [41], and $\vec{p}_{\Lambda_b}$ is the Λ_b momentum. In the rest frame of Λ_b the quantization axis z is chosen parallel to $\hat{n}$. The choice of the orthogonal axis xy is not important since the production process ensures azimuthal symmetry.

The $\Lambda_b \to J/\psi\,\Lambda$ decay into the $\mu^+\mu^-\ p\pi^-$ final state is illustrated in Fig. 2.2. Particles in the $\Lambda_b \to J/\psi\,\Lambda$ decay have well defined spins 1/2, 1/2 and 1 for Λ_b, Λ and J/ψ, respectively. If λ_1 and λ_2 are the helicities for Λ and J/ψ, respectively, it follows that possible helicities are $\lambda_1 = \pm 1/2$ and $\lambda_2 = 0, \pm 1$. Since the spin projections m_{Λ_b} of the Λ_b along of the $z-$axis are $\pm 1/2$, it must be satisfied $\pm 1/2 = \lambda_1 - \lambda_2$, and then the available matrix elements of $T^{\Lambda_b \to J/\psi\,\Lambda}_{\lambda_1,\lambda_2}$ are T_{--}, T_{+0}, T_{++}, T_{-0}.

The total decay chain $\Lambda_b \to J/\psi(\mu^+\mu^-)\Lambda(p\pi^-)$ is more complicated than the two-body decay $A \to B + C$, however the calculation can be found in Ref. [14] and the joint angular distribution is given by five observable angles

$$\frac{d^5\Gamma}{d\cos\theta_\Lambda d\Omega_p d\Omega_\mu}\left(\theta_\Lambda, \theta_p, \theta_\mu, \varphi_p, \varphi_\mu\right) = W(\theta_\Lambda, \theta_p, \theta_\mu, \varphi_p, \varphi_\mu), \tag{2.15}$$

where, the angle θ_Λ is the polar angle of the Λ momentum relative to $\hat{n}$ in the Λ_b rest frame; θ_p and φ_p are the polar and azimuthal angles of the proton, respectively, defined with respect to the axes $\hat{z}_1 = \vec{p}_\Lambda / |\vec{p}_\Lambda|$ and $\hat{y}_1 = (\hat{n} \times \vec{p}_\Lambda) / |\hat{n} \times \vec{p}_\Lambda|$ in the rest frame of the Λ; and the angles θ_μ and φ_μ are the polar and azimuthal angles, respectively, of the positively charged muon, defined with respect to the axes $\hat{z}_2 = \vec{p}_{\mathrm{J}/\psi}/|\vec{p}_{\mathrm{J}/\psi}|$ and $\hat{y}_2 = (\hat{n} \times \vec{p}_{\mathrm{J}/\psi})/|\hat{n} \times \vec{p}_{\mathrm{J}/\psi}|$ in the J/ψ rest frame. Here, $\vec{p}_\Lambda$ and $\vec{p}_{\mathrm{J}/\psi}$ are the momenta of the Λ and J/ψ, respectively, and $\mathrm{d}\Omega_\mathrm{p} = \mathrm{d}(\cos\theta_\mathrm{p})\mathrm{d}\varphi_\mathrm{p}$ and $\mathrm{d}\Omega_\mu = \mathrm{d}(\cos\theta_\mu)\mathrm{d}\varphi_\mu$ are differential solid angles.

Moreover with a proper parametrization, the angular distribution can be more conveniently present by the sum of 20 terms [15], where each term factorize as

$$\frac{\mathrm{d}^5\Gamma}{\mathrm{d}\cos\theta_\Lambda \mathrm{d}\Omega_\mathrm{p}\mathrm{d}\Omega_\mu}(\theta_\Lambda, \theta_\mathrm{p}, \theta_\mu, \varphi_\mathrm{p}, \varphi_\mu) = \frac{1}{(4\pi)^3}\sum_{i=1}^{20} u_i(T_{\lambda_1\lambda_2})\, v_i(P, \alpha_\Lambda)\, w_i(\theta_\Lambda, \theta_\mathrm{p}, \theta_\mu, \varphi_\mathrm{p}, \varphi_\mu), \quad (2.16)$$

here w_i are trigonometric functions, v_i stands for 1, P, α_Λ, or $P\alpha_\Lambda$; P is the Λ_b polarization and α_Λ is the asymmetry parameter in the decay $\Lambda \to \mathrm{p}\pi^-$; u_i are bilinear combinations of the helicity amplitudes $T_{\lambda_1\lambda_2}$ as proposed in Ref. [15],

$$\begin{aligned}
\alpha_1 &= |T_{++}|^2 - |T_{+0}|^2 + |T_{-0}|^2 - |T_{--}|^2,\\
\alpha_2 &= |T_{++}|^2 + |T_{+0}|^2 - |T_{-0}|^2 - |T_{--}|^2,\\
\alpha_3 &= 2Re(T_{++}T_{+0}^*) - 2Re(T_{--}T_{-0}^*),\\
\alpha_4 &= 2Re(T_{++}T_{-0}^*) - 2Re(T_{--}T_{+0}^*),\\
\beta_1 &= 2Im(T_{+0}T_{-0}^*),\\
\beta_2 &= 2Im(T_{++}T_{--}^*),\\
\beta_3 &= 2Im(T_{++}T_{+0}^*) - 2Im(T_{--}T_{-0}^*),\\
\beta_4 &= 2Im(T_{++}T_{-0}^*) - 2Im(T_{--}T_{+0}^*),\\
\gamma_0 &= |T_{++}|^2 - 2|T_{+0}|^2 - 2|T_{-0}|^2 + |T_{--}|^2,\\
\gamma_1 &= 2Re(T_{+0}T_{-0}^*),\\
\gamma_2 &= 2Re(T_{++}T_{--}^*),\\
\gamma_3 &= 2Re(T_{++}T_{+0}^*) + 2Re(T_{--}T_{-0}^*),\\
\gamma_4 &= 2Re(T_{++}T_{-0}^*) + 2Re(T_{--}T_{+0}^*),\\
\delta_1 &= 2Im(T_{++}T_{+0}^*) + 2Im(T_{--}T_{-0}^*),\\
\delta_2 &= 2Im(T_{++}T_{-0}^*) + 2Im(T_{--}T_{+0}^*),
\end{aligned} \quad (2.17)$$

where the right hand sides are understood to be normalized by

$$1 = |T_{++}|^2 + |T_{+0}|^2 + |T_{-0}|^2 + |T_{--}|^2. \quad (2.18)$$

Corresponding to the four complex helicity amplitudes minus one relevant overall phase and the normalization condition only six angular parameters $(\alpha_k, \alpha_k, \gamma_k, \delta_k)$ are independent observables. The functional forms of u_i, v_i, and w_i are listed in Table 2.2. Assuming uniform detector acceptance over the azimuthal angles φ_p and φ_μ, the

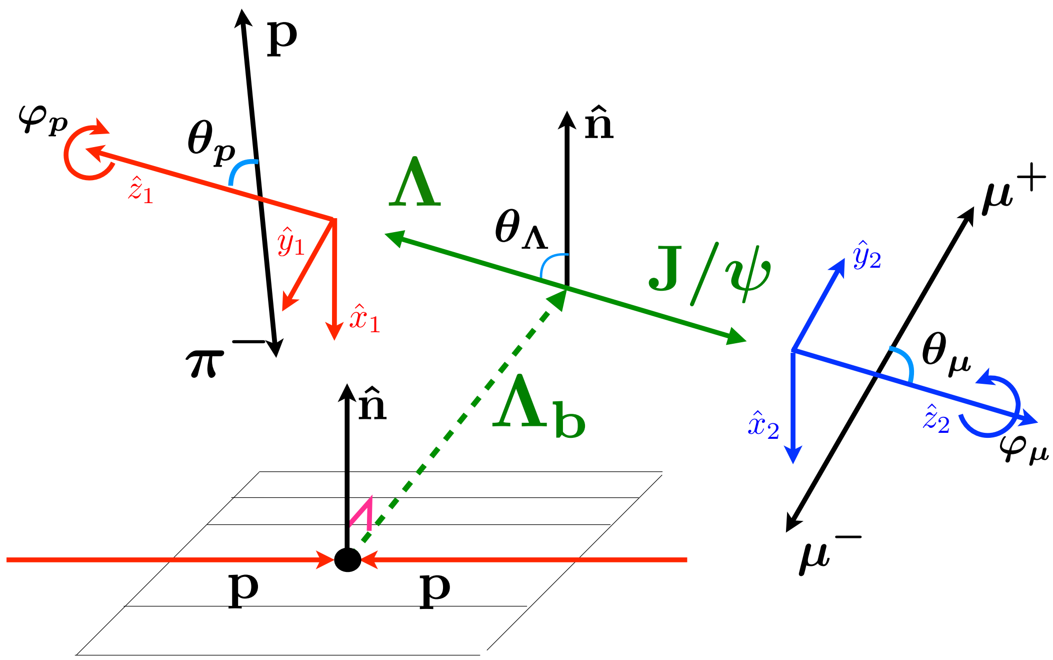

Fig. 2.2 Definition of the angles used to describe the $\Lambda_\mathrm{b} \to \mathrm{J}/\psi(\to \mu^+\mu^-)\Lambda(\to \mathrm{p}\pi^-)$.

angular distribution can be simplified through an integration over these two angles:

$$\begin{aligned}
&\frac{\mathrm{d}^3\Gamma}{\mathrm{d}\cos\theta_\Lambda\,\mathrm{d}\cos\theta_\mathrm{p}\,\mathrm{d}\cos\theta_\mu}(\theta_\Lambda, \theta_\mathrm{p}, \theta_\mu) \\
&\qquad = \int_{-\pi}^{\pi}\int_{-\pi}^{\pi} \frac{\mathrm{d}^5\Gamma}{\mathrm{d}\cos\theta_\Lambda\,\mathrm{d}\Omega_\mathrm{p}\,\mathrm{d}\Omega_\mu}(\theta_\Lambda, \theta_\mathrm{p}, \theta_\mu, \varphi_\mathrm{p}, \varphi_\mu)\mathrm{d}\varphi_\mathrm{p}\,\mathrm{d}\varphi_\mu \\
&\qquad\qquad \sim \sum_{i=1}^{8} u_i\left(\left|T_{\lambda_1\lambda_2}\right|^2\right) v_i(P, \alpha_\Lambda) w_i(\theta_\Lambda, \theta_\mathrm{p}, \theta_\mu). \qquad (2.19)
\end{aligned}$$

The eight u_i factors are written in terms of only three angular decay parameters α_1, α_2, and γ_0 proposed in Ref. [15], and the constant 1, which themselves can be written in terms of the $T_{\lambda_1\lambda_2}$ amplitudes as

$$\begin{aligned} 1 &= |T_{++}|^2 + |T_{+0}|^2 + |T_{-0}|^2 + |T_{--}|^2, \\ \alpha_1 &= |T_{++}|^2 - |T_{+0}|^2 + |T_{-0}|^2 - |T_{--}|^2, \\ \alpha_2 &= |T_{++}|^2 + |T_{+0}|^2 - |T_{-0}|^2 - |T_{--}|^2, \\ \gamma_0 &= |T_{++}|^2 - 2|T_{+0}|^2 - 2|T_{-0}|^2 + |T_{--}|^2, \end{aligned} \tag{2.20}$$

where α_1 is the asymmetry parameter for the decay $\Lambda_b \to J/\psi\,\Lambda$, α_2 represents the longitudinal polarization of the Λ, and γ_0 is a parameter that depends on the longitudinal and transverse polarizations of the J/ψ[16]. From the normalization condition and the definitions above the allowed range for α_1 and α_2 is $[-1,+1]$ and for γ_0 is $[-2,+1]$. Moreover, the angular decay parameters are related to the four helicity amplitudes through the following expressions:

$$\begin{aligned} |\,T_{+0}\,|^2 &= \frac{-3(\alpha_1-\alpha_2)+2(1-\gamma_0)}{12}, \qquad |\,T_{-0}\,|^2 = \frac{3(\alpha_1-\alpha_2)+2(1-\gamma_0)}{12}, \\ |\,T_{++}\,|^2 &= \frac{3(\alpha_1+\alpha_2)+2(2+\gamma_0)}{12}, \qquad |\,T_{--}\,|^2 = \frac{-3(\alpha_1+\alpha_2)+2(2+\gamma_0)}{12} \end{aligned} \tag{2.21}$$

so that, α_1, α_2 and γ_0 are required to satisfy the four additional constraints imposed by the positiveness of $|T_{\lambda_1\lambda_2}|$ and Eq. 2.21:

$$\begin{aligned} 0 &\leq -3(\alpha_1-\alpha_2)+2(1-\gamma_0), \\ 0 &\leq 3(\alpha_1-\alpha_2)+2(1-\gamma_0), \\ 0 &\leq -3(\alpha_1+\alpha_2)+2(2+\gamma_0), \\ 0 &\leq 3(\alpha_1+\alpha_2)+2(2+\gamma_0). \end{aligned} \tag{2.22}$$

The CP invariance of Eq. 2.19 implies that the parameters for Λ_b and $\overline{\Lambda_b}$ are related as follows:

$$\begin{aligned} \overline{P} &= -P, \\ \overline{\alpha}_1 &= -\alpha_1, \\ \overline{\alpha}_2 &= -\alpha_2, \\ \overline{\gamma}_0 &= \gamma_0. \end{aligned} \tag{2.23}$$

In addition the CP conservation in $\Lambda \to p\pi^-$ decays implies that $\overline{\alpha_\Lambda} = -\alpha_\Lambda$ [3]. In this analysis, the four parameters $(P, \alpha_1, \alpha_2, \gamma_0)$ are extracted from an analysis of the angular distribution given in Eq. (2.19), where α_Λ is fixed to its world-average value of 0.642 ± 0.013 [3].

Table 2.2 Functions used in Eq. 2.16 to describe the angular distribution in the decay $\Lambda_b \to J/\psi\,\Lambda$, with $J/\psi \to \mu^+\mu^-$ and $\Lambda \to p\pi^-$.

i	u_i	v_i	w_i
1	1	1	1
2	α_2	α_Λ	$\cos\theta_p$
3	$-\alpha_1$	P	$\cos\theta_\Lambda$
4	$-(1+2\gamma_0)/3$	$\alpha_\Lambda P$	$\cos\theta_\Lambda \cos\theta_p$
5	$\gamma_0/2$	1	$(3\cos^2\theta_\mu - 1)/2$
6	$(3\alpha_1 - \alpha_2)/4$	α_Λ	$\cos\theta_p\,(3\cos^2\theta_\mu - 1)/2$
7	$(\alpha_1 - 3\alpha_2)/4$	P	$\cos\theta_\Lambda\,(3\cos^2\theta_\mu - 1)/2$
8	$(\gamma_0 - 4)/6$	$\alpha_\Lambda P$	$\cos\theta_\Lambda \cos\theta_p\,(3\cos^2\theta_\mu - 1)/2$
9	$-3\alpha_3/(2\sqrt{2})$	P	$\sin\theta_\Lambda \sin\theta_\mu \cos\theta_\mu \cos\varphi_\mu$
10	$+3\delta_1/(2\sqrt{2})$	P	$\sin\theta_\Lambda \sin\theta_\mu \cos\theta_\mu \sin\varphi_\mu$
11	$+3\alpha_4/(2\sqrt{2})$	α_Λ	$\sin\theta_p \sin\theta_\mu \cos\theta_\mu \cos(\varphi_p + \varphi_\mu)$
12	$-3\delta_2/(2\sqrt{2})$	α_Λ	$\sin\theta_p \sin\theta_\mu \cos\theta_\mu \sin(\varphi_p + \varphi_\mu)$
13	$-3\gamma_1/2$	$\alpha_\Lambda P$	$\sin\theta_\Lambda \sin\theta_p \sin^2\theta_\mu \cos\varphi_p$
14	$+3\beta_1/2$	$\alpha_\Lambda P$	$\sin\theta_\Lambda \sin\theta_p \sin^2\theta_\mu \sin\varphi_p$
15	$-3\gamma_2/4$	$\alpha_\Lambda P$	$\sin\theta_\Lambda \sin\theta_p \sin^2\theta_\mu \cos(\varphi_p + 2\varphi_\mu)$
16	$+3\beta_2/4$	$\alpha_\Lambda P$	$\sin\theta_\Lambda \sin\theta_p \sin^2\theta_\mu \sin(\varphi_p + 2\varphi_\mu)$
17	$-3\gamma_3/(2\sqrt{2})$	$\alpha_\Lambda P$	$\sin\theta_\Lambda \cos\theta_p \sin\theta_\mu \cos\theta_\mu \cos\varphi_\mu$
18	$+3\beta_3/(2\sqrt{2})$	$\alpha_\Lambda P$	$\sin\theta_\Lambda \cos\theta_p \sin\theta_\mu \cos\theta_\mu \sin\varphi_\mu$
19	$-3\gamma_4/(2\sqrt{2})$	$\alpha_\Lambda P$	$\sin\theta_\Lambda \cos\theta_p \sin\theta_\mu \cos\theta_\mu \cos(\varphi_p + \varphi_\mu)$
20	$+3\beta_4/(2\sqrt{2})$	$\alpha_\Lambda P$	$\sin\theta_\Lambda \cos\theta_p \sin\theta_\mu \cos\theta_\mu \sin(\varphi_p + \varphi_\mu)$

Chapter 3

The experimental setup

The CERN (Conseil Europèen pour la Recherche Nuclèaire) laboratory sits in the Franco-Swiss border near Geneva. The laboratory was founded in 1954 with the mandate of establishing a fundamental physics research organization in Europe. At that time, physics research was concentrated on understanding the inside of the atom, hence the word "nuclear". Now, our understanding of matter goes much deeper than the nucleus and the main area of research at CERN is particle physics, with a global community of more than 13 000 visiting scientist and engineers of which Mexico is part. This chapter contains an overview of the accelerator machine located at CERN, followed by a more detailed description of the CMS (Compact Muon Solenoid) detector and the relevant subdetectors in the analysis.

3.1 The Large Hadron Collider

The accelerator complex at CERN (Fig. 3.1) is a succession of machines that accelerate particles to increasingly higher energies, each machine boosts the energy of a beam of particles and injecting the beam into the next machine in the sequence. The Large Hadron Collider (LHC) - the last element in this chain - is one of the largest scientific instruments ever built, with the prime motivation of to collide protons and heavy ions at TeV energy scales. The LHC is installed inside the former 27 km long LEP (Large Electron-Positron Collider) tunnel, and located at an average depth of 100 m below the surface.

The protons source for the LHC is a simple bottle of hydrogen gas, an electric field is used to strip hydrogen atoms of their electrons and leaving only protons to enter in the accelerator. The protons are guided into the first accelerator machine,

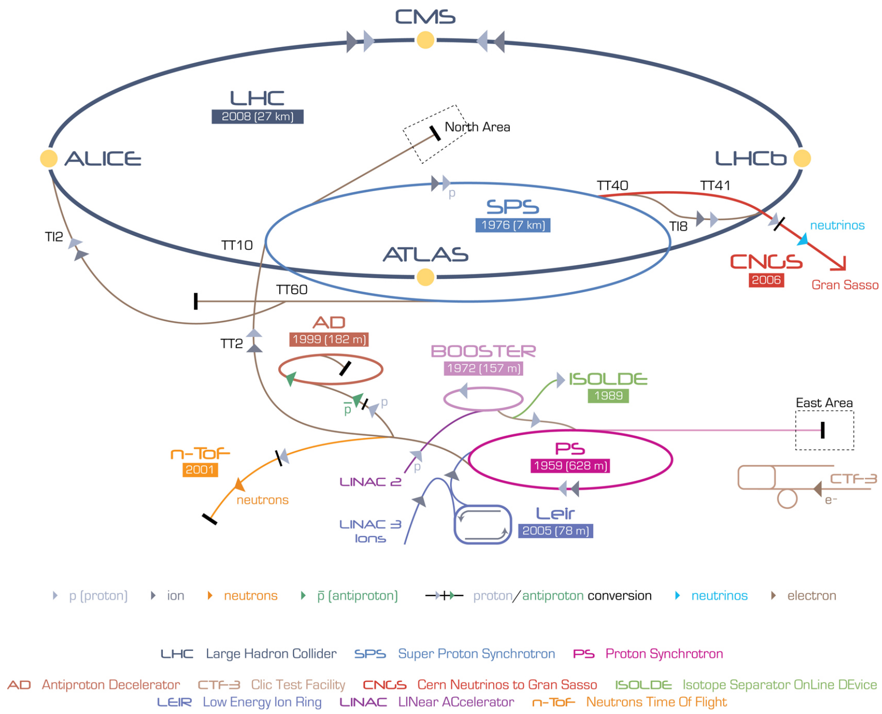

Fig. 3.1 The LHC accelerator complex at CERN.

LINAC2, where particles are accelerated to the energy of 50 MeV; then the beam is injected into the Proton Synchrotron Booster (PSB) which pushes the beam up to 1.4 GeV; as a next step the Proton Synchrotron (PS) accelerates the beam to 25 GeV, and the 6 bunches injected from the booster are split into four 4 trains of 72 bunches; the bunches are transfered into the Super Proton Synchrotron (SPS) and further accelerated up to 450 GeV, the injection energy of the LHC (see Fig. 3.1). The protons are finally transferred to the two beam pipes of the LHC. The beam in one pipe circulates clockwise while the beam in the other pipe circulates anticlockwise. It takes 4 minutes and 20 seconds to fill each LHC ring, and 20 minutes for the protons to reach their maximum energy of 6.5 TeV.

An schematic view of the LHC is shown in Figure. 3.2, the ring is divided in eight arcs (octant's) occupy most of the ring whereas interaction points (IP) are located at the centers of the octants. Two insertion points are located in IP2 and IP8 and the two largest experiments ATLAS and CMS are diametrically opposite in IP1 and IP5, respectively.

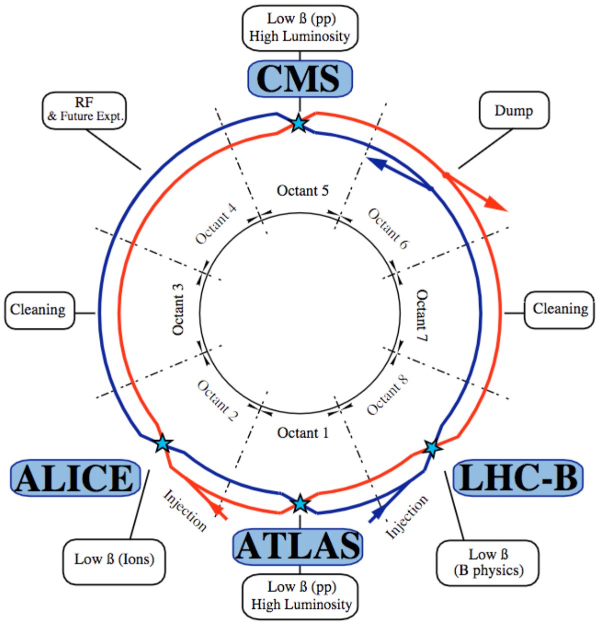

Fig. 3.2 Layout and experiments in the LHC. The LHC machine accelerates protons in two separated beams and opposite directions as shown in the blue and red lines. The ring is divided in eight sections, with pits at the middle of the octants. The two large experiments CMS and ATLAS are diametrically opposite in pits 5 and 1, respectively.

3.1.1 The RF system

To accelerate and collide particles of the same charge, radio frequency (RF) cavities generate dipole fields in opposite directions. To ensure the particles always see an accelerating voltage when they transit the RF cavities, the frequency of the electric field has to be an integer multiple of the machine revolution frequency. Each period of the electric field define a *RF bucket*. The harmonic number of the electric field or number of buckets is given by:

$$h = \frac{f_{\mathrm{RF}}}{f_{\mathrm{rev}}}, \tag{3.1}$$

where f_{RF} is the frequency of the RF system and f_{rev} is the revolution frequency. The total number of bunches is limited by h and the desired bunch spacing. The LHC RF frequency is 400 MHz and a bucket corresponds to 2.5ns. The total number of available buckets are 35640. For a bunch spacing design of 25 ns, the maximum number of bunches will be 3564. In the reality, due to the injection and dump kicker gaps, the maximum number of bunches is only 2808.

A description about the physics in the accelerators can be found in Ref. [42], and a more detailed description about the electric field and RF cavities can be found in Ref [43].

3.1.2 Magnets

To guide charged particles on a circular path, a dipole magnetic field orthogonal to the traveling direction is required. An ingenious design of the magnetic field in every dipole generates a vector $\vec{\mathrm{B}}$ (Fig. 3.3a) on each pipe opposite in direction to that of the other pipe. This makes the forces over both proton beams act in the same direction towards the center of the ring (Fig. 3.3a). The LHC comprises 1232 dipole magnets located on the eight arches, each one having a magnetic length of 14.3 m and deflecting the beam by $2\pi/1232 = 5.1\,\mathrm{mrad}$. In addition to just curving the beam, it is also necessary to focus it, this allows width and height to be constrained so that it stays inside of the pipe. To provide the focusing, a total of 858 quadrupole magnets are installed around the ring in the arcs. Other magnetic multipoles act to help in beam focusing and counteracting other interactions that each beam suffers (gravitational interactions over protons, electromagnetic interactions among bunches, electron clouds from the pipe walls, etc). The arrangement of multipoles magnets can be shown schematically as a sequence of divergent and convergent lenses, focuses and defocuses the beam in the transverse plane with respect to the nominal beam trajectory. An typical pattern in an arc would be seen in Figure 3.3b.

A description about the design of the magnets in the LHC can be found in Ref [43].

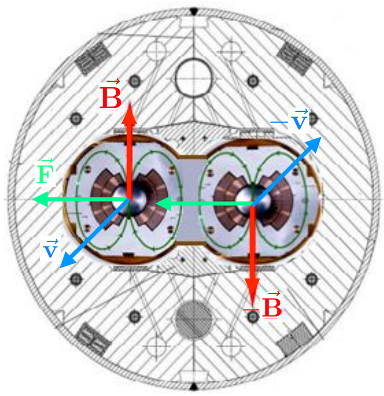

(a) The dipolar magnetic field (B) is created for superconductive currents which circulate on each side of the pipe by where the protons travel with a velocity v in opposite directions. The acting force (F) is pointing out towards the center of the ring.

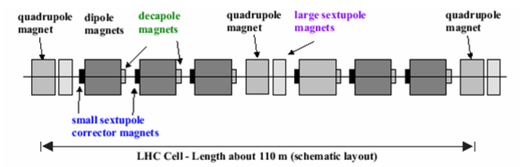

(b) An schematic view of the basic multipolar magnetic cell, the cell can be seen as a sequence of divergent and convergent lenses that focuses and defocuses the beam in different directions.

Fig. 3.3 Magnetic multipoles in LHC.

3.1.3 The LHC machine parameters

The machine parameters relevant for the operation of CMS are listed in Table 3.1. Taking the nominal beam trajectory as the longitudinal axis, the transverse beam size can be expressed in terms of two quantities, the transverse emittance ϵ[1], and the betatron function β [42, 43]. Assuming the transverse beam shape as a Gaussian, the beam size is $\sigma(s) = \sqrt{\epsilon\beta(s)}$, where s is the location along of the nominal beam trajectory and $\sigma(s)$ as the width of the Gaussian.

The luminosity is a measure of the number of collisions that occur each second, it is often given in $\mathrm{cm}^{-2}\,\mathrm{s}^{-1}$ and defined by:

$$\mathcal{L} = \frac{\gamma f_{\mathrm{rev}} k_{\mathrm{B}} N_{\mathrm{p}}^{2}}{4\pi \epsilon_{n} \beta^{*}} F, \tag{3.2}$$

[1]The emittance ϵ is a measure for the average spread of particle coordinates in position-and-momentum

Table 3.1 The machine parameters relevant for the CMS. For HI operation the design luminosity for Pb-Pb collisions is given.

		pp	HI	
Energy per nucleon	E	7	2.76	TeV
Dipole field at 7 TeV	B	8.33	8.33	T
Design Luminosity	$\mathcal{L}$	10^{34}	10^{27}	$\text{cm}^{-2}\,\text{s}^{-1}$
Bunch separation		25	100	ns
No. of bunches	k_B	2808	592	
No. of particles/bunch	N_p	1.15×10^{11}	7.0×10^{7}	
In collisions				
$\beta-$value at IP	β^*	0.55	0.5	m
RMS beam radius at IP	σ^*	16.7	15.9	μm
Luminosity lifetime	τ_L	15	6	hr
No. of collisions/crossing	n_c	≈ 20	–	

where γ is the Lorentz factor, f_rev is the revolution frequency, k_B is the number of bunches, N_p is the number of protons/bunch, ϵ_n is the transverse emittance normalized to Lorentz factor (with a design value of 3.75 μm), β^* is the betatron function at the IP, and F is the reduction factor due to the crossing angle at the IP. The design energy of each proton beam is 7 TeV, which instantaneous luminosity of $\mathcal{L} = 1 \times 10^{34}\,\text{cm}^{-2}\,\text{s}^{-1}$ leads to around 1 billion pp interactions per second.

The main performance parameter of a collider is the integrated luminosity measured in area units. At a time T the integrated luminosity is given by:

$$\mathcal{L}_\text{int} = \int_0^T \mathcal{L}\text{d}t. \tag{3.3}$$

During the first full year of physics running for pp collisions and with at 7 TeV center-of-mass energy, the LHC reached a peak of maximum luminosity of $\mathcal{L} = 4\,\text{Hz}\,\text{nb}^{-1}$ (=$4\times10^{33}\,\text{cm}^{-2}\,\text{s}^{-1}$)[2] and the total integrated luminosity delivered to CMS was $\mathcal{L}_\text{int} = 6\,\text{fb}^{-1}$. In the "low luminosity" phase in 2012, the maximum delivered luminosity by LHC was $\approx 7.6\,\text{Hz}\,\text{nb}^{-1}$ and a total delivered integrated luminosity of $\mathcal{L}_\text{int} = 23\,\text{fb}^{-1}$ (see Fig. 3.4a). To the nominal regime of 13–14 TeV at center-of-mass energy, in the actual period 2015–2022, it is expected a total integrated luminosity of $40\,\text{fb}^{-1}$ per year (see Fig. 3.4a), but $100 - 300\,\text{fb}^{-1}$ over next years of operations (Fig. 3.4b) [44].

[2] barn= $1 \times 10^{-24}\,\text{cm}^2$, then $\text{nb}^{-1} = 1 \times 10^{33}\,\text{cm}^{-2}$ and so on.

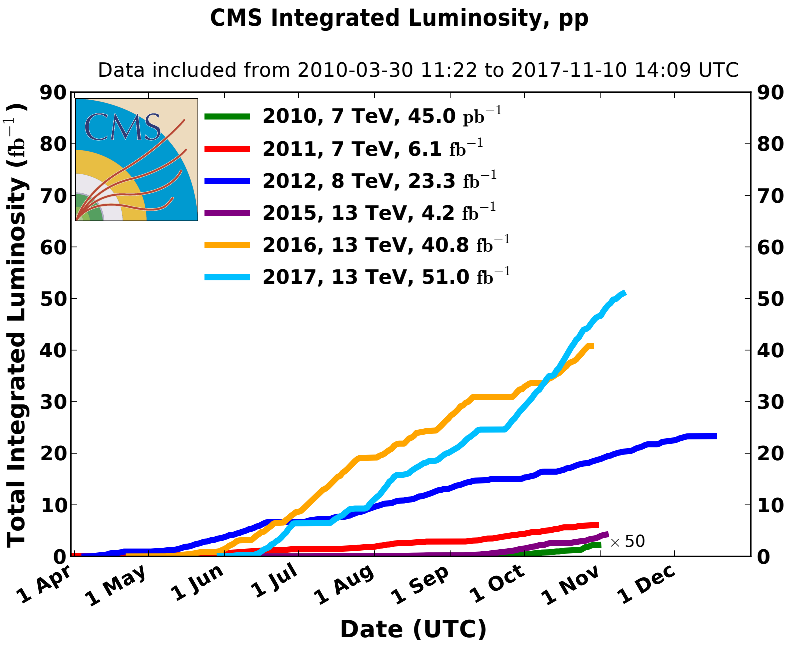

(a) Total integrated luminosity delivered by LHC to CMS per year at different center-of-mass energies.

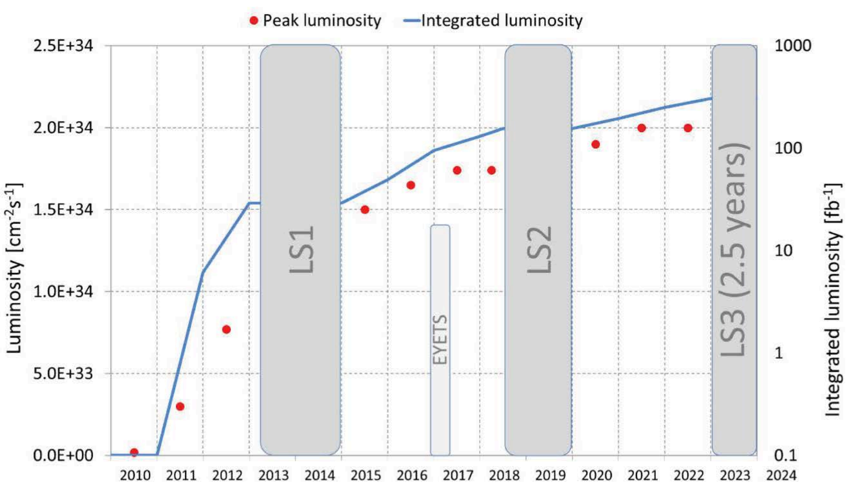

(b) LHC luminosity plan for this decade and beyond, both instantaneous (red dots) and integrated (blue line). Main long shutdown (LS) periods are indicated.

Fig. 3.4 LHC luminosity.

3.2 Coordinate conventions

The coordinate system adopted by CMS has the origin at the nominal collision point inside the experiment, the $y-$axis pointing vertically upward, and the $x-$axis pointing radially inward toward to the center of the LHC. Thus $z-$axis points along the counterclockwise proton beam. The azimuthal angle ϕ is measured from the $x-$axis in the $x-y$ plane. The polar angle θ is measured from the $z-$axis. Pseudorapidity is defined as $\eta = -\ln\tan(\theta/2)$. The momentum transverse to the beam direction, denoted by p_{T} is computed from x and y. A description of the coordinate conventions can be found in Ref. [41] and a representative figure is shown in Fig. 3.5.

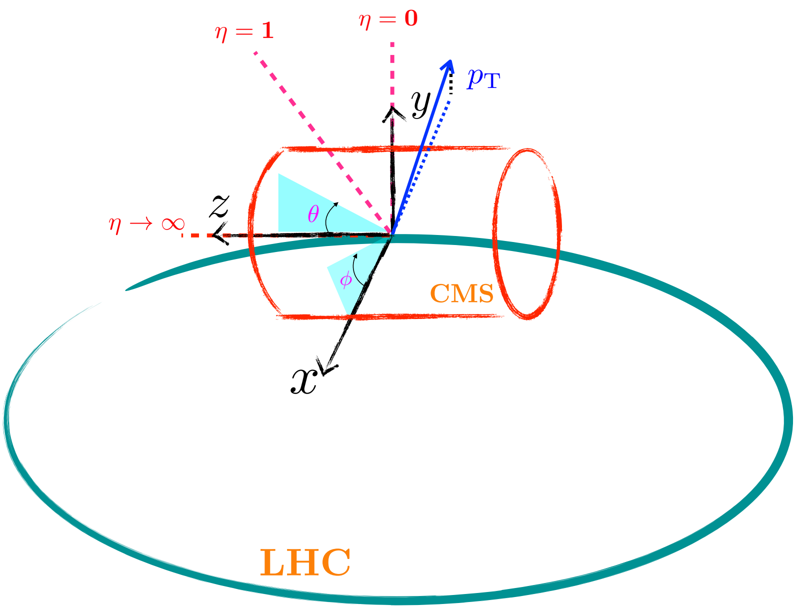

Fig. 3.5 Coordinate system adopted by CMS.

3.3 CMS overview

The overall concept and the design of the detector can be found in Refs. [41, 45]. The detector is installed about 100 m underground at the LHC IP5 close to the French village of Cessy, between Lake Geneva and the Jura mountains. CMS is a multi-purpose apparatus used to study a wide range of phenomena produced in high-energy collision.

An important aspect driving the detector design and layout is the reconstruction lepton signatures which is essential for an excellent muon and electron identification and momentum resolution; moreover, a precise measurement of secondary vertexes and impact parameter is necessary for an efficient identification of heavy flavor and lepton decays.

The short bunch crossing separation and the high event rate at the LHC impose further challenges to the design. At design luminosity, 20 inelastic interaction per bunch crossing will occur on average (see Table 3.1). This phenomenon is know as pile-up. The effect of pile-up can be reduced by using high-granularity detectors resulting in low occupancy. This requires a large number of detector channels and an excellent synchronization among them. In addition, a good time resolution is needed to discriminate the interaction under study from the interactions occurring in neighboring bunch crossings. Another difficulty arises from the large flux of particles near the interaction point which leads to high radiation levels and the need of radiation hard detectors and front-end electronics.

The CMS detector is 22 m long, has a diameter of 15 m and a overall weight 12.5 t, an schematic view is shown in Figure 3.6. The main features are high-field magnetic field of 4 T in the superconducting solenoid, a full-silicon based inner tracking system, a homogeneous scintillating-crystals-based electromagnetic calorimeter, a large enough return field to saturate 1.5 m of iron, allowing 4 muon "stations" to be integrated to ensure robustness and full geometric coverage. All these features are implemented to meet the challenges of the LHC.

3.3.1 Solenoid

At the heart of CMS sits a 13 m long, 6 m inner-diameter, 4 T superconducting solenoid. A high magnetic field was chosen to provide a large bending power for high-energy charged particles and achieve a good momentum resolution in the tracking detectors. The inner bore of the solenoid is large enough to accommodate the inner tracker and the calorimetry inside. With this dimensions the CMS solenoid is the largest superconducting magnet ever built and has a capacity to store an energy of 2.6GJ at full current. The magnetic flux is returned through a 10,000 iron yoke in which the muon detector are integrated.

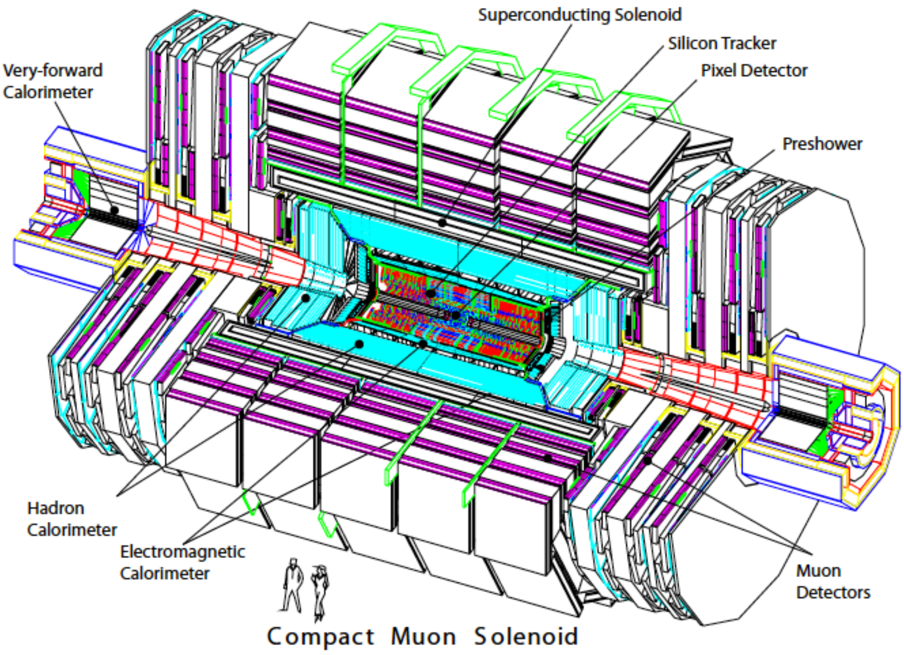

Fig. 3.6 A perspective view of the CMS detector.

3.3.2 Electromagnetic calorimeter

The CMS electromagnetic calorimeter (ECAL) is a hermetic and homogeneous detector with a large pseudorapidity coverage up to $|\eta| < 3$. The ECAL is divided into barrel and endcap detectors. Scintillation crystals made from lead tungsten ($PbWO_4$) are used to measure the energy of electromagnetically interacting particles, mainly electrons and photons. The choice of $PbWO_4$ as the scintillation material is motivated by its fast response time and high radiation resistance. The scintillation light output and the amplification have a strong temperature dependence. The response to an incident electron changes by $(3.8 \pm 0.4)\%/^{\circ}$ C which in turn means that temperature has to be closely monitored and kept stable to a precision of $\pm 0.05^{\circ}$ C and is provided by a water cooling system.

3.3.3 Hadronic calorimeter

The energy measurement of the ECAL is complemented by the measurement of the hadronic calorimeter (HCAL). The HCAL is a sampling calorimeter built from alternating layers of massive absorbing brass plates and plastic scintillator tiles arranged in trays. The quality of the energy measurements depends on the fraction of the hadronic shower detected in the calorimeter. Consequently, the thickness of the material in the tray has to be large enough to absorb the major part of the shower. The HCAL is divided into a barrel part HB and HO [3] at $|\eta| < 1.3$, an endcap HE on each side at $1.3 < |\eta| < 3$, and forward calorimeter HF extending up to $|\eta| < 5.2$ to achieve a most hermetic detector coverage.

3.3.4 Tracking detectors

One of the oldest tricks in particle physics is to put a track-measuring device in a strong magnetic field so that trajectories of the charged particles are helical tracks, with a radius proportional to their momenta (see Eq. 4.1). The CMS Tracker [46], shown in Fig.3.7, consists in two main detectors: a silicon pixel detector, covering the region 4 to 15 cm in radius, and 49 cm on either side of the collision point along the LHC beam axis, and silicon strip detector covering the region 25 to 110 cm in radius, and within 280 cm on either side of the collision point along the LHC beam axis.

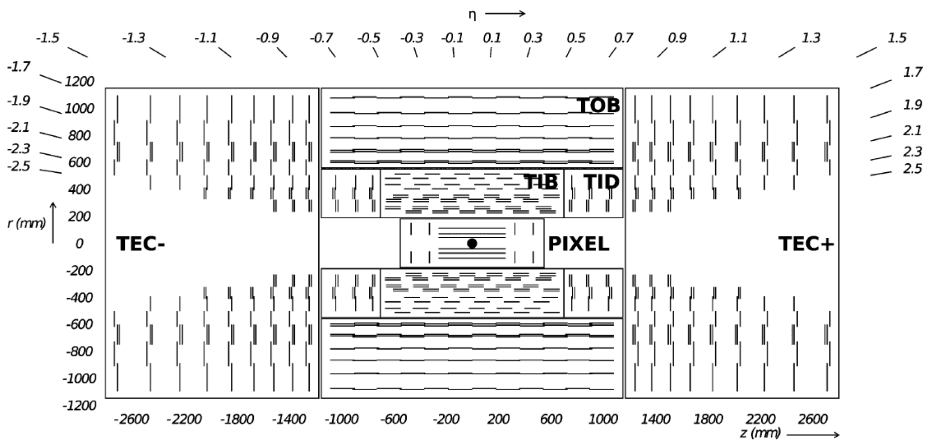

Fig. 3.7 *r-z* slice of the CMS tracker detector.

By considering the charged particle flux at various radii at high luminosity, three regions can be delineated:

[3]HO outer detector located between the solenoid and the muon detectors

- Closest to the interaction vertex where the particle flux is the highest ($\approx 10^7$ / s at $r \approx 10\,\text{cm}$), pixel detector are placed. The size of a pixel is $\approx 100 \times 150\,\mu\text{m}^2$, giving an occupancy[4] of about 10^{-4} per pixel per LHC bunch crossing.

- In the intermediate region ($20 < r < 55\,\text{cm}$), the particle flux is low enough to enable use of silicon microstrip detectors with a minimum cell size of $10\,\text{cm} \times 80\,\mu\text{m}$ with a thickness of $320\,\mu\text{m}$, and a strip pitch which varies from 80 to $120\,\mu\text{m}$. The occupancy in this region is about of $\approx 2 - 3\%$ / LHC crossing.

- In the outermost region ($r > 55\,\text{cm}$) of the inner tracker, the particle flux has dropped sufficiently to allow use of larger-pitch silicon microstrips varying from 120 to $180\,\mu\text{m}$ and a thicker silicon sensors of $500\,\mu\text{m}$. The maximum cell size of $25\,\text{cm} \times 180\,\mu\text{m}$, whilst keeping the occupancy to $\approx 1\%$.

Even in heavy-ion running, the occupancy is expected to be at the level of 1% in the pixel detectors and less than 20% in the outer silicon strip detectors, permitting track reconstruction in the high density environment.

Strip tracker

The barrel tracker region is divided in two parts: a TIB (Tracker Inner Barrel) in the intermediate region interaction, and a TOB (Tracker Outer Barrel) in the outermost region. The TIB is made of 4 layers, the first two of those are made with double-sided detector modules. The double-sided modules are made of two single-sided detectors mounted back to back with a strip inclination of 5.7° against each other. Thus, these "*stereo*" modules deliver two-dimensional hit position, and lead to a single point resolution of between 23–24 μm in the $r - \phi$ direction and 230 μm in z. The TOB comprises 6 layers, also for the TOB, the first 2 layers provide a *stereo* module with the same angle strip inclination, then single-point resolution varies from 35–53 μm in the $r - \phi$ direction and 530 μm in the z.

The endcaps are divided into the TEC (Tracker End Cap) and TID (Tracker Inner Disks). Each TEC comprises 9 disks that extend into the region $120\,\text{cm} < |z| < 280\,\text{cm}$, and each TID comprises 3 small disks that fill the gap between the TIB and the TEC. The TEC and TID modules are arranged in rings, centered on the beam line, and have strips that point towards the beam line, therefore having a variable pitch. The first 2 rings of the TID and the innermost 2 rings and the fifth ring of the TEC have *stereo* modules.

[4]The occupancy measures the number of particles traversing a detector cell per event.

Pixel tracker

The pixel detector is located in the closest region to the interaction point, it consists of 3 barrel layers with 2 endcap disks on each side on them. The 3 barrel layers are located at mean radii of 4.4 cm, 7.3 cm and 10.2 cm, and have a length of 53 cm. The 2 end disks, extending from 6 to 15 cm in radius, are placed on each side at $|z| = 34.5$ cm and 46.5 cm.

To achieve the optimal vertex position resolution, CMS has been adopted a design with square pixel shape of $100 \times 150\,\mu\text{m}^2$ in both the $(r.\phi)$ and z. The barrel comprises 768 pixel modules arranged into half-ladders of 4 identical modules. The endcap disks are assembled in a turbine-like geometry with blades rotated by 20°.

The spatial resolution is measured to be about $10\,\mu$m for the $r - \phi$ measurement and $20\,\mu$m for the z measurement.

3.3.5 Muon detectors

Centrally produced muons are measured 3 times: in the inner tracker, after the coil, and in the return flux. Measurement of the momentum of muons using only the muons system is essentially determinate by the muon bending angle at the exit of the 4 T coil, taking the interaction point (which will be known to $\approx 20\,\mu$m) as the origin of the muon. For low-momentum muons (p_T <10 GeV), the best momentum resolution is given by the resolution obtained from the silicon tracker. However, the muon trajectory beyond the return yoke extrapolates back to the beam-line due to the compensation of the bend before and after the coil when multiple scattering and energy loss can be neglected.

Three types of gaseous detectors are used to identify and measure muons [47]. The choice of the detector technologies has been driven by the very large surface to be covered and the different radiation environments, an schematic view is shown in Fig. 3.8. In the barrel region ($|\eta| < 1.2$), where the neutron induced background is small, the muon rate is low and the residual magnetic field in the chambers is low, drift tube (DT) chambers are used. In the 2 endcaps, where the muon rate is high as well as the neutron induced background rate, and the magnetic field is also high, cathode strip chambers (CSC) are developed and cover the region up to $|\eta| < 2.4$, which provide a faster response, high granularity and a better resistance against radiation. In addition to this, resistive plate chambers (RPC) are used in both the barrel and the endcap regions. These RPCs are operated in avalanche mode to ensure good operation at high rates (up to $10\,\mathrm{cm}^{-2}\,\mathrm{s}^{-1}$) and have double gaps which are 2 mm each one.

RPCs provide a fast response with good time resolution but with a wider position resolution than the DTs or CSCs. RPCs can therefore identify unambiguously the correct bunch crossing.

The DTs or CSCs and the RPCs operate within the first level trigger system, providing 2 independent and complementary sources of information. The complete system results in a robust, precise and flexible trigger device.

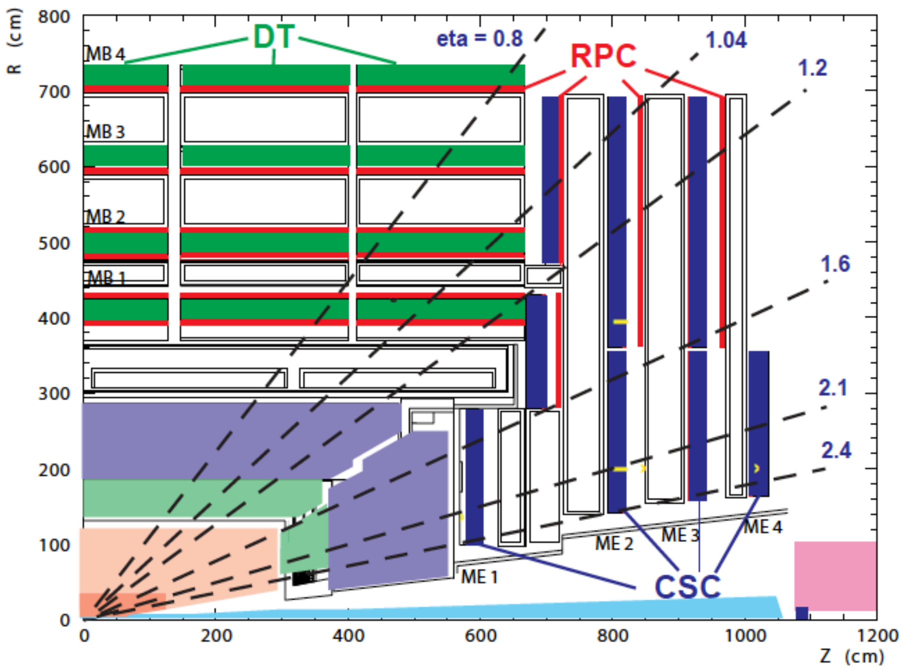

Fig. 3.8 *r*-*z* layout of one quarter of the CMS muon system for initial low luminosity running. New RPCs have been installed to cover region of $|\eta| < 2.4$.

3.3.6 Trigger

The CMS trigger system [48, 49] is designed to cope with the high luminosity and interaction rates. It must ensure high data recording efficiency for a wide variety of physics objects and event topologies, while applying online selective requirements to reduce the 40 MHz event rate to an output rate of 100 Hz allowing permanent storage of an event.

The CMS trigger system reduces the event rate in two steps called level-1 (L1) and high-level-trigger (HLT). The L1 trigger is designed to achieve a maximum output rate of 100 kHz and consist of custom-designed, programmable electronics while the HLT is based on software algorithms running on a large cluster of commercial processors, the event filter farm.

The L1 trigger system uses only raw data from the muon system and calorimeters, while the full granularity data stored in the front-end electronics is waiting for the L1 decision. The L1 decision has to be taken within a latency time of 3.2 μs and is based on the decision of local, regional and global trigger components. It also depends on the readiness of the other subdetectors and the data acquisition system (DAQ) which is supervised by the trigger control system. The trigger architecture is displayed in Fig. 3.9.

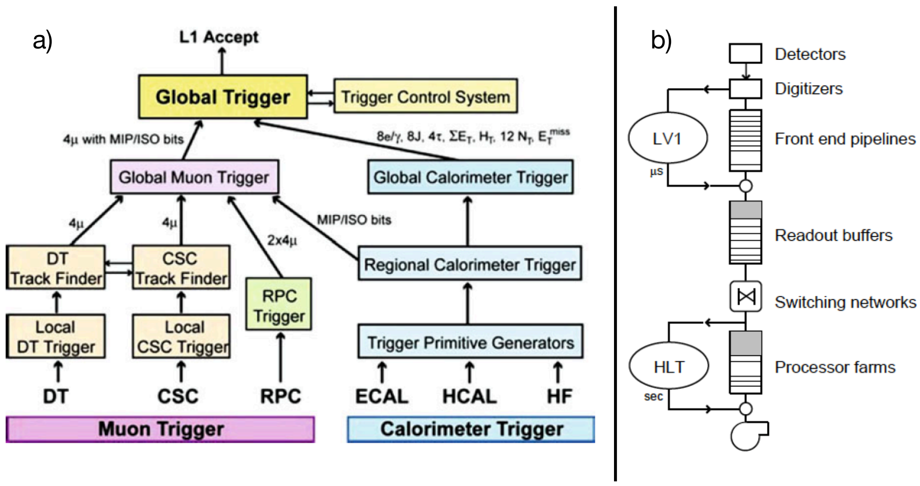

Fig. 3.9 CMS trigger overview. a) L1 trigger architecture. b) the CMS choice data flow, the HLT providing all filtering after the L1 decision.

The ECAL and HCAL cells form trigger towers in (η, ϕ). The L1 decision is based on the presence of "*trigger primitives*", they are objects such as muons, electrons, photons above set transverse energy E_T[5] or p_T thresholds. The primitives are generated by calculating the E_T of a trigger tower and assigning it to the correct bunch crossing. Then a regional calorimeter trigger determines regional electron, photon and information relevant for muon and tau identification. Finally the global calorimeter trigger uses the information from all parts of the calorimeters and provides information about the total transverse energy in the event.

On the other hand, in the muon system the three types of detectors take part in the trigger decision. The DTs provide track segments in the ϕ projection and

[5]The transverse energy is defined by $E_T = \sqrt{m^2 + p_T^2}$ for a particle of mass m.

hit pattern in the η, while the CSCs determine three-dimensional track segments. The track finders in the DTs and CSCs calculate the p_T of a track segment, its location, and quality. The RPCs deliver an independent measurement derived from regional hit patterns. Finally the global muon receives up to four candidates from each subsystem (DT and barrel RPC, CSC and endcap RPC) together with information regional calorimeter trigger. The aim is to improve the efficiency and reduce the rate by making use the redundancy of subsystems. Finally the global muon trigger selects a maximum of four muon trigger candidates and determines their momentum, charge, position and quality.

The trigger objects extracted by the global muon and calorimeter trigger are sent to a further global trigger where the decision to accept or reject an event is taken. The decision is the results of algorithms which apply momentum thresholds or to a single object or require object multiplicities to exceed predefined values.

When a event is accepted by the L1 trigger, the full detector information (1 MB/event) is read out by the DAQ system at a rate up to 100 kHz, and passed to the event filter farm as input for the HLT. The HLT algorithms are implemented in the same software as used in the offline reconstruction and analysis. The framework uses a modular architecture, those are executed in subsequent steps from the reconstruction to the selection. The HLT trigger is applied as a menu of trigger paths, each path addressing a specific physics object selection. The execution of a path is interrupted if the processed event does not fulfill the conditions imposed by a given module, a description about the HLT selection is given in Ref. [50].

The HLT paths are grouped according to the different physics analysis groups (PAGs). The accepted events are streamed into the corresponding primary data sets, for instance MuOnia is the primary data set for b-physics (BPH) PAG which is the responsible for the development, maintenance and validation.

3.4 CMS software overview

The overall collection of software, referred to as CMSSW [45], is built around a Framework, Event Data Model (EDM), and Services needed by simulation, calibration and alignment of the detector; reconstruction modules that process event and analysis data; and the support of a distributed computing infrastructure. The main goal of the Framework and EDM is to facilitate the development and deployment of reconstruction and analysis software.

The CMSSW event processing model consists of one executable, called cmsRun, and many plug-in modules which are managed by the Framework. All the code needed in the event processing (calibration, reconstruction algorithms, etc.) is contained in the modules (C++ classes). The same executable is used for both detector and Monte Carlo simulations.

The CMSSW executable (cmsRun) is configured at run time by a configuration file. The file tells cmsRun:

- which data to use,
- which module to execute,
- which parameter settings to use for each module,
- what is the order or the executions of modules, called path,
- how the events are filtered within each path, and
- the output files.

The CMS EDM is centered around the concept of an Event. An Event is a C++ object container for all raw and reconstructed data related to a particular collision. During processing, data are passed from one module to the next via the Event, and are accessed only through the Event.

The event reconstruction, selection and simulations (discussed in Chapter 4 and Appendix A) was developed using the CMSSW_4_2_8 and CMSSW_5_3_X releases. Since the work architecture on lxplus was changed and the CMSSW_4_X series was deprecated, our final results are obtained with the CMSSW_5_3_X version.

Chapter 4

Event reconstruction and selection

The goal of this chapter is to show how the decays $\Lambda_b \to J/\psi\,\Lambda$ into the $\mu^+\mu^-$ $p\pi^-$ final states are reconstructed and give a measure of the number of Λ_b events. Charged-conjugate modes are implied throughout this chapter unless otherwise stated. We shall see a brief review of the track and vertex reconstruction, the used data sets selected by a trigger and its definition. The offline selection is described first to the $J/\psi \to \mu^+\mu^-$ candidates and then for the $\Lambda \to p\pi^-$ candidates. Finally we shall see the reconstruction of Λ_b particles as well as the measurements of the numbers of Λ_b signal and background events.

4.1 Track reconstruction

The Lorentz force causes the charged particles to follow circular or helical trajectories in a magnetic field. The bending radius of particle paths (tracks) is related to the magnetic field strength and the momentum component of the particular perpendicular to the magnetic field by the relation [51]:

$$p_T[\mathrm{GeV}] = 0.03\,\mathrm{B}[\,\mathrm{T}]\rho[\,\mathrm{cm}], \tag{4.1}$$

where B is the magnitude of the magnetic field and ρ is the bending radius. This allows us to measure a dynamic property (momentum) from a geometric property (radius of curvature). The track reconstruction [52, 45] refers to the process of both searching and linking hits[1] to form a track and obtain estimates of the momentum and position parameters of the associated charged particles. A basic element to

[1] Charged particles produce signals in several detector modules to form clusters called "*hits*".

start the CMS tracking is the definition of beam spot (BS)[2] and the corresponding uncertainties, which are around σ_x, $\sigma_y = 15 - 20\,\mu$m and $\sigma_z = 5\,$cm. Then a track can be expressed by five parameters (but the parametrization is not unique) which are:

- the p_{T} of the tracks in terms the radius of curvature;
- the ϕ angle of the trajectory at a given point on the track;
- the angle of the trajectory at a given point on the track with respect to the beam line, which is usually expressed in terms of the pseudorapidity η;
- the transverse distance of closest approach (DCA) with respect to BS, referred as "impact parameter" $\mathrm{d_{xy}}$;
- the DCA with respect to BS along of the beam line, usually called $\mathrm{d_z}$.

The track reconstruction is an iterative process, repeating several times a combinatorial track finder (CTF) which is an adaptation of the combinatorial Kalman filter [53, 54]. The basic idea in each iteration is search tracks from the easiest to the most difficult to find and reduce the combinatorial, by applying different requirements on the track parameters, using the normalized χ^2 of the track and the number of hits. Tracks that pass the tightest selection are labeled *high-purity*. The iterations 0 and 1 are designed to recover prompt tracks (originating near to the IP) with high–p_{T} and searching for three or two pixel hits, respectively. The iteration 2 is configured to find low–p_{T} prompt tracks. Iterations 3–5 are intended to find high and low–p_{T} tracks that originate outside of the BS referred as displaced vertex tracks. After each iteration, the fully reconstructed tracks are added to the collection from the previous iterations and hits associated with tracks are removed. An improvement in the efficiency of the track reconstruction for the next data taking and beyond is on the number of iterations, being more than eight iterations.

The reconstruction starts with the hit reconstruction, which consist of clustering of pixels or strips and estimating a position and its uncertainty. Then the CTF is used in each iteration and performed in four main parts, the seed generation, track finding, track-fitting, and the track selection. The Figure 4.1 shows an sketch of CTF.

[2]The beam spot is the beam position averaged over multiple bunch crossing.

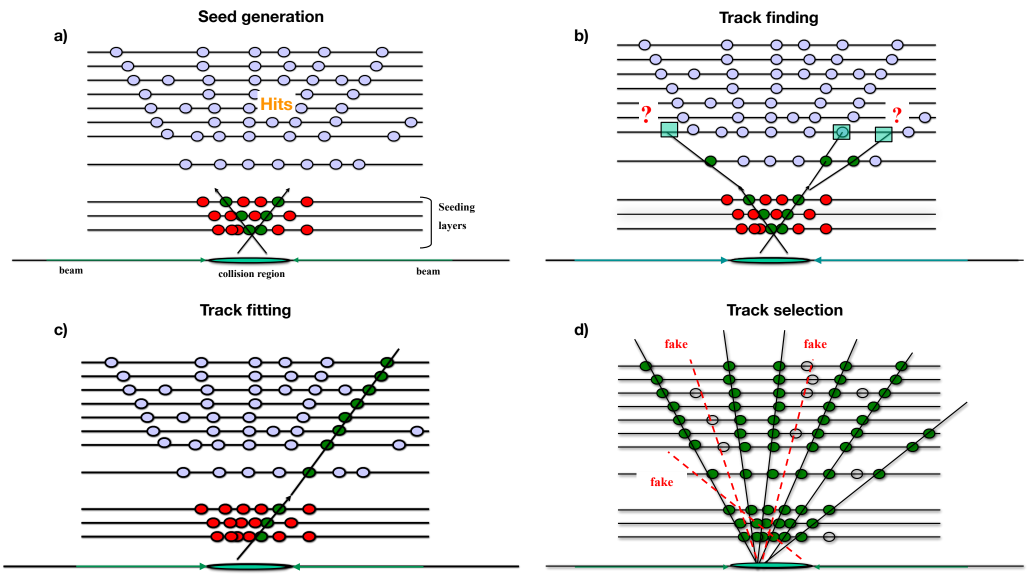

Fig. 4.1 Sketch of the combinatorial track finder. After hit reconstruction the CTF is used in each iteration as follows: a) the seed generation provides initial track candidates, b) the track finding extrapolates the seed trajectories searching for additional hits, c) the track-fitting is used to provide the best possible trajectory, and d) the track selection discards tracks that fail specified criteria [55] .

Seed generation

The seed generation provides initial track pattern recognition using pairs or triplets of hits and information of the position of the beam spot or primary vertexes (PV). A seed defines the initial estimate of the trajectory and their uncertainties.

The seed generation algorithm is controlled by two sets of parameters: *seeding layers*, and *tracking regions*. The seeding layers are pairs or triplets of detector layers in which hits are searched for. In the main iterations triplets of pixel layers are used, and the following iterations use combination of pixel and strip layers. On the other hand, the tracking regions specify the limits on the acceptable track parameters. It is well known that a circular or helical trajectory can be constructed with at least three points. If we get a pair of hits plus the BS position or three hits from different layers, we can construct a trajectory and then we can compute their associated track parameters. A hit pair is accepted as a seed if their corresponding track parameters are consistent with the requirements of tracking region. If the seeding layers decision corresponds to triplets, then, after a hit pair is accepted a search for a third hit is performed in the next layer. If the track parameters derived three hits are compatible with the tracking region the seed is accepted [52].

Track finding

The track finding is a pattern recognition algorithm that determines which layers are compatible with the seed trajectory. Then the algorithm builds track candidates by adding hits from successive layers, updating the parameters at each layer. The information needed at each layer includes the location and uncertainty of the detected hits, as well as the amount of material crossed, which is used to estimate the effects of multiple Coulomb scattering and energy loss.

The track is implemented in four steps. The first step evaluates which adjacent layers of the detector can be intersected through an extrapolation of the trajectory. At this step the effects of multiple scattering are not included and it assumes a uniform magnetic field. With this assumptions, the track trajectory is a perfect helix and the trajectory can be extrapolated using fast analytical calculations. The second step, involves a search for compatible modules in the layers returned by the first step. The third step forms groups of hits found in the compatible modules. If several compatible hits are found, a new trajectory candidate is built. Even if no hit is found, a virtual hit is created, to take into account the possibility that the charged particle did not leave a hit in the layer. The trajectory candidates are then updated with the information from the additional hit and its uncertainties. In the fourth step when the trajectory is updated, the algorithms create ambiguities in cases where several trajectory candidates are built from the same seed, or in cases where the track may be reconstructed from different seeds. To avoid a double counting of tracks, the fraction of shared hits between two trajectory candidates, if the fraction exceeds 19% a trajectory cleaner algorithm removes the track with the fewest number of hits, if not the track with the largest χ^2 is discarded [52].

Track fitting

The track fitting algorithm starts from the tracks that pass the ambiguity resolution requirements and estimates the final tracks parameters. The trajectory candidates are refitted with a Kalman filter approach, from the innermost to the outermost layers. In a second step the obtained trajectory is smoothed by employing a second Kalman filter, initialized by the information in the first filter in the outermost layer, and run backwards towards the innermost pixel layers. This procedure provides optimal estimates of the track parameters [52]..

Track selection

Finally, the track selection candidates is carried out to avoid the usage of fake tracks or tracks which are poorly reconstructed with large uncertainties on the tracks parameters. The selection is done by using different selection criteria a minimum number of layers in which track has a hit; the number of hits on the track; requirements on the p_T, η, impact parameters, and on the reduced χ^2 of the track fit [52]..

4.2 Muon reconstruction

A muon is identified as a track in the silicon tracker consistent with either a track or several hits in the muon system, associated with an energy deficit in the calorimeters. Based on this, there are two different muons reconstruction algorithms, the so-called "*global muons*" and "*tracker muons*" which are detailed in Ref [47].

Global muons. The tracks detected in the muon system[3] are matched to a track in the inner tracker if the parameters of the two tracks propagated are compatible. The global muon track is built by refitting the combined tracks using a Kalman filter.

Tracker muons. Each track with p_T larger than 0.5 GeV and a total momentum in excess of 2.5 GeV is extrapolated to the muon system. If at least muon segment (DT or CSC subdetectors) of the muon system matches the extrapolated track, the tracker track qualifies as a tracker muon.

Global muon reconstruction is designed to have high efficiency for muons penetrating through more one muon detector plane. It typically requires segments to be associated in a least two muon detector planes. For momenta below 10, this requirement fails because of the larger multiple scattering in the steel yoke. For these muons, the tracker muon reconstruction is more efficient, as it requires one segment in the muon system. Combination of two algorithms improves the momentum resolution as it can be seen in Fig. 4.2.

[3] Also called stand alone muons

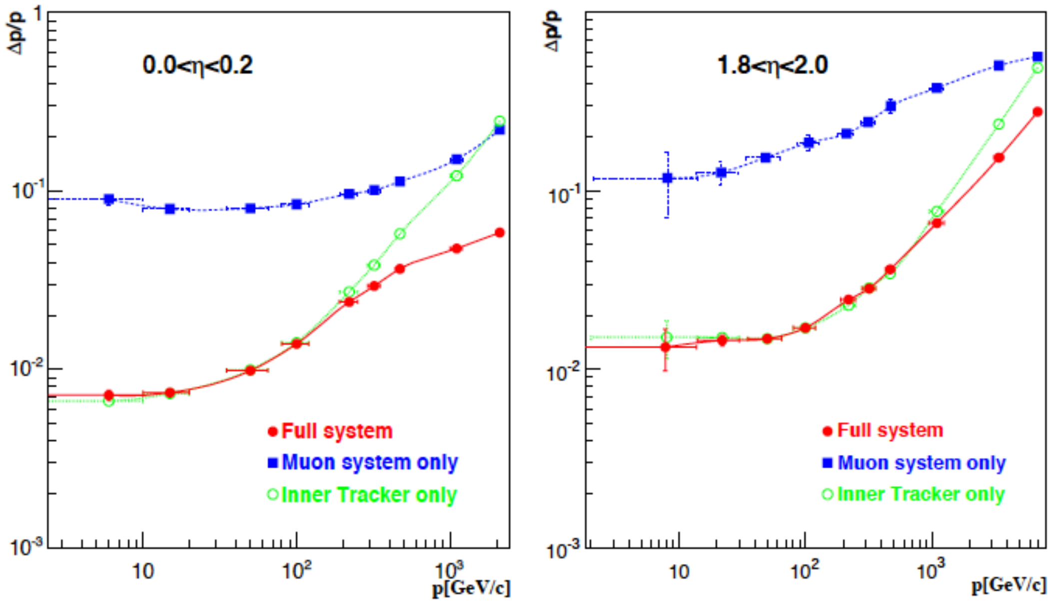

Fig. 4.2 The muon momentum resolution *vs* p using the muon system only, the tracker only, or both. In the barrel $|\eta| < 0.2$ (left plot); and endcap, $1.8 < |\eta| < 2.0$ (right plot) [45].

4.3 Primary vertex reconstruction

The reconstruction of the primary vertex (PV) in the event starts from the track collection. The tracks are clustered based on longitudinal impact parameter (d_Z). The clusters are fit with an adaptive vertex fit [56], where tracks in the vertex are assigned a weight 0 and 1 based on their proximity to the common vertex.

The primary vertex resolution depends on the number of tracks used in fitting and their p_T, and improved with higher-p_T tracks and the number of tracks. The values of the PV resolution vary from 10 μm up to 100 μm for the transverse coordinates, and from 15 μm up to 150 μm [52].

4.3.1 Secondary vertex reconstruction

A good estimation of the secondary (SV) parameters is important for the b-hadron decays. The SV reconstruction is constructed with a kinematic vertex fitting approach, using all tracks and vertexes of the current decay and applying physics constraints. The final vertex position is calculated from a simultaneous χ^2 minimization of the transverse impact parameter with respect the final vertex position.

4.4 Event selection

This work use data collected by CMS detector during the LHC Run I (2011 and 2012), when head-on collisions of protons took place at a center-of-mass energy of $\sqrt{s} = 7$ (2011) and 8 TeV (2012), corresponding to an integrated luminosity of 5.28 fb^{-1} (2011) and 19.7 fb^{-1} (2012). The data sets and their integrated luminosities are listed in Table 4.1.

The data sets were collected with a L1 and HLT trigger designed for events containing a pair of muons that form a vertex. In Figure 4.3 it is shown an overview of the dimuon mass collected with various dimuon triggers in the first data taking in 2011.

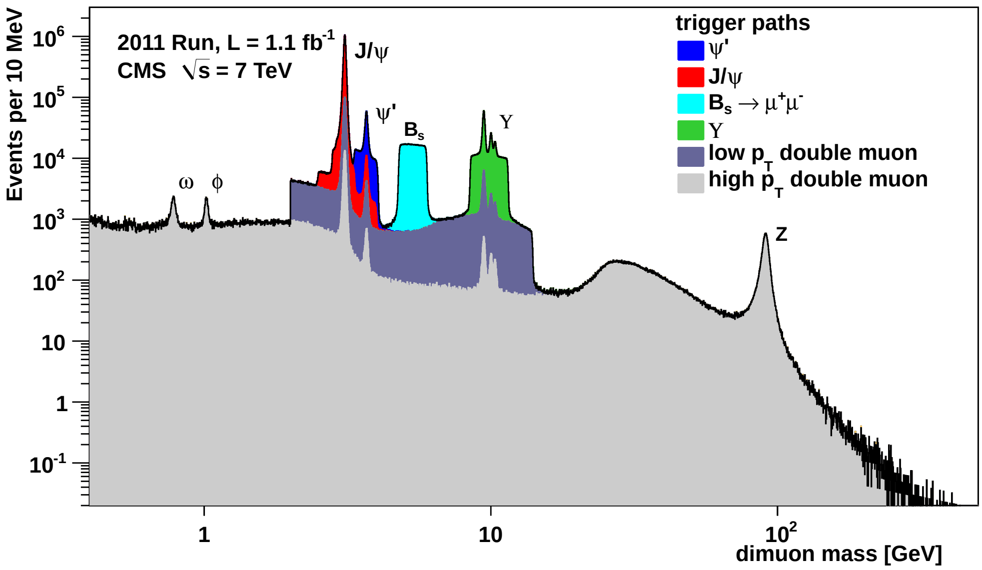

Fig. 4.3 Dimuon mass distribution collected with various dimuon triggers, during the first 1.1 fb^{-1} of data taking in 2011. The colored paths correspond to dimuon triggers with low p_T thresholds collected in a narrow mass window, while the light gray continuous distribution represents events collected with a dimuon trigger with high p_T thresholds. The dark gray band was a "quarkonium" dimuon trigger collected during the first 220 pb^{-1} only [57].

Since the Λ_b baryons travel a significant distance [3] with respect to the BS before decaying into $J/\psi\Lambda$, this analysis relies on HLT triggers that require a pair muons coming from a J/ψ with the decay vertex displaced relative to the BS, and commonly referred as "*Displaced*". The displacement requirement does not affect the angular distributions of the decay products. The dimuon trigger configuration were changed during the data taking at different center-of-mass energies, with

Table 4.1 Data sample used in this analysis.

Dataset	Integrated luminosity fb^{-1}	
	2011	2012
/MuOnia/Run2011A-May10ReReco-v1/AOD	0.233	–
/MuOnia/Run2011A-PromptReco-v4/AOD	0.984	–
/MuOnia/Run2011A-05Aug2011-v1/AOD	0.476	–
/MuOnia/Run2011A-PromptReco-v6/AOD	0.722	–
/MuOnia/Run2011B-PromptReco-v1/AOD	2.863	–
/MuOnia/Run2012A-22Jan2013-v1/AOD	–	0.876
/MuOnia/Run2012B-22Jan2013-v1/AOD	–	4.412
/MuOnia/Run2012C-22Jan2013-v1/AOD	–	7.054
/MuOnia/Run2012D-22Jan2013-v1/AOD	–	7.363
Total integrated luminosity	5.278	19.705

increasingly stringent requirements to maintain an acceptable trigger rate as the instantaneous luminosity increased. The requirements of the different trigger versions are as follows:

- Each muon must be in $|\eta(\mu)| < 2.2$ and have $p_{\mathrm{T}}^{\mu} > 3.5$ or $4\,\mathrm{GeV}$ in the different versions.
- The DCA of each muon to the common vertex in the transverse plane must be less than 0.5 cm.
- The muon pair must satisfy $p_{\mathrm{T}}^{\mu\mu} > 6.5$ or $6.9\,\mathrm{GeV}$ in the different versions.
- The χ^2 probability of the fit of the two muons to a common vertex must exceed 0.05, 0.10, or 0.15 from the earliest to the latest version.
- The distance from the PV and the dimuon vertex in the transverse plane ($\mathrm{L_{xy}}(\mathrm{J}/\psi)$) must have a value that is at least a factor of three larger than its uncertainty (standard deviation or SD).
- The "pointing" angle (β) between the reconstructed momentum vector $p^{\mu\mu}$ of the dimuon system and the vector pointing from the BS position to the dimuon vertex must have a value of $\cos\beta > 0.9$.
- The J/ψ candidates are selected in the invariant mass window 2.5–4.0 GeV and 2.9–3.3 GeV depending on the different versions.

Table 4.2 lists the triggers which are fired by events that pass the selection requirements in 2011 and 2012.

Table 4.2 Triggers fired by events in 2011 and 2012.

Trigger path	2011	2012
HLT_DoubleMu4_Jpsi_Displaced_v1	X	
HLT_DoubleMu3p5_Jpsi_Displaced_v2	X	
HLT_Dimuon7_Jpsi_Displaced_v1	X	
HLT_DoubleMu4_Jpsi_Displaced_v4	X	
HLT_Dimuon7_LowMass_Displaced_v4	X	
HLT_Dimuon6p5_LowMass_Displaced_v1	X	
HLT_DoubleMu4_Jpsi_Displaced_v5	X	
HLT_Dimuon7_LowMass_Displaced_v3	X	
HLT_DoubleMu3p5_LowMass_Displaced_v6	X	
HLT_DoubleMu4_Jpsi_Displaced_v9		X
HLT_DoubleMu4_Jpsi_Displaced_v10		X
HLT_DoubleMu4_Jpsi_Displaced_v11		X

4.5 Offline selection

4.5.1 J/ψ selection

The offline selection requires pairs of oppositely charged muons originating from a common vertex (displaced) to form the J/ψ candidates. The standard muon reconstruction procedure is used to identify muons as mentioned in Sec. 4.2. The displaced vertex is reconstructed as described in Sec. 4.3.1.

Since the trigger changed slightly over the different data-taking periods, the offline selection is required to be more restrictive than the most-stringent trigger, and are summarized as follows:

- Each muon must have $p_T^{\mu} > 4$GeV and the dimuon transverse momentum must satisfy $p_T^{\mu\mu} > 8$GeV.
- The χ^2 probability must exceed 0.15.
- The dimuon invariant mass must lie within ± 150MeV of the world-average J/ψ mass [3].

- The additional requirements are applied as the trigger selection except for the condition on the colinearity $\cos\beta > 0.99$, even though this cut reduces the signal events (S) it also reduces background (B), and the resulting significance $S/\sqrt{S+B}$ increases.

The J/ψ mass distribution is shown in Figure 4.4 after to apply the offline selection cuts to 7 and $\sqrt{s} = 8$ TeV data. The signal is modeled with the sum of three Gaussian functions with a common mean and the background with a first-order polynomial.

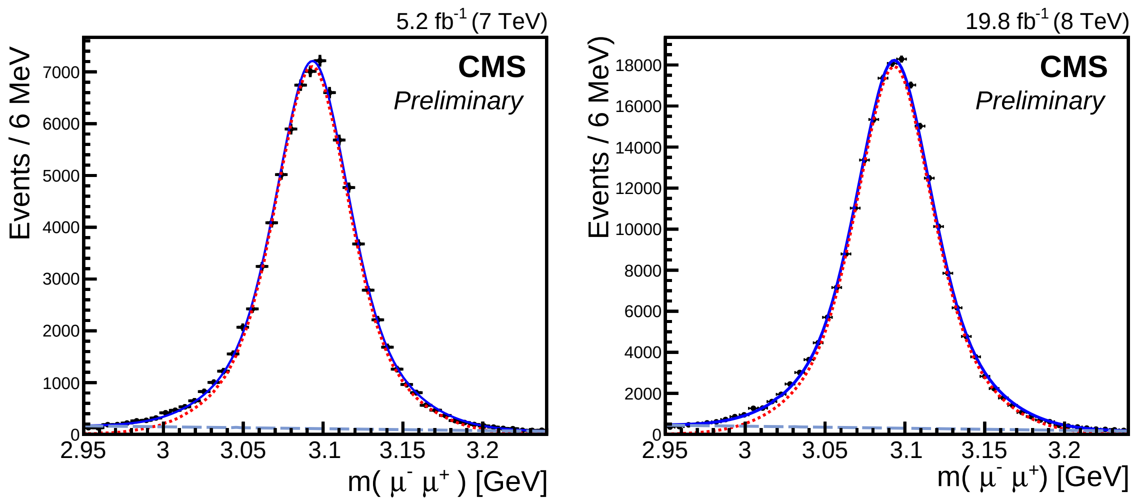

Fig. 4.4 The reconstructed mass distribution of J/$\psi \to \mu^+\mu^-$ candidates in data at center-of-mass of 7 (left) and $\sqrt{s} = 8$ TeV (right). The solid blue line represents the simultaneous fit to 7 and $\sqrt{s} = 8$ TeV data, and the dotted and dashed line represent the signal and background components, respectively.

4.5.2 Λ selection

The Λ particles are long-lived ($c\tau > 1$ cm) neutral particles reconstructed by their decay to two charged particles[4] $\Lambda \to \mathrm{p}\pi^-$. The Λ decays are constructed by finding oppositely charged tracks and requiring a successful vertex fit. The kinematics of $\Lambda \to \mathrm{p}\pi^-$ decay requires $p^{\mathrm{p}} > p^{\pi}$ for all particles, which allows to identify the highest and lowest momentum track as a proton and pion, respectively. To make sure that assumption is true we look at the MC simulation (see appendix A). A scatter plot of the p($\bar{\mathrm{p}}$) and $\pi^-(\pi^+)$ momenta from simulated tracks is shown in Figure 4.5, also a solid line described by the equation $y = x$ is shown. It can be seen

[4]Conjugate states are implied in this document

that there are not events on the line or below, i.e. the proton momentum is always greater than pion momentum (see also Figure 4.6).

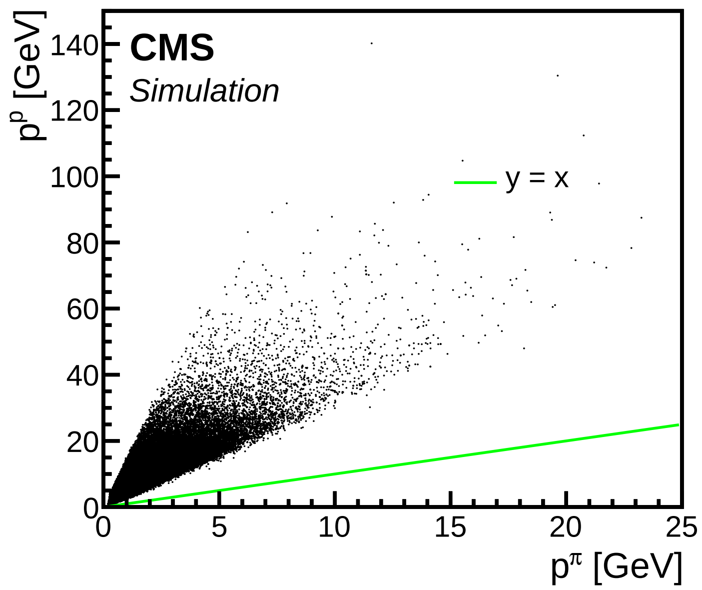

Fig. 4.5 Distribution of the p and π momentum from MC simulation. The solid line represents the equation $y = x$. It can be seen there are not events on the line or below, such that the momentum of p is always greater than the π momentum.

The selection of the Λ candidates is detailed in Ref. [58] and has been adopted as the standard selection criteria for long-lived particles in CMS. The selection requirements for Λ are as follows:

- High-purity tracks are used. A pair of oppositely charged tracks fit to a common vertex with $\chi^2 < 7$ per degree of freedom (dof), and the probability is required to be greater than 2%.
- The d_{xy} of the tracks with respect to the BS is required to be greater than 3 SD, where SD represents the square root of the beam spot and vertex uncertainties added in quadrature.
- The tracks with the higher and lower momentum are assigned to the world-average proton and pion masses [3].
- The transverse distance of the vertex to the BS, $L_{xy}(\Lambda)$ is required to be greater than 15 SD, where SD represents the square root of the beam spot and vertex uncertainties added in quadrature.

Energy loss (dE/dx) [59] studies in the silicon tracker [60] show that a large concentration of pions are observed from 0.3 GeV and protons from 1 GeV (see Fig. 4.6). It can also be seen the highest momentum tracks are generally found near to the proton curve (solid red) while the lowest momentum track are inconsistent with the proton curve. The few exceptions are consistent with background. In addition to this, other requirements in the selection are $p^{\rm p} > 1\,\text{GeV}$, $p^{\pi} > 0.3\,\text{GeV}$ and $p^{\rm p\pi} > 1.3\,\text{GeV}$.

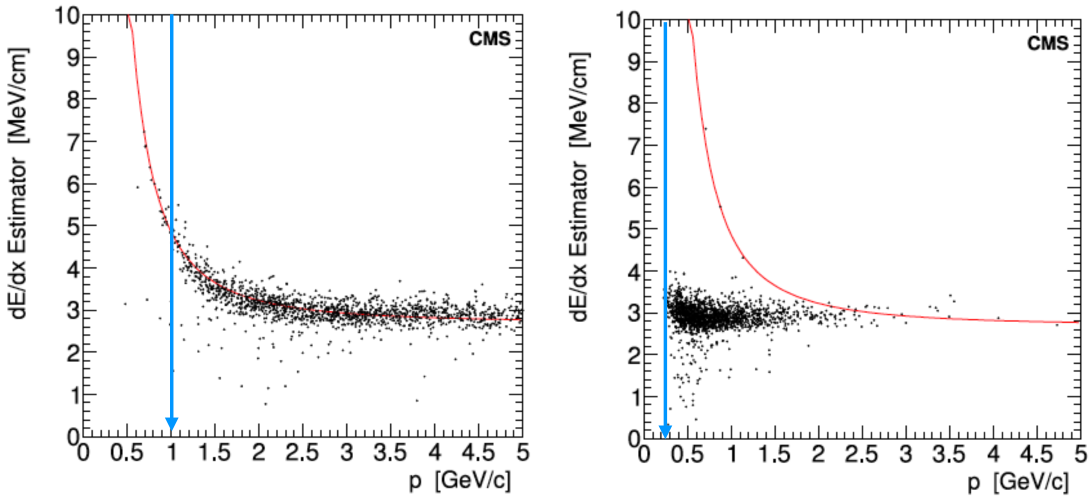

Fig. 4.6 Estimated energy loss as a function of the momentum for the highest (left) and the lowest (right) track from Λ decays. The solid curve represents the proton curve taken from calibration runs [60].

Contamination from $K^0_S \to \pi^+\pi^-$ decays arises when pions are misidentified with protons (Fig. 4.7). The events are removed if their invariant mass falls within $\pm 20\,\text{MeV}$ of the K^0_S mass when the proton candidate is given the charged pion mass.

Finally the reconstructed invariant mass in $\Lambda \to {\rm p}\pi^-$ decays is shown in Fig. 4.5.2. The Λ candidates are selected within the mass range $m_{\rm PDG} \pm 9\,\text{MeV}$, where $m_{\rm PDG}$ is the world-average Λ mass [3].

4.5.3 $\Lambda_{\rm b}$ reconstruction

The $\Lambda_{\rm b}$ candidates are fitted to a common vertex by combining the J/ψ and Λ candidates, with the respective mass constraints to the world-average values of the J/ψ and Λ masses [3]. The selection of $\Lambda_{\rm b}$ candidates is optimized to reduce

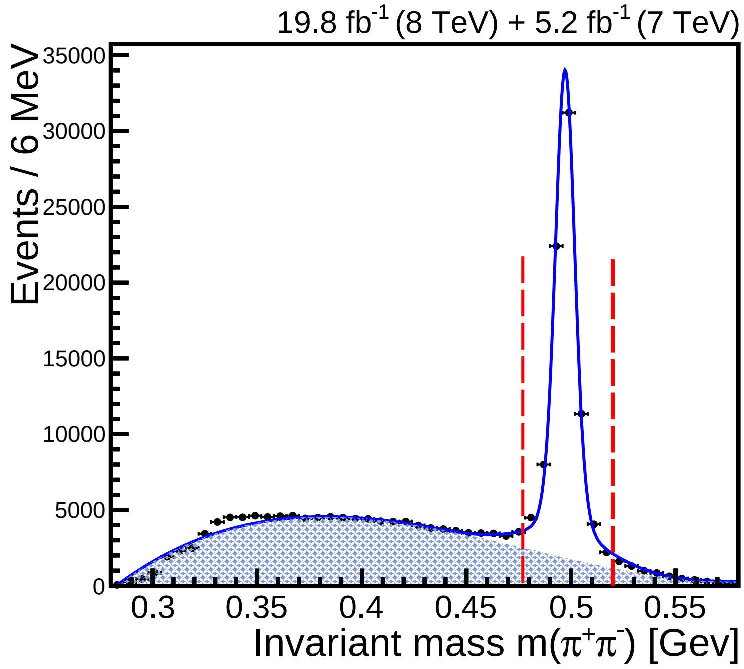

Fig. 4.7 Contamination from $K_S^0 \to \pi^-\pi^+$ candidates when a pion is misidentified as a proton. Events are removed if their invariant mass falls within ±20 MeV (dashed lines).

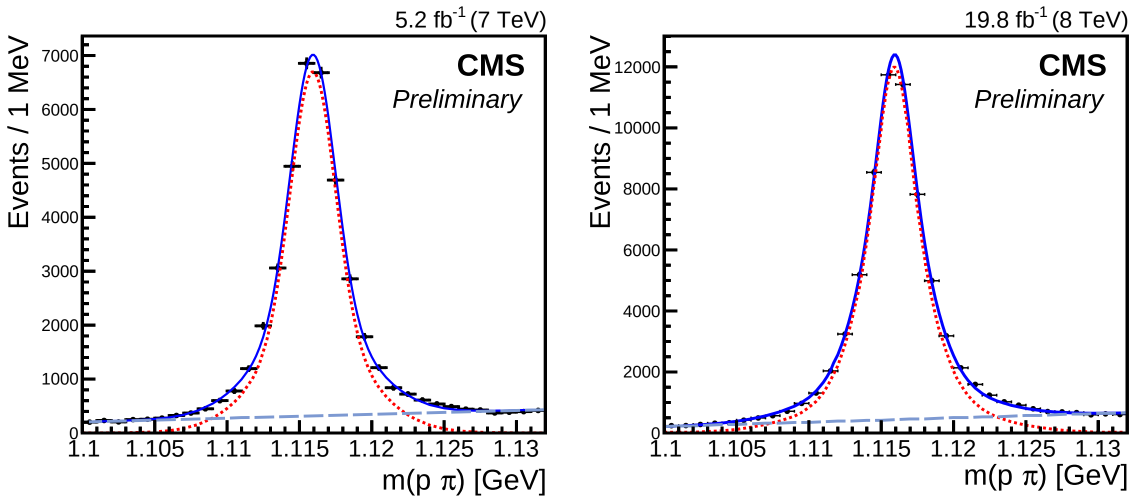

Fig. 4.8 Invariant mass distribution of the Λ candidates after to apply the selection criteria to data at center-of-mass of 7 (left) and $\sqrt{s} = 8$ TeV. The solid blue line represents the simultaneous fit to $\sqrt{s} = 7$ and 8 TeV data, and the dotted and dashed line show the signal and background components, respectively.

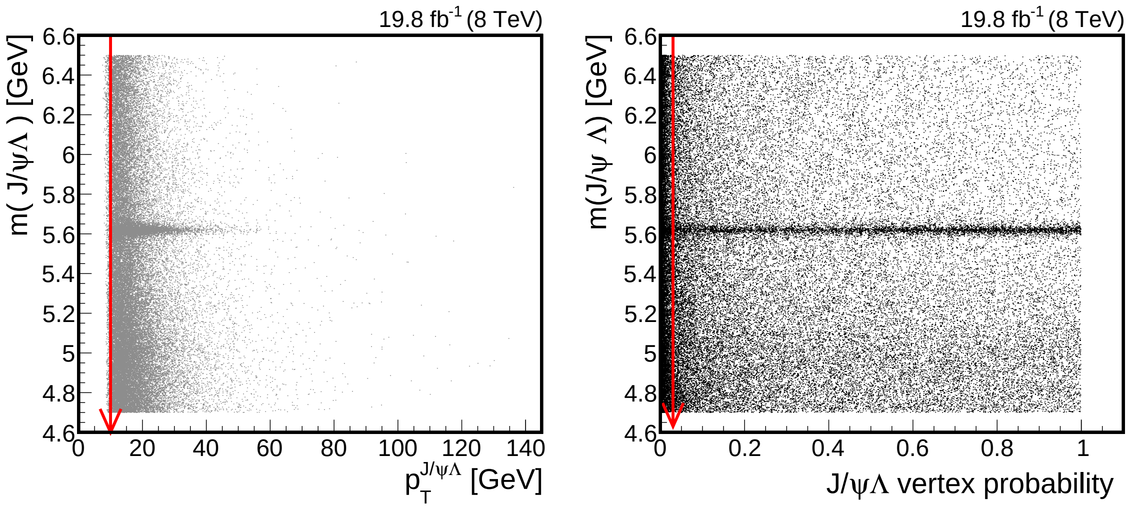

Fig. 4.9 Final requirements on Λ_b candidates are $p_T^{J/\psi\Lambda} > 10\,\text{GeV}$ and the vertex probability of the J/ψ Λ have to be greater than 3%. These cuts are to be applied in the selection of 2011 and 2012 data. The 2012 data is taken as an example.

background (Fig. 4.9) with the additional requirements: $p_T^{J/\psi\Lambda} > 10\,\text{GeV}$, a χ^2 probability of the fit to the J/$\psi\Lambda$ vertex $> 3\%$. The final reconstructed Λ_b and $\overline{\Lambda_b}$ particles are shown in Figure 4.10 for data at center-of-mass energy of 7 and $\sqrt{s} = 8\,\text{TeV}$. The correctly reconstructed candidates are expected to peak at world-average of $m_{J/\psi\Lambda}$ [3] within $5.40 < m_{J/\psi\Lambda} < 5.84\,\text{GeV}$ window mass region.

The dominant Gaussian-like signal peaks are modeled by the sum of two Gaussian functions with different SDs, σ_1 and σ_2, but common mean $\mu_{J/\psi\Lambda}$:

$$G(m_{J/\psi\Lambda};\mu_{J/\psi\Lambda},\sigma_1,\sigma_2,f) = f\,G_1(m_{J/\psi\Lambda};\mu_{J/\psi\Lambda},\sigma_1) + (1-f)\,G_2(m_{J/\psi\Lambda};\mu_{J/\psi\Lambda},\sigma_2), \quad (4.2)$$

where f is the fraction of the Gaussian functions. The background is modeled by a first-order polynomial $Q(m_{J/\psi\Lambda};a) = 1 + a\,m_{J/\psi\Lambda}$. To extract the number of signal (N_{sig}) and background (N_{bkg}) events and to define the signal and sidebands (SBs) regions, an unbinned extended maximum likelihood (ML) fit [61] to the invariant mass ($m_{J/\psi\Lambda}$) distributions is performed, and using simultaneously the four data sets of the Λ_b and $\overline{\Lambda_b}$ candidates at $\sqrt{s} = 7$ and $8\,\text{TeV}$. In this simultaneous fit the only common parameter is $\mu_{J/\psi\Lambda}$, while distinct resolutions (widths and fractions) are different for each data sample. The yields of the fit are presented in Table 4.3. From the fit, the observed Λ_b yields are 981 ± 39 and 2072 ± 55 signal events, and the $\overline{\Lambda_b}$ yields are 916 ± 40 and 1974 ± 53 signal events at $\sqrt{s} = 7$ and $8\,\text{TeV}$, respectively. The definitions of the signal and SB regions are useful in the next chapter to extract the efficiency and angular background and to perform the fit. To define both regions a common SD is used and defined by

$$\mathrm{SD} = \sqrt{f\sigma_1 + (1-f)\,\sigma_2} = 16\,\mathrm{MeV}, \tag{4.3}$$

then the signal region is defined as $\mu_{J/\psi\Lambda} \pm 3.5\mathrm{SD}$. The lower SB region is defined as $[5.46, 5.54]\,\mathrm{GeV}$ and the upper SB region as $[5.70, 5.78]\,\mathrm{GeV}$, which are equivalent to $[\mu_{J/\psi\Lambda} - 10\mathrm{SD}, \mu_{J/\psi\Lambda} - 5\mathrm{SD}]$ and $[\mu_{J/\psi\Lambda} + 5\mathrm{SD}, \mu_{J/\psi\Lambda} + 10\mathrm{SD}]$, respectively. A sketch of the regions are shown in Figure 4.11.

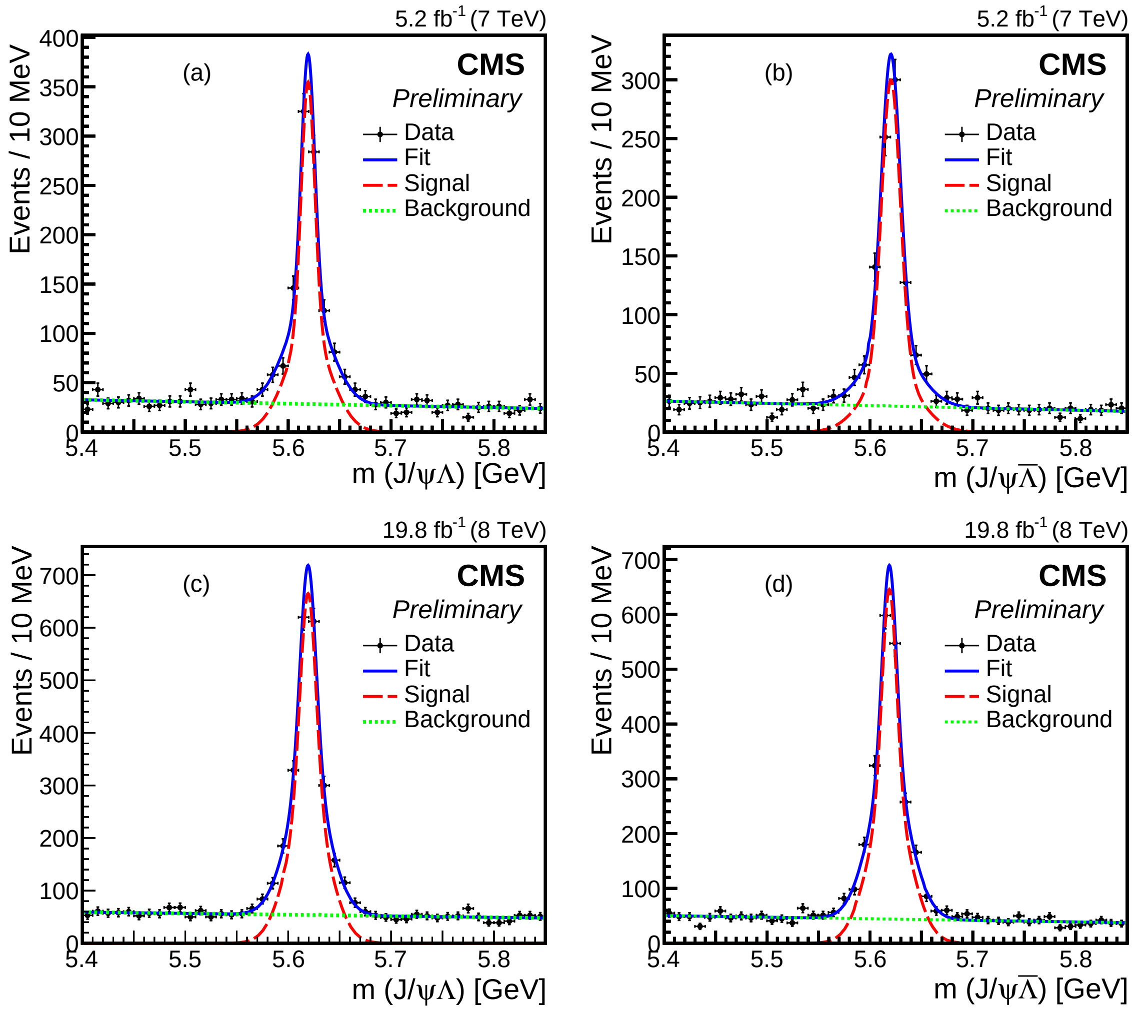

Fig. 4.10 Reconstructed invariant mass for (a) Λ_b, (b) $\overline{\Lambda_b}$ at center-of-mass energy of $\sqrt{s} = 7\,\mathrm{TeV}$, and (c) Λ_b and (d) $\overline{\Lambda_b}$ at $\sqrt{s} = 8\,\mathrm{TeV}$. The solid line indicate the performed fit to the data, where a sum of two Gaussian functions is used to describe the signal (dashed line) and a first-order polynomial to describe the background (dotted line).

Table 4.3 Results of the simultaneous ML fits to $m_{J/\psi\Lambda}$ distributions. Uncertainties are statistical only.

Description	Parameter	Observed values			
		$\sqrt{s}=7\,\text{TeV}$		$\sqrt{s}=8\,\text{TeV}$	
		Λ_b	$\overline{\Lambda_b}$	Λ_b	$\overline{\Lambda_b}$
Numb. of bkg candidate	N_{bkg}	945 ± 40	762 ± 38	1832 ± 54	1542 ± 52
Numb. of sig. candidates	N_{sig}	981 ± 39	916 ± 40	2072 ± 55	1974 ± 55
Mean of Gaussian	μ[GeV]	5.6193 ± 0.0002			
Width of Gaussian	σ_1[GeV]	0.021 ± 0.003	0.024 ± 0.001	0.020 ± 0.001	0.020 ± 0.002
Width of Gaussian	σ_2[GeV]	0.006 ± 0.001	0.009 ± 0.007	0.007 ± 0.001	0.007 ± 0.001
Double Gaussian fraction	f	0.578 ± 0.076	0.610 ± 0.105	0.625 ± 0.070	0.650 ± 0.073
Bkg. coeff.	a	-0.134 ± 0.056	-0.165 ± 0.063	-0.074 ± 0.040	-0.096 ± 0.044

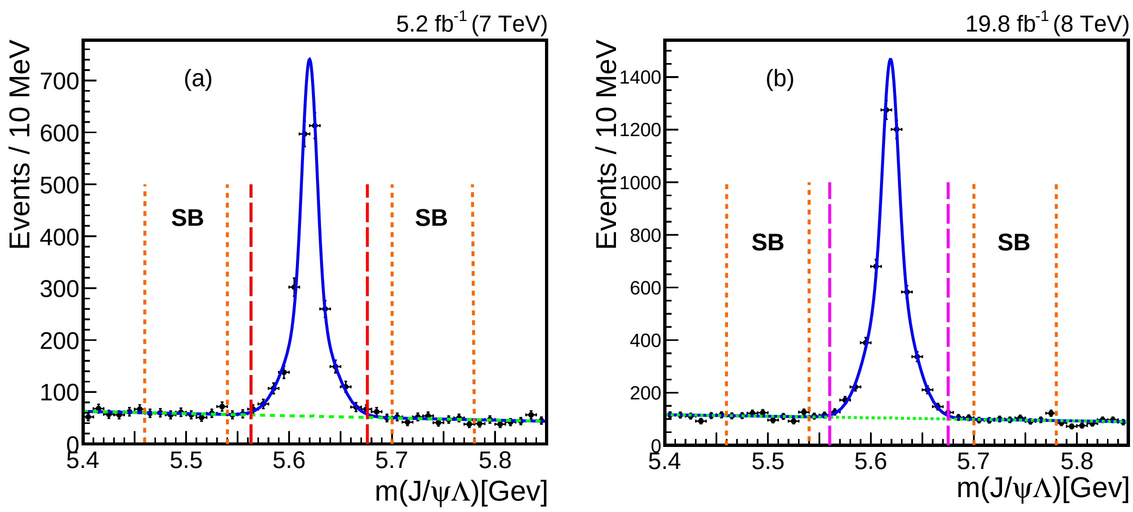

Fig. 4.11 Signal and sidebands (SB) regions of the (a) $m_{J/\psi\Lambda}$ at $\sqrt{s}=7\,\text{TeV}$ and (b) $m_{J/\psi\Lambda}$ at $\sqrt{s}=8\,\text{TeV}$.

Chapter 5

Measurements of the polarization and angular parameters

The Λ_b and $\overline{\Lambda_b}$ decays reconstructed and selected as described in the Chapter 4 are used in an angular analysis to measure the Λ_b polarization, P, and the angular decay parameters α_1, α_2 and γ_0. The measurements are extracted from an 3-dimensional simultaneous fit to the angular variables (observables) $\cos\theta_\Lambda$, $\cos\theta_p$, and $\cos\theta_\mu$ in the four data sets Λ_b, $\overline{\Lambda_b}$ at $\sqrt{s} = 7$ and $\sqrt{s} = 8\,\text{TeV}$.

In this chapter the correlation factors and the angular resolution of the variables are discussed, followed by the analysis strategy to be applied and its validation. The final results from the fit are presented as well as the relevant systematic uncertainties.

5.1 Correlation factors

As shown in the Sec. 2.5.1, the full angular distribution of the $\Lambda_b \to J/\psi(\to \mu^+\mu^-)\,\Lambda(\to p\pi^-)$ decays is described by three polar angles (θ_Λ,θ_p,θ_μ) and two azimuthal angles (φ_p,φ_μ). However under the assumption the detector acceptance over azimuthal angles is uniform the distribution can be simplified in the 3-dimensional angular distribution. This analysis make use of the 3D angular distribution and does not take into account possible correlations involving the azimuthal angles. Such correlations could arise due to the geometrical acceptance and efficiency of the detector and might require explicit correlations coefficients in the measurements.

The level of correlations between two variables X and Y is estimated by the correlation factor ρ_{XY} defined as

$$\rho_{XY} = \frac{Cov(X;Y)}{\sigma_X \sigma_Y}, \tag{5.1}$$

where $Cov(X,Y)$ is the covariance of X and Y, and their SDs σ_X and σ_Y respectively. The correlation factors between the five angles are listed in Table 5.1 for 2012 data. There is no correlation more than 1.5% involving the azimuthal angles and at least of 6% between polar angles. Due to this observations correlation factors are not introduced in the measurements. However the assumption of the uniformity of the azimuthal angles is taken into account in the systematic uncertainty.

Table 5.1 Correlation factors of the observable angles in 2012 data.

Correlation	Λ_b %	$\overline{\Lambda_b}$ %
$\cos\theta_\Lambda;\cos\theta_p$	2.37	-1.21
$\cos\theta_\Lambda;\cos\theta_\mu$	-3.72	-6.26
$\cos\theta_p;\cos\theta_\mu$	0.09	0.95
$\varphi_p;\varphi_\mu$	0.24	1.75
$\varphi_p;\cos\theta_\Lambda$	0.32	0.98
$\varphi_p;\cos\theta_p$	0.48	0.55
$\varphi_p;\cos\theta_\mu$	-1.22	0.41
$\varphi_\mu;\cos\theta_\Lambda$	0.36	0.38
$\varphi_\mu;\cos\theta_p$	0.84	1.21
$\varphi_\mu;\cos\theta_\mu$	-1.29	-0.45

5.2 Angular resolution

The angular resolution of the three angular variables is relevant in the analysis because if the resolution is worse or better than the average along of the distribution of each variable, the overall angular shape might change in a non negligible way.

The resolution is calculated from simulated events (see appendix A) by taking the so-called residuals, which are the differences between the values of the angular variables at generation level (before of detector simulation), and the resulting after to apply the full simulation. Then residuals are fitted using Gaussian functions. The means of the Gaussian functions near to 0 indicate no bias, and σ (or SD) is considered as the resolution. The differences of the variables are taken in the range $[-1,1]$ divided into 10 intervals of the same length, the yields of the fits are shown in Table 5.2. It can be seen the mean of the distributions are practically 0 indicates there is no bias in the reconstruction. On the other hand, the resolution is almost constant along of the distributions, however differences are considered in the systematic uncertainties.

Table 5.2 Angular resolutions of the angular variables in different ranges. The values are obtained by a fit to the data in the range $[-1,1]$ divided into 10 ranges, and using Gaussian functions.

Range	mean $\pm\sigma$		
	$\cos\theta_\Lambda$	$\cos\theta_\mathrm{p}$	$\cos\theta_\mu$
$[-1.0,-0.8]$	$-3e-5\pm0.003$	$-9e-4\pm0.029$	$-1e-4\pm0.004$
$[-0.8,-0.6]$	$-1e-4\pm0.005$	$-1e-4\pm0.037$	$-3e-4\pm0.006$
$[-0.6,-0.4]$	$-4e-5\pm0.005$	$8e-5\pm0.040$	$-3e-4\pm0.008$
$[-0.4,-0.2]$	$-1e-4\pm0.005$	$-5e-4\pm0.037$	$1e-4\pm0.009$
$[-0.2,0.0]$	$-1e-5\pm0.004$	$-3e-4\pm0.037$	$-1e-4\pm0.010$
$[0.0,0.2]$	$1e-4\pm0.004$	$-7e-5\pm0.035$	$7e-6\pm0.009$
$[0.2,0.4]$	$7e-5\pm0.004$	$4e-5\pm0.033$	$8e-5\pm0.009$
$[0.4,0.6]$	$1e-4\pm0.005$	$-6e-4\pm0.030$	$2e-4\pm0.008$
$[0.6,0.8]$	$1e-4\pm0.005$	$6e-4\pm0.028$	$-7e-5\pm0.006$
$[0.8,1.0]$	$8e-5\pm0.003$	$2e-5\pm0.021$	$8e-5\pm0.004$

5.3 Strategy of the measurement

The results are obtained from an unbinned and extended ML fit [61] to the $\mathrm{J}/\psi\Lambda$ invariant mass distribution and the three angular variables $\Theta = (\cos\theta_\Lambda, \cos\theta_\mathrm{p}, \cos\theta_\mu)$, using the full extended likelihood function:

$$\mathrm{L} = \exp(-\mathrm{N_{sig}} - \mathrm{N_{bkg}}) \prod^{\mathrm{N}} [\mathrm{N_{sig}}\,\mathrm{PDF_{sig}} + \mathrm{N_{bkg}}\,\mathrm{PDF_{bkg}}], \tag{5.2}$$

where N is the total number of events, $\mathrm{N_{sig}}$ and $\mathrm{N_{bkg}}$ are the yields of signal and background events, respectively, and $\mathrm{PDF_{sig}}$ and $\mathrm{PDF_{bkg}}$ represent the probability density functions (PDFs) for the signal and background, respectively.

This method takes into account the shape of the distributions and the number of signal and background events. The signal PDF is given by the product of a function of the invariant mass variable, the angular distribution of the decay, and the efficiency shape given by:

$$\mathrm{PDF_{sig}} = \mathrm{F_{sig}}(\Theta)\,\epsilon(\Theta)\,G(m_{\mathrm{J}/\psi\Lambda}), \tag{5.3}$$

where $F_{sig}(\Theta)$ represents the angular distribution at particle level given by Eq. 2.19, while $G(m_{J/\psi\Lambda})$ stands for the sum of two Gaussian functions used to model the invariant mass distribution as in Eq. 4.2. The effect of the detector on the angular distribution is taken into account by the factor ϵ that represents the efficiency as a function of the angles, and obtained by fitting the simulated angular distributions as discussed in Sec 5.3.1.

To model the background events the PDF_{bkg} is given by the product of

$$PDF_{bkg} = F_{bkg}(\Theta)\, Q(m_{J/\psi\Lambda}), \tag{5.4}$$

where a first-order polynomial $Q(m_{J/\psi\Lambda})$ is used to model the invariant mass distribution. The angular distribution of background is modeled with the function $F_{bkg}(\Theta)$, which is obtained using events from SB of the invariant mass distribution as discussed in Sec. 5.3.2.

The complete likelihood function in Eq. (5.2) is maximized by fitting simultaneously the four data sets for Λ_b and $\overline{\Lambda_b}$ at $\sqrt{s} = 7$ and 8 TeV, allowing for the extraction of the common parameters P, α_1, α_2, and γ_0. The fit parameters for the angular background, efficiency distributions, and the signal and background mass parameters are obtained from independent fits and fixed in the full ML function, while the P and the angular parameters are left floating.

5.3.1 Efficiency shapes

For needs of this analysis the absolute value of the efficiency in terms of the fraction reconstructed-selected/generated events is not of interest. The property relevance are the shapes of the distortions introduced by the detector, and the reconstruction and selection effects. Clearly the original flat distributions at generation level (Fig. 5.1) are distorted after full simulation and selection (Fig. 5.2).

The efficiency shapes are estimated from MC simulation (see Appendix A), where $\Lambda_b \to J/\psi\,\Lambda$ decays were generated using the EVTGEN phase space (PHSP) decay models to generate uniform angular distributions, and to achieve a precise angular estimates in all angular region. The flat distributions are shown in Fig. 5.1.

After to apply the same reconstruction and selection processes to the simulation, a few combinatorial background (Fig. A.1) remains and might affect the efficiency calculation. So the remaining background is removed by the SB subtraction method, which is based on the assumption that the background distribution in the SB region is similar to the signal one. The regions are defined using the $m_{J/\psi\Lambda}$ mass distribution

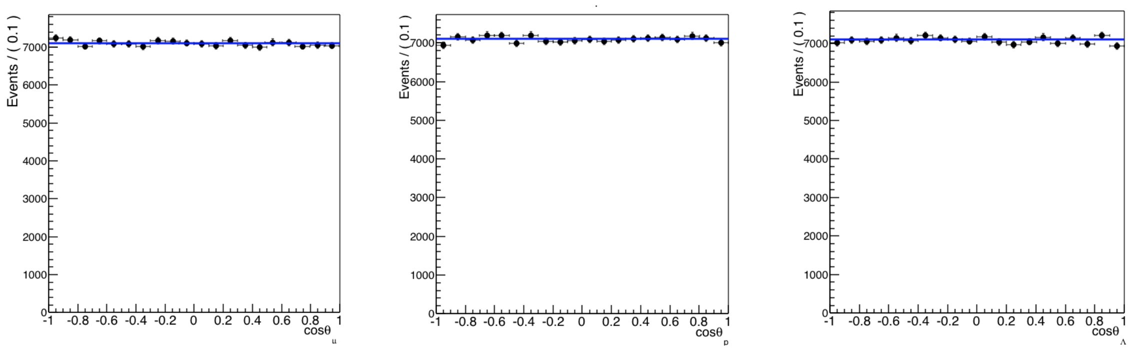

(a) $\cos\theta_\mu$ (b) $\cos\theta_\mathrm{p}$ (c) $\cos\theta_\Lambda$

Fig. 5.1 Angular distributions of the decay $\Lambda_\mathrm{b} \to \mathrm{J}/\psi\,\Lambda$ using the PHSP decay model in EVTGEN.

as in Sec. 4.5.3, and used to create two 3D histograms of the angular variables with events in the signal and SB regions, respectively. The ratio of the integrals of those histograms is taken to get a multiplicative factor. Finally the SB histogram is scaled by the multiplicative factor and subtracted from the signal-region histogram. The resulting distributions are an estimation of pure signal events. The angular shapes after full simulation and background subtraction are shown in Fig. 5.2. Taking the background-subtracted simulation, a comparison of data/simulation is performed to find possible differences between them. To ensure the simulation reproduces the data a weighting process is performed as discussed in Appendix B. The weighted simulation is used to obtain the efficiency distributions (Fig. 5.2).

To model the efficiency distributions we start from the numbers in Table 5.1, where a low correlation is observed between the angular variables in the analysis. Then we choose a product of three Chebyshev polynomials of the first kind as model to the efficiency, and determined by:

$$\epsilon(\cos\theta_\Lambda, \cos\theta_\mathrm{p}, \cos\theta_\mu) = \prod_{i=\Lambda,\mathrm{p},\mu} \left(\sum_{j}^{\mathrm{N}_i} \mathrm{A}_{ij}\,\mathrm{T}_j\,(\cos\theta_i)\right), \tag{5.5}$$

N_i is the maximal degree of the Chebyshev polynomials to be determinate. The free coefficients A_{ij} are obtained for Λ_b and $\overline{\Lambda_\mathrm{b}}$ at $\sqrt{s} = 7$ and $\sqrt{s} = 8\,\mathrm{TeV}$ in separate likelihood fits. The simulated efficiency distributions and the resulting fits are shown in Figure 5.3. It can be seen from Fig. 5.3, the chosen model for the parametrization describes well the shapes of the distributions. Information of the goodness of fit in terms of χ^2/dof per degree of freedom is presented in Table 5.3.

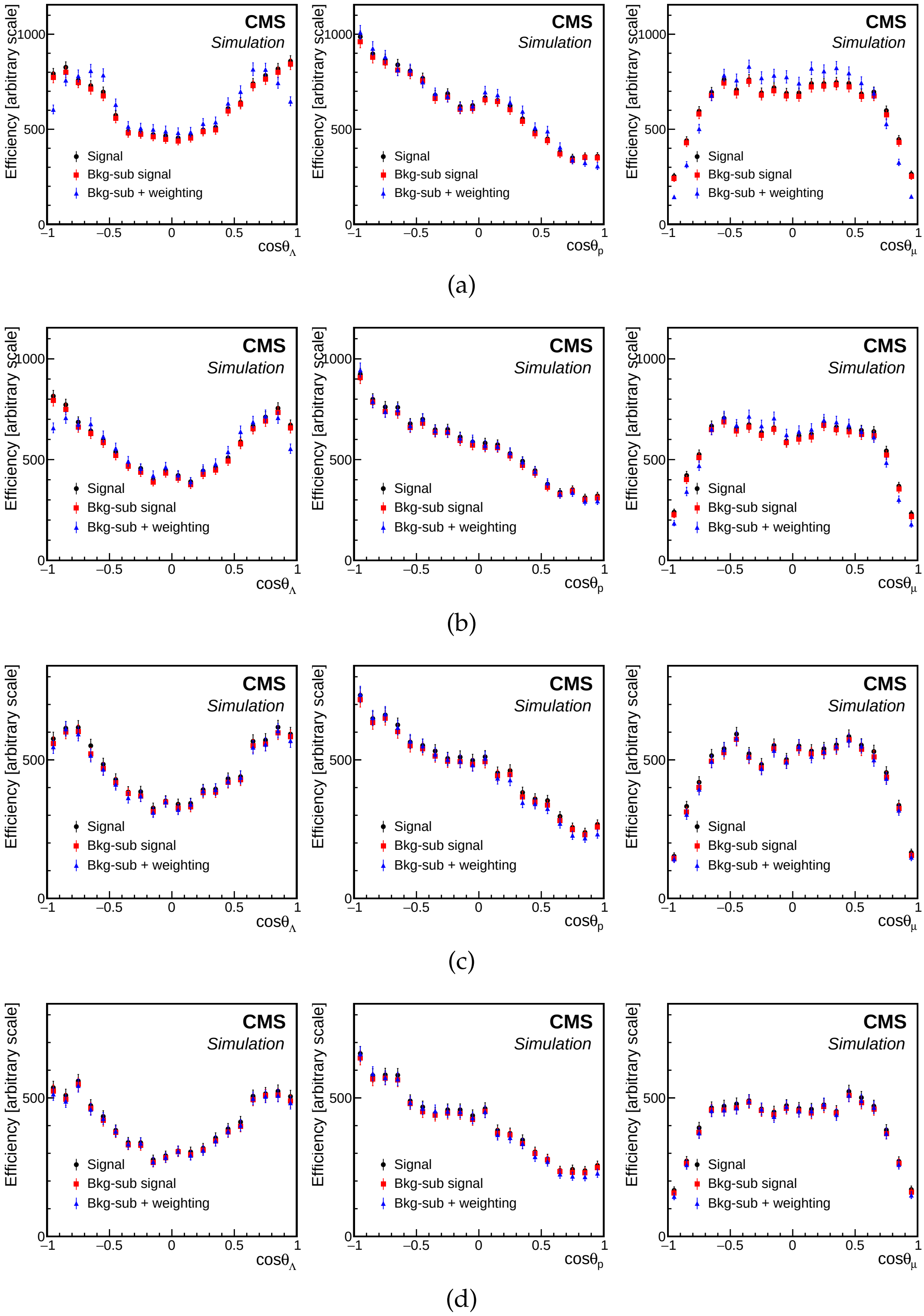

Fig. 5.2 Efficiency distributions of $\cos\theta_\Lambda$, $\cos\theta_\mathrm{p}$, $\cos\theta_\mu$ (from left to right) from full simulations of (a) $\Lambda_\mathrm{b} \to \mathrm{J}/\psi\,\Lambda$ and (b) $\overline{\Lambda}_\mathrm{b} \to \mathrm{J}/\psi\,\Lambda$ decays at $\sqrt{s} = 7\,\mathrm{TeV}$, and (c) $\Lambda_\mathrm{b} \to \mathrm{J}/\psi\,\Lambda$ and (d) $\overline{\Lambda}_\mathrm{b} \to \mathrm{J}/\psi\,\Lambda$ decays at $\sqrt{s} = 8\,\mathrm{TeV}$. The black dots represent the signal events, the squares represent the background-subtracted signal, and triangles show simulation after background subtraction and weighting process.

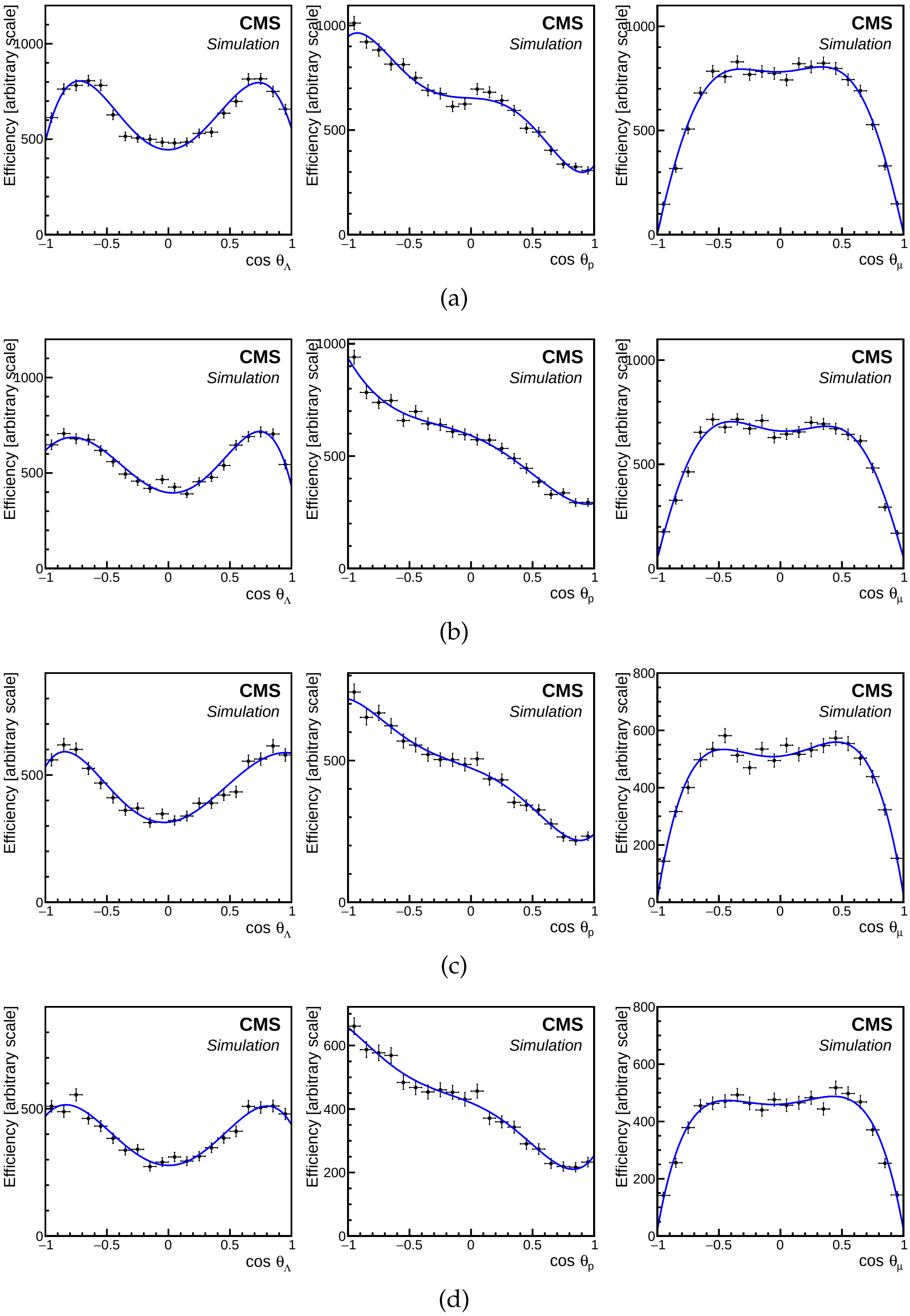

Fig. 5.3 The efficiencies as a function of $\cos\theta_\Lambda$, $\cos\theta_\mathrm{p}$, $\cos\theta_\mu$ (from left to right) obtained from simulated (a) $\Lambda_\mathrm{b} \to \mathrm{J}/\psi\,\Lambda$ and (b) $\overline{\Lambda_\mathrm{b}} \to \mathrm{J}/\psi\,\Lambda$ decays at $\sqrt{s} = 7\,\mathrm{TeV}$, and (c) $\Lambda_\mathrm{b} \to \mathrm{J}/\psi\,\Lambda$ and (d) $\overline{\Lambda_\mathrm{b}} \to \mathrm{J}/\psi\,\Lambda$ decays at $\sqrt{s} = 8\,\mathrm{TeV}$. The vertical bars on the points are the statistical uncertainties in the simulated data and the lines show the projections of a 3D fit to the distributions using Chebyshev polynomials.

Table 5.3 Resulting χ^2/dof by fitting the efficiency distributions

Observable	$\sqrt{s}=7\,\text{TeV}$		$\sqrt{s}=8\,\text{TeV}$	
	Λ_b	$\overline{\Lambda_b}$	Λ_b	$\overline{\Lambda_b}$
$\cos\theta_\Lambda$	2.4	1.3	1.4	1.2
$\cos\theta_p$	1.4	0.9	0.9	0.9
$\cos\theta_\mu$	1.5	1.9	1.3	1.5

5.3.2 Angular background estimation

Angular background is present along $m_{J/\psi\Lambda}$ distribution, an important assumption to estimate the angular background below the mass peak is that the kinematic variables of background events in the signal and sidebands region have a similar statistical behavior (Fig. 5.4). The sidebands region is defined as mentioned in Sec. 4.5.3. Events in SB are taken and modeled to be used in the complete likelihood function. The SB

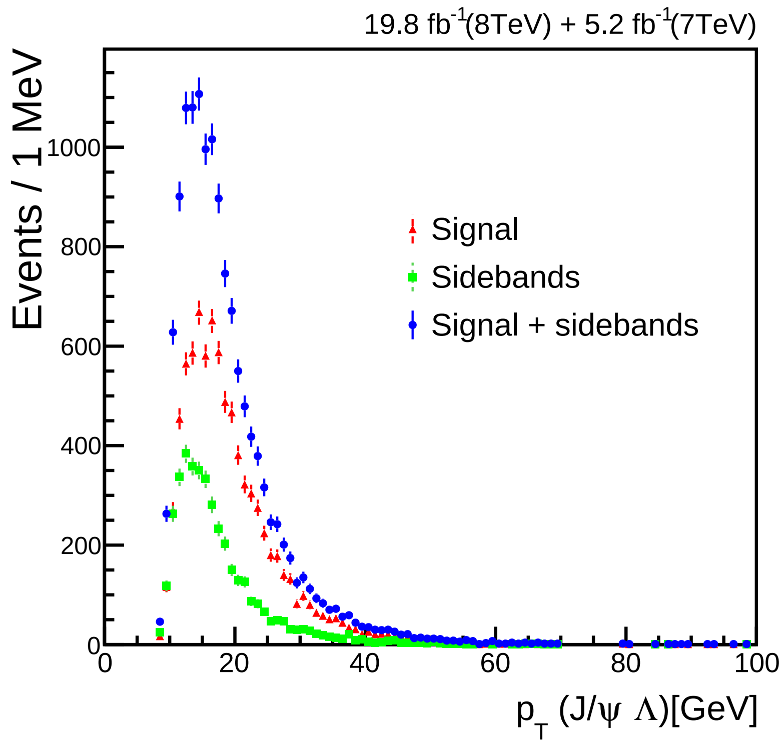

Fig. 5.4 Distribution of $p_T^{J/\psi\Lambda}$ taking events from signal, SB and both regions.

angular distributions are modeled by Chebyshev polynomials of the first kind for $\cos\theta_\Lambda$ and $\cos\theta_p$ and error functions are used to describe the distribution in $\cos\theta_\mu$.

These functions are combined as follows:

$$\mathrm{F_{bkg}}(\Theta) = (\sum_{i=0}^{n_\Lambda} b_i\, T_i(\cos\theta_\Lambda))\,(\sum_{j=0}^{n_\mathrm{p}} c_j\, T_j(\cos\theta_\mathrm{p}))\,\mathrm{E}\,(\cos\theta_\mu), \tag{5.6}$$

where b_i and c_j are the parameters to be determined, n_Λ and n_p represent the maximal degree of the T_i Chebyshev polynomials, and E is defined as

$$\mathrm{E}(\cos\theta_\mu) = (1 + \mathrm{erf}(\frac{\cos\theta_\mu - d_1}{d_2}))\,(1 + \mathrm{erf}(\frac{-\cos\theta_\mu - d_3}{d_4})). \tag{5.7}$$

The b, c and d parameters are determined from separated 3D fits to the four data sets Λ_b and $\overline{\Lambda_\mathrm{b}}$ in 2011 and 2012 and fixed in the complete likelihood function (Eq. 5.2). The results of the fits are shown in Figure 5.5. The $\cos\theta_\mathrm{p}$ distributions are well described by fourth order polynomials, while to model $\cos\theta_\Lambda$ distributions polynomials up to sixth order are used. The χ^2/dof of the resulting angular projections can be found in Table 5.4.

Table 5.4 Resulting χ^2/dof for the unbinned likelihood fit to the sidebands angular distributions

Observable	$\sqrt{s} = 7\,\mathrm{TeV}$		$\sqrt{s} = 8\,\mathrm{TeV}$	
	Λ_b	$\overline{\Lambda_\mathrm{b}}$	Λ_b	$\overline{\Lambda_\mathrm{b}}$
$\cos\theta_\Lambda$	1.53	2.06	1.25	0.87
$\cos\theta_\mathrm{p}$	0.93	0.91	1.02	1.42
$\cos\theta_\mu$	0.38	0.72	0.84	0.76

5.4 Fit results

The complete likelihood function in Eq. (5.2) is maximized by fitting simultaneously the four data sets for Λ_b and $\overline{\Lambda_\mathrm{b}}$ at $\sqrt{s} = 7$ and $8\,\mathrm{TeV}$, allowing for the extraction of the common parameters P, α_1, α_2, and γ_0. The simultaneous fit is performed in the enriched signal mass range within 3.5 SDs of the mean Λ_b mass. This range contains more than 99.9% of the signal events, and significantly reduces the number of background events. As a result, the fit is less sensitive to the modeling discussed. The fit parameters for the angular background and efficiency distributions are fixed to those found in the previous fits in Secs. 5.3.1 and 5.3.2. The signal and background mass parameters are obtained from previous fits to the mass distribution in Sec. 4.5.3,

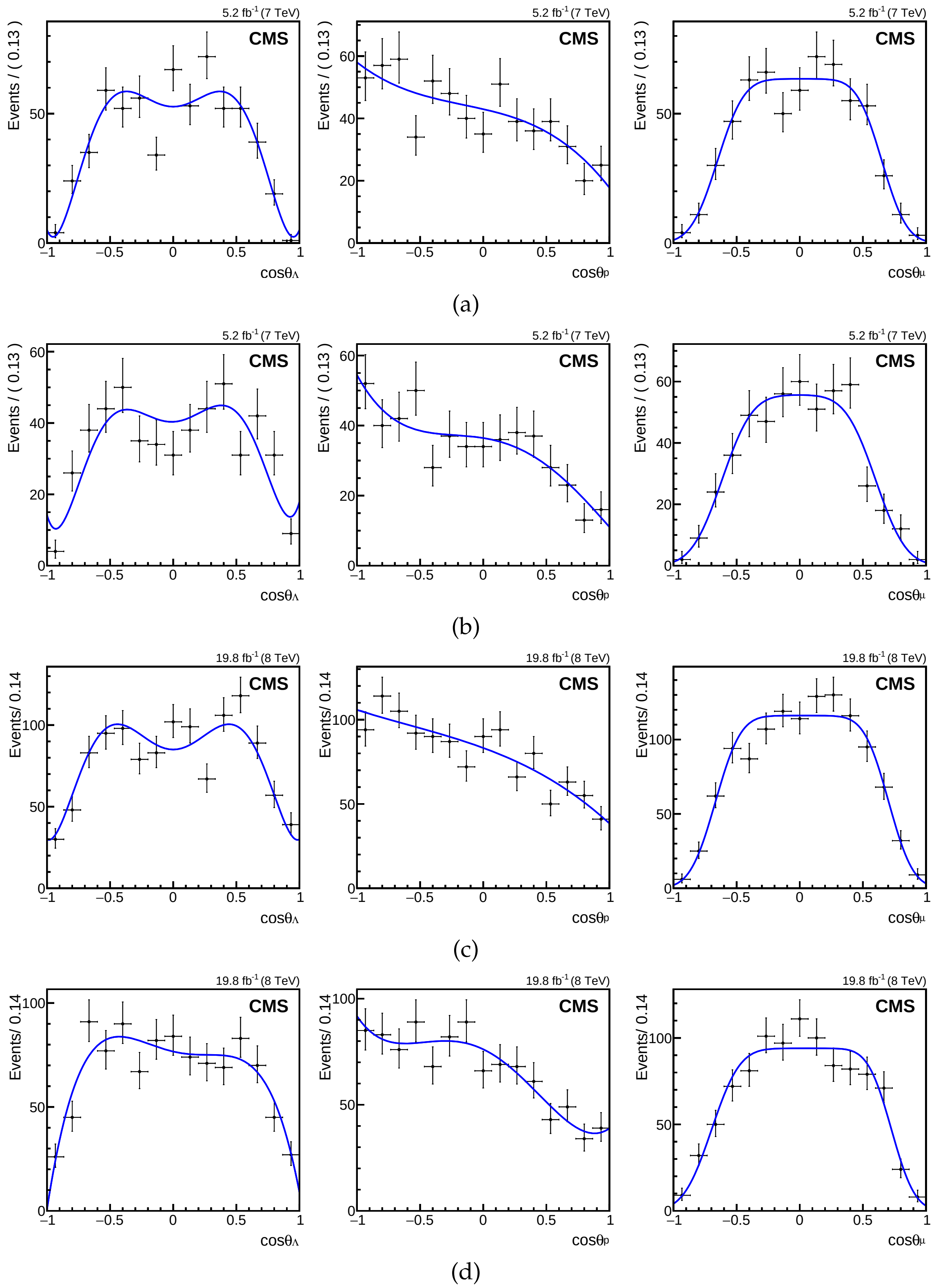

Fig. 5.5 Angular background of $\cos\theta_\Lambda$, $\cos\theta_\mathrm{p}$, $\cos\theta_\mu$ (from left to right) distributions for (a) Λ_b and (b) $\overline{\Lambda_\mathrm{b}}$ decays at $\sqrt{s} = 7\,\mathrm{TeV}$, and (c) Λ_b and (d) $\overline{\Lambda_\mathrm{b}}$ decays at $\sqrt{s} = 8\,\mathrm{TeV}$. The vertical bars on the points are the statistical uncertainties in SB data and the solid line shows the projections of a 3D fit to the distributions using Chebyshev polynomials and the complementary error functions described in Eq 5.6.

and the numbers of signal and backgrounds events are fixed to the propagated values in the signal mass region. The resulting fit values of the polarization and the three angular decay parameters are:

$$\begin{aligned} P &= 0.00 \pm 0.06, \\ \alpha_1 &= 0.14 \pm 0.14, \\ \alpha_2 &= -1.11 \pm 0.04, \\ \gamma_0 &= -0.27 \pm 0.08, \end{aligned}$$

where the uncertainties are statistical only. The correlation matrix of the fitted parameters is shown in Table 5.5. No strong correlations are found among these parameters. Translating these values to the squares of the helicity amplitudes by Eqs. 2.21 and using the correlation factors in Table 5.5, the results are:

$$\begin{aligned} |T_{++}|^2 &= \quad 0.05 \pm 0.04, \\ |T_{+0}|^2 &= -0.10 \pm 0.04, \\ |T_{-0}|^2 &= \quad 0.51 \pm 0.03, \\ |T_{--}|^2 &= \quad 0.52 \pm 0.04, \end{aligned}$$

where the uncertainties are only statistical and propagated using the correlation matrix in Table 5.5. The projections of the fit are shown in Figs. 5.6 and 5.7 for Λ_b and $\overline{\Lambda_b}$, respectively, using the combined data at $\sqrt{s} = 7$ and 8 TeV.

Table 5.5 Correlation matrix for the fitted parameters.

Parameter	P	α_1	α_2	γ_0
P	1	−0.039	−0.029	0.116
α_1		1	−0.207	−0.030
α_2			1	0.285
γ_0				1

The most likely parameter values can be verified looking at the minimum values of $-\ln L$ (i.e. the value that maximizes L) as shown in Figure 5.8, where it shows the likelihood scan in the fit. The method used to determine the uncertainty on maximum likelihood estimates is taking $-\ln L_{min} + \frac{1}{2}$ [62]. This approach may lead to asymmetric errors, but better follows the non-local behavior of the likelihood func-

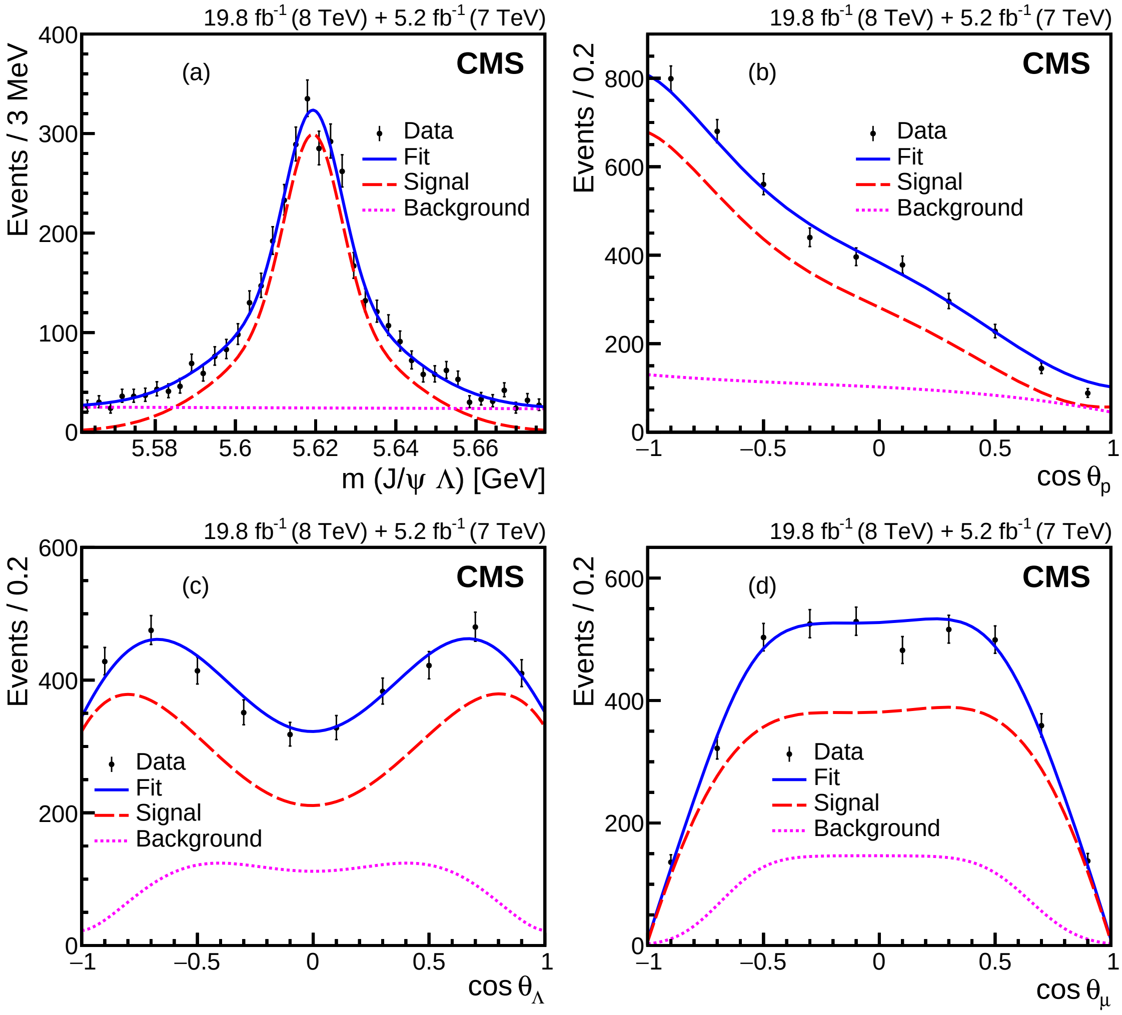

Fig. 5.6 Distributions in (a) $m_{J/\psi\Lambda}$, (b) $\cos\theta_p$, (c) $\cos\theta_\Lambda$, and (d) $\cos\theta_\mu$ for Λ_b candidates in the combined $\sqrt{s} = 7$ and 8 TeV data. The vertical bars on the points are the statistical uncertainties in the data, the solid line shows the result of the fit, and the dashed and dotted lines represent, respectively, the signal and background contributions from the fit.

tion. In practice the systematic uncertainties are estimated using MINUIT/MINOS as implemented in Roofit [63].

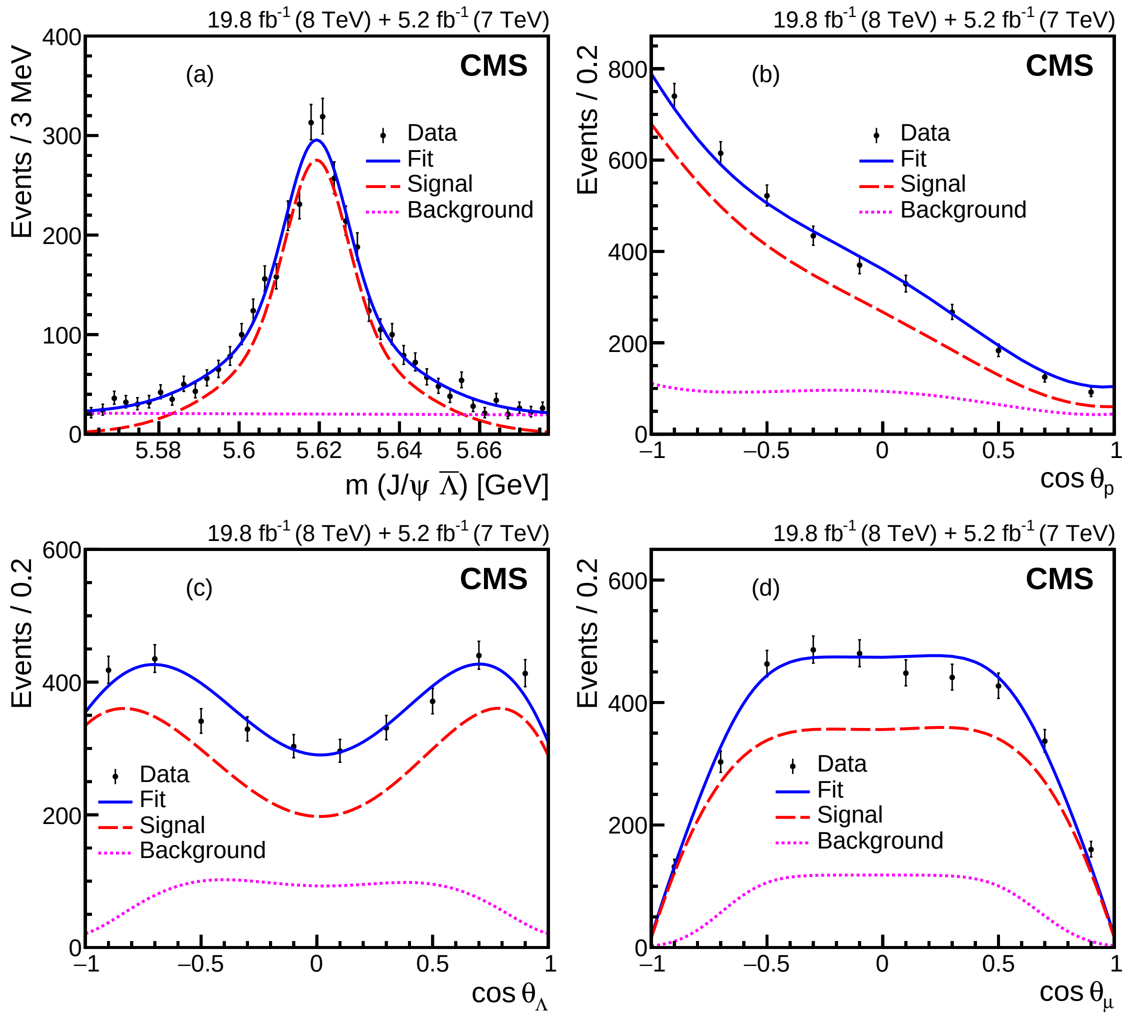

Fig. 5.7 Distributions in (a) , (b) $\cos\theta_{\mathrm{p}}$, (c) $\cos\theta_{\Lambda}$, and (d) $\cos\theta_{\mu}$ for $\overline{\Lambda}_{\mathrm{b}}$ candidates in the combined $\sqrt{s} = 7$ and 8 TeV data. The vertical bars on the points are the statistical uncertainties in the data, the solid line shows the result of the fit, and the dashed and dotted lines represent, respectively, the signal and background contributions from the fit.

5.5 Validation of the likelihood fit

5.5.1 Toy Monte Carlo studies

The bias of an estimator is the average deviation of the estimate from its true value:

$$b(\iota) = <\hat{\iota} - \iota> = <\hat{\iota}> - \iota.$$

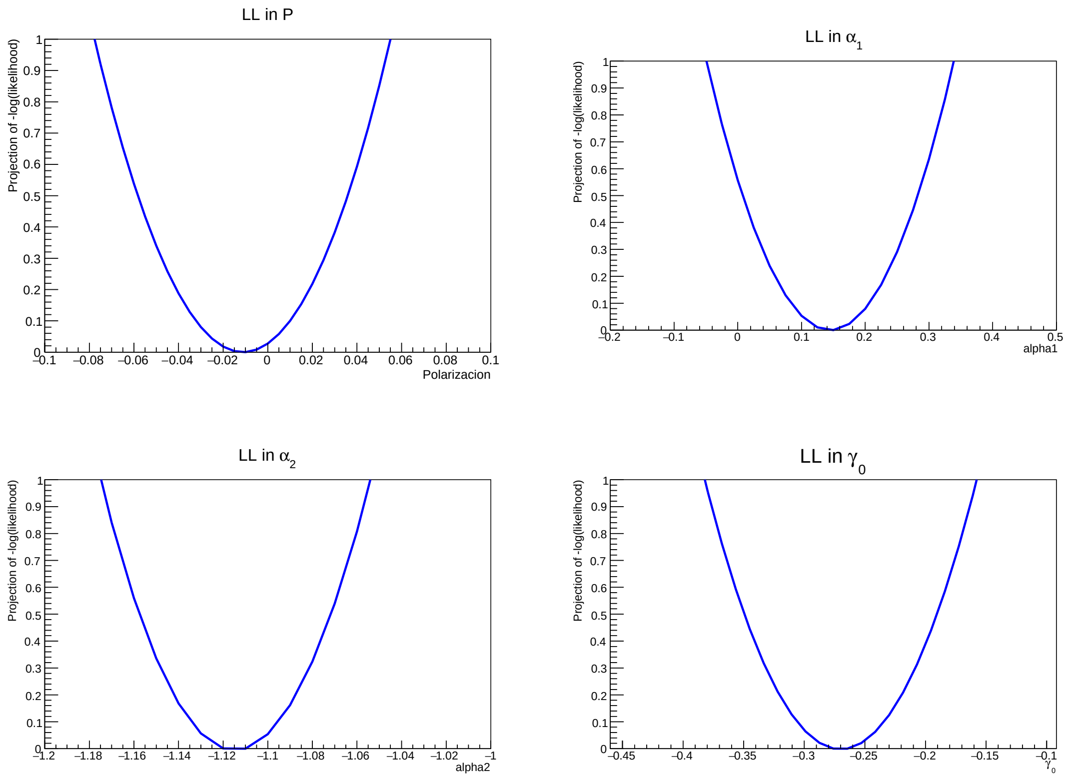

Fig. 5.8 Resulting projections of likelihood function of (a) P, (b) α_1, (c) α_2, and (d) γ_0 in the fit.

The average is intended as the expected value over an infinitely large number of repeated experiments. A possible bias due to the fitting procedure is investigated using toy Monte Carlo samples generated according to the total 2011, 2012 PDF's for Λ_b and $\overline{\Lambda_b}$. The samples are generated in the mass region ($[\mu - 10\sigma, \mu + 10\sigma]$) with the number of signal and background events in accordance with the numbers observed in data, then a fit in the smaller region ($[\mu - 3.5\sigma, \mu + 3.5\sigma]$) of the $m(J/\psi\Lambda)$ invariant mass peak is performed. The simultaneous full likelihood fit is then applied to the generated samples to test if the fit is able to recover the input values of the angular decay parameters and the Λ_b polarization used to generate the samples. Results from 1,000 pseudo-experiments were used to study the distributions for the four fitted parameters and their corresponding pull distributions, where the pull of a quantity x in the i-Th pseudo-experiment is defined as

$$pull(x_i) = \frac{x_i^{fit} - x_i^{true}}{\sigma_i^{fit}} \tag{5.8}$$

with x_i^{fit} being the fitted value, x_i^{true} the true (generated) value and σ_i^{fit} is the error on x_i^{fit} computed by the fit. Pulls normally distributed with a mean value at 0 indicates no bias, and width at 1 suggest if the calculated errors are correct. The distributions of the fitted parameters are shown in Fig. 5.9 with their error distribution in Fig. 5.10, and their corresponding pulls distributions. Fig. 5.11 do not show any bias introduced by the fitting procedure. The fit is able to recover the input values. Table 5.6 presents the central values of the fit results and the pull distributions along with the values used to generate the test samples.

Table 5.6 Input values and results from 1,000 toy Monte Carlo pseudo-experiments

Parameter	Input Value	Fit results	pull mean	pull deviation	pull width
P	0.00	0.001 ± 0.002	-0.006 ± 0.034	0.4σ	1.04 ± 0.02
α_1	0.12	0.123 ± 0.004	-0.0192 ± 0.030	0.97σ	1.14 ± 0.02
α_2	-0.93	-0.931 ± 0.04	-0.019 ± 0.030	0.64σ	0.95 ± 0.02
γ_0	-0.45	-0.452 ± 0.002	-0.032 ± 0.031	1.1σ	1.03 ± 0.02

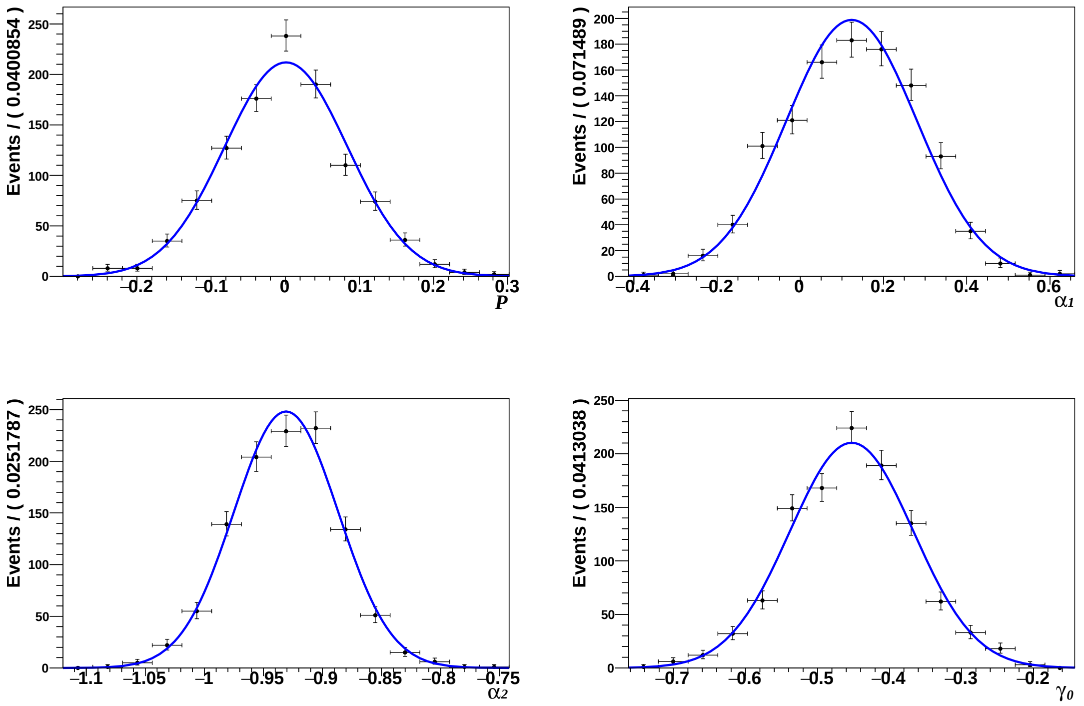

Fig. 5.9 Distributions of the fitted parameters from 1,000 simultaneous likelihood fit to the toy MC test samples.

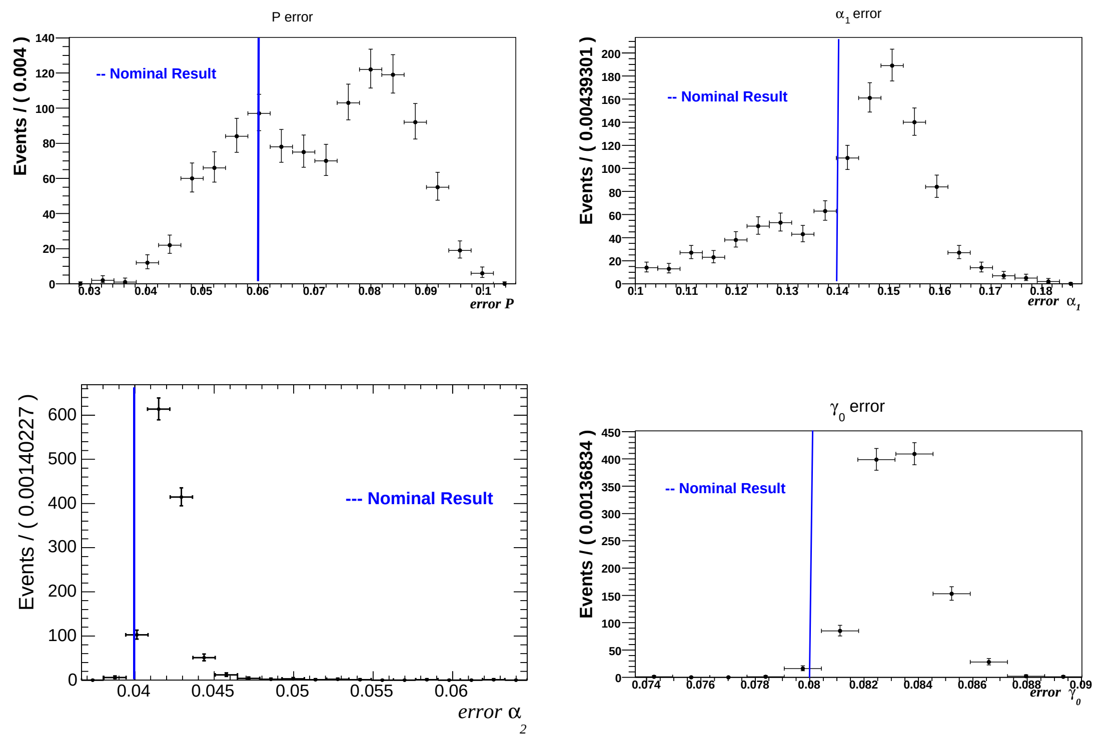

Fig. 5.10 Error distributions from 1,000 simultaneous likelihood fit to the toy MC test samples.

5.5.2 Testing the fit procedure

A closure test is performed by generating simulations of Λ_b and $\overline{\Lambda_b}$ decays at $\sqrt{s} = 7\,\text{TeV}$ and $8\,\text{TeV}$ as in Appendix A, but taking different input values of the helicities and polarization in HELAMP decay model [64] for the Λ_b and Λ decays, and VLL [64] models for the J/ψ decays which are implemented in EVTGEN. Then after reconstruction and selection processes, a similar fit is performed as in data in order to get back the input values. The input parameter values of each sample are shown in Table 5.7. Equations. 2.20 are used to translate the angular parameters to the helicity amplitudes, and the resulting values are set in the generation. The distributions at generation level are shown in Figure 5.12. The yields of signal and background from a fit to the full simulation are shown in Table 5.8.

After the generation step (Fig. 5.12), the same reconstruction procedure and selection cuts as data were applied. An unbinned simultaneous likelihood fit is applied to Λ_b and $\overline{\Lambda_b}$ candidates of each test. The maximum likelihood function defined in Eq. 5.2 is used to fit the simulated data. The efficiency models are obtained from dif-

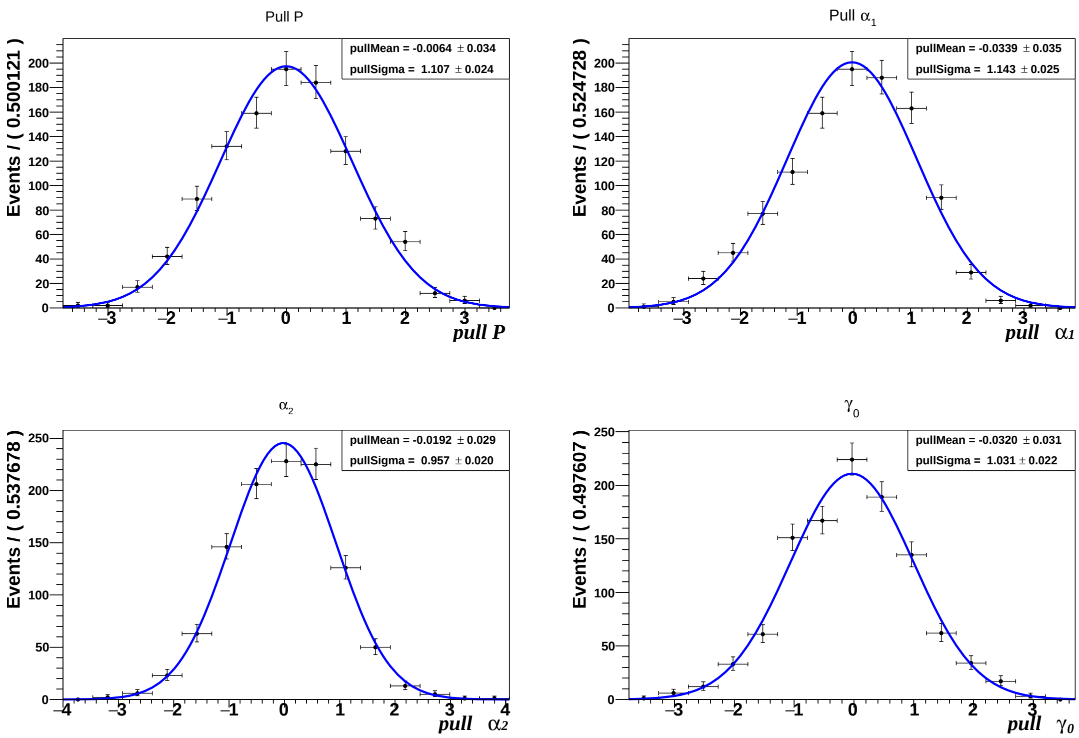

Fig. 5.11 Pull distributions from 1,000 simultaneous likelihood fit to the toy MC test samples.

Table 5.7 Input parameter values to be translated by using the Eqs. 2.21 and then set in EVTGEN. All samples were generated at $\sqrt{s} = 7\,\text{TeV}$ conditions except for the sample 4 which were at $\sqrt{s} = 8\,\text{TeV}$ conditions.

Parameter	Input Values			
	Sample 1	Sample 2	Sample 3	Sample 4
P	0.0	-0.3	0.8	0.002
α_1	0.46	0.16	-0.13	0.11
α_2	0.68	-0.99	0.008	-0.90
γ_0	0.26	-0.72	-1.10	-0.50

ferent simulations, which are generated using the same procedure as in Appendix A. The background models are obtained from a few combinatorial background presented in the simulations. The fit results are summarized in Figures 5.13–5.16, and the resulting numbers in Table 5.9. Comparisons of the fit result and input values are presented in absolute and SD differences. Both values are compatible within

Table 5.8 Different MC samples were generated with different input values of polarization and helicity amplitudes in EVTGEN. The yields of signal and background after fit the simulated data samples are presented.

Sample	N_{sig}		N_{bkg}	
	Λ_b	$\overline{\Lambda_b}$	Λ_b	$\overline{\Lambda_b}$
1	9276 ± 97	8336 ± 92	122 ± 20	96 ± 19
2	11714 ± 109	10511 ± 103	82 ± 14	69 ± 14
3	10381 ± 103	9377 ± 97	50 ± 13	63 ± 13
4	21854 ± 149	19686 ± 141	123 ± 16	87 ± 15

errors, however there are small differences at 3SD (α_2) and they are considered in the systematic uncertainties and discussed in Appendix C.

Table 5.9 Likelihood fit results for different MC test samples. Uncertainties are statistical only.

	P	α_1	α_2	γ_0
Sample 1				
Input	0.00	0.46	0.68	0.26
Fit	0.02 ± 0.02	0.68 ± 0.07	0.74 ± 0.02	0.36 ± 0.04
Absolute Diff	0.02	0.24	0.06	0.10
SD Diff	1.0	3.4	3.0	2.5
Sample 2				
Input	-0.30	0.16	-0.99	-0.72
Fit	-0.33 ± 0.04	0.16 ± 0.03	-0.93 ± 0.02	-0.68 ± 0.03
Absolute Diff	0.03	0.003	0.06	0.03
SD Diff	-0.07	0.0	3.0	1.4
Sample 3				
Input	0.80	-0.13	-0.008	-1.10
Fit	0.76 ± 0.06	-0.13 ± 0.02	-0.02 ± 0.02	-1.10 ± 0.03
Absolute Diff	0.04	0.0	0.01	0.01
SD Diff	-0.6	0.02	-0.6	0.3
Sample 4				
Input	0.002	0.11	-0.90	-0.50
Fit	0.03 ± 0.02	0.206 ± 0.048	-0.857 ± 0.015	-0.386 ± 0.042
Absolute Diff	0.028	0.22	0.047	0.114
SD Diff	1.4	2.0	3.0	2.7

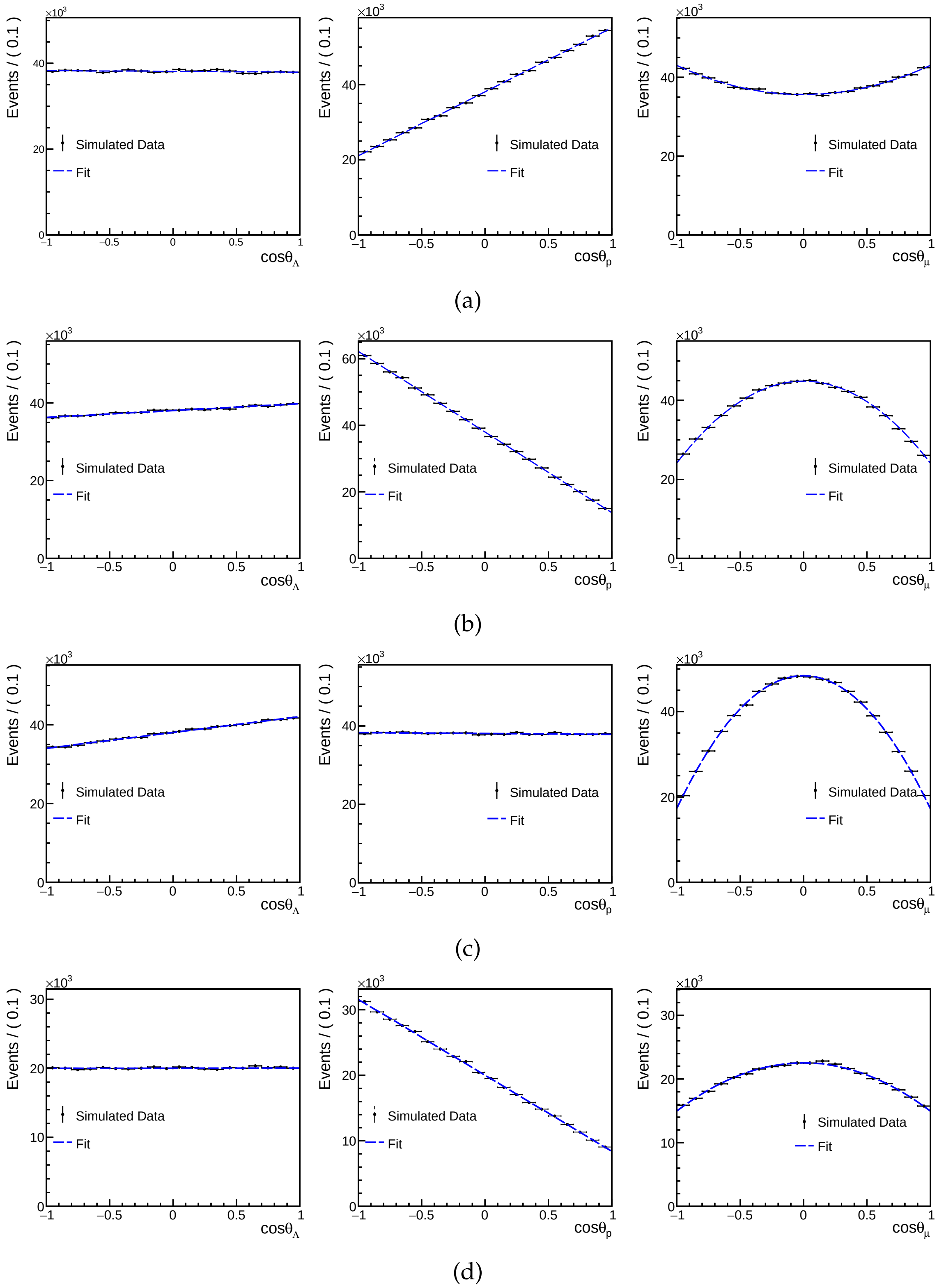

Fig. 5.12 MC truth at generation level using different values of the table 5.7 . Projections of $\cos\theta_\Lambda$, $\cos\theta_\mathrm{p}$, $\cos\theta_\mu$ from left to right of (a) Sample 1, (b) Sample 2 and (c) Sample 3.

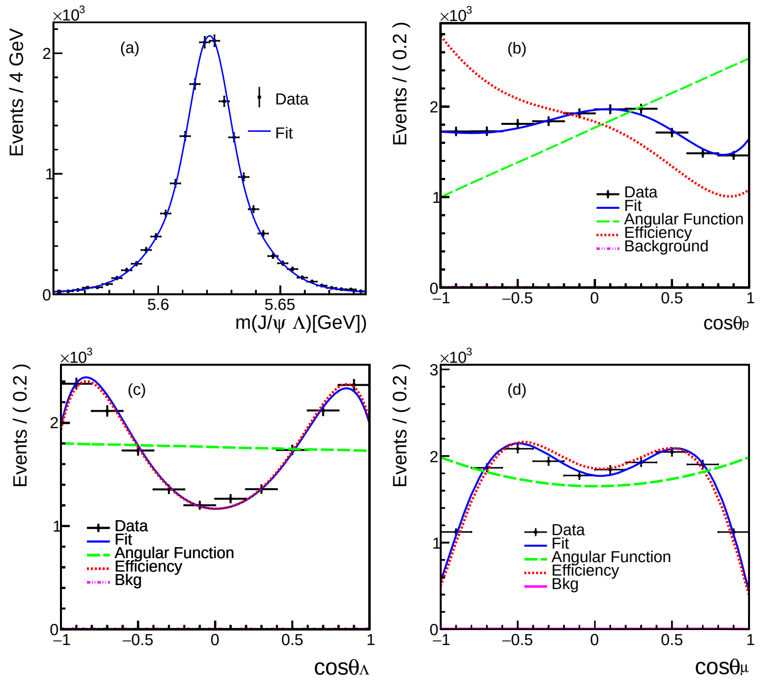

Fig. 5.13 Fit to MC sample 1. Projections of (a) $m_{J/\psi\Lambda}$, (b) $\cos\theta_p$, (c) $\cos\theta_\Lambda$ and (d) $\cos\theta_\mu$ for Λ_b candidates. The solid line shows the likelihood fit to MC events.

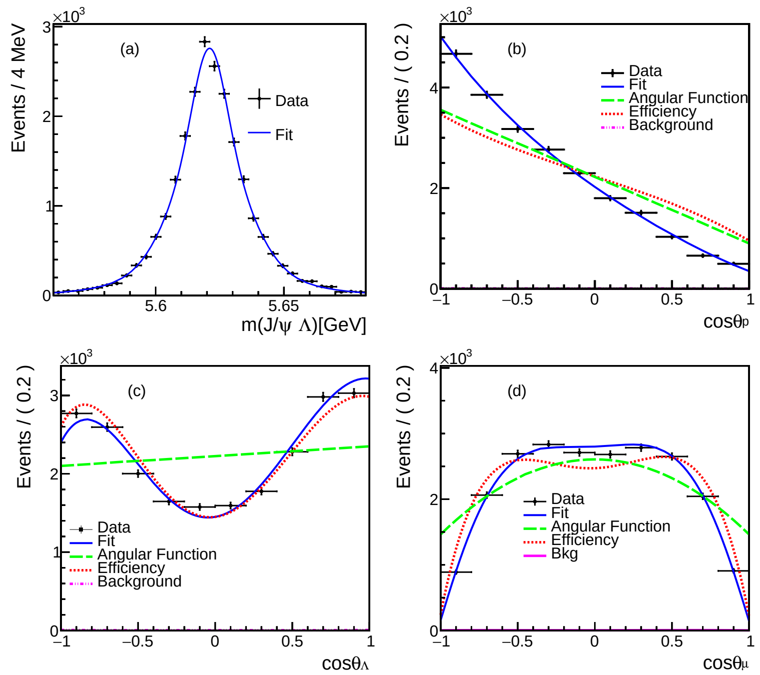

Fig. 5.14 Fit to test sample 2. Projections of $m_{J/\psi\Lambda}$, $\cos\theta_p$, $\cos\theta_\Lambda$ and $\cos\theta_\mu$ for Λ_b candidates. The solid line shows the likelihood fit to MC events.

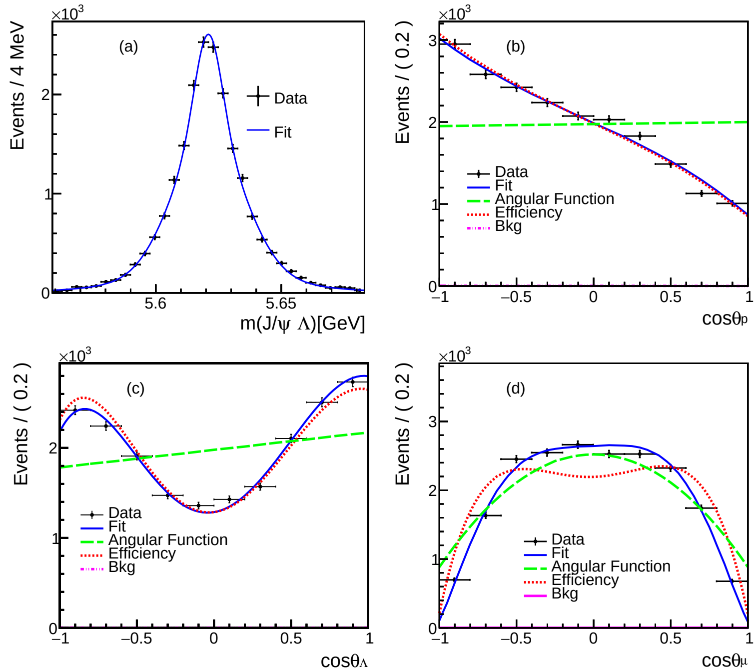

Fig. 5.15 Fit to test sample 3. Projections of (a) $m_{J/\psi\Lambda}$, (b) $\cos\theta_p$, (c) $\cos\theta_\Lambda$ and (d) $\cos\theta_\mu$ for Λ_b candidates. The solid line shows the likelihood fit to MC events.

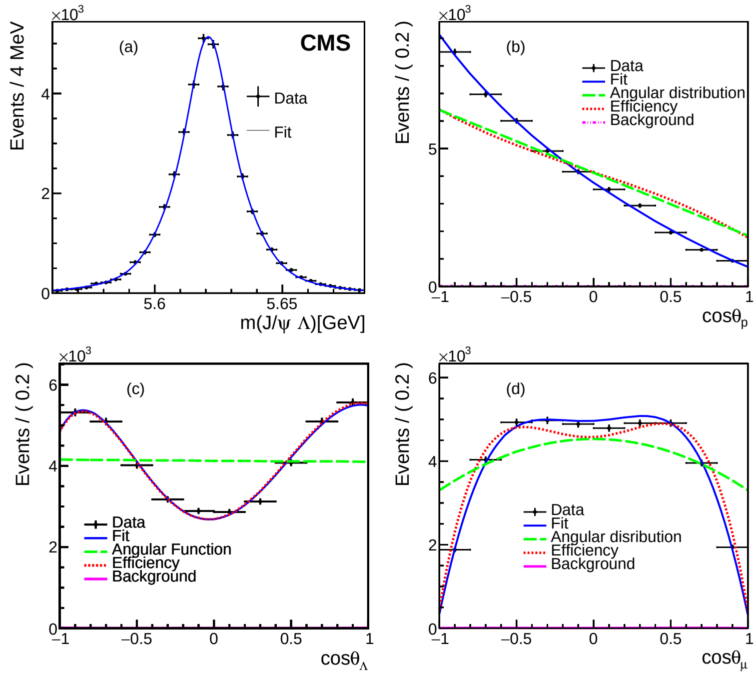

Fig. 5.16 Fit to test sample 4. Projections of (a) $m_{J/\psi\Lambda}$, (b) $\cos\theta_p$, (c) $\cos\theta_\Lambda$ and (d) $\cos\theta_\mu$ for Λ_b candidates. The solid line shows the likelihood fit to MC events.

5.6 Crosschecks

As crosscheck two measurements are performed using the different parametrization proposed by LHCb [18] and ATLAS [19]. The different parametrization and the results obtained from them are discussed in the following.

5.6.1 The LHCb Parametrization

The functions describing the 3D-angular distribution in the parametrization proposed by LHCb are listed in Table 5.10. The angular observables $\cos\theta_\Lambda, \cos\theta_{\mathrm{p}}, \cos\theta_\mu$ are the same as used in this analysis. The u_i expressions are written in terms of the following three angular parameters:

$$
\begin{aligned}
1 =& |T_{+0}|^2 + |T_{-0}|^2 + |T_{--}|^2 + |T_{++}|^2, \\
\alpha_b =& |T_{+0}|^2 - |T_{-0}|^2 + |T_{--}|^2 - |T_{++}|^2, \\
r_0 =& |T_{+0}|^2 + |T_{-0}|^2, \\
r_1 =& |T_{+0}|^2 - |T_{-0}|^2,
\end{aligned}
\tag{5.9}
$$

being (P, α_b, r_0, r_1) the four parameters to be measured simultaneously, which are related to the four helicity amplitudes by

$$
\begin{aligned}
|T_{+0}|^2 =& \frac{r_0 + r_1}{2}, \qquad & |T_{++}|^2 = \frac{1 - \alpha_b - r_0 + r_1}{2}, \\
|T_{-0}|^2 =& \frac{r_0 - r_1}{2}, \qquad & |T_{--}|^2 = \frac{1 + \alpha_b - r_0 - r_1}{2}.
\end{aligned}
\tag{5.10}
$$

Note that α_b, the parity violating-asymmetry parameter, and the other parameters are related with our notation as:

$$
\begin{aligned}
-\alpha_1 =& \alpha_b, \\
\alpha_2 =& (2r_1 - \alpha_b), \\
\gamma_0 =& (1 - 3r_0).
\end{aligned}
\tag{5.11}
$$

The physical ranges for α_b, r_0 and r_1 are $[-1,+1]$, $[0,+1]$ and $[-1,+1]$, respectively and they are constrained by:

$$\begin{aligned} 0 \leq & r_0 + r1, \\ 0 \leq & r_0 - r1, \\ 0 \leq & 1 - \alpha_b - r_0 + r_1, \\ 0 \leq & 1 + \alpha_b - r_0 - r_1. \end{aligned} \tag{5.12}$$

Under the CP conservation the parameters in the angular distribution for particle and antiparticle are related as:

$$\begin{aligned} \overline{\alpha_b} &= -\alpha_b, \\ \overline{r_0} &= r_0, \\ \overline{r_1} &= -r_1, \\ \overline{P} &= -P, \\ \overline{\alpha_\Lambda} &= -\alpha_\Lambda. \end{aligned} \tag{5.13}$$

Table 5.10 Functions describing the angular distribution in three dimensions.

i	$u_i(\alpha_b, r_0, r_1)$	v_i	w_i
1	1	1	1
2	α_b	P	$\cos\theta_\Lambda$
3	$2r_1 - \alpha_b$	α_Λ	$\cos\theta_\mathrm{p}$
4	$2r_0 - 1$	$\alpha_\Lambda P$	$\cos\theta_\Lambda \cos\theta_\mathrm{p}$
5	$(1 - 3r_0)/2$	1	$(3\cos^2\theta_\mu - 1)/2$
6	$-(\alpha_b + r_1)/2$	α_Λ	$\cos\theta_\mathrm{p}(3\cos^2\theta_\mu - 1)/2$
7	$(\alpha_b - 3r_1)/2$	P	$\cos\theta_\Lambda(3\cos^2\theta_\mu - 1)/2$
8	$-(1 + r_0)/2$	$\alpha_\Lambda P$	$\cos\theta_\Lambda \cos\theta_\mathrm{p}(3\cos^2\theta_\mu - 1)/2$

Simultaneous fit

The same strategy described in section 5.3 is applied to measure the angular decay parameters r_0, r_1, α_b and the Λ_b polarization P. Accordingly, the full likelihood function Eq. 5.2 with the angular distribution expressed in terms of the functions shown in Table 5.10 is used to perform a simultaneous fit to 2011 and 2012 data using Λ_b and $\overline{\Lambda_\mathrm{b}}$ events from the signal mass region, $m_{\mathrm{J}/\psi\Lambda} \in [\mu - 3.5\sigma, \mu + 3.5\sigma]$.

The same efficiency shapes, angular background shapes and mass models described in section 5 are implemented here. The results from the fit are:

$$P = 0.00 \pm 0.06,$$
$$\alpha_b = -0.14 \pm 0.14,$$
$$r_0 = 0.43 \pm 0.02,$$
$$r_1 = -0.61 \pm 0.07,$$

where the errors are statistical only. The correlations factors computed by the fit are displayed in Table 5.11. A strong correlation between α_b and r_0, as expected from their definitions, is observed. The central values of the angular decay do not fully agree with the physical constraints given by Eq. 5.12, for instance $-r_1 > r_0$. However, the measured values of the angular parameters are consistent with the physical restrictions at the level of 1 SD. The corresponding measured values for the squared moduli helicity amplitudes are

$$|T_{-0}|^2 = 0.52 \pm 0.03,$$
$$|T_{+0}|^2 = -0.09 \pm 0.04,$$
$$|T_{--}|^2 = 0.52 \pm 0.04,$$
$$|T_{++}|^2 = 0.05 \pm 0.04,$$

This helicity amplitudes are consistent with the values measured using Kramer's parametrization. The same minimum of -lnL is found independently of the election of the angular distribution parametrization. Our results using LHCb's parametrization can also be compared directly with those obtained by them. Table 5.12 summarizes the results obtained by CMS and LHCb where the uncertainties are only statistical and shows the differences in terms of standard deviations.

Table 5.11 Correlation Matrix of the fitted parameters.

	α_b	P	r_0	r_1
α_b	1	0.178	-0.030	0.953
P		1	0.024	0.177
r_0			1	-0.066
r_1				1

Table 5.12 Comparison between the angular decay parameters in LCHb's parametrization as measured by CMS and LHCb.

	CMS result	LHCb result	difference in SD
P	0.00 ± 0.06	0.06 ± 0.07	0.65
α_b	-0.14 ± 0.14	0.05 ± 0.17	0.86
r_0	0.43 ± 0.02	0.58 ± 0.02	5.30
r_1	-0.61 ± 0.07	-0.56 ± 0.10	0.41

Table 5.13 Functions describing the angular distribution in three dimensions.

i	$u_i(\alpha_b, k_+, k_-)$	v_i	w_i
1	1	1	1
2	α_b	P	$\cos\theta_\Lambda$
3	$(k_+^2 + k_-^2 - 1) + \alpha_b(k_+^2 - k_-^2)$	α_Λ	$\cos\theta_\mathrm{p}$
4	$(k_+^2 - k_-^2) + \alpha_b(k_+^2 + k_-^2 - 1)$	$\alpha_\Lambda P$	$\cos\theta_\Lambda \cos\theta_\mathrm{p}$
5	$[(3k_-^2 - 3k_+^2 - 1) + 3\alpha_b(1 - k_-^2 - k_+^2)]/8$	1	$(3\cos^2\theta_\mu - 1)/2$
6	$[(1 - k_-^2 - k_+^2) + \alpha_b(k_-^2 - k_+^2 - 3)]/8$	α_Λ	$\cos\theta_\mathrm{p}(3\cos^2\theta_\mu - 1)/2$
7	$[3(1 - k_+^2 - k_-^2) + \alpha_b(3k_-^2 - 3k_+^2 - 1)]/8$	P	$\cos\theta_\Lambda(3\cos^2\theta_\mu - 1)/2$
8	$[(k_-^2 - k_+^2 - 3) + \alpha_b(1 - k_-^2 - k_+^2)]/8$	$\alpha_\Lambda P$	$\cos\theta_\Lambda \cos\theta_\mathrm{p}(3\cos^2\theta_\mu - 1)/2$

5.6.2 ATLAS parametrization

The angular decay parameters in the parametrization used by ATLAS are:

$$\begin{aligned} \alpha_b =& |T_{+0}|^2 - |T_{-0}|^2 + |T_{--}|^2 - |T_{++}|^2, \\ k_+ =& \frac{|T_{+0}|^2}{|T_{+0}|^2 + |T_{--}|^2}, \\ k_- =& \frac{|T_{++}|^2}{|T_{-0}|^2 + |T_{++}|^2} \end{aligned} \tag{5.14}$$

being P, α_b, k_+^2 and k_-^2 the parameters to be measured. They are related to the helicity amplitudes as follows:

$$\begin{aligned} |T_{+0}|^2 =& \frac{(1+\alpha_b)k_+^2}{2}, \qquad & |T_{-0}|^2 =& \frac{(1-\alpha_b)(1-k_-^2)}{2}, \\ |T_{++}|^2 =& \frac{(1-\alpha_b)k_-^2}{2}, \qquad & |T_{--}|^2 =& \frac{(1+\alpha_b)(1-k_+^2)}{2}. \end{aligned} \tag{5.15}$$

The eight terms to describe the angular distribution of $\Lambda_b \to J/\psi\Lambda$ decays, are shown in Table 5.13. If CP is conserved, the parameters for the antiparticles transform according to

$$\begin{aligned} \overline{\alpha_b} &= -\alpha_b, \\ \overline{k_+^2} &= 1 - k_-^2, \\ \overline{k_-^2} &= 1 - k_+^2, \\ \overline{\alpha_\Lambda} &= -\alpha_\Lambda \\ \overline{P} &= -P \end{aligned} \tag{5.16}$$

and the angular distributions for Λ_b and $\overline{\Lambda_b}$ remain the same.

Simultaneous fit

The fit to the data is the same as described in Sec 5.3 using the same models for the angular background, efficiencies, and mass distributions. The resulting values obtained from the simultaneous fit to data are

$$\begin{aligned} P &= 0.00 \pm 0.08, \\ \alpha_b &= -0.14 \pm 0.14, \\ k_+^2 &= -0.04 \pm 0.08, \\ k_-^2 &= 0.10 \pm 0.06, \end{aligned}$$

The correlations factors are shown in Table 5.14. Despite ATLAS states that its parametrization have only small correlation we have found strong correlations between the angular decay parameters making it the less suitable among the three parametrizations. The corresponding measured values for the helicity amplitudes are

$$\begin{aligned} |T_{-0}|^2 &= 0.52 \pm 0.03, \\ |T_{+0}|^2 &= -0.08 \pm 0.04, \\ |T_{--}|^2 &= 0.51 \pm 0.04, \\ |T_{++}|^2 &= 0.05 \pm 0.04. \end{aligned}$$

The results of the helicities are compatibles with the values obtained in Sec. 5.4 within errors at the order of 1 SD. Clearly the minimum values of -lnL does not depend on the election of the parametrization in the angular distribution. We can compare our results with those obtained by ATLAS under the assumption of a polarization zero [19]. The comparison between our results and ATLAS's results are presented in Table 5.15, uncertainties are only statistical, the differences between both results in SD units are also given.

Table 5.14 Correlation Matrix of the fitted parameters.

	α_b	P	k_-^2	k_+^2
α_b	1	0.655	−0.668	0.904
P		1	−0.419	0.644
k_-^2			1	−0.665
k_+^2				1

Table 5.15 Comparison between the angular decay parameters in ATLAS' parametrization as measured by CMS and ATLAS.

	CMS result	ATLAS result	difference in SD
α_b	-0.14 ± 0.14	0.30 ± 0.16	2.07
k_+^2	-0.04 ± 0.08	$0.04^{+0.06}_{-0.09}$	0.66
k_-^2	0.10 ± 0.06	$0.02^{+0.05}_{-0.03}$	1.02

5.7 Systematic uncertainties

Various sources of systematic uncertainty that affect the measurement of the parameters P, α_1, α_2, and γ_0 are discussed below.

Fit bias The bias introduced through the fitting procedure is studied by generating 1000 pseudo-experiments using the measured parameters as inputs. The difference between the input and the mean of the fitted values is taken as the systematic uncertainty.

Asymmetry parameter α_Λ This parameter is varied up and down by its uncertainty and the maximum deviation in the final result for each parameter is taken as the systematic uncertainty.

Model for the background $m_{J/\psi\Lambda}$ distribution An exponential function is used instead of the first-order polynomial in the likelihood fit. The parameter of the exponential and the background yield are varied by their uncertainties. The fit is redone taking into account this variation on the background model for the mass, and the differences between these results and the nominal fit results are taken as the systematic uncertainty for this source.

Model for the background angular distributions Alternative parametrizations of the background angular distributions are used to estimate the systematic uncertainty. For $\cos\theta_{\Lambda}$ and $\cos\theta_{\mu}$ the alternative models comprise a superposition of Gaussian kernels, as implemented in Roofit RooKeysPdf [63], while for $\cos\theta_{p}$ the alternative model is an error function. The differences relative to the nominal results are taken as the systematic uncertainties from the modeling of the background angular distributions.

Model for the signal $m_{J/\psi\Lambda}$ distribution We estimate this uncertainty by changing the parameters by their uncertainties, taking into account their correlations. In each sample of Λ_b and $\overline{\Lambda_b}$ at $\sqrt{s} = 7$ and 8 TeV, we use the parameter of the signal mass model with the largest global correlation and add 1 SD to its nominal value if the correlation is positive and subtract 1 SD if the correlation is negative. The difference relative to the nominal result is quoted as a systematic uncertainty.

Angular efficiencies The values of the Chebyshev polynomial coefficients that model the angular dependence of the efficiencies are changed by their uncertainties. The difference relative to the nominal fitted result is taken as the systematic uncertainty.

Angular resolution We study the systematic uncertainty in the angular resolution of the measured observables $\cos\theta_{\Lambda}$, $\cos\theta_{p}$, and $\cos\theta_{\mu}$ by first determining the resolution using simulated events, then taking the difference between the generated (before detector simulation) and reconstructed (fully simulated) distributions of the cosines of the three polar angles, and fitting the resulting distributions to Gaussian functions. Using these models, we generate random numbers that are added to the three polar angles of the events at generation. The difference between the obtained parameters from the likelihood fits using the same events, with and without the added random terms, it is quoted as the systematic uncertainty from the angular resolution.

Azimuthal angle efficiency Uniform azimuthal efficiencies are assumed throughout the analysis. Besides simplifying the measurement from a five- to a three-dimensional angular analysis, this assumption also reduces the number of angular parameters from 6 to 3. The effect of the non uniformity in the φ_{p} and φ_{μ} efficiencies is investigated with 500 pseudo-experiments generated using the five-dimensional angular distribution, multiplied by the polar and azimuthal efficiencies obtained from the full simulation, as well as initializing the 3 extra parameters to values away from the physical boundary. The resulting distributions are then fitted to the nominal three-dimensional angular model. Differences in the mean values of P, α_1, α_2, and γ_0 relative to the input values (set to the nominal results) are taken as the systematic uncertainties from the impact of the non uniformity of the azimuthal efficiencies.

Weighting procedure To estimate the uncertainty from the weighting procedure, we vary each weight by its uncertainty and use this as a new weight to correct the efficiencies, then redo the fit with these new values. The differences between the results of this fit and the nominal values are taken as the systematic uncertainty in each parameter.

Reconstruction bias Possible unaccounted reconstruction biases are also considered. To estimate this systematic uncertainty, we use a simulated event sample with input values of the helicity amplitudes and polarization similar to those observed in data (see the Appendix C). Then, after reconstruction and selection as in data, we fit the simulated events and take the differences between the input and fit values for every angular parameter and polarization. Since we are using the full reconstruction of the simulated events, we subtract in quadrature the systematic sources involved in the fit from those observed differences, and finally take the square root of this subtraction as the estimate of the systematic uncertainty component due to reconstruction bias. This systematic uncertainty is by far the largest uncertainty however, it is still smaller or comparable to the corresponding statistical uncertainty.

The contributions from the different uncertainty sources are assumed to be independent and the total systematic uncertainty is calculated as the quadrature sum of all uncertainties. The values of the systematic uncertainties in each parameter from the individual sources and their quadrature sum are given in Table 5.16.

Table 5.16 The sources and values of the systematic uncertainties in each parameter and the total uncertainty. Each value in the table should be multiplied by 10^{-2} to obtain the corresponding systematic uncertainty.

Source	$P(\times 10^{-2})$	$\alpha_1(\times 10^{-2})$	$\alpha_2(\times 10^{-2})$	$\gamma_0(\times 10^{-2})$
Fit bias	0.1	0.3	0.1	0.2
Asymmetry parameter α_Λ	0.4	0.7	2.0	0.6
Bkg. $m_{J/\psi\Lambda}$ dist.	0.01	0.5	1.0	0.9
Bkg. angular dist.	0.4	0.5	0.9	5.0
Sig. $m_{J/\psi\Lambda}$ dist.	0.01	0.3	1.0	1.0
Angular efficiencies	0.1	0.3	3.0	1.0
Angular resolution	1.0	0.1	2.6	0.8
Azimuthal efficiency	0.1	1.0	0.3	0.1
Weighting procedure	0.1	1.3	0.4	2.0
Reconstruction bias	5.7	9.8	2.0	9.1
Total (quadrature sum)	5.8	10.0	5.1	11.1

Chapter 6

Summary and conclusions

Based on an angular analysis of about 6000 events collected by the CMS experiment at $\sqrt{s} = 7$ and 8 TeV, a measurement of the Λ_b polarization P, the parity-violating asymmetry parameter in the Λ_b decay α_1, the Λ longitudinal polarization α_2, and the parameter γ_0 has been performed. The obtained values are

$$\begin{aligned} P &= 0.00 \pm 0.06\,(\text{stat}) \pm 0.06\,(\text{syst}), \\ \alpha_1 &= 0.14 \pm 0.14\,(\text{stat}) \pm 0.10\,(\text{syst}), \\ \alpha_2 &= -1.11 \pm 0.04\,(\text{stat}) \pm 0.05\,(\text{syst}), \\ \gamma_0 &= -0.27 \pm 0.08\,(\text{stat}) \pm 0.11\,(\text{syst}), \end{aligned}$$

corresponding to the squares of the helicity amplitudes

$$\begin{aligned} |T_{++}|^2 &= 0.05 \pm 0.04\,(\text{stat}) \pm 0.04\,(\text{syst}), \\ |T_{+0}|^2 &= -0.10 \pm 0.04\,(\text{stat}) \pm 0.04\,(\text{syst}), \\ |T_{-0}|^2 &= 0.51 \pm 0.03\,(\text{stat}) \pm 0.04\,(\text{syst}), \\ |T_{--}|^2 &= 0.52 \pm 0.04\,(\text{stat}) \pm 0.04\,(\text{syst}). \end{aligned}$$

The measured Λ_b polarization value given above is consistent with the LHCb measurement [18] and theoretical predictions of 0.10 [12] and 0.20 [13]. Note that in our notation, α_1 is the negative value of α_b referred to in the theory [34, 35, 17, 36, 37, 16], LHCb [18], and ATLAS [19] papers. To compare with the theoretical predictions and the other measurements, we use the negative of our measured value of α_1. The many theoretical predictions for $-\alpha_1$ include -0.2 to -0.1 from quark model techniques [34–37, 16], -0.17 to -0.14 from perturbative quantum chromodynamics calculations [17], and 0.78 from heavy-quark effective theory [13, 11]. The measured value is inconsistent at more than 5 standard deviations with the heavy-quark effective theory prediction, but is consistent at less than one standard deviation with the other predictions. The presented measurement of α_1 is also consistent with the measurements $0.05 \pm 0.17\,(\text{stat}) \pm 0.07\,(\text{syst})$ and $0.30 \pm 0.16\,(\text{stat}) \pm 0.06\,(\text{syst})$ by LHCb [18] and ATLAS [19], respectively, and with no parity violation at the level of one standard deviation. The measurement of α_2, compatible with -1, indicates that the positive-helicity states of the Λ coming from the Λ_b decay are suppressed.

The measured values for the helicity amplitudes are consistent with the values reported by LHCb and ATLAS. Table 6.1 shows the polarization and the helicity amplitudes reported by CMS and the measurements from LHCb and ATLAS along with its corresponding deviation from CMS results.

This work was published in Physical Review D(see Appendix D), and could be improved with more statistic to reduce the statistical uncertainty, clearly a better understanding about the dominant systematic uncertainty improves the measurement. On the other hand, with the the prominent computing power that comes we will be able to measure the all 20 parameters in the angular decay and to improve the measurement with new data collected by CMS.

Table 6.1 Values of the helicity amplitudes and Λ_b polarization as measured by CMS and the results from LHCb and ATLAS along with its corresponding difference from CMS value in σ units. For the reported values, the first uncertainty is statistical and the second systematic one.

	CMS	LHCb		ATLAS	
		result	diff. SD	result	diff. SD
$\|T_{++}\|^2$	$0.05 \pm 0.04 \pm 0.04$	$-0.10 \pm 0.04 \pm 0.03$	1.98	$0.01^{+0.02}_{-0.01} \pm 0.01$	0.65
$\|T_{+0}\|^2$	$-0.10 \pm 0.04 \pm 0.04$	$0.01 \pm 0.04 \pm 0.03$	1.45	$0.03^{+0.04}_{-0.06} \pm 0.03$	1.48
$\|T_{-0}\|^2$	$0.51 \pm 0.03 \pm 0.04$	$0.57 \pm 0.06 \pm 0.03$	0.72	$0.35^{+0.07}_{-0.08} \pm 0.04$	1.60
$\|T_{--}\|^2$	$0.52 \pm 0.04 \pm 0.04$	$0.51 \pm 0.05 \pm 0.02$	0.13	$0.62^{+0.06}_{-0.08} \pm 0.02$	1.00
P	$0.00 \pm 0.06 \pm 0.06$	$0.06 \pm 0.07 \pm 0.06$	0.47	$--$	$--$
α_b	$-0.14 \pm 0.14 \pm 0.10$	$0.05 \pm 0.17 \pm 0.07$	0.79	$0.30 \pm 0.16.06$	1.8

References

[1] Makoto Kobayashi and Toshihide Maskawa. Cp-violation in the renormalizable theory of weak interaction. *Progress of Theoretical Physics*, 49(2):652–657, 1973.

[2] S. W. Herb et al. Observation of a dimuon resonance at 9.5 gev in 400-gev proton-nucleus collisions. *Phys. Rev. Lett.*, 39:252–255, Aug 1977.

[3] Particle Data Group, C. Patrignani, et al. Review of particle physics. *Chin. Phys. C*, 40:100001, 2016.

[4] C. Albajar et al. First observation of the beauty baryon in the decay channel at the cern proton-antiproton collider. *Phys. Lett. B*, 273(4):540, 1991.

[5] D. Buskulic et al. Strange b baryon production and lifetime in z decays. *Physics Letters B*, 384(1):449 – 460, 1996.

[6] P. Abreu et al. Production of strange b–baryons decaying into $\Xi_b^{\pm} - l^{\pm}$ pairs at LEP. *Z Phys. C*, 68(4):541, 1995.

[7] Wolfgang Altmannshofer et al. Symmetries and asymmetries of $B \to K^* \mu^+ \mu^-$ decays in the Standard Model and beyond. *Journal of High Energy Physics*, 2009(01):019, 2009.

[8] Adam F. Falk and Michael E. Peskin. Production, decay, and polarization of excited heavy hadrons. *Phys. Rev. D*, 49:3320, 1994.

[9] B. Mele and G. Altarelli. Lepton spectra as a measure of b quark polarization at LEP. *Phys. Lett. B*, 299:345, 1993.

[10] D. Buskulic et al. Measurement of Λ_b polarization in Z decays. *Phys. Lett. B*, 365:437, 1996.

[11] O. Leitner, Z.J. Ajaltouni, and E. Conte. An angular distribution analysis of Λ_b decays. *Nucl. Phys. A*, 755:435, 2005.

[12] G. Hiller, M. Knecht, F. Legger, and T. Schietinger. Photon polarization from helicity suppression in radiative decays of polarized Λ_b to spin-3/2 baryons. *Phys. Lett. B*, 649:152, 2007.

[13] Z. J. Ajaltouni, E. Conte, and O. Leitner. Λ_b decays into $\Lambda-$vector. *Phys. Lett. B*, 614:165, 2005.

[14] P. Bialas, J. G. Korner, M. Kramer, and K. Zalewski. Joint angular decay distributions in exclusive weak decays of heavy mesons and baryons. *Z. Phys. C*, 57:115, 1993.

[15] M. Kramer and H. Simma. Angular correlations in $\Lambda_b \to \Lambda + V$: Polarization measurements, HQET and CP violation. *Nucl. Phys. Proc. Suppl.*, 50:125, 1996.

[16] Thomas Gutsche, Mikhail A. Ivanov, Jürgen G. Körner, Valery E. Lyubovitskij, and Pietro Santorelli. Polarization effects in the cascade decay $\Lambda_b \to \Lambda(\to p\pi^-) + J/\psi(l^+l^-)$ in the covariant confined quark model. *Phys. Rev. D*, 88:114018, 2013.

[17] Hsien-Hung Chou, Chung-Hsien Chouand Shih, Shih-Chang Lee, and Hsiang Li. $\Lambda_b \to \Lambda J/\psi$ decay in perturbative QCD. *Phys. Rev. D*, 65:074030, 2002.

[18] R Aaij et al. Measurements of the $\Lambda_b \to J/\psi\ \Lambda$ decay amplitudes and the Λ_b polarisation in pp collisions at $\sqrt{s} = 7$ TeV. *Phys. Lett. B*, 724:27, 2013.

[19] Aad G. et al. Measurement of the parity-violating asymmetry parameter α_b and the helicity amplitudes for the decay $\Lambda_b \to J/\psi\Lambda$ with the ATLAS detector. *Phys. Rev. D*, 89:092009, 2014.

[20] Bettini A. *Introduction to elementary particle physics*. 2008.

[21] I. J. R. Aitchison and A. J. G. Hey. *Gauge theories in particle physics*. CRC Press, Bristol, UK, 2012.

[22] Blum K. *Density Matrix Theory and Applications*. Springer-Verlag Berlin Heidelberg, 2012.

[23] Leader E. *Spin in Particle Physics*. Cambridge University Press, 2005.

[24] Wikipedia contributors. Standard model wikipedia, the free encyclopedia, 2018.

[25] W. G. D. Dharmaratna and Gary R. Goldstein. Single quark polarization in quantum chromodynamics subprocesses. *Phys. Rev. D*, 53:1073–1086, Feb 1996.

[26] Thomas Mannel and Gerhard A. Schuler. Semileptonic decays of bottom baryons at lep. *Phys. Lett. B*, 279:194, 1992.

[27] G. Abbiendi et al. Measurement of the average polarization of b baryons in hadronic Z decays. *Phys. Lett. B*, 444:539, 1998.

[28] P. Abreu et al. Λ_b polarization in Z decays at LEP. *Phys. Lett. B*, 474:205, 2000.

[29] T. Aaltonen et al. Evidence for a bottom baryon resonance Λ_b^* in CDF data. *Phys. Rev. D*, 88:071101, 2013.

[30] T. Aaltonen et al. Observation of the heavy baryons Σ_b and Σ_b^*. *Phys. Rev. Lett.*, 99:202001, 2007.

[31] T. Aaltonen et al. Measurement of the masses and widths of the bottom baryons $\Sigma_b^\pm$ and $\Sigma_b^{*\pm}$. *Phys. Rev. D*, 85:092011, 2012.

[32] R Aaij et al. Observation of excited Λ_b baryons. *Phys. Rev. Lett.*, 109:172003, 2012.

[33] Mario Galanti et al. Heavy baryons as polarimeters at colliders. *Journal of High Energy Physics*, 2015(11):67, Nov 2015.

[34] Hai-Yang Cheng. Nonleptonic weak decays of bottom baryons. *Phys. Rev. D*, 56:2799, 1997.

[35] Fayyazuddin and Riazuddin. Two-body nonleptonic Λ_b decays in the quark model with factorization ansatz. *Phys. Rev. D*, 58:014016, 1998.

[36] Rukmani Mohanta, Anjan K. Giri, Mohinder P. Khanna, Muneyuki Ishida, Shin Ishida, and Masuho Oda. Hadronic weak decays of Λ_b baryon in the covariant oscillator quark model. *Prog. Theor. Phys.*, 101:959, 1999.

[37] Zheng-Tao Wei, Hong-Wei Ke, and Xue-Qian Li. Evaluating decay rates and asymmetries of Λ_b into light baryons in LFQM. *Phys. Rev. D*, 80:094016, 2009.

[38] M. Jacob and G.C. Wick. On the general theory of collisions for particles with spin. *Annals of Physics*, 7(4):404 – 428, 1959.

[39] J. D. Richman. An experimenter's guide to the helicity formalism. Technical report, Calif. Inst. Technol., Jun 1984.

[40] R. Aaij et al. Observation of resonances ronsistent with pentaquark states in $\rightarrow$ decays.

[41] S. Chatrchyan et al. The CMS experiment at the CERN LHC. *JINST*, 3:S08004, 2008.

[42] S Baird. Accelerators for pedestrians. Technical Report CERN-AB-Note-2007-014, CERN, Feb 2007.

[43] O. S. Bruning et al. *LHC Design Report Vol.1: The LHC Main Ring*. 2004.

[44] G. Apollinari et al. *High-Luminosity Large Hadron Collider (HL-LHC): Preliminary Design Report*. CERN, 2015.

[45] G. L. Bayatian et al. *CMS Physics: Technical Design Report Volume 1: Detector performance software*. 2006.

[46] H. Breuker et al. The CMS tracker system project: Technical design report. 1997.

[47] Serguei Chatrchyan et al. Performance of CMS muon reconstruction in pp collision events at $\sqrt{s} = 7\,\text{TeV}$. *JINST*, 7:P10002, 2012.

[48] Vardan Khachatryan et al. The CMS trigger system. *JINST*, 12:P01020, 2017.

[49] S. Cittolin et al. CMS the TriDAS project: Technical design report, volume 2: Data acquisition and high-level trigger. CMS trigger and data-acquisition project. 2002.

[50] Domenico Giordano. The cms high-level trigger selection. *Nucl. Phys. B*, 150:299, 2006.

[51] John David Jackson. *Classical Electrodynamics*. Wiley, 1998.

[52] Serguei Chatrchyan et al. Description and performance of track and primary-vertex reconstruction with the CMS tracker. *JINST*, 9:P10009, 2014.

[53] P. Billoir and S. Qian. Simultaneous pattern recognition and track fitting by the kalman filtering method. *Nucl. Instrum. and Meth. A*, 294(1):219, 1990.

[54] Pierre Billoir. Progressive track recognition with a kalman-like fitting procedure. *Comput. Phys. Commun.*, 57(1):390, 1989.

[55] Boris Mangano. Track building and final fit. Conference: Tracking training day, 10 2014.

[56] Wolfgang Waltenberger, Rudolf Fruhwirth, and Pascal Vanlae. Adaptive vertex fitting. *Journal of Physics G: Nuclear and Particle Physics*, 34(12):N343, 2007.

[57] CMS Collaboration. CMS b-physics and quarkonia results. 07 2011.

[58] Vardan Khachatryan et al. Strange particle production in pp collisions at $\sqrt{s} = 0.9$ and 7 TeV. *JHEP*, 05:064, 2011.

[59] Claus Grupen and Boris Schwartz. *Particle detectors*. 2008.

[60] V. Khachatryan, A. M Sirunyan, et al. CMS tracking performance results from early LHC operation. *Eur. Phys. J. C*, 70:1165, 2010.

[61] Roger Barlow. Extended maximum likelihood. *Nuclear Instruments and Methods in Physics Research Section A: Accelerators, Spectrometers, Detectors and Associated Equipment*, 297(3):496, 1990.

[62] *Statistical Methods for Data Analysis in Particle Physics*. Springer International Publishing, 2017.

[63] Wouter Verkerke and David P. Kirkby. The RooFit toolkit for data modeling. *eConf*, C0303241:MOLT007, 2003.

[64] D. J. Lange. The EVTGEN particle decay simulation package. *Nucl. Instrum. Meth. A*, 462:152, 2001.

[65] T. Sjöstrand, S. Mrenna and P. Z. Skands. PYTHIA 6.4 physics and manual. *JHEP*, 05:026, 2006.

[66] Agostinellia S. et al. GEANT4: a simulation toolkit. *Nucl. Instrum. Meth. A*, 506:250, 2003.

[67] Banerjee S. CMS simulation software. *Journal of Physics: Conference Series*, 396(2):022003, 2012.

Appendix A

Monte Carlo simulation

The CMS experiment chooses to use a data driven, realistic and accurate Monte Carlo (MC) program, a brief review of the simulation is discussed here.

Simulated events of the signal decay $\Lambda_b \to J/\psi\,\Lambda$ are used to study the effects of detector acceptance and selection on the reconstructed angular distributions. The events are generated using PYTHIA 6.4 [65] for production and hadronization, and EVTGEN [64] is used to describe the b and c hadron decays. The generated events are passed through the full CMS detector simulation based on GEANT4 [66]. The simulated event samples are generated to reproduce $\sqrt{s} = 7$ and 8 TeV data-taking conditions, where additional simulation of pp interactions in the same or nearby beam crossings and the impact of the HLT are included.

The MC events are reconstructed with the same algorithms and requirements as used in data, and the offline selection requirements imposed in data are applied to the MC, as well. The number of signal events and the simulation samples are shown in Table A.1. The invariant mass distributions are shown in Figure A.1.

Table A.1 Official Monte-Carlo samples used in this analysis. The events were obtained using a double-Gaussian function with the same mean.

Sample	Λ_b (events)	$\overline{\Lambda_b}$(events)
/LambdaBToJPsiLambda_lambdaFilter_7TeV-pythia6evtgen/Summer11LegDR-PU_S13_START53_LV6-v1/AODSIM	15706	14161
/LambdaBToJPsiLambda_lambdaFilter_8TeV-pythia6-evtgen/Summer12DR53X-PU_RD2_START53_V19F-v2/GEN-SIM-RECO	11599	10278

PYTHIA simulates pp collisions. The aim of the generator is to provide as accurate as possible a description of what happens in a hadron collision. The software

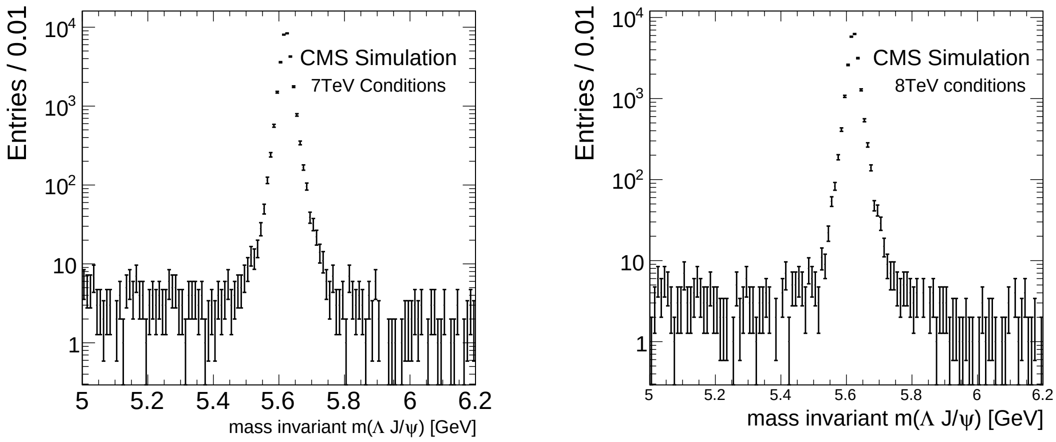

Fig. A.1 Invariant mass distribution of Λ_b candidates in the 7 (left) and 8 TeV (right) MC samples. The plots show a few combinatorial background events remaining after final selection requirements.

contains theoretical models for a number of physics aspects, such as hard and soft interactions, parton distributions, initial and final state parton showers, multiple interactions, fragmentation and decays. PYTHIA allows the generation of $b\overline{b}$ quark pairs with massive matrix elements: $q\overline{q} \to b\overline{b}$, $gg \to b\overline{b}$, $g\gamma \to b\overline{b}$, $\gamma\gamma \to b\overline{b}$ and secondary vertex of gauge bosons. After hadronization, b hadrons are manually set stable. The rest of the particles can suffer fragmentation and decays.

EVTGEN implements specialized models according to the properties of the hadron, such as models for semileptonic decays, CP-violating decays and spin correlations. For the $\Lambda_b \to J/\psi\,\Lambda$ and $J/\psi \to \mu^+\mu^-$ we use a phase space decay model, and in particular for $J/\psi \to \mu^+\mu^-$ decays the decay is combined with a routine that allows QED photon radiative corrections for muons (see Ref. [64]). Since Λ is a long lived particle that decay far away the PV, it can not forced to decay to a specific channel.

PYTHIA and EVTGEN work as an input to the full detector simulation as signal collisions and decays. The CMS simulation [67] is based on GEANT4 [66], which provides a rich set of physics process describing electromagnetic and hadronic interactions. Also provides tools for modeling the full CMS detector geometry and interfaces to retrieve information from particle tracking through those detectors and magnetic field. The simulation is implemented in all CMS detectors in both the central and forwards regions, including the field map from the solenoid. The program implements the sensitive detector behavior, track selection mechanism hit collection and digitization. The effect of the L1 and HLT triggers are implemented as in data by L1 seeds and HLT menus. The pile-up effect is simulated separately from the signal collisions by producing simulated hits and then merging the events randomly to the signal events.

Appendix B

Comparisons of simulation and data

The MC simulation is generated as discussed in Appendix A. The variables used in the selection (Sections. 4.4 and 4.5) are taken to compare data with simulated events and fix possible discrepancies that could change the efficiency distributions. The comparisons of the data and MC simulation are shown in Figures B.1 and B.2 for the variables used in the J/ψ selection, Figures B.3 and B.4 show distributions of the variables used in the Λ selection, and B.5 and B.6 in the Λ_b selection. The histograms are normalized to their number of events and a background subtraction is performed to each histograms. The data/MC ratio plot and the Kolmogorov test are shown in Figures as well. It can be seen there are discrepancies between distributions, however to ensure that MC reproduces data a weighting procedure is performed, so that weights are assigned to the simulated events to match the data.

The weights are computed in an iterative process in which, for each iteration, the ratio (weight) between data and simulation histograms is calculated bin by bin with its propagated systematic uncertainty. The weights are assigned to each bin in the next simulation histogram recomputing the data/MC ratio again, and the same process is repeated until all histograms are used. The final weight per event is the product of the weights in each iteration. The discrepancies are reduced after weighting as shown in Figures B.7– B.12. Finally the weighted simulation is used in the estimation of the efficiencies.

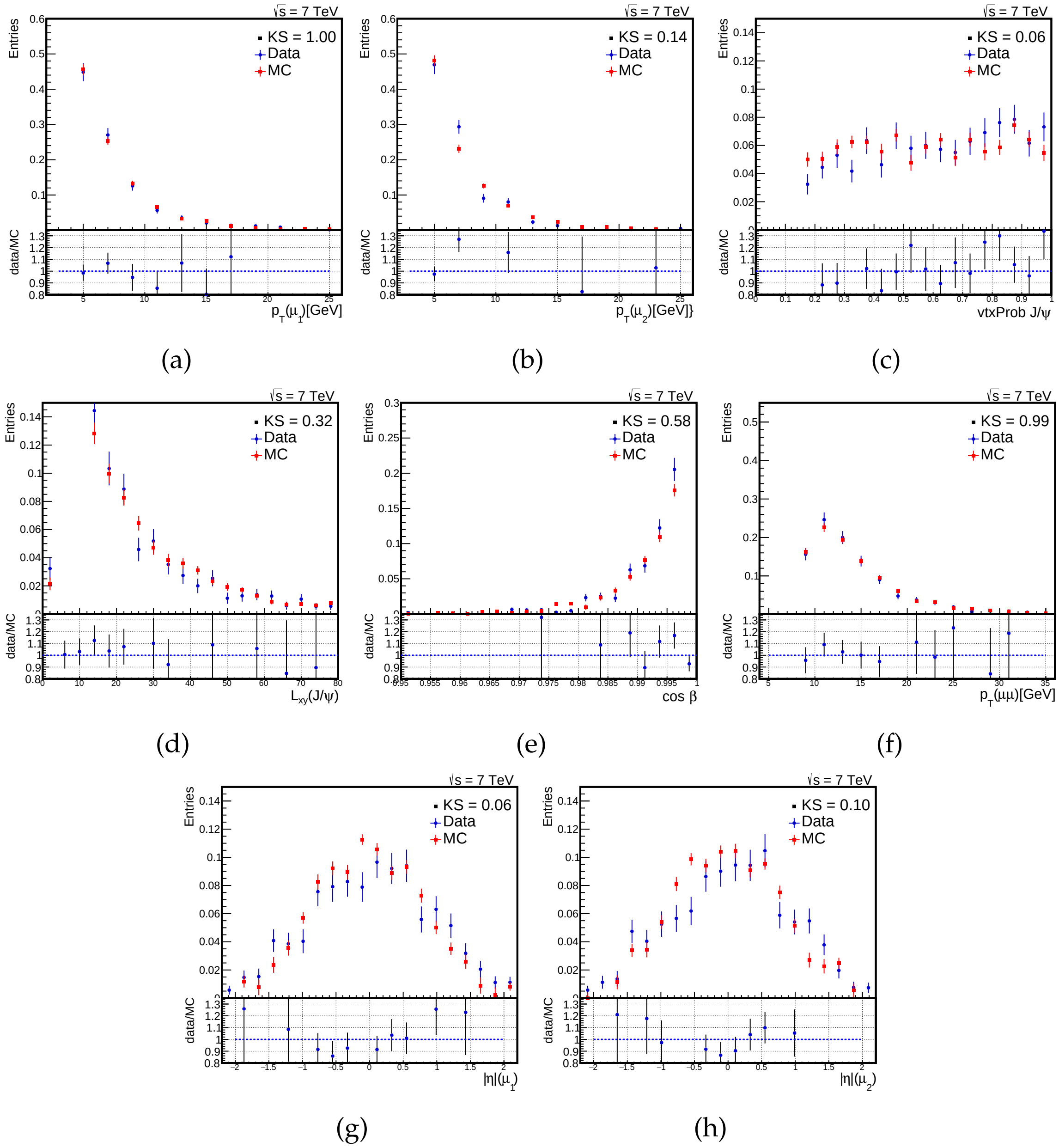

Fig. B.1 Comparison of data and simulation at $\sqrt{s} = 7\,\text{TeV}$ using the J/ψ selection variables. The variables are (a) $p_{\mathrm{T}}^{\mu_1}$, (b) $p_{\mathrm{T}}^{\mu_2}$, (c) vertex probability of J/ψ, (d) $\mathrm{L_{xy}}(\mathrm{J}/\psi)/\sigma$, (e) $\cos\beta$, (f) $p_{\mathrm{T}}^{\mu\mu}$, (g) $|\eta(\mu_1)|$ and (h) $|\eta(\mu_2)|$. The round and square points represent the data sample and the simulation, respectively.

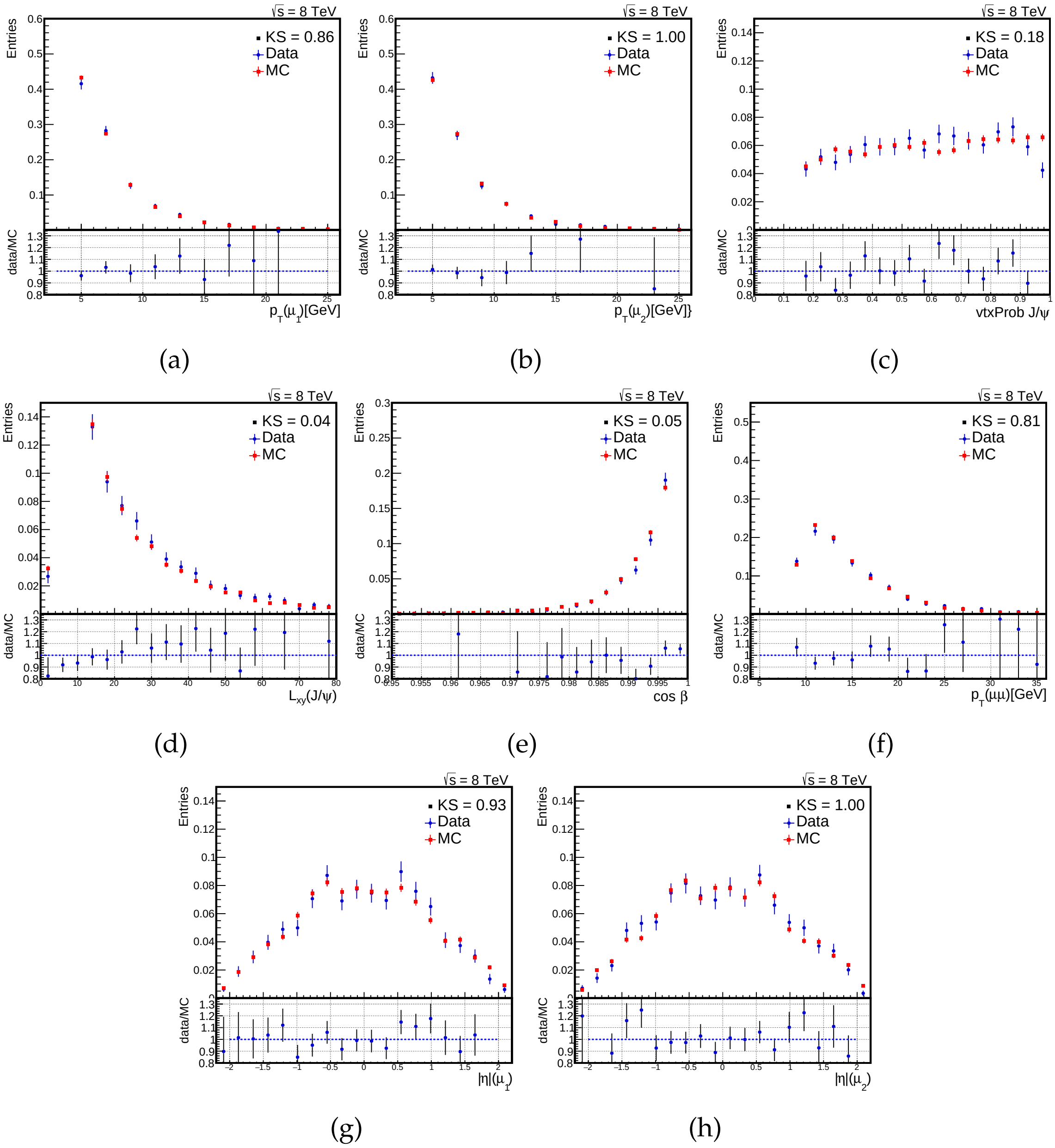

Fig. B.2 Comparison of data and simulation at $\sqrt{s} = 8\,\text{TeV}$ using the J/ψ selection variables. The variables are (a) $p_{\mathrm{T}}^{\mu_1}$, (b) $p_{\mathrm{T}}^{\mu_2}$, (c) vertex probability of J/ψ, (d) $\mathrm{L_{xy}}(\mathrm{J}/\psi)/\sigma$, (e) $\cos\beta$, (f) $p_{\mathrm{T}}^{\mu\mu}$, (g) $|\eta(\mu_1)|$ and (h) $|\eta(\mu_2)|$. The round and square points represent the data sample and the simulation, respectively.

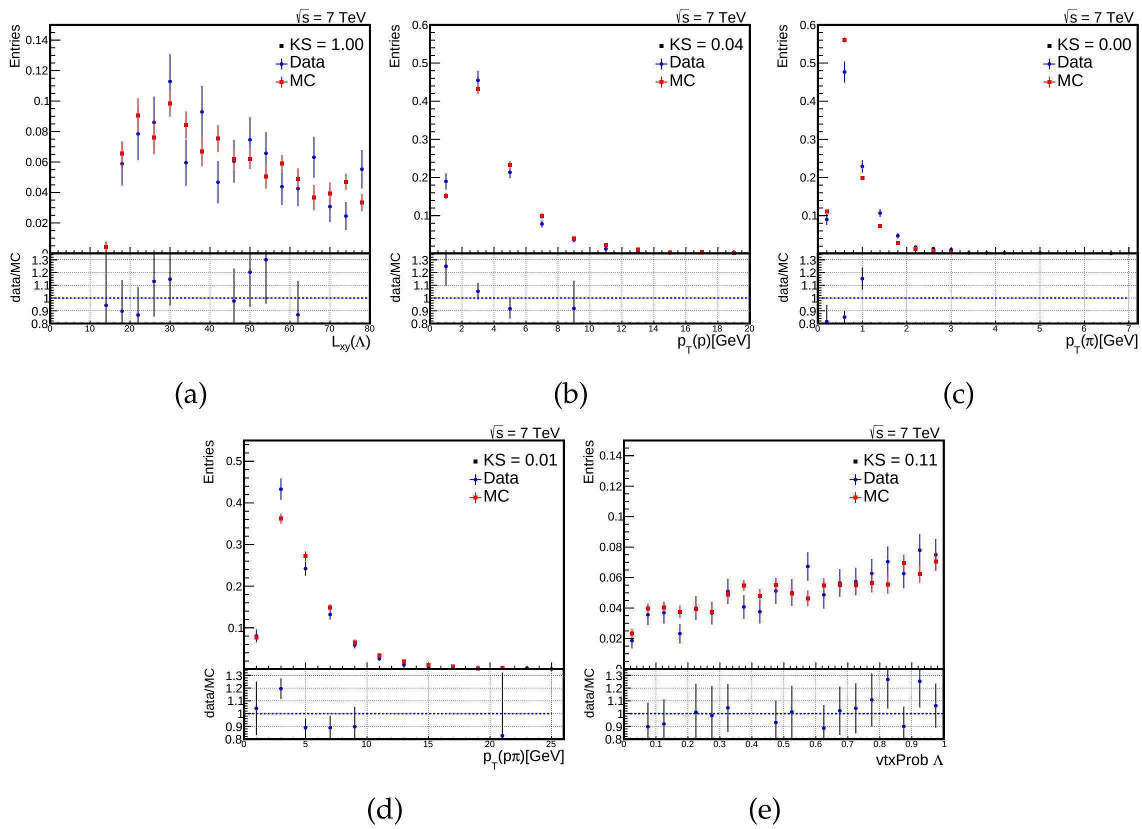

Fig. B.3 Comparison data and simulation at $\sqrt{s} = 7\,\text{TeV}$ using the Λ selection variables. The used variables are (a) $\mathrm{L_{xy}}(\Lambda)/\sigma$, (b) $p_{\mathrm{T}}^{\mathrm{p}}$, (c) p_{T}^{π}, (d) $p_{\mathrm{T}}^{\mathrm{p}\pi}$ and (e) vertex probability of Λ. The square and round points represent the simulation and data, respectively.

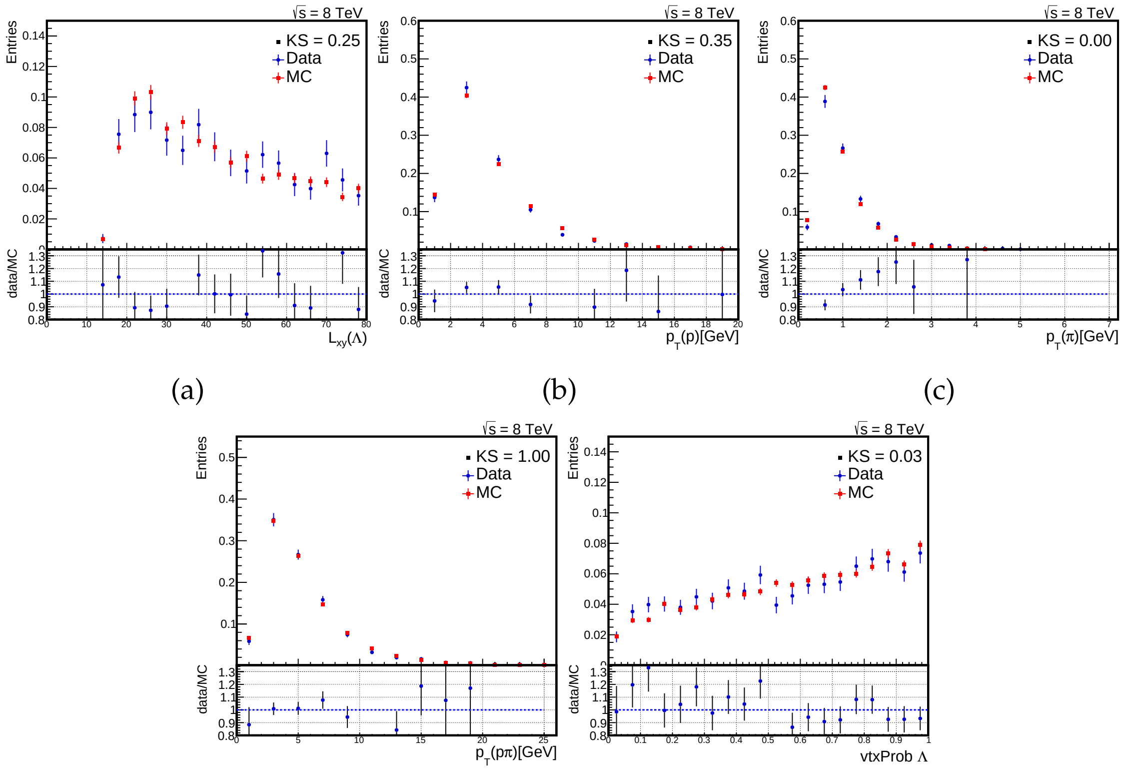

(a) (b) (c)

(d) (e)

Fig. B.4 Comparison data and simulation at $\sqrt{s} = 8\,\mathrm{TeV}$ using the Λ selection variables. The used variables are (a) $\mathrm{L_{xy}}(\Lambda)/\sigma$, (b) $p_{\mathrm{T}}^{\mathrm{p}}$, (c) p_{T}^{π}, (d) $p_{\mathrm{T}}^{\mathrm{p}\pi}$ and (e) vertex probability of Λ. The round points represent the data distribution and the square points represent the MC simulation.

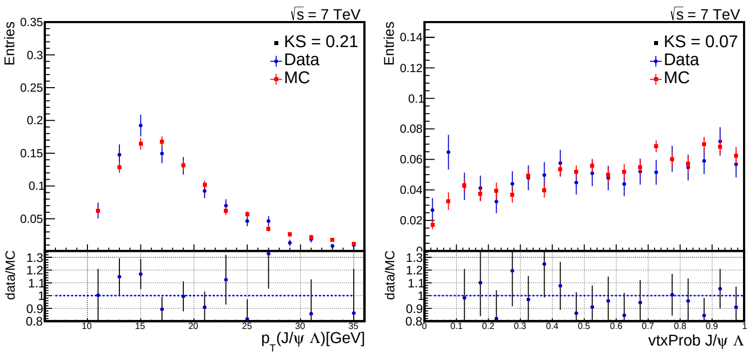

(a) (b)

Fig. B.5 Comparison data and simulation at $\sqrt{s} = 7\,\mathrm{TeV}$ for variables used in the Λ_{b} selection where the square and round points represent the MC simulation and data, respectively. The variables used are (a) $p_{\mathrm{T}}^{J/\psi\Lambda}$, and (b) vertex probability of Λ_{b}.

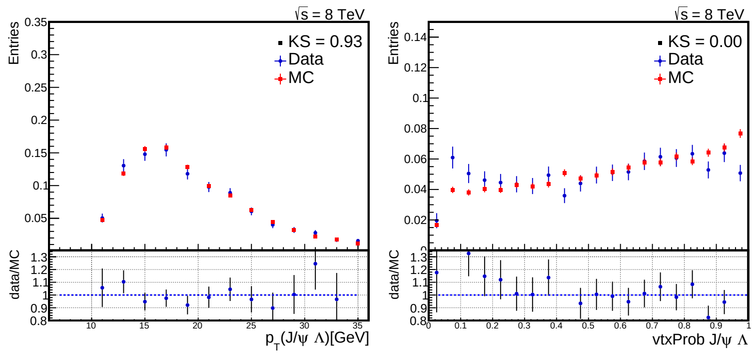

(a) (b)

Fig. B.6 Comparison data and simulation at $\sqrt{s} = 8\,\text{TeV}$ for variables used in the Λ_b selection. The used variables are (a) $p_T^{J/\psi\Lambda}$ and (b) vertex probability of Λ_b. The square and round points represent the simulation and data, respectively.

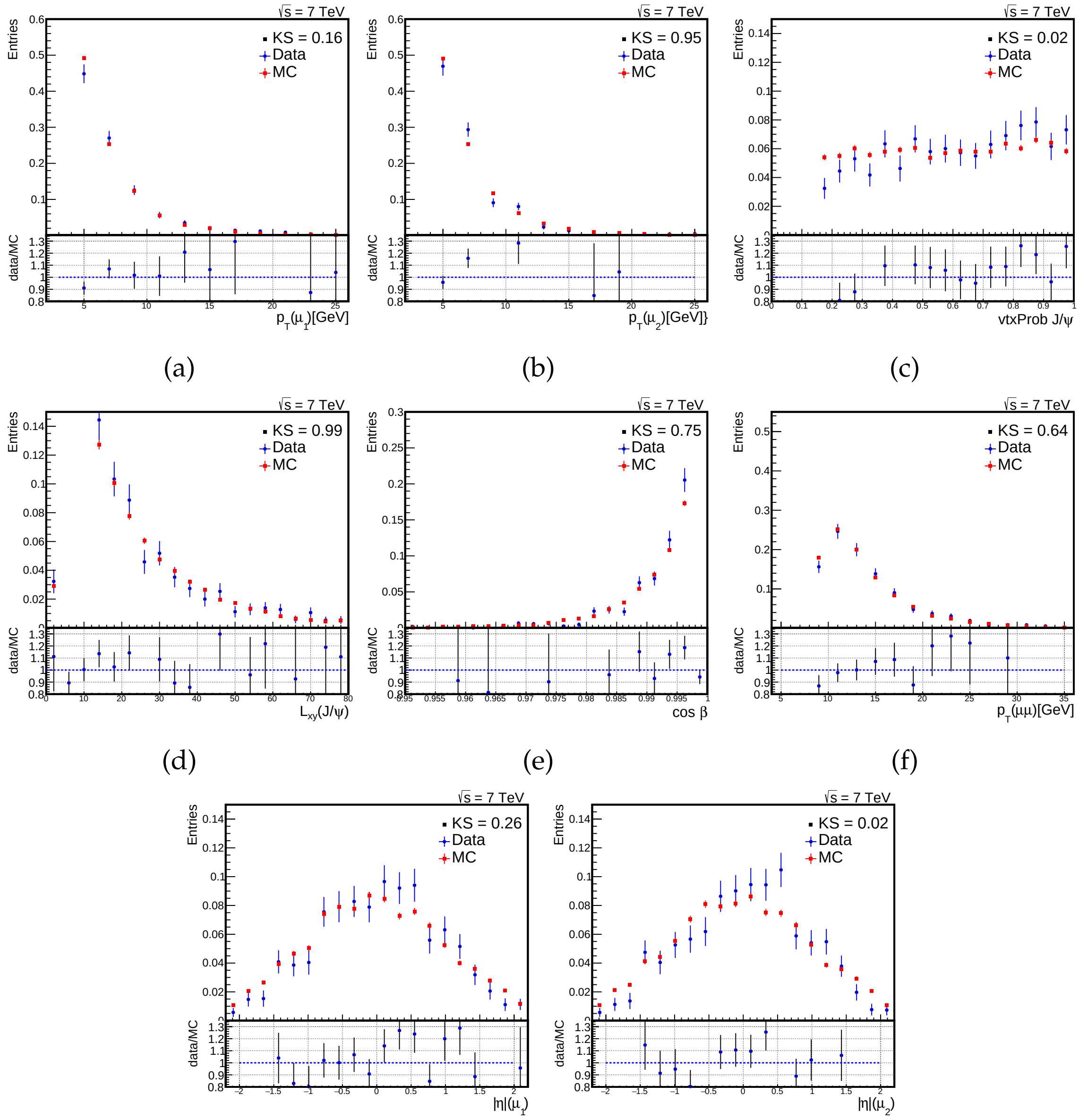

Fig. B.7 Comparison data and simulation at $\sqrt{s} = 7\,\text{TeV}$ of the J/ψ selection variables after weighting process. After to assign weights to the simulation discrepancies of data and MC are reduced. It shows the distributions of (a) $p_{\text{T}}^{\mu_1}$, (b) $p_{\text{T}}^{\mu_2}$, (c) vertex probability of J/ψ, (d) $\text{L}_{\text{xy}}(\text{J}/\psi)/\sigma$, (e) $\cos\beta$, (f) $p_{\text{T}}^{\mu\mu}$, (g) $|\eta(\mu_1)|$ and (h) $|\eta(\mu_1)|$. The square and round points represent the simulation and data, respectively.

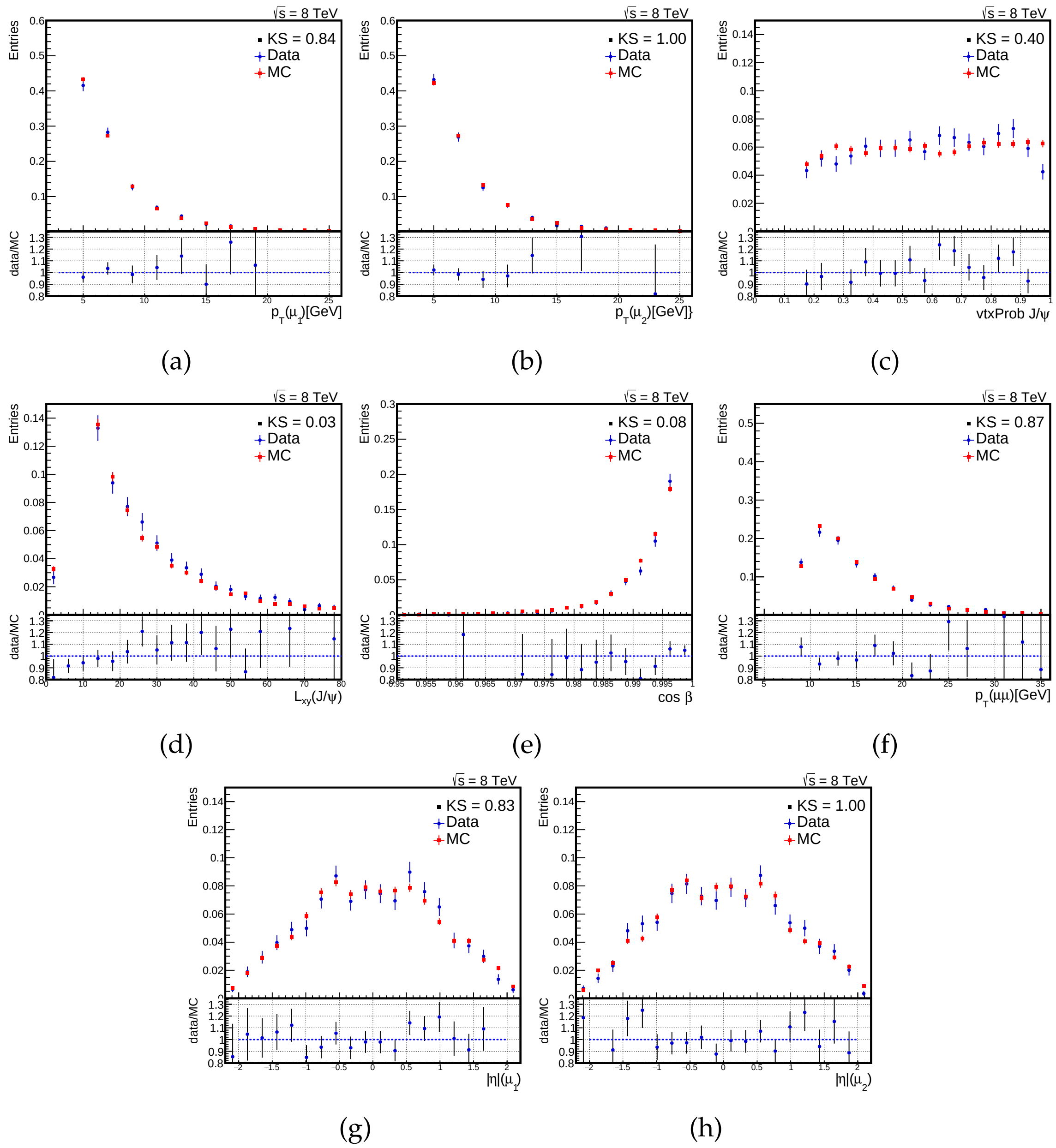

Fig. B.8 Comparison data and simulation at $\sqrt{s} = 8\,\mathrm{TeV}$ of the J/ψ selection variables after weighting process. After to assign weights to the simulation discrepancies of data and MC are reduced. It shows the distributions of (a) $p_{\mathrm{T}}^{\mu_1}$, (b) $p_{\mathrm{T}}^{\mu_2}$, (c) vertex probability of J/ψ, (d) $\mathrm{L_{xy}}(\mathrm{J}/\psi)/\sigma$, (e) $\cos\beta$, (f) $p_{\mathrm{T}}^{\mu\mu}$, (g) $|\eta(\mu_1)|$ and (h) $|\eta(\mu_1)|$. The square and round points represent the simulation and data, respectively.

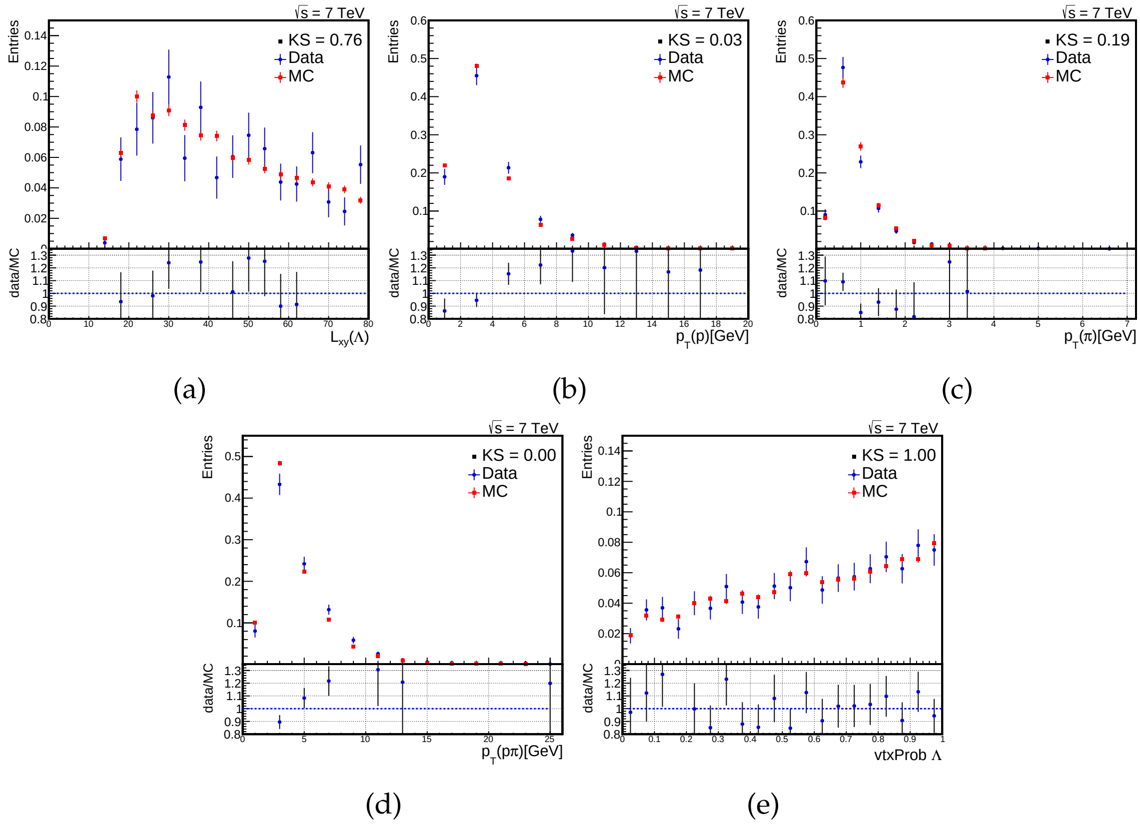

(a) (b) (c)

(d) (e)

Fig. B.9 Comparison data and simulation at $\sqrt{s} = 7\,\text{TeV}$ of Λ selection variables after weighting process. It shows the variables (a) $\mathrm{L_{xy}}(\Lambda)/\sigma$, (b) $p_{\mathrm{T}}^{\mathrm{p}}$, (c) p_{T}^{π}, (d) $p_{\mathrm{T}}^{\mathrm{p}\pi}$ and (e) vertex probability of Λ. The round and square dots represent the data and simulation distributions, respectively.

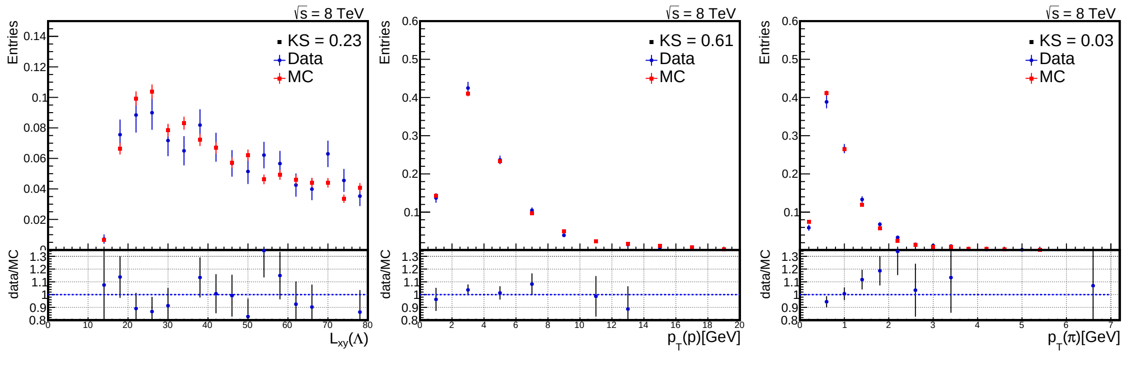

(a) (b) (c)

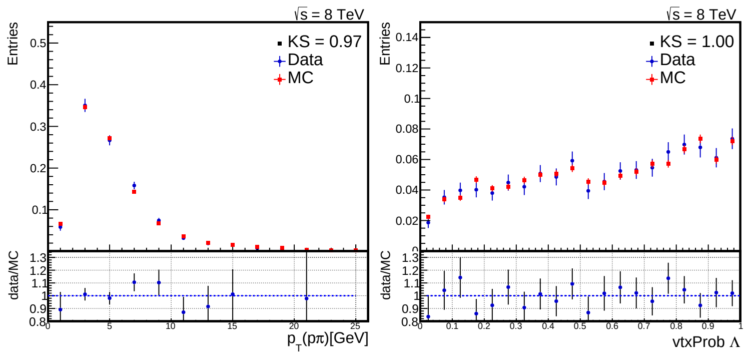

(d) (e)

Fig. B.10 Comparison data and simulation at $\sqrt{s} = 8\,\text{TeV}$ of the Λ selection variables after weighting process. An improvement is clearly in the distributions. It shows the variables (a) $L_{xy}(\Lambda)/\sigma$, (b) p_T^p, (c) p_T^π, (d) $p_T^{p\pi}$ and (e) vertex probability of Λ. The round and square dots represent the data and simulation distributions, respectively.

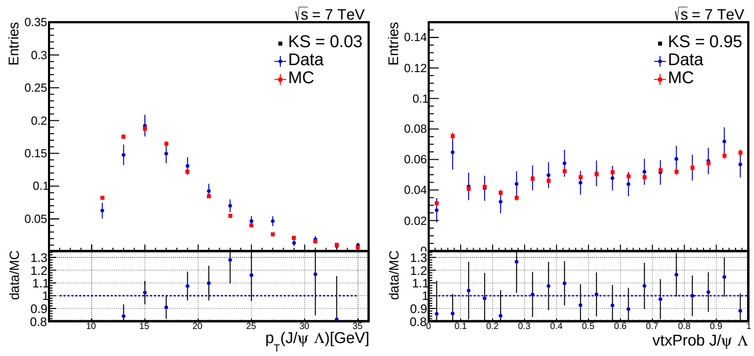

(a) (b)

Fig. B.11 Comparison data and simulation at $\sqrt{s} = 7\,\text{TeV}$ after weighting process in the Λ_b selection variables. There is an improvement in the quality variables. It shows used variables (a) $p_T^{J/\psi\Lambda}$ and (b) vertex probability of Λ_b. The round and square points represent the data and simulation distributions.

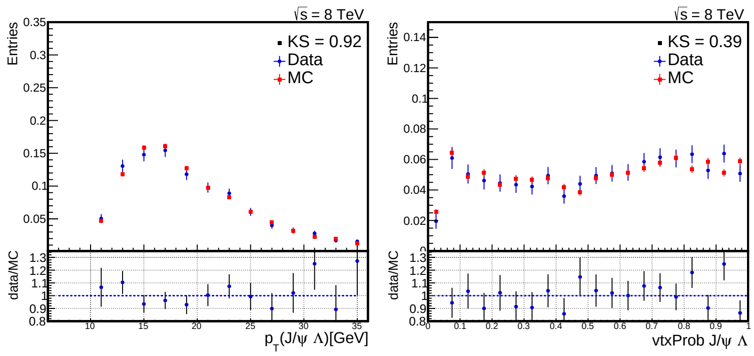

(a) (b)

Fig. B.12 Comparison data and simulation at $\sqrt{s} = 8\,\mathrm{TeV}$ after weighting process in the Λ_b selection variables. There is an improvement in the quality variables. It shows used variables (a) $p_T^{J/\psi\Lambda}$ and (b) vertex probability of Λ_b. The round and square points represent the data and simulation distributions.

Appendix C

Estimation of the reconstruction bias systematic uncertainty.

In order to test the measuring procedure, we generated different MC samples using different input values of the angular parameters (see section 5.5.2). The source of the systematic uncertainty comes from a possible unaccounted reconstruction bias showed in this closure test. Although the fit results and input values are consistent within errors some discrepancies are showed (see Table 5.9). To estimate this systematic uncertainty we consider only the MC sample where the input values are similar to those observed in data (Table 5.9), after reconstruction and selection processes we divide the sample in four partitions with ~ 11000 Λ_b and $\overline{\Lambda_b}$ candidates per partition. We get the fit results presented in the Table C.1.

Taking into account the values shown in the Table C.1, we compute the difference between the input and fit values $\Delta_{i,k} = inputVal^{i,k} - fitVal^{i,k}$, with $i = \{P, \alpha_1, \alpha_2, \gamma_0\}$ and $k = \{1,2,3,4\}$ the number of the partition, and then we compute the mean of those differences $\bar{\Delta}_{\{P,\alpha_1,\alpha_2,\gamma_0\}}$ as it can be seen in the Table C.2.

Since we are considering Full MC, some systematic sources are involved in the fit results. In order to avoid redundancy, we subtract the quadratic sum of the other systematic sources from $\bar{\Delta}_{\{P,\alpha_1,\alpha_2,\gamma_0\}}$ and finally the square root of this quantity is taken as systematic uncertainty. The results of the final estimation are shown in the Table 5.16.

It should be said we are not taking into account the following systematics in the computation: the asymmetry parameter α_Λ (known in MC), re-weight procedure (no apply), and background sources (low influence in MC).

Table C.1 Likelihood fit results for different partitions of MC sample described in the section 5.5.2. Uncertainties are statistical only.

	P	α_1	α_2	γ_0
Input values	0.002	0.109	-0.909	-0.5
Partition 1				
Fit results	0.033 ± 0.042	0.200 ± 0.096	-0.874 ± 0.029	-0.374 ± 0.056
SD diff.	-0.7	-0.9	-1.2	-2.2
Partition 2				
Fit results	0.055 ± 0.046	0.184 ± 0.092	-0.854 ± 0.030	-0.380 ± 0.052
SD diff.	-1.1	-0.8	-1.8	-2.3
Partition 3				
Fit results	0.055 ± 0.042	0.263 ± 0.096	-0.851 ± 0.029	-0.500 ± 0.052
SD diff.	-1.3	-1.6	-1.9	0.0
Partition 4				
Fit results	0.097 ± 0.050	0.183 ± 0.097	-0.873 ± 0.033	-0.360 ± 0.060
SD diff.	-1.9	-0.8	-1.1	-2.3

Table C.2 Considering the fit results in the Table C.1, we compute the differences between input and fit values for every angular parameter in the different partitions and then their means. We use the mean of the differences $\bar{\Delta}$ to give an estimation of the final statistical uncertainty of reco-bias.

	Δ_1	Δ_2	Δ_3	Δ_4	$\bar{\Delta}$
P	-0.0318	-0.053	-0.053	-0.095	-0.058
α_1	-0.091	-0.075	-0.154	-0.074	-0.099
α_2	-0.034	-0.054	-0.057	-0.035	-0.045
γ_0	-0.126	-0.120	0.001	-0.140	-0.096

Appendix D

Published paper

To publish a paper in the CMS Collaboration it must to go through many filters, the whole process culminates with the following announcement:

Dear colleagues,

BPH-15-002 has been published in PRD
as DOI : 10.1103/PhysRevD.97.072010
http://dx.doi.org/10.1103/PhysRevD.97.072010

Congratulations to all involved,

Best regards,

George and Tom

Publication committee

CMS

Measurement of the Λ_b polarization and angular parameters in $\Lambda_b \to J/\psi\Lambda$ decays from pp collisions at $\sqrt{s} = 7$ and 8 TeV

A. M. Sirunyan *et al.*[*]
(CMS Collaboration)

(Received 13 February 2018; published 17 April 2018)

An analysis of the bottom baryon decay $\Lambda_b \to J/\psi(\to \mu^+\mu^-)\Lambda(\to p\pi^-)$ is performed to measure the Λ_b polarization and three angular parameters in data from pp collisions at $\sqrt{s} = 7$ and 8 TeV, collected by the CMS experiment at the Large Hadron Collider. The Λ_b polarization is measured to be $0.00 \pm 0.06(\mathrm{stat}) \pm 0.06(\mathrm{syst})$ and the parity-violating asymmetry parameter is determined to be $0.14 \pm 0.14(\mathrm{stat}) \pm 0.10(\mathrm{syst})$. The measurements are compared to various theoretical predictions, including those from perturbative quantum chromodynamics.

DOI: 10.1103/PhysRevD.97.072010

I. INTRODUCTION

The decay $\Lambda_b \to J/\psi\Lambda$ is a rich source of information about the effect of strong interactions in hadronic decays. For this particular decay, perturbative quantum chromodynamics can be applied and therefore a systematic approach can be taken to study its characteristics. Several techniques [1–10] are used to study and calculate the decay amplitudes and the effect of the b quark polarization on this decay. The most interesting parameters that can be measured are the polarization, P, and the parity-violating decay asymmetry of the Λ_b, which is called α_b in some papers and is equal to $-\alpha_1$ in the notation used in this analysis. The LHCb and ATLAS experiments have reported measurements on this decay [11,12]. The LHCb Collaboration measured the Λ_b polarization and the decay amplitudes, while ATLAS assumed a Λ_b polarization of zero and measured the amplitudes. In this paper, a measurement of the Λ_b transverse polarization is presented using the decay $\Lambda_b \to J/\psi\Lambda$, with $J/\psi \to \mu^+\mu^-$ and $\Lambda \to p\pi^-$. Charge-conjugate modes are implied throughout this paper unless otherwise stated. The Λ_b baryons used in this measurement come from both direct production in pp collisions and decays of heavier b baryons [1,13–16]. The data were collected with the CMS detector in pp collisions at center-of-mass energies of 7 and 8 TeV, corresponding to integrated luminosities of 5.2 and 19.8 fb^{-1}, respectively.

[*]Full author list given at the end of the article.

II. ANGULAR DISTRIBUTION

The $\Lambda_b \to J/\psi\Lambda$ decay into the $\mu^+\mu^-\ p\pi^-$ final state is illustrated in Fig. 1. In pp collisions, we define the polarization of the Λ_b as the mean value of the Λ_b spin along the unit vector:

$$\hat{n} = \frac{\vec{p}_{\mathrm{beam}} \times \vec{p}_{\Lambda_b}}{|\vec{p}_{\mathrm{beam}} \times \vec{p}_{\Lambda_b}|}, \qquad (1)$$

normal to its production plane, where $\vec{p}_{\mathrm{beam}}$ is in the direction of the counterclockwise proton beam direction [17], and $\vec{p}_{\Lambda_b}$ is the Λ_b momentum. The decay is described by four complex helicity amplitudes $T_{\lambda_1\lambda_2}$, with $\lambda_1 = \pm 1/2$ and $\lambda_2 = \pm 1, 0$ referring to the helicities of the Λ and J/ψ particles, respectively. The angular distribution is a function of five decay angles $(\theta_\Lambda, \theta_p, \theta_\mu, \varphi_p, \varphi_\mu)$ and has the form [8]

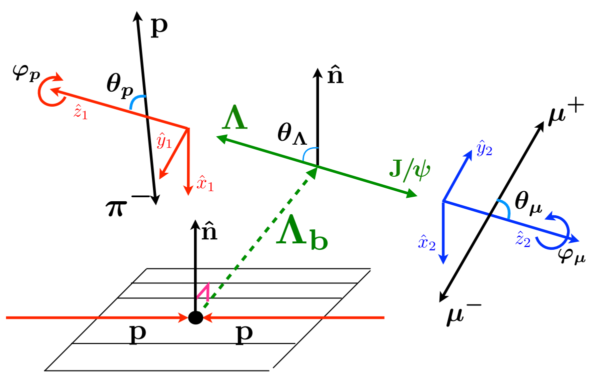

FIG. 1. Definition of the angles used to describe the $\Lambda_b \to J/\psi\Lambda$ decay into the $\mu^+\mu^-\ p\pi^-$ final state as explained in the text.

$$\frac{d^5\Gamma}{d\cos\theta_\Lambda d\Omega_p d\Omega_\mu}(\theta_\Lambda,\theta_p,\theta_\mu,\varphi_p,\varphi_\mu) = \frac{1}{(4\pi)^3}\sum_{i=1}^{20} u_i(T_{\lambda_1\lambda_2}) v_i(P,\alpha_\Lambda) w_i(\theta_\Lambda,\theta_p,\theta_\mu,\varphi_p,\varphi_\mu), \quad (2)$$

where w_i are trigonometric functions, u_i are bilinear combinations of the helicity amplitudes $T_{\lambda_1\lambda_2}$, and v_i stands for 1, P, α_Λ, or $P\alpha_\Lambda$; P is the Λ_b polarization and α_Λ is the asymmetry parameter in the decay $\Lambda \to p\pi^-$. The angle θ_Λ is the polar angle of the Λ momentum relative to $\hat{n}$ in the Λ_b rest frame; θ_p and φ_p are the polar and azimuthal angles of the proton, respectively, defined with respect to the axes $\hat{z}_1 = \vec{p}_\Lambda/|\vec{p}_\Lambda|$ and $\hat{y}_1 = (\hat{n}\times\vec{p}_\Lambda)/|\hat{n}\times\vec{p}_\Lambda|$ in the rest frame of the Λ; and the angles θ_μ and φ_μ are the polar and azimuthal angles, respectively, of the positively charged muon, defined with respect to the axes $\hat{z}_2 = \vec{p}_{J/\psi}/|\vec{p}_{J/\psi}|$ and $\hat{y}_2 = (\hat{n}\times\vec{p}_{J/\psi})/|\hat{n}\times\vec{p}_{J/\psi}|$ in the J/ψ rest frame. Here, $\vec{p}_\Lambda$ and $\vec{p}_{J/\psi}$ are the momenta of the Λ and J/ψ, respectively, and $d\Omega_p = d(\cos\theta_p)d\varphi_p$ and $d\Omega_\mu = d(\cos\theta_\mu)d\varphi_\mu$ are differential solid angles. Assuming uniform detector acceptance over the azimuthal angles φ_p and φ_μ, the angular distribution can be simplified through an integration over these two angles:

$$\frac{d^3\Gamma}{d\cos\theta_\Lambda d\cos\theta_p d\cos\theta_\mu}(\theta_\Lambda,\theta_p,\theta_\mu) = \int_{-\pi}^{\pi}\int_{-\pi}^{\pi}\frac{d^5\Gamma}{d\cos\theta_\Lambda d\Omega_p d\Omega_\mu}(\theta_\Lambda,\theta_p,\theta_\mu,\varphi_p,\varphi_\mu)d\varphi_p d\varphi_\mu \sim \sum_{i=1}^{8} u_i(|T_{\lambda_1\lambda_2}|^2) v_i(P,\alpha_\Lambda) w_i(\theta_\Lambda,\theta_p,\theta_\mu). \quad (3)$$

The eight functional forms of u_i, v_i, and w_i are listed in Table I. The u_i factors are written in terms of the three angular decay parameters α_1, α_2, and γ_0 proposed in Ref. [8], and the constant 1, which themselves can be written in terms of the $T_{\lambda_1\lambda_2}$ amplitudes as

$$\begin{aligned} 1 &= |T_{++}|^2 + |T_{+0}|^2 + |T_{-0}|^2 + |T_{--}|^2, \\ \alpha_1 &= |T_{++}|^2 - |T_{+0}|^2 + |T_{-0}|^2 - |T_{--}|^2, \\ \alpha_2 &= |T_{++}|^2 + |T_{+0}|^2 - |T_{-0}|^2 - |T_{--}|^2, \\ \gamma_0 &= |T_{++}|^2 - 2|T_{+0}|^2 - 2|T_{-0}|^2 + |T_{--}|^2, \end{aligned} \quad (4)$$

where α_1 is the asymmetry parameter for the decay $\Lambda_b \to J/\psi\Lambda$, α_2 represents the longitudinal polarization of the Λ, and γ_0 is a parameter that depends on the longitudinal and transverse polarizations of the J/ψ [9]. The CP invariance of Eq. (3) implies that the parameters for Λ_b and $\bar{\Lambda}_b$ are related as follows:

TABLE I. Functions used in Eq. (3) to describe the angular distribution in the decay $\Lambda_b \to J/\psi\Lambda$, with $J/\psi \to \mu^+\mu^-$ and $\Lambda \to p\pi^-$.

i	u_i	v_i	w_i
1	1	1	1
2	α_2	α_Λ	$\cos\theta_p$
3	$-\alpha_1$	P	$\cos\theta_\Lambda$
4	$-(1+2\gamma_0)/3$	$\alpha_\Lambda P$	$\cos\theta_\Lambda\cos\theta_p$
5	$\gamma_0/2$	1	$(3\cos^2\theta_\mu - 1)/2$
6	$(3\alpha_1-\alpha_2)/4$	α_Λ	$\cos\theta_p(3\cos^2\theta_\mu - 1)/2$
7	$(\alpha_1-3\alpha_2)/4$	P	$\cos\theta_\Lambda(3\cos^2\theta_\mu - 1)/2$
8	$(\gamma_0-4)/6$	$\alpha_\Lambda P$	$\cos\theta_\Lambda\cos\theta_p(3\cos^2\theta_\mu - 1)/2$

$$\bar{P} = -P, \quad \bar{\alpha}_1 = -\alpha_1, \quad \bar{\alpha}_2 = -\alpha_2, \quad \bar{\gamma}_0 = \gamma_0. \quad (5)$$

In addition, CP conservation in $\Lambda \to p\pi^-$ decays implies that $\bar{\alpha}_\Lambda = -\alpha_\Lambda$ [18]. In this analysis, the four parameters $(P, \alpha_1, \alpha_2, \gamma_0)$ are extracted from an analysis of the angular distribution given in Eq. (3), where α_Λ is fixed to its world-average value of 0.642 ± 0.013 [18].

III. THE CMS DETECTOR

The CMS detector is used to study a wide range of phenomena produced in high-energy collisions, with its central feature being a superconducting solenoid of 6m internal diameter, providing a magnetic field of 3.8 T. A silicon pixel and strip tracker, a lead tungstate scintillating crystal electromagnetic calorimeter, and a brass and scintillator sampling hadron calorimeter, including a central barrel and endcap detectors, are located within the magnetic volume.

The silicon tracker detects charged particles within the pseudorapidity range $|\eta| < 2.5$. It consists of 1440 silicon pixel and 15 148 silicon strip detector modules. For non-isolated particles with transverse momentum of $1 < p_T < 10$ GeV and $|\eta| < 1.4$, the track resolutions are typically 1.5% in p_T and 25–90 (45–150) μm in the transverse (longitudinal) impact parameter [19]. Muons are detected in gas-ionization chambers within the pseudorapidity range $|\eta| < 2.4$, with detection planes made using three technologies: drift tubes, cathode strip chambers, and resistive plate chambers [20]. The global event reconstruction (also called particle-flow event reconstruction [21]) consists of reconstructing and identifying each individual particle with an optimized combination of all subdetector information. In this process, muons are identified as a track in the silicon tracker consistent with either a track or several hits in the muon system, associated with an energy deficit in the calorimeters.

Events of interest are selected using a two-tiered trigger system [22]. The first level (L1), composed of custom hardware processors, uses information from the calorimeters and muon detectors to select events at a rate of around

100 kHz within a time interval of less than 4 μs. The second level, known as the high-level trigger (HLT), consists of a farm of processors running a version of the full event reconstruction software optimized for fast processing, and reduces the event rate to around 1 kHz before data storage.

A more detailed description of the CMS detector, a definition of the coordinate system used and the relevant kinematic variables, can be found in Ref. [17].

IV. DATA AND SIMULATED EVENTS

We use data collected with a trigger designed for events containing a J/ψ meson decaying to two muons that form a displaced vertex relative to the mean pp collision point (beamspot). The requirement on the displacement does not affect the angular distributions of the reconstructed Λ_b decay products. The dimuon trigger configurations were changed during the data taking at different center-of-mass energies, with increasingly stringent requirements to maintain an acceptable trigger rate as the instantaneous luminosity increased. The requirements of the different trigger versions are as follows: the J/ψ candidates are selected in the invariant mass window 2.5–4.0 GeV and 2.9–3.3 GeV depending on the version; the angle (β) between the reconstructed momentum vector of the dimuon system and the vector pointing from the beamspot position to the dimuon vertex must have a value of $\cos\beta > 0.9$; the distance between the beamspot and the dimuon vertex in the transverse plane must have a value that is at least a factor of 3 larger than its uncertainty (standard deviation or SD); the muon pair must satisfy $p_{\mathrm{T}}^{\mu\mu} > 6.5$ or 6.9 GeV in the different versions; the χ^2 probability of the fit of the two muons to a common vertex must exceed 0.05, 0.10, or 0.15 from the earliest to the latest version; each muon must be in $|\eta(\mu)| < 2.2$ and have $p_{\mathrm{T}}^{\mu} > 3.5$ or 4 GeV; and the distance of closest approach of each muon to the common vertex in the transverse plane must be less than 0.5 cm.

Simulated events of the signal decay are used to study the effects of detector acceptance and selection on the reconstructed angular distributions. The events are generated using PYTHIA 6.4[23] for production and hadronization, and EVTGEN [24] is used to describe the b and c hadron decays. The generated events are passed through the full CMS detector simulation based on GEANT4 [25]. The simulated event samples are generated to reproduce $\sqrt{s} = 7$ and 8 TeV data-taking conditions, where additional simulation of pp interactions in the same or nearby beam crossings and the impact of the HLT are included. Simulated events are reconstructed and selected using the same algorithms and requirements as used for data.

V. RECONSTRUCTION AND EVENT SELECTION

The offline selection requires pairs of oppositely charged muons originating from a common vertex to form the J/ψ candidates. The standard CMS muon reconstruction procedure [20] is used to identify the muons. Since the trigger changed slightly over the different data-taking periods, the offline selection is required to be more restrictive than the most-stringent trigger, and is summarized as follows: (i) each muon must have $p_{\mathrm{T}}^{\mu} > 4$ GeV and the dimuon transverse momentum must satisfy $p_{\mathrm{T}}^{\mu\mu} > 8$ GeV; (ii) the χ^2 probability must exceed 0.15; and (iii) the dimuon invariant mass must lie within ± 150 MeV of the world-average J/ψ mass [18]. Additional requirements are the same as the trigger selection and, to reduce background, the J/ψ candidates must satisfy $\cos\beta > 0.99$.

The Λ candidates are constructed from pairs of oppositely charged tracks that have a successful fit to a common vertex. Since the default CMS algorithms cannot distinguish between pions and protons, the higher- and lower-momentum tracks are assumed to have the proton and pion masses [18], respectively. The selections used for Λ and K_S^0 particles are detailed in Ref. [26]. They are optimized to reduce background using the following additional requirements: (i) each track is required to have at least 6 hits in the silicon tracker and a χ^2 track fit per degree of freedom < 7; (ii) the tracks coming from the Λ decay are required to have $p_{\mathrm{T}}^{\pi} > 0.3$ GeV, $p_{\mathrm{T}}^{p} > 1.0$ GeV; (iii) the transverse impact parameter of the tracks relative to the beamspot is required to be greater than 3 SD; (iv) the probability of the two-track vertex fit must exceed 2%; (v) the transverse separation of the two-track vertex from the beamspot is required to be larger than 15 SD; (vi) the invariant mass of the Λ candidate is selected to lie within ± 9 MeV of the world-average value [18] and satisfy $p_{\mathrm{T}}^{p\pi} > 1.3$ GeV; and (vii) to reduce the contamination of $K_S^0 \to \pi^+\pi^-$ decays, events are removed if their invariant mass falls within ± 20 MeV of the K_S^0 mass when the proton candidate is given the charged pion mass.

The Λ_b candidates are fitted to a common vertex by combining the J/ψ and Λ candidates, with the respective mass constraints to the world-average values of the J/ψ and Λ masses [18]. The selection of Λ_b candidates is optimized to reduce background with the additional requirements: $p_{\mathrm{T}}^{J/\psi\Lambda} > 10$ GeV, a χ^2 probability of the fit to the $J/\psi\Lambda$ vertex $> 3\%$, and the $J/\psi\Lambda$ invariant mass $5.40 < m_{J/\psi\Lambda} < 5.84$ GeV.

To extract the number of signal and background events and to define the signal and sidebands regions, unbinned maximum likelihood fits to the reconstructed invariant mass ($m_{J/\psi\Lambda}$) distributions are performed, using separate data sets of the Λ_b and $\bar{\Lambda}_b$ candidates at $\sqrt{s} = 7$ and 8 TeV. The signal shape is modeled by two Gaussian functions with different SDs, σ_1 and σ_2, but common mean $\mu_{J/\psi\Lambda}$, and the background by a first-order polynomial. We define in the four data sets the signal region as $\mu_{J/\psi\Lambda} \pm 16$ MeV, the lower sideband region as [5.46, 5.54] GeV, and the upper sideband region as

[5.70, 5.78] GeV. From the fits the Λ_b yields are 981 ± 39 and 2072 ± 55 signal events, and the $\bar{\Lambda}_b$ yields are 916 ± 40 and 1974 ± 53 signal events at $\sqrt{s} = 7$ and 8 TeV, respectively.

VI. MEASUREMENT OF THE POLARIZATION AND ANGULAR PARAMETERS

The analysis extracts the Λ_b polarization, P, and the angular decay parameters α_1, α_2, and γ_0. The results are obtained from an unbinned maximum likelihood fit to the $J/\psi\Lambda$ invariant mass distribution and the three angular variables $\Theta_3 = (\cos\theta_\Lambda, \cos\theta_p, \cos\theta_\mu)$, using the extended likelihood function:

$$L = \exp(-N_{\text{sig}} - N_{\text{bkg}}) \prod^{N} [N_{\text{sig}} PDF_{\text{sig}} + N_{\text{bkg}} PDF_{\text{bkg}}], \tag{6}$$

where N is the total number of events, N_{sig} and N_{bkg} are the yields of signal and background events, respectively, determined from the fit in Sec. V, and PDF_{sig} and PDF_{bkg} represent the probability density functions (PDFs) for the signal and background, respectively. The PDF_{sig} has the form

$$PDF_{\text{sig}} = F_{\text{sig}}(\Theta_3)\epsilon(\Theta_3)G(m_{J/\psi\Lambda}), \tag{7}$$

where F_{sig} represents the theoretical angular distribution given by Eq. (3) and G is the sum of two Gaussian functions used to model the $J/\psi\Lambda$ invariant mass distribution, as mentioned in Sec. V. The effect of the detector on the angular distribution is taken into account by the factor ϵ that represents the efficiency as a function of the angles.

To estimate the angular efficiency, simulated events of $\Lambda_b \to J/\psi\Lambda$ decays are generated with uniform distributions in $\cos\theta_\Lambda$, $\cos\theta_p$, and $\cos\theta_\mu$. After full detector simulation, reconstruction, and implementation of the final selection requirements, the slight differences between the simulated events and the background-subtracted data are minimized through a weighting procedure where weights are assigned to the simulated events to match the data. The weights are computed with an iterative process in which, for each iteration, the histograms of a selection variable in background-subtracted data and simulated events are used to calculate the ratio bin by bin (weight) with its propagated statistical uncertainty. The final weight per event is the product of the weights in each iteration. The efficiency distributions as a function of the variables are fit with a product of Chebyshev polynomials, where the coefficients are obtained for Λ_b and $\bar{\Lambda}_b$ at $\sqrt{s} = 7$ and 8 TeV in separate likelihood fits. The simulated efficiency distributions and the results of these fits are shown in Fig. 2 for the Λ_b candidates at $\sqrt{s} = 8$ TeV.

The background PDF_{bkg} is given by the product of a first-order polynomial $\mathcal{P}(m_{J/\psi\Lambda})$ for the invariant mass and an angular distribution function $F_{\text{bkg}}(\Theta_3)$:

$$PDF_{\text{bkg}} = \mathcal{P}(m_{J/\psi\Lambda})F_{\text{bkg}}(\Theta_3). \tag{8}$$

The background angular distributions $F_{\text{bkg}}(\Theta_3)$ are estimated using events from the $m_{J/\psi\Lambda}$ invariant mass sidebands. They are modeled using Chebyshev polynomials for $\cos\theta_\Lambda$ and $\cos\theta_p$, and a product of two complementary error functions for $\cos\theta_\mu$, as shown in Fig. 3 for Λ_b candidates at $\sqrt{s} = 8$ TeV.

The complete likelihood function in Eq. (6) is maximized by fitting simultaneously the four data sets for Λ_b and $\bar{\Lambda}_b$ at $\sqrt{s} = 7$ and 8 TeV, allowing for the extraction of the common parameters P, α_1, α_2, and γ_0. The simultaneous fit is performed in the enriched signal mass range within 3.5 SDs of the mean Λ_b mass. This range contains more than 99.9% of the signal events, and significantly reduces the number of background events. As a result, the fit is less sensitive to the modeling discussed above. The fit parameters for the background and efficiency distributions

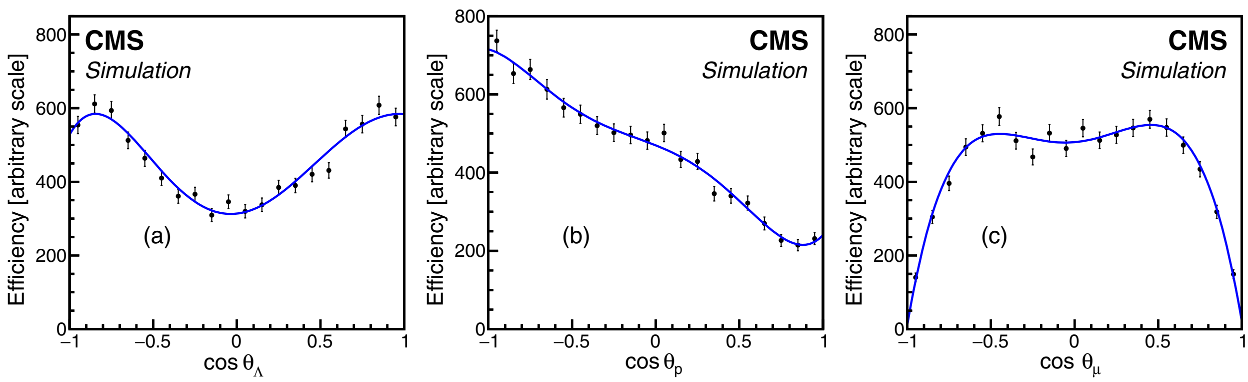

FIG. 2. The efficiencies as a function of (a) $\cos\theta_\Lambda$, (b) $\cos\theta_p$, and (c) $\cos\theta_\mu$ obtained from simulated $\Lambda_b \to J/\psi\Lambda$ decays at $\sqrt{s} = 8$ TeV. The vertical bars on the points are the statistical uncertainties in the simulated data, and the lines show the projections of a 3D fit to the distributions using Chebyshev polynomials. The scales of the vertical axes are arbitrary.

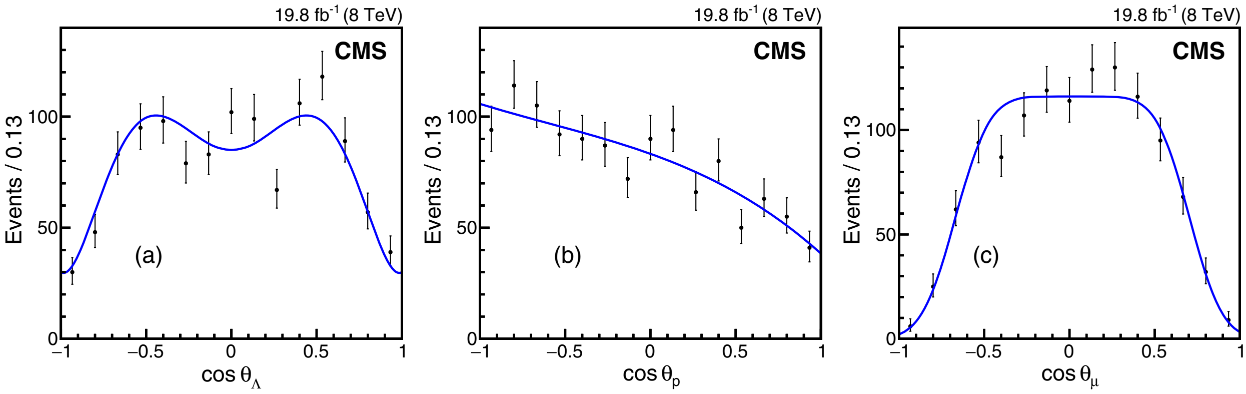

FIG. 3. The background angular distributions of (a) $\cos\theta_\Lambda$, (b) $\cos\theta_p$, and (c) $\cos\theta_\mu$ are shown, as obtained from the sidebands in the $J/\psi\Lambda$ invariant mass distribution at $\sqrt{s} = 8$ TeV. The vertical bars on the points represent the statistical uncertainties, and the solid lines are the results of the fits to data as described in the text.

are fixed to those found in the previous fits. The signal and background mass parameters are obtained from previous fits to the mass distribution within 10 SDs, and the numbers of signal and backgrounds events are fixed to the propagated values in the signal mass region. The resulting fit values of the polarization and the three angular decay parameters are

$$P = 0.00 \pm 0.06, \qquad \alpha_1 = 0.14 \pm 0.14,$$
$$\alpha_2 = -1.11 \pm 0.04, \qquad \gamma_0 = -0.27 \pm 0.08,$$

where the uncertainties are statistical only. The correlation matrix of the fitted parameters is shown in Table II. No strong correlations are found among these parameters. Translating these values to the squares of the helicity amplitudes, the results are

$$|T_{++}|^2 = 0.05 \pm 0.04, \qquad |T_{+0}|^2 = -0.10 \pm 0.04,$$
$$|T_{-0}|^2 = 0.51 \pm 0.03, \qquad |T_{--}|^2 = 0.52 \pm 0.04,$$

where the uncertainties are statistical only. The projections of the fit are shown in Figs. 4 and 5 for Λ_b and $\bar{\Lambda}_b$, respectively, using the combined data at $\sqrt{s} = 7$ and 8 TeV.

VII. SYSTEMATIC UNCERTAINTIES

Various sources of systematic uncertainty that affect the measurement of the parameters P, α_1, α_2, and γ_0 are discussed below.

TABLE II. Correlation matrix for the fitted parameters.

Parameter	P	α_1	α_2	γ_0
P	1	−0.039	−0.029	0.116
α_1		1	−0.207	−0.030
α_2			1	0.285
γ_0				1

Fit bias.—The bias introduced through the fitting procedure is studied by generating 1000 pseudoexperiments using the measured parameters as inputs. The difference between the input and the mean of the fitted values is taken as the systematic uncertainty.

Asymmetry parameter α_Λ.—This parameter is varied up and down by its uncertainty and the maximum deviation in the final result for each parameter is taken as the systematic uncertainty.

Model for the background $m_{J/\psi\Lambda}$ distribution.—An exponential function is used instead of the first-order polynomial in the likelihood fit. The parameter of the exponential and the background yield are varied by their uncertainties. The fit is redone taking into account this variation on the background model for the mass, and the differences between these results and the nominal fit results are taken as the systematic uncertainty for this source.

Model for the background angular distributions.—Alternative parametrizations of the background angular distributions are used to estimate the systematic uncertainty. For $\cos\theta_\Lambda$ and $\cos\theta_\mu$ the alternative models comprise a superposition of Gaussian kernels, as implemented in Roofit RooKeysPdf [27], while for $\cos\theta_p$ the alternative model is an error function. The differences relative to the nominal results are taken as the systematic uncertainties from the modeling of the background angular distributions.

Model for the signal $m_{J/\psi\Lambda}$ distribution.—We estimate this uncertainty by changing the parameters by their uncertainties, taking into account their correlations. In each sample of Λ_b and $\bar{\Lambda}_b$ at $\sqrt{s} = 7$ and 8 TeV, we use the parameter of the signal mass model with the largest global correlation and add 1 SD to its nominal value if the correlation is positive and subtract 1 SD if the correlation is negative. The difference relative to the nominal result is quoted as a systematic uncertainty.

Angular efficiencies.—The values of the Chebyshev polynomial coefficients that model the angular dependence of the efficiencies are changed by their uncertainties. The

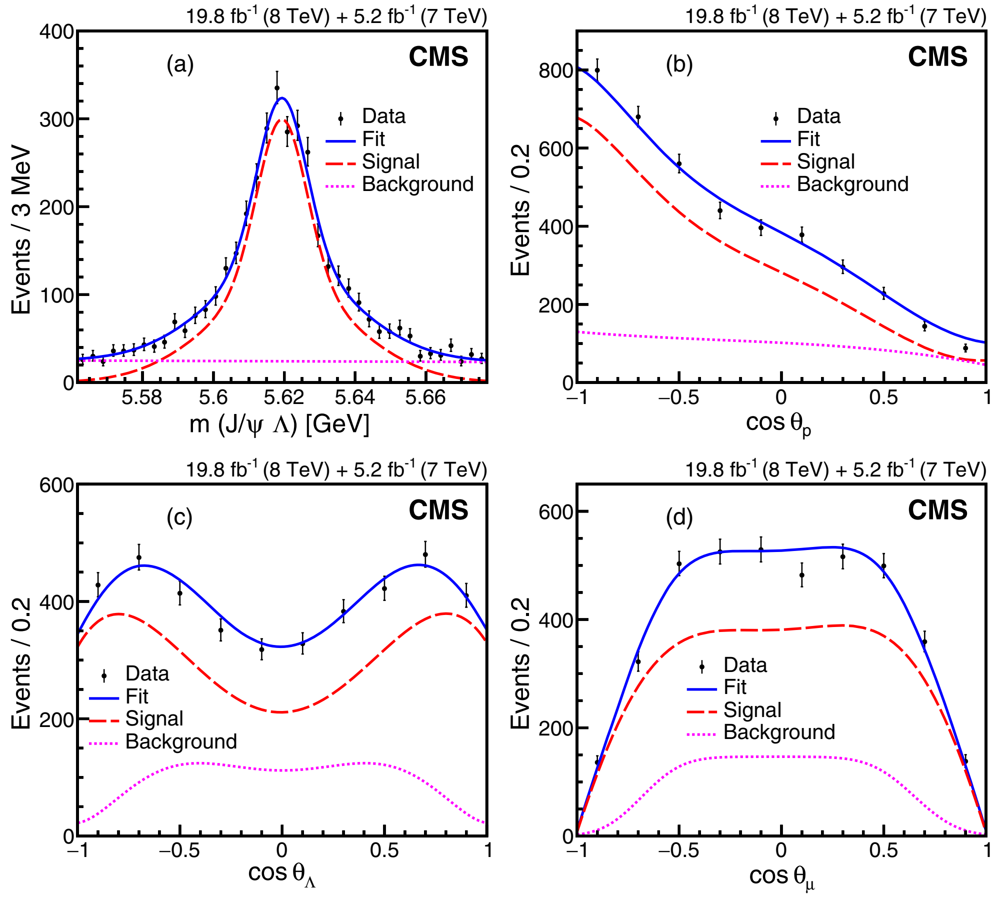

FIG. 4. Distributions in (a) $m_{J/\psi\Lambda}$, (b) $\cos\theta_p$, (c) $\cos\theta_\Lambda$, and (d) $\cos\theta_\mu$ for Λ_b candidates in the combined $\sqrt{s} = 7$ and 8 TeV data. The vertical bars on the points are the statistical uncertainties in the data, the solid line shows the result of the fit, and the dashed and dotted lines represent, respectively, the signal and background contributions from the fit.

difference relative to the nominal fitted result is taken as the systematic uncertainty.

Angular resolution.—We study the systematic uncertainty in the angular resolution of the measured observables $\cos\theta_\Lambda$, $\cos\theta_p$, and $\cos\theta_\mu$ by first determining the resolution using simulated events, then taking the difference between the generated (before detector simulation) and reconstructed (fully simulated) distributions of the cosines of the three polar angles, and fitting the resulting distributions to Gaussian functions. Using these models, we generate random numbers that are added to the three polar angles of the events at generation. The difference between the obtained parameters from the likelihood fits using the same events, with and without the added random terms, is quoted as the systematic uncertainty from the angular resolution.

Azimuthal angle efficiency.—Uniform azimuthal efficiencies are assumed throughout the analysis. Besides simplifying the measurement from a five- to a three-dimensional angular analysis, this assumption also reduces the number of angular parameters from 6 to 3. The effect of the nonuniformity in the φ_p and φ_μ efficiencies is investigated with 500 pseudoexperiments generated using the five-dimensional angular distribution, multiplied by the polar and azimuthal efficiencies obtained from the full simulation, as well as initializing the 3 extra parameters to values away from the physical boundary. The resulting distributions are then fitted to the nominal three-dimensional angular model. Differences in the mean values of P, α_1, α_2, and γ_0 relative to the input values (set to the nominal results) are taken as the systematic uncertainties from the impact of the nonuniformity of the azimuthal efficiencies.

Weighting procedure.— To estimate the uncertainty from the weighting procedure, we vary each weight by its uncertainty and use this as a new weight to correct the efficiencies, then redo the fit with these new values. The differences between the results of this fit and the nominal values are taken as the systematic uncertainty in each parameter.

Reconstruction bias.—Possible unaccounted reconstruction biases are also considered. To estimate this systematic uncertainty, we use a simulated event sample with input values of the helicity amplitudes and polarization similar to those observed in data. Then, after reconstruction and selection as in data, we fit the simulated events and take

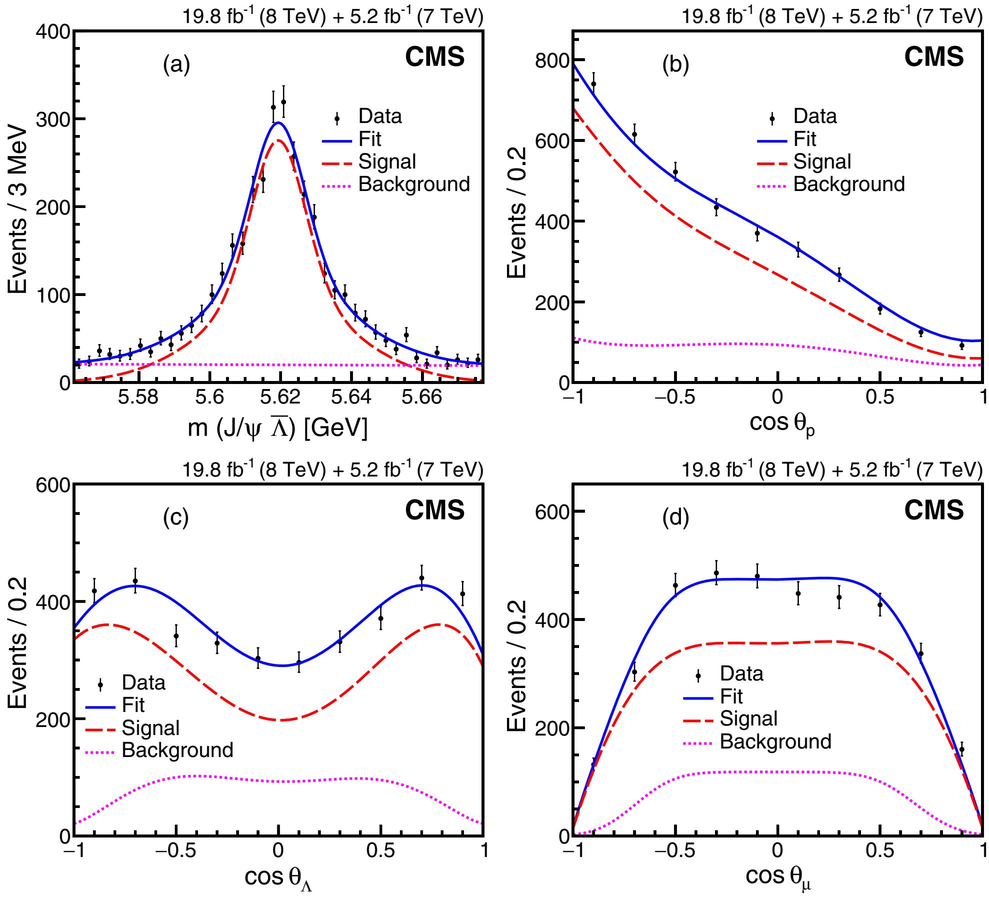

FIG. 5. Distributions in (a) $m_{J/\psi\bar{\Lambda}}$, (b) $\cos\theta_p$, (c) $\cos\theta_\Lambda$, and (d) $\cos\theta_\mu$ for $\bar{\Lambda}_b$ candidates in the combined $\sqrt{s} = 7$ and 8 TeV data. The vertical bars on the points are the statistical uncertainties in the data, the solid line shows the result of the fit, and the dashed and dotted lines represent, respectively, the signal and background contributions from the fit.

the differences between the input and fit values for every angular parameter and polarization. Since we are using the full reconstruction of the simulated events, we subtract in quadrature the systematic sources involved in the fit from those observed differences, and finally take the square root of this subtraction as the estimate of the systematic uncertainty component due to reconstruction bias. This systematic uncertainty is by far the largest uncertainty; however, it is still smaller or comparable to the corresponding statistical uncertainty.

TABLE III. The sources and values of the systematic uncertainties in each parameter and the total uncertainty. Each value in the table should be multiplied by 10^{-2} to obtain the corresponding systematic uncertainty.

Source	$P(\times 10^{-2})$	$\alpha_1(\times 10^{-2})$	$\alpha_2(\times 10^{-2})$	$\gamma_0(\times 10^{-2})$
Fit bias	0.1	0.3	0.1	0.2
Asymmetry parameter α_Λ	0.4	0.7	2.0	0.6
Background $m_{J/\psi\Lambda}$ distribution	0.01	0.5	1.0	0.9
Background angular distribution	0.4	0.5	0.9	5.0
Signal $m_{J/\psi\Lambda}$ distribution	0.01	0.3	1.0	1.0
Angular efficiencies	0.1	0.3	3.0	1.0
Angular resolution	1.0	0.1	2.6	0.8
Azimuthal angle efficiency	0.1	1.0	0.3	0.1
Weighting procedure	0.1	1.3	0.4	2.0
Reconstruction bias	5.7	9.8	2.0	9.1
Total (quadrature sum)	5.8	10.0	5.1	11.1

The contributions from the different uncertainty sources are assumed to be independent and the total systematic uncertainty is calculated as the quadrature sum of all uncertainties. The values of the systematic uncertainties in each parameter from the individual sources and their quadrature sum are given in Table III.

VIII. SUMMARY AND CONCLUSIONS

Based on an angular analysis of about 6000 $\Lambda_b \to J/\psi(\to\mu^+\mu^-)\Lambda(\to p\pi^-)$ events collected by the CMS experiment at $\sqrt{s}=7$ and 8 TeV, a measurement of the Λ_b polarization P, the parity-violating asymmetry parameter in the Λ_b decay α_1, the Λ longitudinal polarization α_2, and the parameter γ_0 has been performed. The obtained values are

$$P = 0.00 \pm 0.06(\text{stat}) \pm 0.06(\text{syst}),$$
$$\alpha_1 = 0.14 \pm 0.14(\text{stat}) \pm 0.10(\text{syst}),$$
$$\alpha_2 = -1.11 \pm 0.04(\text{stat}) \pm 0.05(\text{syst}),$$
$$\gamma_0 = -0.27 \pm 0.08(\text{stat}) \pm 0.11(\text{syst}),$$

corresponding to the squares of the helicity amplitudes

$$|T_{++}|^2 = 0.05 \pm 0.04(\text{stat}) \pm 0.04(\text{syst}),$$
$$|T_{+0}|^2 = -0.10 \pm 0.04(\text{stat}) \pm 0.04(\text{syst}),$$
$$|T_{-0}|^2 = 0.51 \pm 0.03(\text{stat}) \pm 0.04(\text{syst}),$$
$$|T_{--}|^2 = 0.52 \pm 0.04(\text{stat}) \pm 0.04(\text{syst}).$$

The measured Λ_b polarization value given above is consistent with the LHCb measurement [11] and theoretical predictions of 0.10 [5] and 0.20 [6]. Note that in our notation, α_1 is the negative value of α_b referred to in the theory [9,10,28–31], LHCb [11], and ATLAS [12] papers. To compare with the theoretical predictions and the other measurements, we use the negative of our measured value of α_1. The many theoretical predictions for $-\alpha_1$ include -0.2 to -0.1 from quark model techniques [9,28–31], -0.17 to -0.14 from perturbative quantum chromodynamics calculations [10], and 0.78 from heavy-quark effective theory [4,6]. The measured value is inconsistent at more than 5 standard deviations with the heavy-quark effective theory prediction, but is consistent at less than one standard deviation with the other predictions. The presented measurement of α_1 is also consistent with the measurements $0.05 \pm 0.17(\text{stat}) \pm 0.07(\text{syst})$ and $0.30 \pm 0.16(\text{stat}) \pm 0.06(\text{syst})$ by LHCb [11] and ATLAS [12], respectively, and with no parity violation at the level of one standard deviation. The measurement of α_2, compatible with -1, indicates that the positive-helicity states of the Λ coming from the Λ_b decay are suppressed.

ACKNOWLEDGMENTS

We congratulate our colleagues in the CERN accelerator departments for the excellent performance of the LHC and thank the technical and administrative staffs at CERN and at other CMS institutes for their contributions to the success of the CMS effort. In addition, we gratefully acknowledge the computing centers and personnel of the Worldwide LHC Computing Grid for delivering so effectively the computing infrastructure essential to our analysis. Finally, we acknowledge the enduring support for the construction and operation of the LHC and the CMS detector provided by the following funding agencies: BMWFW and FWF (Austria); FNRS and FWO (Belgium); CNPq, CAPES, FAPERJ, and FAPESP (Brazil); MES (Bulgaria); CERN; CAS, MoST, and NSFC (China); COLCIENCIAS (Colombia); MSES and CSF (Croatia); RPF (Cyprus); SENESCYT (Ecuador); MoER, ERC IUT, and ERDF (Estonia); Academy of Finland, MEC, and HIP (Finland); CEA and CNRS/IN2P3 (France); BMBF, DFG, and HGF (Germany); GSRT (Greece); OTKA and NIH (Hungary); DAE and DST (India); IPM (Iran); SFI (Ireland); INFN (Italy); MSIP and NRF (Republic of Korea); LAS (Lithuania); MOE and UM (Malaysia); BUAP, CINVESTAV, CONACYT, LNS, SEP, and UASLP-FAI (Mexico); MBIE (New Zealand); PAEC (Pakistan); MSHE and NSC (Poland); FCT (Portugal); JINR (Dubna); MON, RosAtom, RAS, RFBR and RAEP (Russia); MESTD (Serbia); SEIDI, CPAN, PCTI and FEDER (Spain); Swiss Funding Agencies (Switzerland); MST (Taipei); ThEPCenter, IPST, STAR, and NSTDA (Thailand); TUBITAK and TAEK (Turkey); NASU and SFFR (Ukraine); STFC (United Kingdom); DOE and NSF (USA). Individuals have received support from the Marie-Curie program and the European Research Council and Horizon 2020 Grant, Contract No. 675440 (European Union); the Leventis Foundation; the A. P. Sloan Foundation; the Alexander von Humboldt Foundation; the Belgian Federal Science Policy Office; the Fonds pour la Formation à la Recherche dans l'Industrie et dans l'Agriculture (FRIA-Belgium); the Agentschap voor Innovatie door Wetenschap en Technologie (IWT-Belgium); the Ministry of Education, Youth and Sports (MEYS) of the Czech Republic; the Council of Science and Industrial Research, India; the HOMING PLUS program of the Foundation for Polish Science, cofinanced from European Union, Regional Development Fund, the Mobility Plus program of the Ministry of Science and Higher Education, the National Science Center (Poland), Contracts No. Harmonia 2014/14/M/ST2/00428, Opus 2014/13/B/ST2/02543, 2014/15/B/ST2/03998, and 2015/19/B/ST2/02861, Sonata-bis 2012/07/E/ST2/01406; the National Priorities Research Program by Qatar National Research Fund; the program Severo Ochoa del Principado de Asturias; the Thalis and Aristeia programs cofinanced by EU-ESF and the Greek NSRF; the Rachadapisek Sompot Fund for Postdoctoral Fellowship, Chulalongkorn University and the Chulalongkorn Academic into Its 2nd Century Project Advancement Project (Thailand); the Welch Foundation, Contract No. C-1845; and the Weston Havens Foundation (USA).

---

[1] A. F. Falk and M. E. Peskin, Production, decay, and polarization of excited heavy hadrons, Phys. Rev. D **49**, 3320 (1994).

[2] B. Mele and G. Altarelli, Lepton spectra as a measure of b quark polarization at LEP, Phys. Lett. B **299**, 345 (1993).

[3] D. Buskulic *et al.* (ALEPH Collaboration), Measurement of Λ_b polarization in Z decays, Phys. Lett. B **365**, 437 (1996).

[4] Z. J. Ajaltouni, E. Conte, and O. Leitner, An angular distribution analysis of Λ_b decays, Nucl. Phys. **A755**, 435 (2005).

[5] G. Hiller, M. Knecht, F. Legger, and T. Schietinger, Photon polarization from helicity suppression in radiative decays of polarized Λ_b to spin–3/2 baryons, Phys. Lett. B **649**, 152 (2007).

[6] Z. J. Ajaltouni, E. Conte, and O. Leitner, Λ_b decays into Λ–vector, Phys. Lett. B **614**, 165 (2005).

[7] P. Bialas, J. G. Korner, M. Kramer, and K. Zalewski, Joint angular decay distributions in exclusive weak decays of heavy mesons and baryons, Z. Phys. C **57**, 115 (1993).

[8] M. Kramer and H. Simma, Angular correlations in $\Lambda_b \to \Lambda + V$: polarization measurements, HQET and CP violation, Nucl. Phys. B, Proc. Suppl. **50**, 125 (1996).

[9] T. Gutsche, M. A. Ivanov, J. G. Körner, V. E. Lyubovitskij, and P. Santorelli, Polarization effects in the cascade decay $\Lambda_b \to \Lambda(\to p\pi^-) + J/\psi(l^+l^-)$ in the covariant confined quark model, Phys. Rev. D **88**, 114018 (2013).

[10] C.-H. Chou, H.-H. Shih, S.-C. Lee, and H.-n. Li, $\Lambda_b \to \Lambda J/\psi$ decay in perturbative QCD, Phys. Rev. D **65**, 074030 (2002).

[11] LHCb Collaboration, Measurements of the $\Lambda_b \to J/\psi\Lambda$ decay amplitudes and the Λ_b polarisation in pp collisions at $\sqrt{s} = 7$TeV, Phys. Lett. B **724**, 27 (2013).

[12] ATLAS Collaboration, Measurement of the parity-violating asymmetry parameter α_b and the helicity amplitudes for the decay $\Lambda_b \to J/\psi\Lambda$ with the ATLAS detector, Phys. Rev. D **89**, 092009 (2014).

[13] T. Aaltonen *et al.* (CDF Collaboration), Observation of the Heavy Baryons Σ_b and Σ_b^*, Phys. Rev. Lett. **99**, 202001 (2007).

[14] T. Aaltonen *et al.* (CDF Collaboration), Measurement of the masses and widths of the bottom baryons ${\Sigma_b}^\pm$ and ${\Sigma_b}^{*\pm}$, Phys. Rev. D **85**, 092011 (2012).

[15] T. Aaltonen *et al.* (CDF Collaboration), Evidence for a bottom baryon resonance ${\Lambda_b}^*$ in CDF data, Phys. Rev. D **88**, 071101 (2013).

[16] R Aaij *et al.* (LHCb Collaboration), Observation of Excited Λ_b Baryons, Phys. Rev. Lett. **109**, 172003 (2012).

[17] CMS Collaboration, The CMS experiment at the CERN LHC, J. Instrum. **3**, S08004 (2008).

[18] C. Patrignani *et al.* (Particle Data Group Collaboration), Review of particle physics, Chin. Phys. C **40**, 100001 (2016).

[19] CMS Collaboration, Description and performance of track and primary-vertex reconstruction with the CMS tracker, J. Instrum. **9**, P10009 (2014).

[20] CMS Collaboration, Performance of CMS muon reconstruction in pp collision events at $\sqrt{s} = 7$ TeV, J. Instrum. **7**, P10002 (2012).

[21] CMS Collaboration, Particle-flow reconstruction and global event description with the CMS detector, J. Instrum. **12**, P10003 (2017).

[22] CMS Collaboration, The CMS trigger system, J. Instrum. **12**, P01020 (2017).

[23] T. Sjöstrand, S. Mrenna, and P. Z. Skands, PYTHIA 6.4 physics and manual, J. High Energy Phys. 05 (2006) 026.

[24] D. J. Lange, The EVTGEN particle decay simulation package, Proceedings of the 7th International Conference on B physics at hadron machines (BEAUTY 2000), Nucl. Instrum. Methods Phys. Res., Sect. A **462**, 152 (2001).

[25] S. Agostinelli *et al.* (GEANT4 Collaboration), GEANT4—a simulation toolkit, Nucl. Instrum. Methods Phys. Res., Sect. A **506**, 250 (2003).

[26] CMS Collaboration, Strange particle production in pp collisions at $\sqrt{s} = 0.9$ and 7 TeV, J. High Energy Phys. 05 (2011) 064.

[27] W. Verkerke and D. P. Kirkby, The RooFit toolkit for data modeling, eConference C0303241, MOLT007 (2003).

[28] H.-Y. Cheng, Nonleptonic weak decays of bottom baryons, Phys. Rev. D **56**, 2799 (1997).

[29] Fayyazuddin and Riazuddin, Two-body nonleptonic Λ_b decays in the quark model with factorization ansatz, Phys. Rev. D **58**, 014016 (1998).

[30] R. Mohanta, A. K. Giri, M. P. Khanna, M. Ishida, S. Ishida, and M. Oda, Hadronic weak decays of Λ_b baryon in the covariant oscillator quark model, Prog. Theor. Phys. **101**, 959 (1999).

[31] Z.-T. Wei, H.-W. Ke, and X.-Q. Li, Evaluating decay rates and asymmetries of Λ_b into light baryons in LFQM, Phys. Rev. D **80**, 094016 (2009).

A. M. Sirunyan,[1] A. Tumasyan,[1] W. Adam,[2] F. Ambrogi,[2] E. Asilar,[2] T. Bergauer,[2] J. Brandstetter,[2] E. Brondolin,[2] M. Dragicevic,[2] J. Erö,[2] A. Escalante Del Valle,[2] M. Flechl,[2] M. Friedl,[2] R. Frühwirth,[2,b] V. M. Ghete,[2] J. Grossmann,[2] J. Hrubec,[2] M. Jeitler,[2,b] A. König,[2] N. Krammer,[2] I. Krätschmer,[2] D. Liko,[2] T. Madlener,[2] I. Mikulec,[2] E. Pree,[2] N. Rad,[2] H. Rohringer,[2] J. Schieck,[2,b] R. Schöfbeck,[2] M. Spanring,[2] D. Spitzbart,[2] A. Taurok,[2] W. Waltenberger,[2] J. Wittmann,[2] C.-E. Wulz,[2,b] M. Zarucki,[2] V. Chekhovsky,[3] V. Mossolov,[3] J. Suarez Gonzalez,[3] E. A. De Wolf,[4] D. Di Croce,[4] X. Janssen,[4] J. Lauwers,[4] H. Van Haevermaet,[4] P. Van Mechelen,[4] N. Van Remortel,[4] S. Abu Zeid,[5] F. Blekman,[5] J. D'Hondt,[5] I. De Bruyn,[5] J. De Clercq,[5] K. Deroover,[5] G. Flouris,[5] D. Lontkovskyi,[5] S. Lowette,[5] I. Marchesini,[5] S. Moortgat,[5] L. Moreels,[5] Q. Python,[5] K. Skovpen,[5] S. Tavernier,[5] W. Van Doninck,[5] P. Van Mulders,[5] I. Van Parijs,[5] D. Beghin,[6] B. Bilin,[6] H. Brun,[6] B. Clerbaux,[6] G. De Lentdecker,[6] H. Delannoy,[6] B. Dorney,[6] G. Fasanella,[6] L. Favart,[6] R. Goldouzian,[6] A. Grebenyuk,[6] A. K. Kalsi,[6] T. Lenzi,[6] J. Luetic,[6] T. Maerschalk,[6] A. Marinov,[6] T. Seva,[6] E. Starling,[6] C. Vander Velde,[6] P. Vanlaer,[6] D. Vannerom,[6] R. Yonamine,[6] F. Zenoni,[6] T. Cornelis,[7] D. Dobur,[7] A. Fagot,[7] M. Gul,[7] I. Khvastunov,[7,c] D. Poyraz,[7] C. Roskas,[7] S. Salva,[7] D. Trocino,[7] M. Tytgat,[7] W. Verbeke,[7] N. Zaganidis,[7] H. Bakhshiansohi,[8] O. Bondu,[8] S. Brochet,[8] G. Bruno,[8] C. Caputo,[8] A. Caudron,[8] P. David,[8] S. De Visscher,[8] C. Delaere,[8] M. Delcourt,[8] B. Francois,[8] A. Giammanco,[8] M. Komm,[8] G. Krintiras,[8] V. Lemaitre,[8] A. Magitteri,[8] A. Mertens,[8] M. Musich,[8] K. Piotrzkowski,[8] L. Quertenmont,[8] A. Saggio,[8] M. Vidal Marono,[8] S. Wertz,[8] J. Zobec,[8] W. L. Aldá Júnior,[9] F. L. Alves,[9] G. A. Alves,[9] L. Brito,[9] G. Correia Silva,[9] C. Hensel,[9] A. Moraes,[9] M. E. Pol,[9] P. Rebello Teles,[9] E. Belchior Batista Das Chagas,[10] W. Carvalho,[10] J. Chinellato,[10,d] E. Coelho,[10] E. M. Da Costa,[10] G. G. Da Silveira,[10,e] D. De Jesus Damiao,[10] S. Fonseca De Souza,[10] L. M. Huertas Guativa,[10] H. Malbouisson,[10] M. Melo De Almeida,[10] C. Mora Herrera,[10] L. Mundim,[10] H. Nogima,[10] L. J. Sanchez Rosas,[10] A. Santoro,[10] A. Sznajder,[10] M. Thiel,[10] E. J. Tonelli Manganote,[10,d] F. Torres Da Silva De Araujo,[10] A. Vilela Pereira,[10] S. Ahuja,[11a] C. A. Bernardes,[11a] T. R. Fernandez Perez Tomei,[11a] E. M. Gregores,[11b] P. G. Mercadante,[11b] S. F. Novaes,[11a] Sandra S. Padula,[11a] D. Romero Abad,[11b] J. C. Ruiz Vargas,[11a] A. Aleksandrov,[12] R. Hadjiiska,[12] P. Iaydjiev,[12] M. Misheva,[12] M. Rodozov,[12] M. Shopova,[12] G. Sultanov,[12] A. Dimitrov,[13] L. Litov,[13] B. Pavlov,[13] P. Petkov,[13] W. Fang,[14,f] X. Gao,[14,f] L. Yuan,[14] M. Ahmad,[15] J. G. Bian,[15] G. M. Chen,[15] H. S. Chen,[15] M. Chen,[15] Y. Chen,[15] C. H. Jiang,[15] D. Leggat,[15] H. Liao,[15] Z. Liu,[15] F. Romeo,[15] S. M. Shaheen,[15] A. Spiezia,[15] J. Tao,[15] C. Wang,[15] Z. Wang,[15] E. Yazgan,[15] T. Yu,[15] H. Zhang,[15] J. Zhao,[15] Y. Ban,[16] G. Chen,[16] J. Li,[16] Q. Li,[16] S. Liu,[16] Y. Mao,[16] S. J. Qian,[16] D. Wang,[16] Z. Xu,[16] F. Zhang,[16,f] Y. Wang,[17] C. Avila,[18] A. Cabrera,[18] L. F. Chaparro Sierra,[18] C. Florez,[18] C. F. González Hernández,[18] J. D. Ruiz Alvarez,[18] M. A. Segura Delgado,[18] B. Courbon,[19] N. Godinovic,[19] D. Lelas,[19] I. Puljak,[19] P. M. Ribeiro Cipriano,[19] T. Sculac,[19] Z. Antunovic,[20] M. Kovac,[20] V. Brigljevic,[21] D. Ferencek,[21] K. Kadija,[21] B. Mesic,[21] A. Starodumov,[21,g] T. Susa,[21] M. W. Ather,[22] A. Attikis,[22] G. Mavromanolakis,[22] J. Mousa,[22] C. Nicolaou,[22] F. Ptochos,[22] P. A. Razis,[22] H. Rykaczewski,[22] M. Finger,[23,h] M. Finger Jr.,[23,h] E. Carrera Jarrin,[24] A. Mohamed,[25,i] Y. Mohammed,[25,j] E. Salama,[25,k,l] S. Bhowmik,[26] R. K. Dewanjee,[26] M. Kadastik,[26] L. Perrini,[26] M. Raidal,[26] A. Tiko,[26] C. Veelken,[26] P. Eerola,[27] H. Kirschenmann,[27] J. Pekkanen,[27] M. Voutilainen,[27] J. Havukainen,[28] J. K. Heikkilä,[28] T. Järvinen,[28] V. Karimäki,[28] R. Kinnunen,[28] T. Lampén,[28] K. Lassila-Perini,[28] S. Laurila,[28] S. Lehti,[28] T. Lindén,[28] P. Luukka,[28] T. Mäenpää,[28] H. Siikonen,[28] E. Tuominen,[28] J. Tuominiemi,[28] T. Tuuva,[29] M. Besancon,[30] F. Couderc,[30] M. Dejardin,[30] D. Denegri,[30] J. L. Faure,[30] F. Ferri,[30] S. Ganjour,[30] S. Ghosh,[30] A. Givernaud,[30] P. Gras,[30] G. Hamel de Monchenault,[30] P. Jarry,[30] I. Kucher,[30] C. Leloup,[30] E. Locci,[30] M. Machet,[30] J. Malcles,[30] G. Negro,[30] J. Rander,[30] A. Rosowsky,[30] M. Ö. Sahin,[30] M. Titov,[30] A. Abdulsalam,[31,m] C. Amendola,[31] I. Antropov,[31] S. Baffioni,[31] F. Beaudette,[31] P. Busson,[31] L. Cadamuro,[31] C. Charlot,[31] R. Granier de Cassagnac,[31] M. Jo,[31] S. Lisniak,[31] A. Lobanov,[31] J. Martin Blanco,[31] M. Nguyen,[31] C. Ochando,[31] G. Ortona,[31] P. Paganini,[31] P. Pigard,[31] R. Salerno,[31] J. B. Sauvan,[31] Y. Sirois,[31] A. G. Stahl Leiton,[31] T. Strebler,[31] Y. Yilmaz,[31] A. Zabi,[31] A. Zghiche,[31] J.-L. Agram,[32,n] J. Andrea,[32] D. Bloch,[32] J.-M. Brom,[32] M. Buttignol,[32] E. C. Chabert,[32] N. Chanon,[32] C. Collard,[32] E. Conte,[32,n] X. Coubez,[32] F. Drouhin,[32,n] J.-C. Fontaine,[32,n] D. Gelé,[32] U. Goerlach,[32] M. Jansová,[32] P. Juillot,[32] A.-C. Le Bihan,[32] N. Tonon,[32] P. Van Hove,[32] S. Gadrat,[33] S. Beauceron,[34] C. Bernet,[34] G. Boudoul,[34] R. Chierici,[34] D. Contardo,[34] P. Depasse,[34] H. El Mamouni,[34] J. Fay,[34] L. Finco,[34] S. Gascon,[34] M. Gouzevitch,[34] G. Grenier,[34] B. Ille,[34] F. Lagarde,[34] I. B. Laktineh,[34] M. Lethuillier,[34] L. Mirabito,[34] A. L. Pequegnot,[34] S. Perries,[34] A. Popov,[34,o] V. Sordini,[34] M. Vander Donckt,[34] S. Viret,[34] S. Zhang,[34] T. Toriashvili,[35,p] Z. Tsamalaidze,[36,h] C. Autermann,[37] L. Feld,[37] M. K. Kiesel,[37] K. Klein,[37] M. Lipinski,[37] M. Preuten,[37] C. Schomakers,[37] J. Schulz,[37] M. Teroerde,[37] B. Wittmer,[37] V. Zhukov,[37,o] A. Albert,[38] D. Duchardt,[38] M. Endres,[38] M. Erdmann,[38] S. Erdweg,[38] T. Esch,[38] R. Fischer,[38] A. Güth,[38] M. Hamer,[38] T. Hebbeker,[38] C. Heidemann,[38] K. Hoepfner,[38] S. Knutzen,[38] M. Merschmeyer,[38]

A. Meyer,[38] P. Millet,[38] S. Mukherjee,[38] T. Pook,[38] M. Radziej,[38] H. Reithler,[38] M. Rieger,[38] F. Scheuch,[38] D. Teyssier,[38] S. Thüer,[38] G. Flügge,[39] B. Kargoll,[39] T. Kress,[39] A. Künsken,[39] T. Müller,[39] A. Nehrkorn,[39] A. Nowack,[39] C. Pistone,[39] O. Pooth,[39] A. Stahl,[39,q] M. Aldaya Martin,[40] T. Arndt,[40] C. Asawatangtrakuldee,[40] K. Beernaert,[40] O. Behnke,[40] U. Behrens,[40] A. Bermúdez Martínez,[40] A. A. Bin Anuar,[40] K. Borras,[40,r] V. Botta,[40] A. Campbell,[40] P. Connor,[40] C. Contreras-Campana,[40] F. Costanza,[40] C. Diez Pardos,[40] G. Eckerlin,[40] D. Eckstein,[40] T. Eichhorn,[40] E. Eren,[40] E. Gallo,[40,s] J. Garay Garcia,[40] A. Geiser,[40] J. M. Grados Luyando,[40] A. Grohsjean,[40] P. Gunnellini,[40] M. Guthoff,[40] A. Harb,[40] J. Hauk,[40] M. Hempel,[40,t] H. Jung,[40] M. Kasemann,[40] J. Keaveney,[40] C. Kleinwort,[40] I. Korol,[40] D. Krücker,[40] W. Lange,[40] A. Lelek,[40] T. Lenz,[40] J. Leonard,[40] K. Lipka,[40] W. Lohmann,[40,t] R. Mankel,[40] I.-A. Melzer-Pellmann,[40] A. B. Meyer,[40] M. Missiroli,[40] G. Mittag,[40] J. Mnich,[40] A. Mussgiller,[40] E. Ntomari,[40] D. Pitzl,[40] A. Raspereza,[40] M. Savitskyi,[40] P. Saxena,[40] R. Shevchenko,[40] N. Stefaniuk,[40] G. P. Van Onsem,[40] R. Walsh,[40] Y. Wen,[40] K. Wichmann,[40] C. Wissing,[40] O. Zenaiev,[40] R. Aggleton,[41] S. Bein,[41] V. Blobel,[41] M. Centis Vignali,[41] T. Dreyer,[41] E. Garutti,[41] D. Gonzalez,[41] J. Haller,[41] A. Hinzmann,[41] M. Hoffmann,[41] A. Karavdina,[41] R. Klanner,[41] R. Kogler,[41] N. Kovalchuk,[41] S. Kurz,[41] T. Lapsien,[41] D. Marconi,[41] M. Meyer,[41] M. Niedziela,[41] D. Nowatschin,[41] F. Pantaleo,[41,q] T. Peiffer,[41] A. Perieanu,[41] C. Scharf,[41] P. Schleper,[41] A. Schmidt,[41] S. Schumann,[41] J. Schwandt,[41] J. Sonneveld,[41] H. Stadie,[41] G. Steinbrück,[41] F. M. Stober,[41] M. Stöver,[41] H. Tholen,[41] D. Troendle,[41] E. Usai,[41] A. Vanhoefer,[41] B. Vormwald,[41] M. Akbiyik,[42] C. Barth,[42] M. Baselga,[42] S. Baur,[42] E. Butz,[42] R. Caspart,[42] T. Chwalek,[42] F. Colombo,[42] W. De Boer,[42] A. Dierlamm,[42] N. Faltermann,[42] B. Freund,[42] R. Friese,[42] M. Giffels,[42] M. A. Harrendorf,[42] F. Hartmann,[42,q] S. M. Heindl,[42] U. Husemann,[42] F. Kassel,[42,q] S. Kudella,[42] H. Mildner,[42] M. U. Mozer,[42] Th. Müller,[42] M. Plagge,[42] G. Quast,[42] K. Rabbertz,[42] M. Schröder,[42] I. Shvetsov,[42] G. Sieber,[42] H. J. Simonis,[42] R. Ulrich,[42] S. Wayand,[42] M. Weber,[42] T. Weiler,[42] S. Williamson,[42] C. Wöhrmann,[42] R. Wolf,[42] G. Anagnostou,[43] G. Daskalakis,[43] T. Geralis,[43] A. Kyriakis,[43] D. Loukas,[43] I. Topsis-Giotis,[43] G. Karathanasis,[44] S. Kesisoglou,[44] A. Panagiotou,[44] N. Saoulidou,[44] K. Kousouris,[45] I. Evangelou,[46] C. Foudas,[46] P. Gianneios,[46] P. Katsoulis,[46] P. Kokkas,[46] S. Mallios,[46] N. Manthos,[46] I. Papadopoulos,[46] E. Paradas,[46] J. Strologas,[46] F. A. Triantis,[46] D. Tsitsonis,[46] M. Csanad,[47] N. Filipovic,[47] G. Pasztor,[47] O. Surányi,[47] G. I. Veres,[47,u] G. Bencze,[48] C. Hajdu,[48] D. Horvath,[48,v] Á. Hunyadi,[48] F. Sikler,[48] V. Veszpremi,[48] G. Vesztergombi,[48,u] N. Beni,[49] S. Czellar,[49] J. Karancsi,[49,w] A. Makovec,[49] J. Molnar,[49] Z. Szillasi,[49] M. Bartók,[50,u] P. Raics,[50] Z. L. Trocsanyi,[50] B. Ujvari,[50] S. Choudhury,[51] J. R. Komaragiri,[51] S. Bahinipati,[52,x] P. Mal,[52] K. Mandal,[52] A. Nayak,[52,y] D. K. Sahoo,[52,x] N. Sahoo,[52] S. K. Swain,[52] S. Bansal,[53] S. B. Beri,[53] V. Bhatnagar,[53] R. Chawla,[53] N. Dhingra,[53] A. Kaur,[53] M. Kaur,[53] S. Kaur,[53] R. Kumar,[53] P. Kumari,[53] A. Mehta,[53] J. B. Singh,[53] G. Walia,[53] Ashok Kumar,[54] Aashaq Shah,[54] A. Bhardwaj,[54] S. Chauhan,[54] B. C. Choudhary,[54] R. B. Garg,[54] S. Keshri,[54] A. Kumar,[54] S. Malhotra,[54] M. Naimuddin,[54] K. Ranjan,[54] R. Sharma,[54] R. Bhardwaj,[55] R. Bhattacharya,[55] S. Bhattacharya,[55] U. Bhawandeep,[55] S. Dey,[55] S. Dutt,[55] S. Dutta,[55] S. Ghosh,[55] N. Majumdar,[55] A. Modak,[55] K. Mondal,[55] S. Mukhopadhyay,[55] S. Nandan,[55] A. Purohit,[55] A. Roy,[55] S. Roy Chowdhury,[55] S. Sarkar,[55] M. Sharan,[55] S. Thakur,[55] P. K. Behera,[56] R. Chudasama,[57] D. Dutta,[57] V. Jha,[57] V. Kumar,[57] A. K. Mohanty,[57,q] P. K. Netrakanti,[57] L. M. Pant,[57] P. Shukla,[57] A. Topkar,[57] T. Aziz,[58] S. Dugad,[58] B. Mahakud,[58] S. Mitra,[58] G. B. Mohanty,[58] N. Sur,[58] B. Sutar,[58] S. Banerjee,[59] S. Bhattacharya,[59] S. Chatterjee,[59] P. Das,[59] M. Guchait,[59] Sa. Jain,[59] S. Kumar,[59] M. Maity,[59,z] G. Majumder,[59] K. Mazumdar,[59] T. Sarkar,[59,z] N. Wickramage,[59,aa] S. Chauhan,[60] S. Dube,[60] V. Hegde,[60] A. Kapoor,[60] K. Kothekar,[60] S. Pandey,[60] A. Rane,[60] S. Sharma,[60] S. Chenarani,[61,bb] E. Eskandari Tadavani,[61] S. M. Etesami,[61,bb] M. Khakzad,[61] M. Mohammadi Najafabadi,[61] M. Naseri,[61] S. Paktinat Mehdiabadi,[61,cc] F. Rezaei Hosseinabadi,[61] B. Safarzadeh,[61,dd] M. Zeinali,[61] M. Felcini,[62] M. Grunewald,[62] M. Abbrescia,[63a,63b] C. Calabria,[63a,63b] A. Colaleo,[63a] D. Creanza,[63a,63c] L. Cristella,[63a,63b] N. De Filippis,[63a,63c] M. De Palma,[63a,63b] F. Errico,[63a,63b] L. Fiore,[63a] G. Iaselli,[63a,63c] S. Lezki,[63a,63b] G. Maggi,[63a,63c] M. Maggi,[63a] G. Miniello,[63a,63b] S. My,[63a,63b] S. Nuzzo,[63a,63b] A. Pompili,[63a,63b] G. Pugliese,[63a,63c] R. Radogna,[63a] A. Ranieri,[63a] G. Selvaggi,[63a,63b] A. Sharma,[63a] L. Silvestris,[63a,q] R. Venditti,[63a] P. Verwilligen,[63a] G. Abbiendi,[64a] C. Battilana,[64a,64b] D. Bonacorsi,[64a,64b] L. Borgonovi,[64a,64b] S. Braibant-Giacomelli,[64a,64b] R. Campanini,[64a,64b] P. Capiluppi,[64a,64b] A. Castro,[64a,64b] F. R. Cavallo,[64a] S. S. Chhibra,[64a,64b] G. Codispoti,[64a,64b] M. Cuffiani,[64a,64b] G. M. Dallavalle,[64a] F. Fabbri,[64a] A. Fanfani,[64a,64b] D. Fasanella,[64a,64b] P. Giacomelli,[64a] C. Grandi,[64a] L. Guiducci,[64a,64b] S. Marcellini,[64a] G. Masetti,[64a] A. Montanari,[64a] F. L. Navarria,[64a,64b] A. Perrotta,[64a] A. M. Rossi,[64a,64b] T. Rovelli,[64a,64b] G. P. Siroli,[64a,64b] N. Tosi,[64a] S. Albergo,[65a,65b] S. Costa,[65a,65b] A. Di Mattia,[65a] F. Giordano,[65a,65b] R. Potenza,[65a,65b] A. Tricomi,[65a,65b] C. Tuve,[65a,65b] G. Barbagli,[66a] K. Chatterjee,[66a,66b] V. Ciulli,[66a,66b] C. Civinini,[66a] R. D'Alessandro,[66a,66b] E. Focardi,[66a,66b] P. Lenzi,[66a,66b] M. Meschini,[66a] S. Paoletti,[66a] L. Russo,[66a,ee] G. Sguazzoni,[66a] D. Strom,[66a] L. Viliani,[66a] L. Benussi,[67] S. Bianco,[67]

F. Fabbri,[67] D. Piccolo,[67] F. Primavera,[67,q] V. Calvelli,[68a,68b] F. Ferro,[68a] F. Ravera,[68a,68b] E. Robutti,[68a] S. Tosi,[68a,68b] A. Benaglia,[69a] A. Beschi,[69b] L. Brianza,[69a,69b] F. Brivio,[69a,69b] V. Ciriolo,[69a,69b,q] M. E. Dinardo,[69a,69b] S. Fiorendi,[69a,69b] S. Gennai,[69a] A. Ghezzi,[69a,69b] P. Govoni,[69a,69b] M. Malberti,[69a,69b] S. Malvezzi,[69a] R. A. Manzoni,[69a,69b] D. Menasce,[69a] L. Moroni,[69a] M. Paganoni,[69a,69b] K. Pauwels,[69a,69b] D. Pedrini,[69a] S. Pigazzini,[69a,69b,ff] S. Ragazzi,[69a,69b] T. Tabarelli de Fatis,[69a,69b] S. Buontempo,[70a] N. Cavallo,[70a,70c] S. Di Guida,[70a,70d,q] F. Fabozzi,[70a,70c] F. Fienga,[70a,70b] A. O. M. Iorio,[70a,70b] W. A. Khan,[70a] L. Lista,[70a] S. Meola,[70a,70d,q] P. Paolucci,[70a,q] C. Sciacca,[70a,70b] F. Thyssen,[70a] P. Azzi,[71a] N. Bacchetta,[71a] L. Benato,[71a,71b] D. Bisello,[71a,71b] A. Boletti,[71a,71b] R. Carlin,[71a,71b] A. Carvalho Antunes De Oliveira,[71a,71b] P. Checchia,[71a] M. Dall'Osso,[71a,71b] P. De Castro Manzano,[71a] T. Dorigo,[71a] U. Dosselli,[71a] F. Fanzago,[71a] F. Gasparini,[71a,71b] A. Gozzelino,[71a] S. Lacaprara,[71a] P. Lujan,[71a] M. Margoni,[71a,71b] N. Pozzobon,[71a,71b] P. Ronchese,[71a,71b] R. Rossin,[71a,71b] F. Simonetto,[71a,71b] E. Torassa,[71a] M. Zanetti,[71a,71b] P. Zotto,[71a,71b] G. Zumerle,[71a,71b] A. Braghieri,[72a] A. Magnani,[72a] P. Montagna,[72a,72b] S. P. Ratti,[72a,72b] V. Re,[72a] M. Ressegotti,[72a,72b] C. Riccardi,[72a,72b] P. Salvini,[72a] I. Vai,[72a,72b] P. Vitulo,[72a,72b] L. Alunni Solestizi,[73a,73b] M. Biasini,[73a,73b] G. M. Bilei,[73a] C. Cecchi,[73a,73b] D. Ciangottini,[73a,73b] L. Fanò,[73a,73b] P. Lariccia,[73a,73b] R. Leonardi,[73a,73b] E. Manoni,[73a] G. Mantovani,[73a,73b] V. Mariani,[73a,73b] M. Menichelli,[73a] A. Rossi,[73a,73b] A. Santocchia,[73a,73b] D. Spiga,[73a] K. Androsov,[74a] P. Azzurri,[74a,q] G. Bagliesi,[74a] T. Boccali,[74a] L. Borrello,[74a] R. Castaldi,[74a] M. A. Ciocci,[74a,74b] R. Dell'Orso,[74a] G. Fedi,[74a] L. Giannini,[74a,74c] A. Giassi,[74a] M. T. Grippo,[74a,ee] F. Ligabue,[74a,74c] T. Lomtadze,[74a] E. Manca,[74a,74c] G. Mandorli,[74a,74c] A. Messineo,[74a,74b] F. Palla,[74a] A. Rizzi,[74a,74b] A. Savoy-Navarro,[74a,gg] P. Spagnolo,[74a] R. Tenchini,[74a] G. Tonelli,[74a,74b] A. Venturi,[74a] P. G. Verdini,[74a] L. Barone,[75a,75b] F. Cavallari,[75a] M. Cipriani,[75a,75b] N. Daci,[75a] D. Del Re,[75a,75b] E. Di Marco,[75a,75b] M. Diemoz,[75a] S. Gelli,[75a,75b] E. Longo,[75a,75b] F. Margaroli,[75a,75b] B. Marzocchi,[75a,75b] P. Meridiani,[75a] G. Organtini,[75a,75b] R. Paramatti,[75a,75b] F. Preiato,[75a,75b] S. Rahatlou,[75a,75b] C. Rovelli,[75a] F. Santanastasio,[75a,75b] N. Amapane,[76a,76b] R. Arcidiacono,[76a,76c] S. Argiro,[76a,76b] M. Arneodo,[76a,76c] N. Bartosik,[76a] R. Bellan,[76a,76b] C. Biino,[76a] N. Cartiglia,[76a] F. Cenna,[76a,76b] M. Costa,[76a,76b] R. Covarelli,[76a,76b] A. Degano,[76a,76b] N. Demaria,[76a] B. Kiani,[76a,76b] C. Mariotti,[76a] S. Maselli,[76a] E. Migliore,[76a,76b] V. Monaco,[76a,76b] E. Monteil,[76a,76b] M. Monteno,[76a] M. M. Obertino,[76a,76b] L. Pacher,[76a,76b] N. Pastrone,[76a] M. Pelliccioni,[76a] G. L. Pinna Angioni,[76a,76b] A. Romero,[76a,76b] M. Ruspa,[76a,76c] R. Sacchi,[76a,76b] K. Shchelina,[76a,76b] V. Sola,[76a] A. Solano,[76a,76b] A. Staiano,[76a] P. Traczyk,[76a,76b] S. Belforte,[77a] M. Casarsa,[77a] F. Cossutti,[77a] G. Della Ricca,[77a,77b] A. Zanetti,[77a] D. H. Kim,[78] G. N. Kim,[78] M. S. Kim,[78] J. Lee,[78] S. Lee,[78] S. W. Lee,[78] C. S. Moon,[78] Y. D. Oh,[78] S. Sekmen,[78] D. C. Son,[78] Y. C. Yang,[78] H. Kim,[79] D. H. Moon,[79] G. Oh,[79] J. A. Brochero Cifuentes,[80] J. Goh,[80] T. J. Kim,[80] S. Cho,[81] S. Choi,[81] Y. Go,[81] D. Gyun,[81] S. Ha,[81] B. Hong,[81] Y. Jo,[81] Y. Kim,[81] K. Lee,[81] K. S. Lee,[81] S. Lee,[81] J. Lim,[81] S. K. Park,[81] Y. Roh,[81] J. Almond,[82] J. Kim,[82] J. S. Kim,[82] H. Lee,[82] K. Lee,[82] K. Nam,[82] S. B. Oh,[82] B. C. Radburn-Smith,[82] S. h. Seo,[82] U. K. Yang,[82] H. D. Yoo,[82] G. B. Yu,[82] H. Kim,[83] J. H. Kim,[83] J. S. H. Lee,[83] I. C. Park,[83] Y. Choi,[84] C. Hwang,[84] J. Lee,[84] I. Yu,[84] V. Dudenas,[85] A. Juodagalvis,[85] J. Vaitkus,[85] I. Ahmed,[86] Z. A. Ibrahim,[86] M. A. B. Md Ali,[86,hh] F. Mohamad Idris,[86,ii] W. A. T. Wan Abdullah,[86] M. N. Yusli,[86] Z. Zolkapli,[86] R Reyes-Almanza,[87] G. Ramirez-Sanchez,[87] M. C. Duran-Osuna,[87] H. Castilla-Valdez,[87] E. De La Cruz-Burelo,[87] I. Heredia-De La Cruz,[87,jj] R. I. Rabadan-Trejo,[87] R. Lopez-Fernandez,[87] J. Mejia Guisao,[87] A. Sanchez-Hernandez,[87] S. Carrillo Moreno,[88] C. Oropeza Barrera,[88] F. Vazquez Valencia,[88] J. Eysermans,[89] I. Pedraza,[89] H. A. Salazar Ibarguen,[89] C. Uribe Estrada,[89] A. Morelos Pineda,[90] D. Krofcheck,[91] P. H. Butler,[92] A. Ahmad,[93] M. Ahmad,[93] Q. Hassan,[93] H. R. Hoorani,[93] A. Saddique,[93] M. A. Shah,[93] M. Shoaib,[93] M. Waqas,[93] H. Bialkowska,[94] M. Bluj,[94] B. Boimska,[94] T. Frueboes,[94] M. Górski,[94] M. Kazana,[94] K. Nawrocki,[94] M. Szleper,[94] P. Zalewski,[94] K. Bunkowski,[95] A. Byszuk,[95,kk] K. Doroba,[95] A. Kalinowski,[95] M. Konecki,[95] J. Krolikowski,[95] M. Misiura,[95] M. Olszewski,[95] A. Pyskir,[95] M. Walczak,[95] P. Bargassa,[96] C. Beirão Da Cruz E Silva,[96] A. Di Francesco,[96] P. Faccioli,[96] B. Galinhas,[96] M. Gallinaro,[96] J. Hollar,[96] N. Leonardo,[96] L. Lloret Iglesias,[96] M. V. Nemallapudi,[96] J. Seixas,[96] G. Strong,[96] O. Toldaiev,[96] D. Vadruccio,[96] J. Varela,[96] I. Golutvin,[97] V. Karjavin,[97] I. Kashunin,[97] V. Korenkov,[97] G. Kozlov,[97] A. Lanev,[97] A. Malakhov,[97] V. Matveev,[97,ll,mm] V. V. Mitsyn,[97] P. Moisenz,[97] V. Palichik,[97] V. Perelygin,[97] S. Shmatov,[97] N. Skatchkov,[97] V. Smirnov,[97] V. Trofimov,[97] B. S. Yuldashev,[97,nn] A. Zarubin,[97] V. Zhiltsov,[97] Y. Ivanov,[98] V. Kim,[98,oo] E. Kuznetsova,[98,pp] P. Levchenko,[98] V. Murzin,[98] V. Oreshkin,[98] I. Smirnov,[98] D. Sosnov,[98] V. Sulimov,[98] L. Uvarov,[98] S. Vavilov,[98] A. Vorobyev,[98] Yu. Andreev,[99] A. Dermenev,[99] S. Gninenko,[99] N. Golubev,[99] A. Karneyeu,[99] M. Kirsanov,[99] N. Krasnikov,[99] A. Pashenkov,[99] D. Tlisov,[99] A. Toropin,[99] V. Epshteyn,[100] V. Gavrilov,[100] N. Lychkovskaya,[100] V. Popov,[100] I. Pozdnyakov,[100] G. Safronov,[100] A. Spiridonov,[100] A. Stepennov,[100] V. Stolin,[100] M. Toms,[100] E. Vlasov,[100] A. Zhokin,[100] T. Aushev,[101] A. Bylinkin,[101,mm] R. Chistov,[102,qq] M. Danilov,[102,qq] P. Parygin,[102] D. Philippov,[102] S. Polikarpov,[102] E. Tarkovskii,[102] V. Andreev,[103] M. Azarkin,[103,mm] I. Dremin,[103,mm]

M. Kirakosyan,[103,mm] S. V. Rusakov,[103] A. Terkulov,[103] A. Baskakov,[104] A. Belyaev,[104] E. Boos,[104] M. Dubinin,[104,rr] L. Dudko,[104] A. Ershov,[104] A. Gribushin,[104] V. Klyukhin,[104] O. Kodolova,[104] I. Lokhtin,[104] I. Miagkov,[104] S. Obraztsov,[104] S. Petrushanko,[104] V. Savrin,[104] A. Snigirev,[104] V. Blinov,[105,ss] D. Shtol,[105,ss] Y. Skovpen,[105,ss] I. Azhgirey,[106] I. Bayshev,[106] S. Bitioukov,[106] D. Elumakhov,[106] A. Godizov,[106] V. Kachanov,[106] A. Kalinin,[106] D. Konstantinov,[106] P. Mandrik,[106] V. Petrov,[106] R. Ryutin,[106] A. Sobol,[106] S. Troshin,[106] N. Tyurin,[106] A. Uzunian,[106] A. Volkov,[106] P. Adzic,[107,tt] P. Cirkovic,[107] D. Devetak,[107] M. Dordevic,[107] J. Milosevic,[107] V. Rekovic,[107] J. Alcaraz Maestre,[108] I. Bachiller,[108] M. Barrio Luna,[108] M. Cerrada,[108] N. Colino,[108] B. De La Cruz,[108] A. Delgado Peris,[108] C. Fernandez Bedoya,[108] J. P. Fernández Ramos,[108] J. Flix,[108] M. C. Fouz,[108] O. Gonzalez Lopez,[108] S. Goy Lopez,[108] J. M. Hernandez,[108] M. I. Josa,[108] D. Moran,[108] A. Pérez-Calero Yzquierdo,[108] J. Puerta Pelayo,[108] I. Redondo,[108] L. Romero,[108] M. S. Soares,[108] A. Triossi,[108] A. Álvarez Fernández,[108] C. Albajar,[109] J. F. de Trocóniz,[109] J. Cuevas,[110] C. Erice,[110] J. Fernandez Menendez,[110] I. Gonzalez Caballero,[110] J. R. González Fernández,[110] E. Palencia Cortezon,[110] S. Sanchez Cruz,[110] P. Vischia,[110] J. M. Vizan Garcia,[110] I. J. Cabrillo,[111] A. Calderon,[111] B. Chazin Quero,[111] E. Curras,[111] J. Duarte Campderros,[111] M. Fernandez,[111] J. Garcia-Ferrero,[111] G. Gomez,[111] A. Lopez Virto,[111] J. Marco,[111] C. Martinez Rivero,[111] P. Martinez Ruiz del Arbol,[111] F. Matorras,[111] J. Piedra Gomez,[111] T. Rodrigo,[111] A. Ruiz-Jimeno,[111] L. Scodellaro,[111] N. Trevisani,[111] I. Vila,[111] R. Vilar Cortabitarte,[111] D. Abbaneo,[112] B. Akgun,[112] E. Auffray,[112] P. Baillon,[112] A. H. Ball,[112] D. Barney,[112] J. Bendavid,[112] M. Bianco,[112] P. Bloch,[112] A. Bocci,[112] C. Botta,[112] T. Camporesi,[112] R. Castello,[112] M. Cepeda,[112] G. Cerminara,[112] E. Chapon,[112] Y. Chen,[112] D. d'Enterria,[112] A. Dabrowski,[112] V. Daponte,[112] A. David,[112] M. De Gruttola,[112] A. De Roeck,[112] N. Deelen,[112] M. Dobson,[112] T. du Pree,[112] M. Dünser,[112] N. Dupont,[112] A. Elliott-Peisert,[112] P. Everaerts,[112] F. Fallavollita,[112] G. Franzoni,[112] J. Fulcher,[112] W. Funk,[112] D. Gigi,[112] A. Gilbert,[112] K. Gill,[112] F. Glege,[112] D. Gulhan,[112] P. Harris,[112] J. Hegeman,[112] V. Innocente,[112] A. Jafari,[112] P. Janot,[112] O. Karacheban,[112,t] J. Kieseler,[112] V. Knünz,[112] A. Kornmayer,[112] M. J. Kortelainen,[112] M. Krammer,[112,b] C. Lange,[112] P. Lecoq,[112] C. Lourenço,[112] M. T. Lucchini,[112] L. Malgeri,[112] M. Mannelli,[112] A. Martelli,[112] F. Meijers,[112] J. A. Merlin,[112] S. Mersi,[112] E. Meschi,[112] P. Milenovic,[112,uu] F. Moortgat,[112] M. Mulders,[112] H. Neugebauer,[112] J. Ngadiuba,[112] S. Orfanelli,[112] L. Orsini,[112] L. Pape,[112] E. Perez,[112] M. Peruzzi,[112] A. Petrilli,[112] G. Petrucciani,[112] A. Pfeiffer,[112] M. Pierini,[112] D. Rabady,[112] A. Racz,[112] T. Reis,[112] G. Rolandi,[112,vv] M. Rovere,[112] H. Sakulin,[112] C. Schäfer,[112] C. Schwick,[112] M. Seidel,[112] M. Selvaggi,[112] A. Sharma,[112] P. Silva,[112] P. Sphicas,[112,ww] A. Stakia,[112] J. Steggemann,[112] M. Stoye,[112] M. Tosi,[112] D. Treille,[112] A. Tsirou,[112] V. Veckalns,[112,xx] M. Verweij,[112] W. D. Zeuner,[112] W. Bertl,[113,a] L. Caminada,[113,yy] K. Deiters,[113] W. Erdmann,[113] R. Horisberger,[113] Q. Ingram,[113] H. C. Kaestli,[113] D. Kotlinski,[113] U. Langenegger,[113] T. Rohe,[113] S. A. Wiederkehr,[113] M. Backhaus,[114] L. Bäni,[114] P. Berger,[114] L. Bianchini,[114] B. Casal,[114] G. Dissertori,[114] M. Dittmar,[114] M. Donegà,[114] C. Dorfer,[114] C. Grab,[114] C. Heidegger,[114] D. Hits,[114] J. Hoss,[114] G. Kasieczka,[114] T. Klijnsma,[114] W. Lustermann,[114] B. Mangano,[114] M. Marionneau,[114] M. T. Meinhard,[114] D. Meister,[114] F. Micheli,[114] P. Musella,[114] F. Nessi-Tedaldi,[114] F. Pandolfi,[114] J. Pata,[114] F. Pauss,[114] G. Perrin,[114] L. Perrozzi,[114] M. Quittnat,[114] M. Reichmann,[114] D. A. Sanz Becerra,[114] M. Schönenberger,[114] L. Shchutska,[114] V. R. Tavolaro,[114] K. Theofilatos,[114] M. L. Vesterbacka Olsson,[114] R. Wallny,[114] D. H. Zhu,[114] T. K. Aarrestad,[115] C. Amsler,[115,zz] M. F. Canelli,[115] A. De Cosa,[115] R. Del Burgo,[115] S. Donato,[115] C. Galloni,[115] T. Hreus,[115] B. Kilminster,[115] D. Pinna,[115] G. Rauco,[115] P. Robmann,[115] D. Salerno,[115] K. Schweiger,[115] C. Seitz,[115] Y. Takahashi,[115] A. Zucchetta,[115] V. Candelise,[116] Y. H. Chang,[116] K. y. Cheng,[116] T. H. Doan,[116] Sh. Jain,[116] R. Khurana,[116] C. M. Kuo,[116] W. Lin,[116] A. Pozdnyakov,[116] S. S. Yu,[116] Arun Kumar,[117] P. Chang,[117] Y. Chao,[117] K. F. Chen,[117] P. H. Chen,[117] F. Fiori,[117] W.-S. Hou,[117] Y. Hsiung,[117] Y. F. Liu,[117] R.-S. Lu,[117] E. Paganis,[117] A. Psallidas,[117] A. Steen,[117] J. f. Tsai,[117] B. Asavapibhop,[118] K. Kovitanggoon,[118] G. Singh,[118] N. Srimanobhas,[118] M. N. Bakirci,[119,aaa] A. Bat,[119] F. Boran,[119] S. Damarseckin,[119] Z. S. Demiroglu,[119] C. Dozen,[119] E. Eskut,[119] S. Girgis,[119] G. Gokbulut,[119] Y. Guler,[119] I. Hos,[119,bbb] E. E. Kangal,[119,ccc] O. Kara,[119] U. Kiminsu,[119] M. Oglakci,[119] G. Onengut,[119,ddd] K. Ozdemir,[119,eee] A. Polatoz,[119] B. Tali,[119,fff] U. G. Tok,[119] H. Topakli,[119,aaa] S. Turkcapar,[119] I. S. Zorbakir,[119] C. Zorbilmez,[119] G. Karapinar,[120,ggg] K. Ocalan,[120,hhh] M. Yalvac,[120] M. Zeyrek,[120] E. Gülmez,[121] M. Kaya,[121,iii] O. Kaya,[121,jjj] S. Tekten,[121] E. A. Yetkin,[121,kkk] M. N. Agaras,[122] S. Atay,[122] A. Cakir,[122] K. Cankocak,[122] Y. Komurcu,[122] B. Grynyov,[123] L. Levchuk,[124] F. Ball,[125] L. Beck,[125] J. J. Brooke,[125] D. Burns,[125] E. Clement,[125] D. Cussans,[125] O. Davignon,[125] H. Flacher,[125] J. Goldstein,[125] G. P. Heath,[125] H. F. Heath,[125] L. Kreczko,[125] D. M. Newbold,[125,lll] S. Paramesvaran,[125] T. Sakuma,[125] S. Seif El Nasr-storey,[125] D. Smith,[125] V. J. Smith,[125] K. W. Bell,[126] A. Belyaev,[126,mmm] C. Brew,[126] R. M. Brown,[126] L. Calligaris,[126] D. Cieri,[126] D. J. A. Cockerill,[126] J. A. Coughlan,[126] K. Harder,[126] S. Harper,[126] J. Linacre,[126] E. Olaiya,[126] D. Petyt,[126] C. H. Shepherd-Themistocleous,[126]

A. Thea,[126] I. R. Tomalin,[126] T. Williams,[126] W. J. Womersley,[126] G. Auzinger,[127] R. Bainbridge,[127] J. Borg,[127] S. Breeze,[127] O. Buchmuller,[127] A. Bundock,[127] S. Casasso,[127] M. Citron,[127] D. Colling,[127] L. Corpe,[127] P. Dauncey,[127] G. Davies,[127] A. De Wit,[127] M. Della Negra,[127] R. Di Maria,[127] A. Elwood,[127] Y. Haddad,[127] G. Hall,[127] G. Iles,[127] T. James,[127] R. Lane,[127] C. Laner,[127] L. Lyons,[127] A.-M. Magnan,[127] S. Malik,[127] L. Mastrolorenzo,[127] T. Matsushita,[127] J. Nash,[127] A. Nikitenko,[127,g] V. Palladino,[127] M. Pesaresi,[127] D. M. Raymond,[127] A. Richards,[127] A. Rose,[127] E. Scott,[127] C. Seez,[127] A. Shtipliyski,[127] S. Summers,[127] A. Tapper,[127] K. Uchida,[127] M. Vazquez Acosta,[127,nnn] T. Virdee,[127,q] N. Wardle,[127] D. Winterbottom,[127] J. Wright,[127] S. C. Zenz,[127] J. E. Cole,[128] P. R. Hobson,[128] A. Khan,[128] P. Kyberd,[128] I. D. Reid,[128] L. Teodorescu,[128] S. Zahid,[128] A. Borzou,[129] K. Call,[129] J. Dittmann,[129] K. Hatakeyama,[129] H. Liu,[129] N. Pastika,[129] C. Smith,[129] R. Bartek,[130] A. Dominguez,[130] A. Buccilli,[131] S. I. Cooper,[131] C. Henderson,[131] P. Rumerio,[131] C. West,[131] D. Arcaro,[132] A. Avetisyan,[132] T. Bose,[132] D. Gastler,[132] D. Rankin,[132] C. Richardson,[132] J. Rohlf,[132] L. Sulak,[132] D. Zou,[132] G. Benelli,[133] D. Cutts,[133] M. Hadley,[133] J. Hakala,[133] U. Heintz,[133] J. M. Hogan,[133] K. H. M. Kwok,[133] E. Laird,[133] G. Landsberg,[133] J. Lee,[133] Z. Mao,[133] M. Narain,[133] J. Pazzini,[133] S. Piperov,[133] S. Sagir,[133] R. Syarif,[133] D. Yu,[133] R. Band,[134] C. Brainerd,[134] R. Breedon,[134] D. Burns,[134] M. Calderon De La Barca Sanchez,[134] M. Chertok,[134] J. Conway,[134] R. Conway,[134] P. T. Cox,[134] R. Erbacher,[134] C. Flores,[134] G. Funk,[134] W. Ko,[134] R. Lander,[134] C. Mclean,[134] M. Mulhearn,[134] D. Pellett,[134] J. Pilot,[134] S. Shalhout,[134] M. Shi,[134] J. Smith,[134] D. Stolp,[134] K. Tos,[134] M. Tripathi,[134] Z. Wang,[134] M. Bachtis,[135] C. Bravo,[135] R. Cousins,[135] A. Dasgupta,[135] A. Florent,[135] J. Hauser,[135] M. Ignatenko,[135] N. Mccoll,[135] S. Regnard,[135] D. Saltzberg,[135] C. Schnaible,[135] V. Valuev,[135] E. Bouvier,[136] K. Burt,[136] R. Clare,[136] J. Ellison,[136] J. W. Gary,[136] S. M. A. Ghiasi Shirazi,[136] G. Hanson,[136] J. Heilman,[136] G. Karapostoli,[136] E. Kennedy,[136] F. Lacroix,[136] O. R. Long,[136] M. Olmedo Negrete,[136] M. I. Paneva,[136] W. Si,[136] L. Wang,[136] H. Wei,[136] S. Wimpenny,[136] B. R. Yates,[136] J. G. Branson,[137] S. Cittolin,[137] M. Derdzinski,[137] R. Gerosa,[137] D. Gilbert,[137] B. Hashemi,[137] A. Holzner,[137] D. Klein,[137] G. Kole,[137] V. Krutelyov,[137] J. Letts,[137] M. Masciovecchio,[137] D. Olivito,[137] S. Padhi,[137] M. Pieri,[137] M. Sani,[137] V. Sharma,[137] S. Simon,[137] M. Tadel,[137] A. Vartak,[137] S. Wasserbaech,[137,ooo] J. Wood,[137] F. Würthwein,[137] A. Yagil,[137] G. Zevi Della Porta,[137] N. Amin,[138] R. Bhandari,[138] J. Bradmiller-Feld,[138] C. Campagnari,[138] A. Dishaw,[138] V. Dutta,[138] M. Franco Sevilla,[138] L. Gouskos,[138] R. Heller,[138] J. Incandela,[138] A. Ovcharova,[138] H. Qu,[138] J. Richman,[138] D. Stuart,[138] I. Suarez,[138] J. Yoo,[138] D. Anderson,[139] A. Bornheim,[139] J. Bunn,[139] J. M. Lawhorn,[139] H. B. Newman,[139] T. Q. Nguyen,[139] C. Pena,[139] M. Spiropulu,[139] J. R. Vlimant,[139] R. Wilkinson,[139] S. Xie,[139] Z. Zhang,[139] R. Y. Zhu,[139] M. B. Andrews,[140] T. Ferguson,[140] T. Mudholkar,[140] M. Paulini,[140] J. Russ,[140] M. Sun,[140] H. Vogel,[140] I. Vorobiev,[140] M. Weinberg,[140] J. P. Cumalat,[141] W. T. Ford,[141] F. Jensen,[141] A. Johnson,[141] M. Krohn,[141] S. Leontsinis,[141] T. Mulholland,[141] K. Stenson,[141] K. A. Ulmer,[141] S. R. Wagner,[141] J. Alexander,[142] J. Chaves,[142] J. Chu,[142] S. Dittmer,[142] K. Mcdermott,[142] N. Mirman,[142] J. R. Patterson,[142] D. Quach,[142] A. Rinkevicius,[142] A. Ryd,[142] L. Skinnari,[142] L. Soffi,[142] S. M. Tan,[142] Z. Tao,[142] J. Thom,[142] J. Tucker,[142] P. Wittich,[142] M. Zientek,[142] S. Abdullin,[143] M. Albrow,[143] M. Alyari,[143] G. Apollinari,[143] A. Apresyan,[143] A. Apyan,[143] S. Banerjee,[143] L. A. T. Bauerdick,[143] A. Beretvas,[143] J. Berryhill,[143] P. C. Bhat,[143] G. Bolla,[143,a] K. Burkett,[143] J. N. Butler,[143] A. Canepa,[143] G. B. Cerati,[143] H. W. K. Cheung,[143] F. Chlebana,[143] M. Cremonesi,[143] J. Duarte,[143] V. D. Elvira,[143] J. Freeman,[143] Z. Gecse,[143] E. Gottschalk,[143] L. Gray,[143] D. Green,[143] S. Grünendahl,[143] O. Gutsche,[143] J. Hanlon,[143] R. M. Harris,[143] S. Hasegawa,[143] J. Hirschauer,[143] Z. Hu,[143] B. Jayatilaka,[143] S. Jindariani,[143] M. Johnson,[143] U. Joshi,[143] B. Klima,[143] B. Kreis,[143] S. Lammel,[143] D. Lincoln,[143] R. Lipton,[143] M. Liu,[143] T. Liu,[143] R. Lopes De Sá,[143] J. Lykken,[143] K. Maeshima,[143] N. Magini,[143] J. M. Marraffino,[143] D. Mason,[143] P. McBride,[143] P. Merkel,[143] S. Mrenna,[143] S. Nahn,[143] V. O'Dell,[143] K. Pedro,[143] O. Prokofyev,[143] G. Rakness,[143] L. Ristori,[143] B. Schneider,[143] E. Sexton-Kennedy,[143] A. Soha,[143] W. J. Spalding,[143] L. Spiegel,[143] S. Stoynev,[143] J. Strait,[143] N. Strobbe,[143] L. Taylor,[143] S. Tkaczyk,[143] N. V. Tran,[143] L. Uplegger,[143] E. W. Vaandering,[143] C. Vernieri,[143] M. Verzocchi,[143] R. Vidal,[143] M. Wang,[143] H. A. Weber,[143] A. Whitbeck,[143] W. Wu,[143] D. Acosta,[144] P. Avery,[144] P. Bortignon,[144] D. Bourilkov,[144] A. Brinkerhoff,[144] A. Carnes,[144] M. Carver,[144] D. Curry,[144] R. D. Field,[144] I. K. Furic,[144] S. V. Gleyzer,[144] B. M. Joshi,[144] J. Konigsberg,[144] A. Korytov,[144] K. Kotov,[144] P. Ma,[144] K. Matchev,[144] H. Mei,[144] G. Mitselmakher,[144] K. Shi,[144] D. Sperka,[144] N. Terentyev,[144] L. Thomas,[144] J. Wang,[144] S. Wang,[144] J. Yelton,[144] Y. R. Joshi,[145] S. Linn,[145] P. Markowitz,[145] J. L. Rodriguez,[145] A. Ackert,[146] T. Adams,[146] A. Askew,[146] S. Hagopian,[146] V. Hagopian,[146] K. F. Johnson,[146] T. Kolberg,[146] G. Martinez,[146] T. Perry,[146] H. Prosper,[146] A. Saha,[146] A. Santra,[146] V. Sharma,[146] R. Yohay,[146] M. M. Baarmand,[147] V. Bhopatkar,[147] S. Colafranceschi,[147] M. Hohlmann,[147] D. Noonan,[147] T. Roy,[147] F. Yumiceva,[147] M. R. Adams,[148] L. Apanasevich,[148] D. Berry,[148] R. R. Betts,[148] R. Cavanaugh,[148] X. Chen,[148] O. Evdokimov,[148] C. E. Gerber,[148] D. A. Hangal,[148] D. J. Hofman,[148] K. Jung,[148] J. Kamin,[148] I. D. Sandoval Gonzalez,[148] M. B. Tonjes,[148] H. Trauger,[148] N. Varelas,[148]

H. Wang,[148] Z. Wu,[148] J. Zhang,[148] B. Bilki,[149,ppp] W. Clarida,[149] K. Dilsiz,[149,qqq] S. Durgut,[149] R. P. Gandrajula,[149] M. Haytmyradov,[149] V. Khristenko,[149] J.-P. Merlo,[149] H. Mermerkaya,[149,rrr] A. Mestvirishvili,[149] A. Moeller,[149] J. Nachtman,[149] H. Ogul,[149,sss] Y. Onel,[149] F. Ozok,[149,ttt] A. Penzo,[149] C. Snyder,[149] E. Tiras,[149] J. Wetzel,[149] K. Yi,[149] B. Blumenfeld,[150] A. Cocoros,[150] N. Eminizer,[150] D. Fehling,[150] L. Feng,[150] A. V. Gritsan,[150] P. Maksimovic,[150] J. Roskes,[150] U. Sarica,[150] M. Swartz,[150] M. Xiao,[150] C. You,[150] A. Al-bataineh,[151] P. Baringer,[151] A. Bean,[151] S. Boren,[151] J. Bowen,[151] J. Castle,[151] S. Khalil,[151] A. Kropivnitskaya,[151] D. Majumder,[151] W. Mcbrayer,[151] M. Murray,[151] C. Rogan,[151] C. Royon,[151] S. Sanders,[151] E. Schmitz,[151] J. D. Tapia Takaki,[151] Q. Wang,[151] A. Ivanov,[152] K. Kaadze,[152] Y. Maravin,[152] A. Mohammadi,[152] L. K. Saini,[152] N. Skhirtladze,[152] F. Rebassoo,[153] D. Wright,[153] A. Baden,[154] O. Baron,[154] A. Belloni,[154] S. C. Eno,[154] Y. Feng,[154] C. Ferraioli,[154] N. J. Hadley,[154] S. Jabeen,[154] G. Y. Jeng,[154] R. G. Kellogg,[154] J. Kunkle,[154] A. C. Mignerey,[154] F. Ricci-Tam,[154] Y. H. Shin,[154] A. Skuja,[154] S. C. Tonwar,[154] D. Abercrombie,[155] B. Allen,[155] V. Azzolini,[155] R. Barbieri,[155] A. Baty,[155] G. Bauer,[155] R. Bi,[155] S. Brandt,[155] W. Busza,[155] I. A. Cali,[155] M. D'Alfonso,[155] Z. Demiragli,[155] G. Gomez Ceballos,[155] M. Goncharov,[155] D. Hsu,[155] M. Hu,[155] Y. Iiyama,[155] G. M. Innocenti,[155] M. Klute,[155] D. Kovalskyi,[155] Y.-J. Lee,[155] A. Levin,[155] P. D. Luckey,[155] B. Maier,[155] A. C. Marini,[155] C. Mcginn,[155] C. Mironov,[155] S. Narayanan,[155] X. Niu,[155] C. Paus,[155] C. Roland,[155] G. Roland,[155] J. Salfeld-Nebgen,[155] G. S. F. Stephans,[155] K. Sumorok,[155] K. Tatar,[155] D. Velicanu,[155] J. Wang,[155] T. W. Wang,[155] B. Wyslouch,[155] A. C. Benvenuti,[156] R. M. Chatterjee,[156] A. Evans,[156] P. Hansen,[156] J. Hiltbrand,[156] S. Kalafut,[156] Y. Kubota,[156] Z. Lesko,[156] J. Mans,[156] S. Nourbakhsh,[156] N. Ruckstuhl,[156] R. Rusack,[156] J. Turkewitz,[156] M. A. Wadud,[156] J. G. Acosta,[157] S. Oliveros,[157] E. Avdeeva,[158] K. Bloom,[158] D. R. Claes,[158] C. Fangmeier,[158] F. Golf,[158] R. Gonzalez Suarez,[158] R. Kamalieddin,[158] I. Kravchenko,[158] J. Monroy,[158] J. E. Siado,[158] G. R. Snow,[158] B. Stieger,[158] J. Dolen,[159] A. Godshalk,[159] C. Harrington,[159] I. Iashvili,[159] D. Nguyen,[159] A. Parker,[159] S. Rappoccio,[159] B. Roozbahani,[159] G. Alverson,[160] E. Barberis,[160] C. Freer,[160] A. Hortiangtham,[160] A. Massironi,[160] D. M. Morse,[160] T. Orimoto,[160] R. Teixeira De Lima,[160] T. Wamorkar,[160] B. Wang,[160] A. Wisecarver,[160] D. Wood,[160] S. Bhattacharya,[161] O. Charaf,[161] K. A. Hahn,[161] N. Mucia,[161] N. Odell,[161] M. H. Schmitt,[161] K. Sung,[161] M. Trovato,[161] M. Velasco,[161] R. Bucci,[162] N. Dev,[162] M. Hildreth,[162] K. Hurtado Anampa,[162] C. Jessop,[162] D. J. Karmgard,[162] N. Kellams,[162] K. Lannon,[162] W. Li,[162] N. Loukas,[162] N. Marinelli,[162] F. Meng,[162] C. Mueller,[162] Y. Musienko,[162,ll] M. Planer,[162] A. Reinsvold,[162] R. Ruchti,[162] P. Siddireddy,[162] G. Smith,[162] S. Taroni,[162] M. Wayne,[162] A. Wightman,[162] M. Wolf,[162] A. Woodard,[162] J. Alimena,[163] L. Antonelli,[163] B. Bylsma,[163] L. S. Durkin,[163] S. Flowers,[163] B. Francis,[163] A. Hart,[163] C. Hill,[163] W. Ji,[163] T. Y. Ling,[163] B. Liu,[163] W. Luo,[163] B. L. Winer,[163] H. W. Wulsin,[163] S. Cooperstein,[164] O. Driga,[164] P. Elmer,[164] J. Hardenbrook,[164] P. Hebda,[164] S. Higginbotham,[164] A. Kalogeropoulos,[164] D. Lange,[164] J. Luo,[164] D. Marlow,[164] K. Mei,[164] I. Ojalvo,[164] J. Olsen,[164] C. Palmer,[164] P. Piroué,[164] D. Stickland,[164] C. Tully,[164] S. Malik,[165] S. Norberg,[165] A. Barker,[166] V. E. Barnes,[166] S. Das,[166] S. Folgueras,[166] L. Gutay,[166] M. Jones,[166] A. W. Jung,[166] A. Khatiwada,[166] D. H. Miller,[166] N. Neumeister,[166] C. C. Peng,[166] H. Qiu,[166] J. F. Schulte,[166] J. Sun,[166] F. Wang,[166] R. Xiao,[166] W. Xie,[166] T. Cheng,[167] N. Parashar,[167] J. Stupak,[167] Z. Chen,[168] K. M. Ecklund,[168] S. Freed,[168] F. J. M. Geurts,[168] M. Guilbaud,[168] M. Kilpatrick,[168] W. Li,[168] B. Michlin,[168] B. P. Padley,[168] J. Roberts,[168] J. Rorie,[168] W. Shi,[168] Z. Tu,[168] J. Zabel,[168] A. Zhang,[168] A. Bodek,[169] P. de Barbaro,[169] R. Demina,[169] Y. t. Duh,[169] T. Ferbel,[169] M. Galanti,[169] A. Garcia-Bellido,[169] J. Han,[169] O. Hindrichs,[169] A. Khukhunaishvili,[169] K. H. Lo,[169] P. Tan,[169] M. Verzetti,[169] R. Ciesielski,[170] K. Goulianos,[170] C. Mesropian,[170] A. Agapitos,[171] J. P. Chou,[171] Y. Gershtein,[171] T. A. Gómez Espinosa,[171] E. Halkiadakis,[171] M. Heindl,[171] E. Hughes,[171] S. Kaplan,[171] R. Kunnawalkam Elayavalli,[171] S. Kyriacou,[171] A. Lath,[171] R. Montalvo,[171] K. Nash,[171] M. Osherson,[171] H. Saka,[171] S. Salur,[171] S. Schnetzer,[171] D. Sheffield,[171] S. Somalwar,[171] R. Stone,[171] S. Thomas,[171] P. Thomassen,[171] M. Walker,[171] A. G. Delannoy,[172] J. Heideman,[172] G. Riley,[172] K. Rose,[172] S. Spanier,[172] K. Thapa,[172] O. Bouhali,[173,uuu] A. Castaneda Hernandez,[173,uuu] A. Celik,[173] M. Dalchenko,[173] M. De Mattia,[173] A. Delgado,[173] S. Dildick,[173] R. Eusebi,[173] J. Gilmore,[173] T. Huang,[173] T. Kamon,[173,vvv] R. Mueller,[173] Y. Pakhotin,[173] R. Patel,[173] A. Perloff,[173] L. Perniè,[173] D. Rathjens,[173] A. Safonov,[173] A. Tatarinov,[173] N. Akchurin,[174] J. Damgov,[174] F. De Guio,[174] P. R. Dudero,[174] J. Faulkner,[174] E. Gurpinar,[174] S. Kunori,[174] K. Lamichhane,[174] S. W. Lee,[174] T. Libeiro,[174] T. Mengke,[174] S. Muthumuni,[174] T. Peltola,[174] S. Undleeb,[174] I. Volobouev,[174] Z. Wang,[174] S. Greene,[175] A. Gurrola,[175] R. Janjam,[175] W. Johns,[175] C. Maguire,[175] A. Melo,[175] H. Ni,[175] K. Padeken,[175] P. Sheldon,[175] S. Tuo,[175] J. Velkovska,[175] Q. Xu,[175] M. W. Arenton,[176] P. Barria,[176] B. Cox,[176] R. Hirosky,[176] M. Joyce,[176] A. Ledovskoy,[176] H. Li,[176] C. Neu,[176] T. Sinthuprasith,[176] Y. Wang,[176] E. Wolfe,[176] F. Xia,[176] R. Harr,[177] P. E. Karchin,[177] N. Poudyal,[177] J. Sturdy,[177] P. Thapa,[177] S. Zaleski,[177] M. Brodski,[178] J. Buchanan,[178] C. Caillol,[178] D. Carlsmith,[178] S. Dasu,[178] L. Dodd,[178] S. Duric,[178] B. Gomber,[178] M. Grothe,[178] M. Herndon,[178] A. Hervé,[178]

U. Hussain,[178] P. Klabbers,[178] A. Lanaro,[178] A. Levine,[178] K. Long,[178] R. Loveless,[178] T. Ruggles,[178] A. Savin,[178] N. Smith,[178] W. H. Smith,[178] D. Taylor,[178] and N. Woods[178]

(CMS Collaboration)

[1]*Yerevan Physics Institute, Yerevan, Armenia*
[2]*Institut für Hochenergiephysik, Wien, Austria*
[3]*Institute for Nuclear Problems, Minsk, Belarus*
[4]*Universiteit Antwerpen, Antwerpen, Belgium*
[5]*Vrije Universiteit Brussel, Brussel, Belgium*
[6]*Université Libre de Bruxelles, Bruxelles, Belgium*
[7]*Ghent University, Ghent, Belgium*
[8]*Université Catholique de Louvain, Louvain-la-Neuve, Belgium*
[9]*Centro Brasileiro de Pesquisas Fisicas, Rio de Janeiro, Brazil*
[10]*Universidade do Estado do Rio de Janeiro, Rio de Janeiro, Brazil*
[11a]*Universidade Estadual Paulista, São Paulo, Brazil*
[11b]*Universidade Federal do ABC, São Paulo, Brazil*
[12]*Institute for Nuclear Research and Nuclear Energy, Bulgarian Academy of Sciences, Sofia, Bulgaria*
[13]*University of Sofia, Sofia, Bulgaria*
[14]*Beihang University, Beijing, China*
[15]*Institute of High Energy Physics, Beijing, China*
[16]*State Key Laboratory of Nuclear Physics and Technology, Peking University, Beijing, China*
[17]*Tsinghua University, Beijing, China*
[18]*Universidad de Los Andes, Bogota, Colombia*
[19]*University of Split, Faculty of Electrical Engineering, Mechanical Engineering and Naval Architecture, Split, Croatia*
[20]*University of Split, Faculty of Science, Split, Croatia*
[21]*Institute Rudjer Boskovic, Zagreb, Croatia*
[22]*University of Cyprus, Nicosia, Cyprus*
[23]*Charles University, Prague, Czech Republic*
[24]*Universidad San Francisco de Quito, Quito, Ecuador*
[25]*Academy of Scientific Research and Technology of the Arab Republic of Egypt, Egyptian Network of High Energy Physics, Cairo, Egypt*
[26]*National Institute of Chemical Physics and Biophysics, Tallinn, Estonia*
[27]*Department of Physics, University of Helsinki, Helsinki, Finland*
[28]*Helsinki Institute of Physics, Helsinki, Finland*
[29]*Lappeenranta University of Technology, Lappeenranta, Finland*
[30]*IRFU, CEA, Université Paris-Saclay, Gif-sur-Yvette, France*
[31]*Laboratoire Leprince-Ringuet, Ecole polytechnique, CNRS/IN2P3, Université Paris-Saclay, Palaiseau, France*
[32]*Université de Strasbourg, CNRS, IPHC UMR 7178, Strasbourg, France*
[33]*Centre de Calcul de l'Institut National de Physique Nucleaire et de Physique des Particules, CNRS/IN2P3, Villeurbanne, France*
[34]*Université de Lyon, Université Claude Bernard Lyon 1, CNRS-IN2P3, Institut de Physique Nucléaire de Lyon, Villeurbanne, France*
[35]*Georgian Technical University, Tbilisi, Georgia*
[36]*Tbilisi State University, Tbilisi, Georgia*
[37]*RWTH Aachen University, I. Physikalisches Institut, Aachen, Germany*
[38]*RWTH Aachen University, III. Physikalisches Institut A, Aachen, Germany*
[39]*RWTH Aachen University, III. Physikalisches Institut B, Aachen, Germany*
[40]*Deutsches Elektronen-Synchrotron, Hamburg, Germany*
[41]*University of Hamburg, Hamburg, Germany*
[42]*Institut für Experimentelle Teilchenphysik, Karlsruhe, Germany*
[43]*Institute of Nuclear and Particle Physics (INPP), NCSR Demokritos, Aghia Paraskevi, Greece*
[44]*National and Kapodistrian University of Athens, Athens, Greece*
[45]*National Technical University of Athens, Athens, Greece*
[46]*University of Ioánnina, Ioánnina, Greece*
[47]*MTA-ELTE Lendület CMS Particle and Nuclear Physics Group, Eötvös Loránd University, Budapest, Hungary*

[48]*Wigner Research Centre for Physics, Budapest, Hungary*
[49]*Institute of Nuclear Research ATOMKI, Debrecen, Hungary*
[50]*Institute of Physics, University of Debrecen, Debrecen, Hungary*
[51]*Indian Institute of Science (IISc), Bangalore, India*
[52]*National Institute of Science Education and Research, Bhubaneswar, India*
[53]*Panjab University, Chandigarh, India*
[54]*University of Delhi, Delhi, India*
[55]*Saha Institute of Nuclear Physics, HBNI, Kolkata, India*
[56]*Indian Institute of Technology Madras, Madras, India*
[57]*Bhabha Atomic Research Centre, Mumbai, India*
[58]*Tata Institute of Fundamental Research-A, Mumbai, India*
[59]*Tata Institute of Fundamental Research-B, Mumbai, India*
[60]*Indian Institute of Science Education and Research (IISER), Pune, India*
[61]*Institute for Research in Fundamental Sciences (IPM), Tehran, Iran*
[62]*University College Dublin, Dublin, Ireland*
[63a]*INFN Sezione di Bari, Bari, Italy*
[63b]*Università di Bari, Bari, Italy*
[63c]*Politecnico di Bari, Bari, Italy*
[64a]*INFN Sezione di Bologna, Bologna, Italy*
[64b]*Università di Bologna, Bologna, Italy*
[65a]*INFN Sezione di Catania, Catania, Italy*
[65b]*Università di Catania, Catania, Italy*
[66a]*INFN Sezione di Firenze, Firenze, Italy*
[66b]*Università di Firenze, Firenze, Italy*
[67]*INFN Laboratori Nazionali di Frascati, Frascati, Italy*
[68a]*INFN Sezione di Genova, Genova, Italy*
[68b]*Università di Genova, Genova, Italy*
[69a]*INFN Sezione di Milano-Bicocca, Milano, Italy*
[69b]*Università di Milano-Bicocca, Milano, Italy*
[70a]*INFN Sezione di Napoli, Roma, Italy*
[70b]*Università di Napoli 'Federico II', Roma, Italy*
[70c]*Università della Basilicata, Roma, Italy*
[70d]*Università G. Marconi, Roma, Italy*
[71a]*INFN Sezione di Padova, Trento, Italy*
[71b]*Università di Padova, Trento, Italy*
[71c]*Università di Trento, Trento, Italy*
[72a]*INFN Sezione di Pavia, Pavia, Italy*
[72b]*Università di Pavia, Pavia, Italy*
[73a]*INFN Sezione di Perugia, Perugia, Italy*
[73b]*Università di Perugia, Perugia, Italy*
[74a]*INFN Sezione di Pisa, Pisa, Italy*
[74b]*Università di Pisa, Pisa, Italy*
[74c]*Scuola Normale Superiore di Pisa, Pisa, Italy*
[75a]*INFN Sezione di Roma, Rome, Italy*
[75b]*Sapienza Università di Roma, Rome, Italy*
[76a]*INFN Sezione di Torino, Torino, Italy*
[76b]*Università di Torino, Torino, Italy*
[76c]*Università del Piemonte Orientale, Novara, Italy*
[77a]*INFN Sezione di Trieste, Trieste, Italy*
[77b]*Università di Trieste, Trieste, Italy*
[78]*Kyungpook National University, Daegu, Korea*
[79]*Chonnam National University, Institute for Universe and Elementary Particles, Kwangju, Korea*
[80]*Hanyang University, Seoul, Korea*
[81]*Korea University, Seoul, Korea*
[82]*Seoul National University, Seoul, Korea*
[83]*University of Seoul, Seoul, Korea*
[84]*Sungkyunkwan University, Suwon, Korea*
[85]*Vilnius University, Vilnius, Lithuania*
[86]*National Centre for Particle Physics, Universiti Malaya, Kuala Lumpur, Malaysia*
[87]*Centro de Investigacion y de Estudios Avanzados del IPN, Mexico City, Mexico*

[88]*Universidad Iberoamericana, Mexico City, Mexico*
[89]*Benemerita Universidad Autonoma de Puebla, Puebla, Mexico*
[90]*Universidad Autónoma de San Luis Potosí, San Luis Potosí, Mexico*
[91]*University of Auckland, Auckland, New Zealand*
[92]*University of Canterbury, Christchurch, New Zealand*
[93]*National Centre for Physics, Quaid-I-Azam University, Islamabad, Pakistan*
[94]*National Centre for Nuclear Research, Swierk, Poland*
[95]*Institute of Experimental Physics, Faculty of Physics, University of Warsaw, Warsaw, Poland*
[96]*Laboratório de Instrumentação e Física Experimental de Partículas, Lisboa, Portugal*
[97]*Joint Institute for Nuclear Research, Dubna, Russia*
[98]*Petersburg Nuclear Physics Institute, Gatchina (St. Petersburg), Russia*
[99]*Institute for Nuclear Research, Moscow, Russia*
[100]*Institute for Theoretical and Experimental Physics, Moscow, Russia*
[101]*Moscow Institute of Physics and Technology, Moscow, Russia*
[102]*National Research Nuclear University 'Moscow Engineering Physics Institute' (MEPhI), Moscow, Russia*
[103]*P. N. Lebedev Physical Institute, Moscow, Russia*
[104]*Skobeltsyn Institute of Nuclear Physics, Lomonosov Moscow State University, Moscow, Russia*
[105]*Novosibirsk State University (NSU), Novosibirsk, Russia*
[106]*State Research Center of Russian Federation, Institute for High Energy Physics of NRC "Kurchatov Institute", Protvino, Russia*
[107]*University of Belgrade, Faculty of Physics and Vinca Institute of Nuclear Sciences, Belgrade, Serbia*
[108]*Centro de Investigaciones Energéticas Medioambientales y Tecnológicas (CIEMAT), Madrid, Spain*
[109]*Universidad Autónoma de Madrid, Madrid, Spain*
[110]*Universidad de Oviedo, Oviedo, Spain*
[111]*Instituto de Física de Cantabria (IFCA), CSIC-Universidad de Cantabria, Santander, Spain*
[112]*CERN, European Organization for Nuclear Research, Geneva, Switzerland*
[113]*Paul Scherrer Institut, Villigen, Switzerland*
[114]*ETH Zurich - Institute for Particle Physics and Astrophysics (IPA), Zurich, Switzerland*
[115]*Universität Zürich, Zurich, Switzerland*
[116]*National Central University, Chung-Li, Taiwan*
[117]*National Taiwan University (NTU), Taipei, Taiwan*
[118]*Chulalongkorn University, Faculty of Science, Department of Physics, Bangkok, Thailand*
[119]*Çukurova University, Physics Department, Science and Art Faculty, Adana, Turkey*
[120]*Middle East Technical University, Physics Department, Ankara, Turkey*
[121]*Bogazici University, Istanbul, Turkey*
[122]*Istanbul Technical University, Istanbul, Turkey*
[123]*Institute for Scintillation Materials of National Academy of Science of Ukraine, Kharkov, Ukraine*
[124]*National Scientific Center, Kharkov Institute of Physics and Technology, Kharkov, Ukraine*
[125]*University of Bristol, Bristol, United Kingdom*
[126]*Rutherford Appleton Laboratory, Didcot, United Kingdom*
[127]*Imperial College, London, United Kingdom*
[128]*Brunel University, Uxbridge, United Kingdom*
[129]*Baylor University, Waco, Texas, USA*
[130]*Catholic University of America, Washington, DC, USA*
[131]*The University of Alabama, Tuscaloosa, Alabama, USA*
[132]*Boston University, Boston, Massachusetts, USA*
[133]*Brown University, Providence, Rhode Island, USA*
[134]*University of California, Davis, Davis, California, USA*
[135]*University of California, Los Angeles, Los Angeles, California USA*
[136]*University of California, Riverside, Riverside, California, USA*
[137]*University of California, San Diego, La Jolla, California, USA*
[138]*University of California, Santa Barbara, Department of Physics, Santa Barbara, California, USA*
[139]*California Institute of Technology, Pasadena, California, USA*
[140]*Carnegie Mellon University, Pittsburgh, Pennsylvania, USA*
[141]*University of Colorado Boulder, Boulder, Colorado, USA*
[142]*Cornell University, Ithaca, New York, USA*
[143]*Fermi National Accelerator Laboratory, Batavia, Illinois, USA*
[144]*University of Florida, Gainesville, Florida, USA*
[145]*Florida International University, Miami, Florida, USA*

[146]*Florida State University, Tallahassee, Florida, USA*
[147]*Florida Institute of Technology, Melbourne, Florida, USA*
[148]*University of Illinois at Chicago (UIC), Chicago, Illinois, USA*
[149]*The University of Iowa, Iowa City, Iowa, USA*
[150]*Johns Hopkins University, Baltimore, Maryland, USA*
[151]*The University of Kansas, Lawrence, Kansas, USA*
[152]*Kansas State University, Manhattan, Kansas, USA*
[153]*Lawrence Livermore National Laboratory, Livermore, California, USA*
[154]*University of Maryland, College Park, Maryland, USA*
[155]*Massachusetts Institute of Technology, Cambridge, Massachusetts, USA*
[156]*University of Minnesota, Minneapolis, Minnesota, USA*
[157]*University of Mississippi, Oxford, Mississippi, USA*
[158]*University of Nebraska-Lincoln, Lincoln, Nebraska, USA*
[159]*State University of New York at Buffalo, Buffalo, New York, USA*
[160]*Northeastern University, Boston, Massachusetts, USA*
[161]*Northwestern University, Evanston, Illinois, USA*
[162]*University of Notre Dame, Notre Dame, Indiana, USA*
[163]*The Ohio State University, Columbus, Ohio, USA*
[164]*Princeton University, Princeton, New Jersey, USA*
[165]*University of Puerto Rico, Mayaguez, Puerto Rico*
[166]*Purdue University, West Lafayette, Indiana, USA*
[167]*Purdue University Northwest, Hammond, Indiana, USA*
[168]*Rice University, Houston, Texas, USA*
[169]*University of Rochester, Rochester, New York, USA*
[170]*The Rockefeller University, New York, New York, USA*
[171]*Rutgers, The State University of New Jersey, Piscataway, New Jersey, USA*
[172]*University of Tennessee, Knoxville, Tennessee, USA*
[173]*Texas A&M University, College Station, Texas, USA*
[174]*Texas Tech University, Lubbock, Texas, USA*
[175]*Vanderbilt University, Nashville, Tennessee, USA*
[176]*University of Virginia, Charlottesville, Virginia, USA*
[177]*Wayne State University, Detroit, Michigan, USA*
[178]*University of Wisconsin - Madison, Madison, Wisconsin, USA*

[a]Deceased.
[b]Also at Vienna University of Technology, Vienna, Austria.
[c]Also at IRFU, CEA, Université Paris-Saclay, Gif-sur-Yvette, France.
[d]Also at Universidade Estadual de Campinas, Campinas, Brazil.
[e]Also at Federal University of Rio Grande do Sul, Porto Alegre, Brazil.
[f]Also at Université Libre de Bruxelles, Bruxelles, Belgium.
[g]Also at Institute for Theoretical and Experimental Physics, Moscow, Russia.
[h]Also at Joint Institute for Nuclear Research, Dubna, Russia.
[i]Also at Zewail City of Science and Technology, Zewail, Egypt.
[j]Also at Fayoum University, El-Fayoum, Egypt.
[k]Also at British University in Egypt, Cairo, Egypt.
[l]Also at Ain Shams University, Cairo, Egypt.
[m]Also at Department of Physics, King Abdulaziz University, Jeddah, Saudi Arabia.
[n]Also at Université de Haute Alsace, Mulhouse, France.
[o]Also at Skobeltsyn Institute of Nuclear Physics, Lomonosov Moscow State University, Moscow, Russia.
[p]Also at Tbilisi State University, Tbilisi, Georgia.
[q]Also at CERN, European Organization for Nuclear Research, Geneva, Switzerland.
[r]Also at RWTH Aachen University, III. Physikalisches Institut A, Aachen, Germany.
[s]Also at University of Hamburg, Hamburg, Germany.
[t]Also at Brandenburg University of Technology, Cottbus, Germany.
[u]Also at MTA-ELTE Lendület CMS Particle and Nuclear Physics Group, Eötvös Loránd University, Budapest, Hungary.
[v]Also at Institute of Nuclear Research ATOMKI, Debrecen, Hungary.
[w]Also at Institute of Physics, University of Debrecen, Debrecen, Hungary.
[x]Also at IIT Bhubaneswar, Bhubaneswar, India.
[y]Also at Institute of Physics, Bhubaneswar, India.
[z]Also at University of Visva-Bharati, Santiniketan, India.

[aa]Also at University of Ruhuna, Matara, Sri Lanka.
[bb]Also at Isfahan University of Technology, Isfahan, Iran.
[cc]Also at Yazd University, Yazd, Iran.
[dd]Also at Plasma Physics Research Center, Science and Research Branch, Islamic Azad University, Tehran, Iran.
[ee]Also at Università degli Studi di Siena, Siena, Italy.
[ff]Also at INFN Sezione di Milano-Bicocca, Università di Milano-Bicocca, Milano, Italy.
[gg]Also at Purdue University, West Lafayette, IN, USA.
[hh]Also at International Islamic University of Malaysia, Kuala Lumpur, Malaysia.
[ii]Also at Malaysian Nuclear Agency, MOSTI, Kajang, Malaysia.
[jj]Also at Consejo Nacional de Ciencia y Tecnología, Mexico city, Mexico.
[kk]Also at Warsaw University of Technology, Institute of Electronic Systems, Warsaw, Poland.
[ll]Also at Institute for Nuclear Research, Moscow, Russia.
[mm]Also at National Research Nuclear University 'Moscow Engineering Physics Institute' (MEPhI), Moscow, Russia.
[nn]Also at Institute of Nuclear Physics of the Uzbekistan Academy of Sciences, Tashkent, Uzbekistan.
[oo]Also at St. Petersburg State Polytechnical University, St. Petersburg, Russia.
[pp]Also at University of Florida, Gainesville, FL, USA.
[qq]Also at P. N. Lebedev Physical Institute, Moscow, Russia.
[rr]Also at California Institute of Technology, Pasadena, CA, USA.
[ss]Also at Budker Institute of Nuclear Physics, Novosibirsk, Russia.
[tt]Also at Faculty of Physics, University of Belgrade, Belgrade, Serbia.
[uu]Also at University of Belgrade, Faculty of Physics and Vinca Institute of Nuclear Sciences, Belgrade, Serbia.
[vv]Also at Scuola Normale e Sezione dell'INFN, Pisa, Italy.
[ww]Also at National and Kapodistrian University of Athens, Athens, Greece.
[xx]Also at Riga Technical University, Riga, Latvia.
[yy]Also at Universität Zürich, Zurich, Switzerland.
[zz]Also at Stefan Meyer Institute for Subatomic Physics.
[aaa]Also at Gaziosmanpasa University, Tokat, Turkey.
[bbb]Also at Istanbul Aydin University, Istanbul, Turkey.
[ccc]Also at Mersin University, Mersin, Turkey.
[ddd]Also at Cag University, Mersin, Turkey.
[eee]Also at Piri Reis University, Istanbul, Turkey.
[fff]Also at Adiyaman University, Adiyaman, Turkey.
[ggg]Also at Izmir Institute of Technology, Izmir, Turkey.
[hhh]Also at Necmettin Erbakan University, Konya, Turkey.
[iii]Also at Marmara University, Istanbul, Turkey.
[jjj]Also at Kafkas University, Kars, Turkey.
[kkk]Also at Istanbul Bilgi University, Istanbul, Turkey.
[lll]Also at Rutherford Appleton Laboratory, Didcot, United Kingdom.
[mmm]Also at School of Physics and Astronomy, University of Southampton, Southampton, United Kingdom.
[nnn]Also at Instituto de Astrofísica de Canarias, La Laguna, Spain.
[ooo]Also at Utah Valley University, Orem, UT, USA.
[ppp]Also at Beykent University.
[qqq]Also at Bingol University, Bingol, Turkey.
[rrr]Also at Erzincan University, Erzincan, Turkey.
[sss]Also at Sinop University, Sinop, Turkey.
[ttt]Also at Mimar Sinan University, Istanbul, Istanbul, Turkey.
[uuu]Also at Texas A&M University at Qatar, Doha, Qatar.
[vvv]Also at Kyungpook National University.